Functionalization of Phosphorescent Organometallic Complexes Aimed at Application to Solution-Processed Organic Light-Emitting Diodes

Functionalization of Phosphorescent Organometallic Complexes Aimed at Application to Solution-Processed Organic Light-Emitting Diodes

（塗布型有機発光ダイオードへの応用を指向したりん光性有機金属錯体の機能化）

Naoki Okamura

岡村　奈生己

February 2018

Doctoral Thesis at Osaka Prefecture University

Index

Chapter 1

General Introduction

1.1. Introduction of Organic Light-Emitting Diodes

Organic light-emitting diodes (OLEDs) are self-emissive electronic devices typically consisting of a stack of submicron-order organic thin layers between a transparent anode and metal cathode. They have been attracting much attention because they are thin, weigh light, rapidly on-off responsive and solution-processable to provide very high-quality flat panel displays, ultra-slim lighting, wearable electronics devices, and many other electronic applications.

Electroluminescence (EL) of an organic compound was first obtained by M. Pope *et al.* [1] and W. Helflich *et al.* [2] in 1960s. They obtained blue fluorescence from anthracene by applying high voltage of 100−1000 V to its microcrystal in order to inject holes and electrons because the anthracene crystal is an insulator. The injected holes and electrons recombine together to excite the anthracene molecules. In the case of a molecule-based organic solid, the hole and electron correspond to the radical cation and radical anion of the constituent molecules, respectively. In 1982, P. S. Vincent reported that employment of a submicron-order organic thin film is significantly effective in reducing the applied voltage and obtaining stable EL [3]. They obtained visible EL from vacuum-deposited thin films of anthracene and perylene with *ca*. 600 nm thickness at a much lower applied voltage of 12 V than the previous reports [1,2].

In 1987, C. W. Tang and S. A. VanSlyke demonstrated an innovative device showing a high luminance over 1000 cd m^{-2} and an external quantum efficiency (η_{ext}) of *ca*. 1% under a low applied voltage of less than 10 V [4]. The device has a stack of thin layers of an

electron-transporting emitter, tris(8-hydroxyquinolinato)aluminium (Alq_3), and a hole-transporting material, 4,4'-cyclohexylidenebis[*N*,*N*-bis(4-methylphenyl)benzenamine] (TAPC), on a transparent anode (indium tin oxide, ITO) with a MgAg cathode (Fig. 1). This multilayered structure like a p-n heterojunction in inorganic light-emitting diodes affords efficient charge recombination, and thus this is a prototype of the present devices. They also reported efficient red EL from a red fluorescent coumarin dye by doping it into an Alq_3 layer in 1989 [5]. Alq_3 plays a role of an electron-transporting host material and the excited energy transfer from excited Alq_3 to the doped dye affords efficient emission from the doped dye. Nowadays, luminescent dyes are often doped into charge carrier transporting host materials to prepare the emitting layers (EML) showing various EL colors.

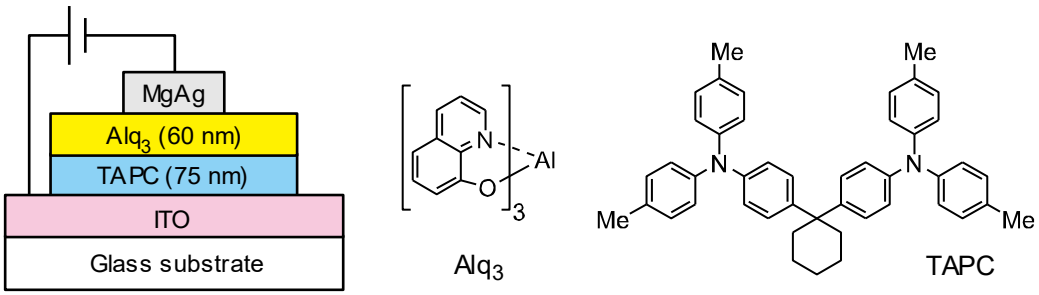

Fig. 1. OLED reported by C. W. Tang and S. A. VanSlyke.

1.2. Phosphorescent Organometallic Complexes

In OLEDs, the excitons generated by the charge recombination are generally divided into the singlet and triplet states in a ratio of 1 : 3 according to spin statistics [6]. Thus when a fluorescent emitter (*e.g.* rubrene, Fig. 2) is used, the device can achieve an internal quantum efficiency (η_{int}) of at most 25%, as shown in Fig. 3a. On the other hand, phosphorescent emitters can achieve η_{int} of as high as 100% in theory, taking account of the intersystem crossing (ISC) from the singlet excited state to the triplet state (Fig. 3b). Therefore, the maximum values of η_{ext}s of fluorescent and phosphorescent OLEDs are *ca*. 5.0% and *ca*. 20%,

respectively, according to eqn 1:

$$\eta_{ext} = \eta_{ex} \times \gamma \times \phi_p \times \eta_{ph} \qquad (1)$$

where η_{ex}, γ, ϕ_p, and η_{ph} are the light-extraction efficiency (*ca*. 0.20 in flat grass devices), the electron-hole charge balance factor (≤ 1), the intrinsic quantum efficiency for radiative decay (≤ 1), and the exciton formation efficiency resulting in radiative transitions (maximum 0.25 and 1 for fluorescent and phosphorescent OLEDs, respectively) [7]. In 1996, S. Hoshino *et al.* obtained phosphorescence-based EL from an OLED employing benzophenone at 100 K, but did not do at 273 K because vibrational deactivation processes are predominant at a relatively high temperature over the spin-forbidden radiative transition with a long emission lifetime [8]. In 1997, M. A. Baldo *et al.* demonstrated a red phosphorescent OLED employing a platinum(II) porphyrin complex, PtOEP (Fig. 2), which exhibited a high η_{ext} of 4% at room temperature [9]. Heavy metal complexes show phosphorescence at room temperature due to the strong spin-orbit coupling facilitating ISC, although organic compounds basically do not show such phenomenon. In 2011, C. Adachi *et al.* achieved a high η_{ext} of 5.3% using a thermally activated delayed fluorescence (TADF) emitter, PIC-TRZ (Fig. 2). The TADF emitter also utilizes both of singlet and triplet excitons for EL due to reverse ISC (RISC) facilitated by the small energy gap between the lowest singlet excited (S_1) state and the triplet (T_1) one, as shown in Fig. 3c [10]. TADF emitters are rare-metal-free, however, it is difficult to obtain EL with high color purity because their strong intramolecular charge transfer characters broaden their EL spectra.

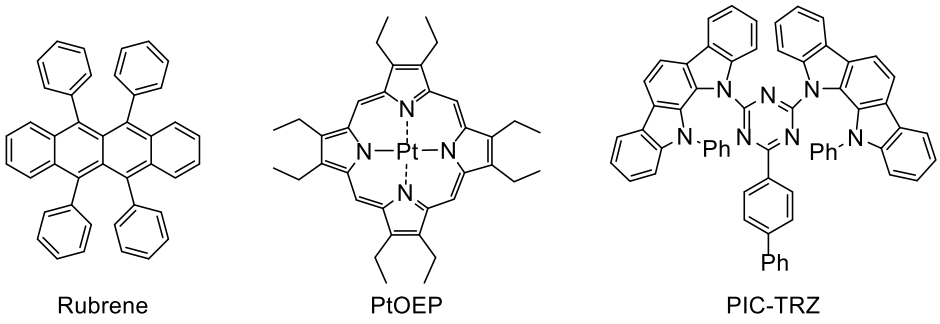

Fig. 2. Structures of early reported fluorescent, phosphorescent, and TADF OLED emitters of rubrene, PtOEP and PIC-TRZ, respectively.

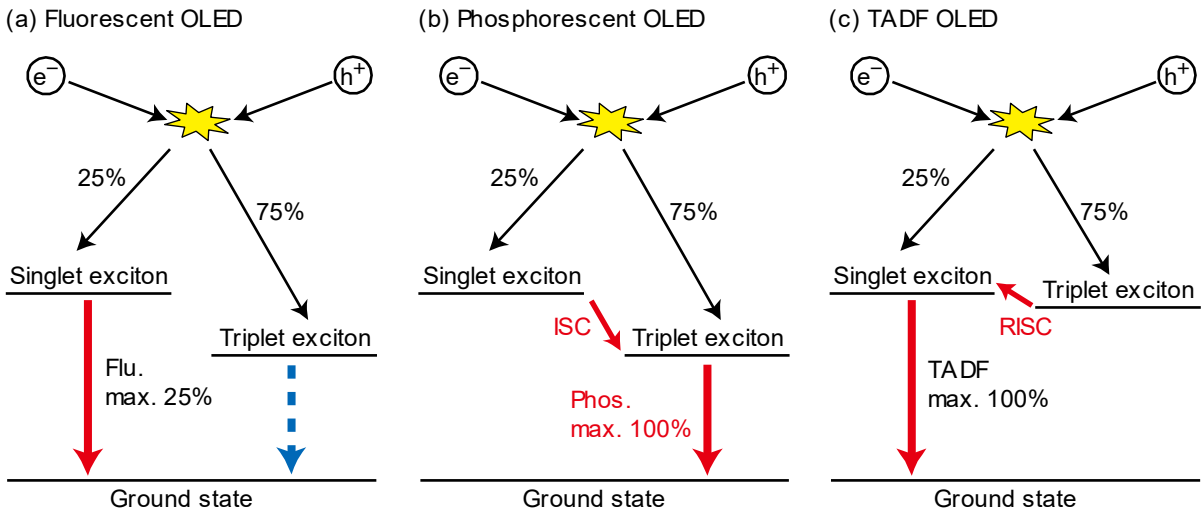

Fig. 3. Exciton generation and EL mechanisms in OLEDs according to spin statistics theorem.

As described above, phosphorescent metal complexes are useful for fabricating efficient OLEDs. In 1999, Baldo *et al.* reported a highly efficient green OLED whose η_{ext} was 7.5%. Therein, a phosphorescent cyclometalated iridium(III) complex *fac*-Ir(*ppy*)$_3$ (*ppy*, 2-phenylpyridinate-*N*,*C*$^{2'}$, Fig. 4) was used [11]. In 2001, C. Adachi reported an extremely high η_{ext} of 19%, or an η_{int} of almost 100%, from an OLED doped with a bis-cyclometalated iridium(III) complex (*ppy*)$_2$Ir(*acac*) (*acac*; acetylacetonate, Fig. 4) [7]. A variety of tris- and bis-cyclometalated iridium(III) complexes have been developed by M. E. Thompson and

many other researchers, showing highly efficient phosphorescence with photoluminescence (PL) quantum yields (Φ_{PL}) of 0.2−0.8 in deaerated solution at ambient temperature (Fig. 4) [12−14]. They generally have an emissive T_1 state based on the metal-to-ligand charge transfer. The emission color is easily designed by modification of their cyclometalated (*C^N*) ligands to tune the T_1 energy level accompanied by the controlled HOMO-LUMO energy gap. For example, $(btp)_2Ir(acac)$ bearing π-extended *C^N* ligands shows red PL with the maximum PL wavelength (λ_{PL}) of 612 nm [14], and a fluorinated complex FIrpic exhibits sky-blue PL at 471 nm in solution (Fig. 4) [15]. Tris- and bis-cyclometalated iridium(III) complexes adopt six-coordinated octahedral geometry. The former have facial (*fac*) and meridional (*mer*) isomers, where the *fac*-isomer is thermodynamically stable in comparison with the kinetically generated *mer*-isomer that is less emissive (Φ_{PL}; 0.40 for *fac*-$(ppy)_3Ir$, 0.036 for *mer*-$(ppy)_3Ir$, in deaerated dichrolomethane) [13]. The latter generally adopts *N*,*N*-*trans*- and *C*,*C*-*cis*-type coordination geometry. An ancillary (*L^X*) ligand is incorporated to the iridium(III) center to give solubility and/or to tune the emission color [15−18]. However, it is more difficult to obtain deep blue emission in phosphorescent organoiridium(III) complexes than in fluorescent organic dyes because the triplet states of bis- and tris-cyclometalated iridium(III) complexes essencially lie at the relatively low energy levels. Therefore, deep-blue phosphorescent complexes have still been under enthusiastic development towards full color OLED devices.

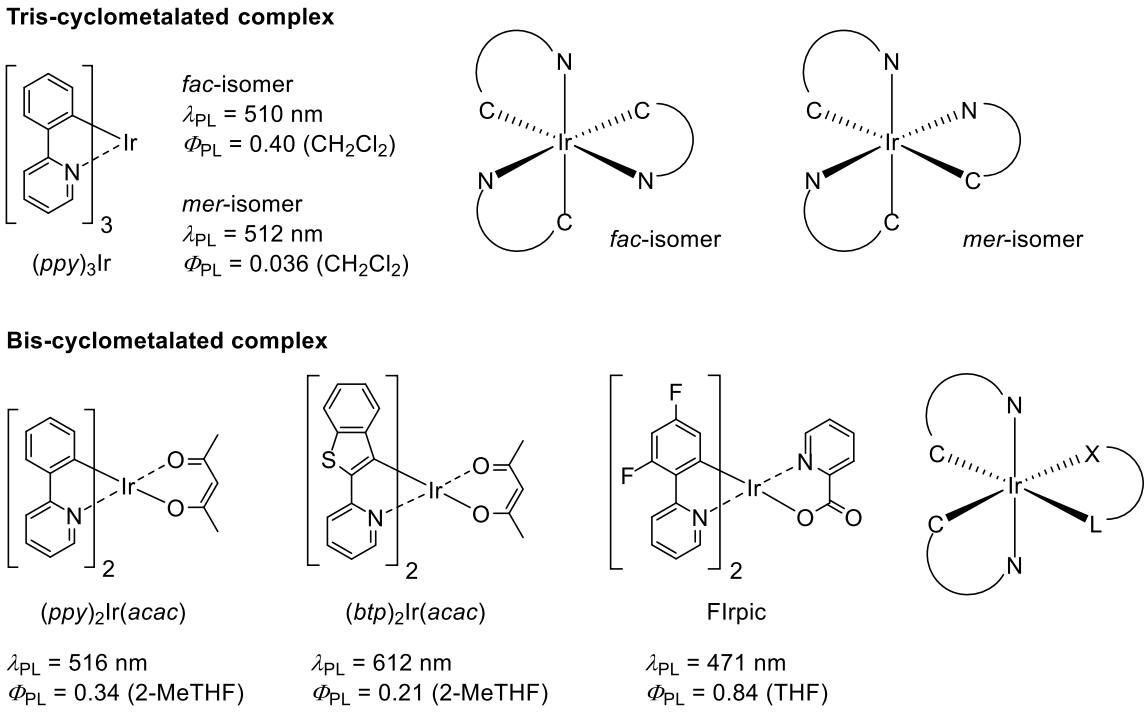

Fig. 4. Structures of typical tris- and bis-cyclometalated iridium(III) complexes with their λ_{PL}s and Φ_{PL}s at rt. 2-MeTHF and THF represent 2-methyltetrahydrofuran and tetrahydrofuran, respectively.

In 2002, M. E. Thompson and co-workers reported that heteroleptic cyclometarated platinum(II) complexes, consisting of *ppy*- and *acac*-based ligands, also show efficient room temperature phosphorescence [19]. The λ_{PL}s are also tuned by modification of their *C^N* ligands as with iridium(III) complexes although the Φ_{PL}s are relatively low in solution. For example, as shown in Fig. 5, (*ppy*)Pt(*acac*) and (*46dfppy*)Pt(*acac*) show bluish green (λ_{PL}; 486 nm) and sky-blue (λ_{PL}; 466 nm) PL with Φ_{PL}s of 0.15 and 0.02, respectively, in 2-methyltetrahydrofuran. Platinum(II) complexes adopt four-coordinated square planer structures that enhance intermolecular π-π interaction along with Pt-Pt interaction to yield excimer phosphorescence in the longer wavelength region than the monomer one [20−22]. Interestingly, M. E. Thompson *et al.* reported a white OLED (WOLED) employing (*46dfppy*)Pt(*acac*) as a single emitter: an optimizing balance of sky-blue monomer and orange

excimer emissions yielded a broadened EL spectrum covering whole visible region as shown in Fig. 6 [20]. This type of WOLEDs is important in low-cost production of display backlights and room lighting apparatuses because precise tuning of the balance of primary color emitters is avoided.

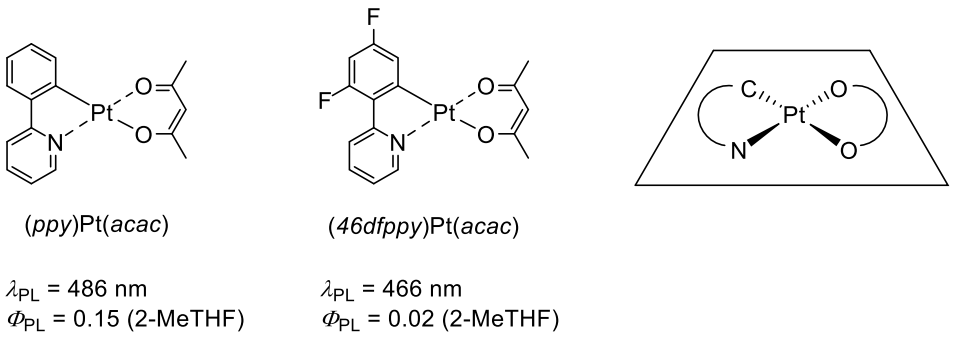

Fig. 5. Structures of typical heteroleptic cyclometalated platinum(II) complexes with their λ_{PL}s and Φ_{PL}s at rt.

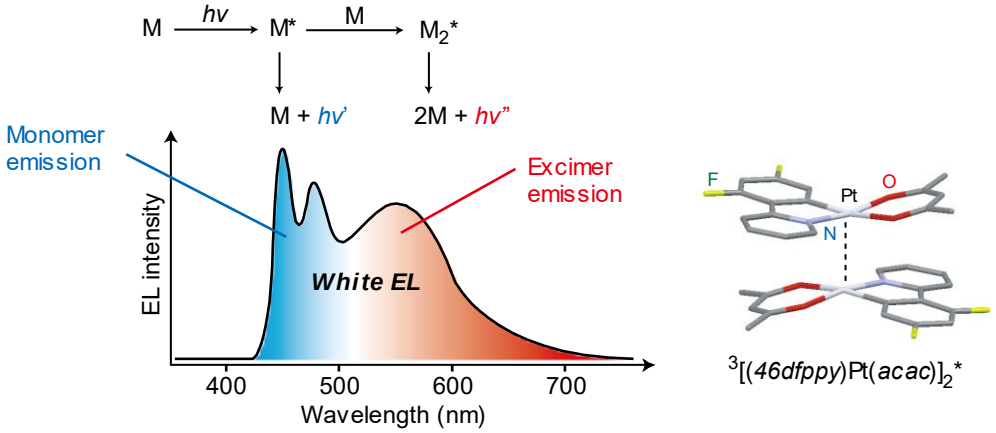

Fig. 6. Illustration of an emission spectrum of excimer-based white EL. The characters M, M^*, and M_2^* represent a ground state monomer, an excited monomer, and an excimer, respectively. The structure of the triplet excimer of (*46dfppy*)Pt(*acac*) is also shown, which was replotted according to the atomic coordinates calculated by Brédas *et al.* [21].

1.3. Device Structures of OLEDs

According to eqn 1, it is also necessary to induce efficient charge recombination (*i.e.* high γ value) for production of efficient OLEDs. The optimized hole-electron recombination is achieved by selecting the suitable device structure [4,23,24]. As shown in Fig. 7, typical device structures of OLEDs bearing one EML are classified into (a) so-called single layer, (b) SH-H, (c) SH-E, and (d) DH structures, although more complicated, multilayered device structures are also employed. The single layer OLED has a simple structure bearing only an EML between a cathode and an anode. The SH-H device has a single heterojunction of a stack of a hole-transporting EML and an electron-transporting layer (ETL). The ETL also acts as a hole-blocking layer (HBL) to afford the efficient charge recombination in EML in the vicinity of the EML/ETL interface. The SH-E device consists of a stack of a hole-transporting layer (HTL) and an electron-transporting EML. As is the case for the SH-H device, the efficient charge recombination is expected because the HTL also plays a role of an electron-blocking layer (EBL). The DH-type OLED has a HTL (EBL)/EML/ETL (HBL)-stacked double-heterojunction structure and generally shows the highest device efficiency due to the confinement of both of holes and electrons in the EML. On the other hand, OLEDs bearing two EMLs, so-called double-EML (D-EML) OLEDs, have also been reported [25−27], which consist of a hole-transporting EML and an electron-transporting EML to utilize the excitons generated in both layers for producing EL. It has been reported that D-EML OLEDs show the longer device lifetimes than single-EML (S-EML) OLEDs as well as the higher device efficiencies.

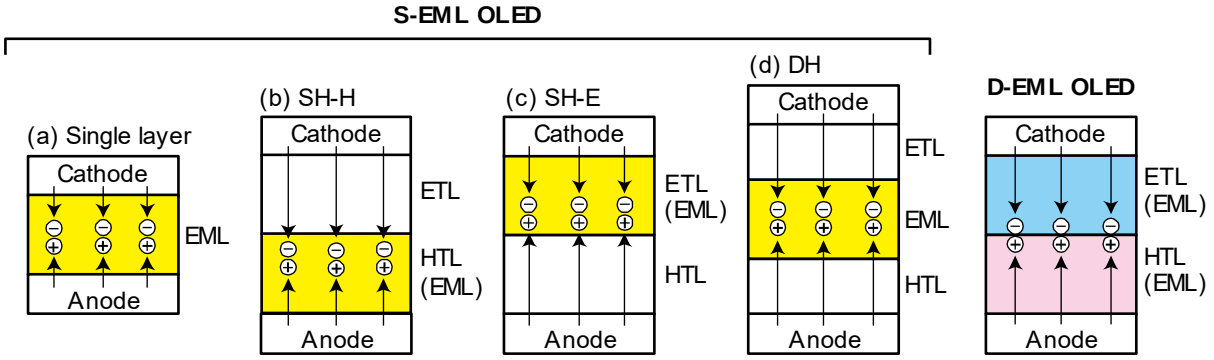

Fig. 7. Typical structures of OLEDs.

Fig. 8 shows a preferable energy diagram of a DH-type dye-doped OLED [28]. Holes and electrons are transported through HOMOs and LUMOs of the organic molecules, respectively, upon application of voltages. Holes injected from the transparent anode (in most cases, ITO) into the HTL *via* the hole-injection layer (HIL) are transported to the EML. Hole-doped conductive polymers such as poly(3,4-ethylenedioxythiophene):poly(styrene sulfonate) (PEDOT:PSS, Fig. 9) [29] are employed as HIL materials to reduce the hole-injection barrier from the anode to the organic layer. The highest energy level of the valence band (E_v) of the HIL is preferred to lie between the E_v of the anode and the HOMO level (E_{HOMO}) of HTL. On the other hand, holes hardly go into the ETL (EBL) because the E_{HOMO} of the ETL is much lower than that of the EML. Electrons are injected from the cathode to the ETL through the electron-injection layer (EIL), and transported to the EML. Electropositive metals such as aluminum, magnesium and calcium are used as the cathode. An ultrathin layer (0.5−5.0 nm) of an alkali metal salt (*e.g.* LiF, Li_2O and CsF) is often employed as the EIL to reduce the electron-injection barrier because it moderates the polarization at the interface between the metal cathode and the organic layer [30,31]. The electrons are pooled in the EML because the LUMO level (E_{LUMO}) of the HTL is higher than that of the EML. As a result, holes and electrons efficiently combine together in the EML, and make the host material excited. Finally,

the excitation energy transfer occurs from the host material to the dye, and the emission is obtained from the excited dye. As another exciton generation mechanism, the dye is directly excited by the charge recombination in some cases. The S_1 and/or T_1 energy levels of host materials should be higher than those of the doped dye to achieve efficient energy transfer and to suppress the reverse process.

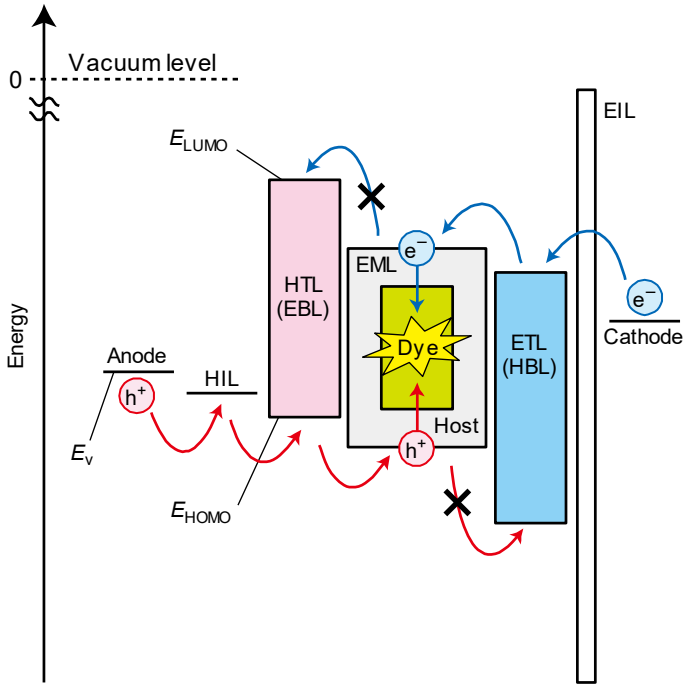

Fig. 8. Preferable energy diagram of a DH-type dye-doped OLED.

Triarylamine (*e.g.* TPD [32]) and carbazole (*e.g.* PVCz [33,34]) derivatives (Fig. 9) are often employed as hole-transporting materials, which form relatively stable radical cations. Electron-deficient benzoimidazole (*e.g.* TPBi [32]), oxadiazole (*e.g.* OXD-7 [32]), and phosphine oxide (*e.g.* DPEPO [35]) derivatives are often used in ETL, most of which are also useful as HBL materials due to their deep HOMO levels (Fig. 9). Amorphous films are preferred for organic layers in OLEDs because the carrier mobilities are reduced in polycrystalline organic films due to the energetic barriers at the grain boundaries. Therefore,

charge carrier transporting materials have been eagerly developed, which are designed to be prevented from crystallization and show high grass transition temperatures to form stable smooth films.

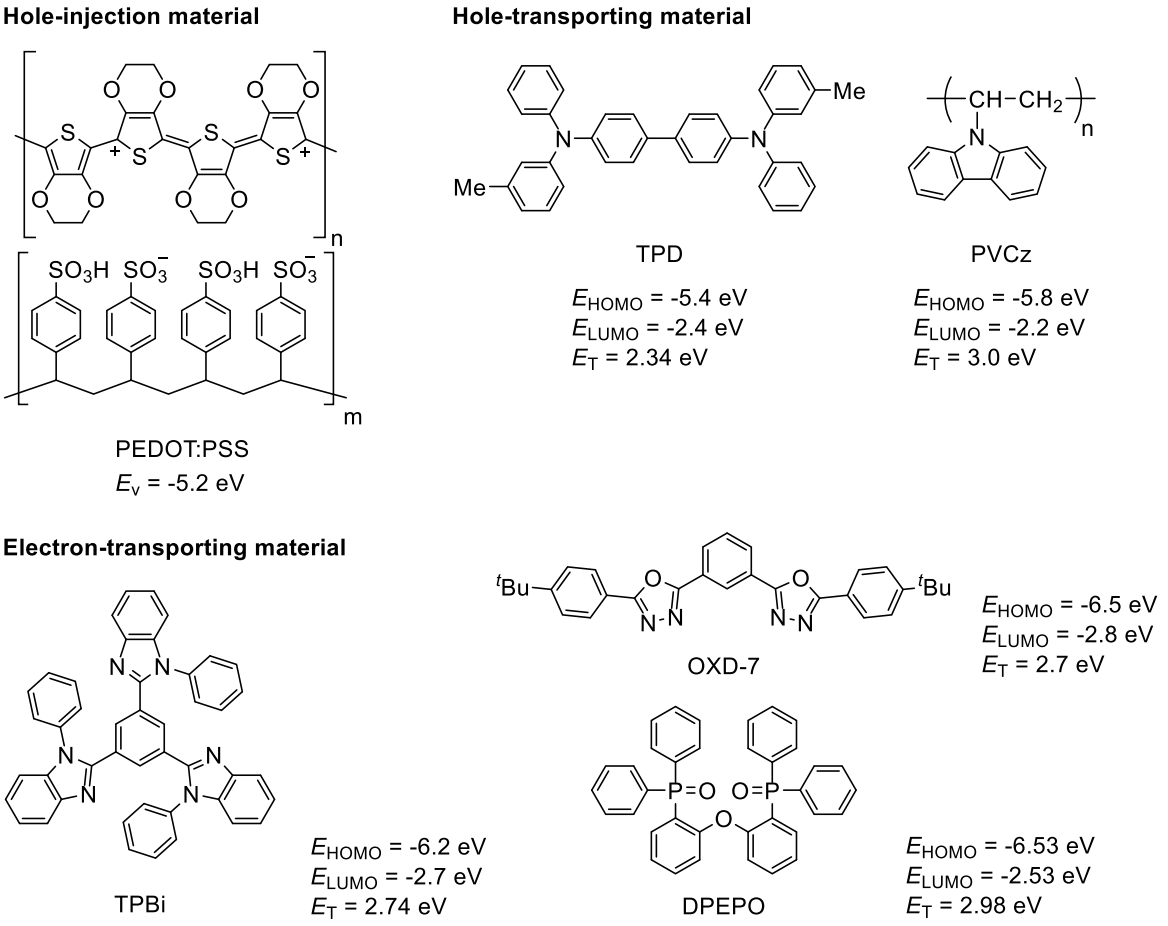

Fig. 9. Structures of hole-injecting, hole-transporting, and electron-transporting materials.

Multilayered OLEDs as discussed above are generally fabricated by a vacuum deposition method: the materials are heated under reduced pressure and sublimed to form layer-by-layer organic thin films on a substrate (Fig. 10) [36,37]. However, in this method, problems such as low efficiency of material utilization, poor scalability, and high running cost to keep high vacuum prevent the mass production of OLEDs. On the other hand, solution processing

methods, such as spin-coating, inkjet printing, and roll coating, have been attracting much attention as a low-cost fabrication method. However, it is difficult to fabricate multilayer devices by solution processing because a lower layer is often eroded when forming the upper layer. In this context, in 2011, G. C. Bazan *et al.* was succeeded in fabrication of a staked structure of HIL/HTL/EML/ETL by successively spin-coating an ethanol solution of a toluene-insoluble HTL material, a toluene solution of ethanol-insoluble EML materials, and an ethanol solution of ETL materials on an ethanol insoluble EIL, as shown in Fig. 11 [38]. They introduced sulfonate groups to HTL and ETL materials to add solubility in ethanol, and employed highly hydrophobic EML materials bearing multiple long alkyl chains. In order to fabricate efficient multilayer OLEDs by solution processing, molecular design strategies to tune the solubility in orthogonal solvents are strongly required.

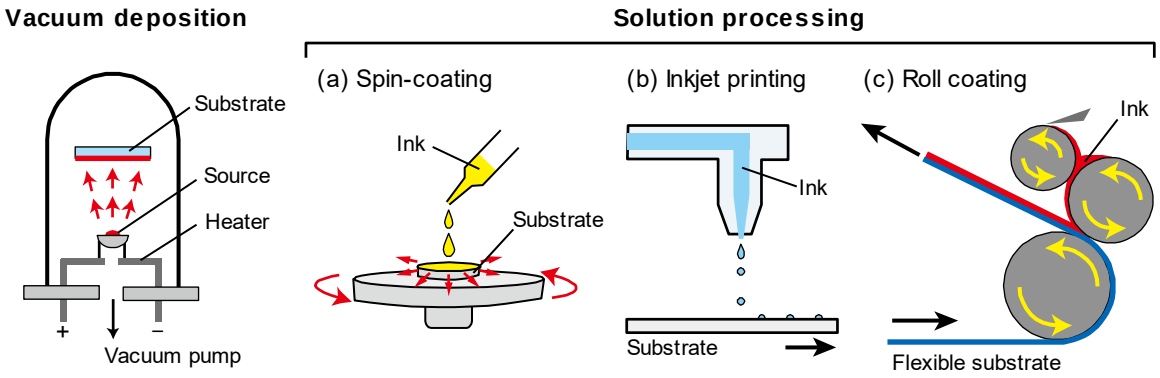

Fig. 10. Illustrations of OLED manufacturing; vacuum deposition and solution-processing.

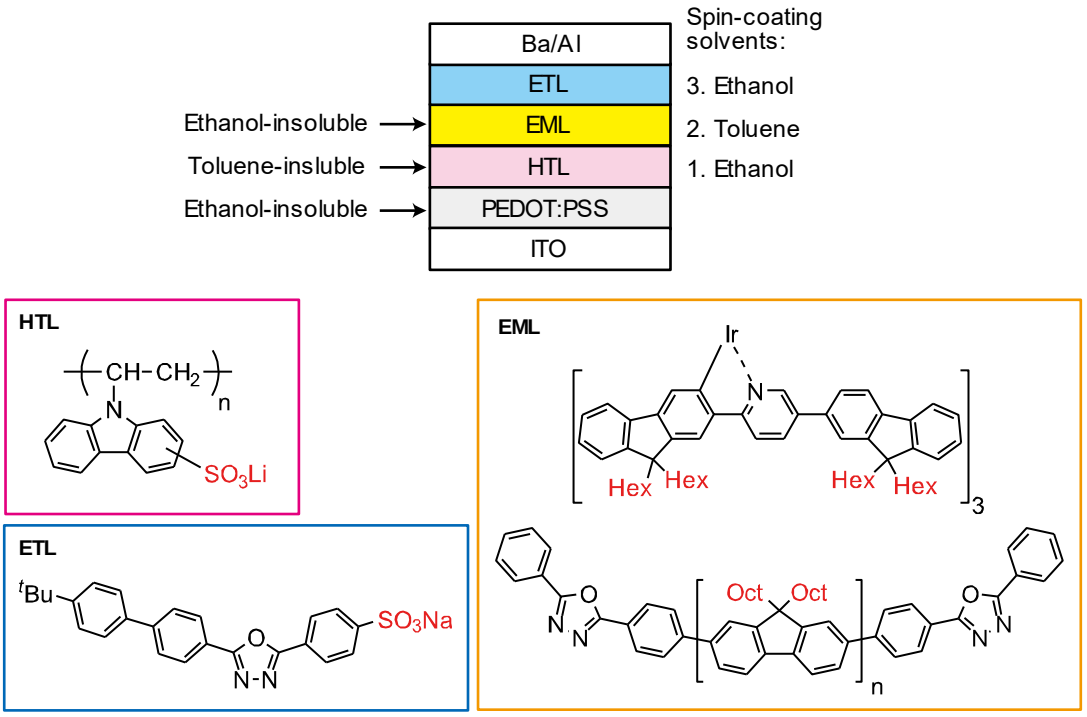

Fig. 11. Solution-processed multilayer OLED reported by G. C. Bazan *et al*.

With respect to low-cost device fabrication, a non-doped OLED whose EML consists of only a single charge carrier transporting emitter has been eagerly developed not only to reduce the number of constituent materials but also to avoid the emitter-host phase separation in EML [39]. S. Tokito *et al.* developed a copolymer, GPP (Fig. 12), consisting of green phosphorescent and hole-transporting comonomers, and fabricated the non-doped OLED showing an η_{ext} of 9% [40]. J. Kido *et al.* developed a dendrimer, $(mCP)_6Ir$ (Fig. 12), bearing a green phosphorescent core and hole-transporting dendrons, and the fabricated non-doped device showed an η_{ext} of 12% at 100 cd m^{-2}, where the bulky dendrons efficiently suppressed concentration quenching between the cores [41].

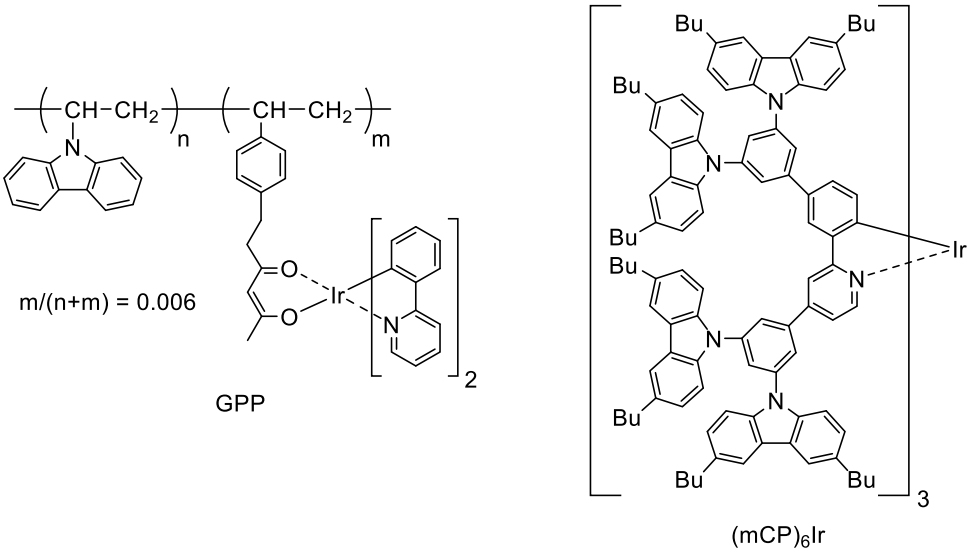

Fig. 12. Structures of hole-transporting phosphorescent emitters for non-doped OLEDs.

1.4. Outline of This Thesis

With the background mentioned above, this thesis is aimed at development of charge carrier transporting phosphorescent organometallics that are applicable to solution-processed multilayer OLEDs, namely, DH-type non-doped devices and D-EML ones (DH and D-EML, see Fig. 7). The author especially focuses on bulky hole-transporting moieties for two purposes: one is to optimize the solubility in orthogonal solvents to fabricate multilayer OLEDs by solution processing, and the other is to control the intermolecular interactions of iridium(III)-based and platinum(II)-based phosphorescent centers to fabricate non-doped sky-blue and white OLEDs, respectively. In addition, the author synthesized an electron-transporting bis-cyclometalated iridium(III) complex for solution-processed D-EML OLEDs. The outline of this thesis is described below.

In Chapter 2, in order to fabricate non-doped multilayer OLEDs by solution processing, the author developed phosphorescent organoiridium(III) complexes bearing hole-transporting dendrons, especially focusing on blue phosphorescent emitters, the

emission color of which is important as one of RGB primary colors.

In Section 2.1, the author synthesized novel bis- and tris-cyclometalated iridium(III) complexes bearing a 5'-benzoyl group on each fluorinated *ppy* ligand, aimed at the development of blue phosphorescent cores of the target dendritc complexes. When *acac* was employed as an ancillary ligand, the λ_{PL} of the 5'-benzoylated bis-cyclometalated complex was blue-shifted up to 479 nm (in dichloromethane at rt) in combination with fluorine substituents at the 4' and 6' positions. Ancillary ligand replacement in the 2-(5-benzoyl-4,6-difluorophenyl)pyridinate-based bis-cyclometalated complex from *acac* (**Ir-3a**) to picolinate (**Ir-3b**, Fig. 13a) gave rise to a further blue shift of λ_{PL} to 464 nm, and sky-blue emission with an excellent Φ_{PL} (0.82 in dichloromethane at rt) was observed. The homoleptic tris-cyclometalated complex consisting of the same cyclometalated ligands (**Ir-3c**, Fig. 13a) had a more blue-shifted λ_{PL} at 463 nm than any other bis- and tris-cyclometalated complexes developed here, emitting sky blue with a photoluminescence quantum yield of 0.90 (in dichloromethane at rt). Using **Ir-3b** and **Ir-3c** as an emitting dopant, solution-processed D-EML OLEDs were fabricated, and excellent sky-blue EL emissions with the Commission Internationale de L'éclairage (CIE) chromaticity coordinates of (0.17, 0.33) and (0.17, 0.29), respectively, were observed, where satisfactory η_{ext}s of 8.55 and 7.46% were obtained, respectively.

In Section 2.2, the author designed and synthesized bis- and tris-cyclometalated iridium(III) complexes **Ir-H1a** and **Ir-H1b** (Fig. 13b) bearing a phosphorescent core based on **Ir-3b** and **Ir-3c**, respectively, and carbazole-appended hole-transporting dendrons. Also, fabrication of non-doped multilayer OLEDs by solution processing was demonstrated by using these complexes as emitting materials. The complexes exhibited sky-blue PL at 460–464 nm with excellent Φ_{PL} of *ca*. 0.8. Their neat films also emitted sky-blue PL: the sterically hindered dendrons effectively suppressed aggregation between the luminescent

cores, although **Ir-3b** and **Ir-3c** exhibited aggregate-based green PL even when they were doped into a model host material of the dendron in the same core-dendron molar ratios as **Ir-H1a** and **Ir-H1b**. As hydrophobic *tert*-butyl groups are placed on the periphery, **Ir-H1** exhibited good solubility in cyclohexane and poor solubility in 2-propanol. Such special properties allowed for fabrication of solution-processed non-doped multilayer OLEDs consisting of a stack of the HTL/EML (**Ir-H1**)/ETL. The devices showed sky-blue EL with η_{ext}s of 4.72−5.72, accompanied with excellent γ values of *ca*. 0.9. These γ values were much higher than those of simple non-doped devices without HTL and ETL (γ; *ca*. 0.1).

In Chapter 3, the author developed organolatinum(II) complexes showing remarkable excimer emission, and investigated the excimer formation process in detail. Also, the author introduced hole-transporting moieties to the excimer-emissive phosphorescnet center in order to control excimer emission and solubility, aimed at solution-processed fabrication of non-doped multilayer WOLEDs.

In Section 3.1, to discover excimer-emissive organoplatinum(II) complexes and investigate the fundamental mechanism of the excimer emission, the author synthesized novel heteroleptic cyclometalated platinum(II) complexes **Pt-1** consisting of 5'-benzoylated *ppy* and *acac* ligands. The complex **Pt-1a** without any other substituents exhibited remarkable excimer emission at *ca*. 600 nm along with the monomer emission at 479 nm in poly(methyl methacrylate) (PMMA) film, showing a relatively high Φ_{PL} of 0.47 at a doping level of 0.20 mmol g^{-1}. In the case of the complexes with unsubstituted, 4'-benzoylated, and 5'-fluorinated *ppy* ligands, excimer emission was modestly generated at the same doping level, and thus the introduction of a benzoyl group to the 5'-position is effective to obtain remarkable excimer emission. The enhancement is likely due to an electronic effect of the carbonyl moiety in the 5'-benzoyl group because a 5'-acetyl group also facilitates the excimer emission. The combination of benzoyl and fluoro groups was

more effective to induce excimer emission, and the intensity of excimer emission of the 2-(5-benzoyl-4,6-difluorophenyl)pyridinate-based complex **Pt-1c** (Fig. 13c) was 3.5 times larger than that of monomer emission at a doping level of 0.20 mmol g^{-1} in PMMA. From the analysis of PL lifetimes at varying concentrations, photokinetic profiles were fully analyzed according to the model system for the irreversible excimer formation, and the excimer formation rate constant of **Pt-1a** was determined in dichloromethane as 2.2×10^9 M^{-1} s^{-1}, which is 4.4 times larger than that of (*ppy*)Pt(*acac*). We also fabricated an OLED using **Pt-1c** as a single emitter. Varying the doping level of the emitter, the ratio of monomer and excimer emissions was optimized to afford an EL spectrum covering the whole visible region, and the device exhibited pseudo-white EL with the CIE chromaticity coordinates of (0.42, 0.42).

In Section 3.2, the author synthesized novel cyclometalated platinum(II) complexes **Pt-H1** and **Pt-H2** (Fig. 13d) bearing oligocarbazole hole-transporting moieties, aimed at fabrication of non-doped WOLED with a single emitter by utilizing excimer-based EL. The structure of **Pt-1c** was incorporated in **Pt-H1** and **Pt-H2** as their luminescent cores to obtain blue monomer and orange excimer emissions. These developed complexes exhibited monomer- and excimer-based emissions in the film state, and their ratio is varied by steric hindrance of the *C^N* and ancillary ligands: combination of less hindered *C^N* and ancillary ligands gave rise to enhanced excimer emission. Using the organoplatinum(II) complexes as an emitting layer, non-doped multilayer OLEDs consisting of a stack of HIL/HTL/EML (**Pt-H1** or **Pt-H2**)/ETL were fabricated by solution processing, where all the organic layers were prepared by taking advantage of the solubility of the complexes in orthogonal solvents; **Pt-H1** and **Pt-H2** are soluble in cyclohexane and insoluble in methanol. The devices employing the complexes with an *acac* ancillary ligand (**Pt-H1a** and **Pt-H2a**) exhibited extremely remarkable excimer-based orange EL, whereas the

devices consisting of the complexes with a dipivaroylmethanate ancillary ligand (**Pt-H1b** and **Pt-H2b**) did pseudo-white EL with the CIE chromaticity coordinates of (0.37, 0.41) and (0.35, 0.40), respectively, accompanied by the high average color rendering indexes of 81 due to balanced combination of blue monomer and orange excimer emissions.

In Chapter 4, aimed at development of phosphorescent emitter for solution-processed D-EML OLEDs, the author introduced triarylphosphine oxide moieties to the diketonate ancillary ligand of the $(ppy)_2$Ir(*acac*) luminescent center to give solubility in alcoholic solvents as well as the electron-transporting ability. In the case of the phosphine oxide-appended complex **Ir-E1** (Fig. 13e), green PL was observed at 525 nm, red-shifted by 7 nm in comparison with $(ppy)_2$Ir(*acac*) in deaerated dichloromethane. As the PL spectrum of $(ppy)_2$Ir(*ppa*) (*ppa*, 3-phenylpentane-2,4-dionate) was identical to **Ir-E1**, this red shift was caused by introduction of the 3-phenyl group to *acac*. Utilizing good solubility of **Ir-E1** in orthogonal solvents such as toluene and 2-propanol, D-EML OLEDs were successfully fabricated by solution-processing. A D-EML OLED doped with **Ir-E1** to both p- and n-type EMLs showed a higher maximum luminance and η_{ext} than those of the device containing the n-type EML doped with $(ppy)_2$Ir(*acac*), in spite of the lower Φ_{PL} of **Ir-E1** than $(ppy)_2$Ir(*acac*) (0.33 and 0.95, respectively, in dichloromethane). In addition, an electron-only devices (EOD) employing an **Ir-E1**-doped PVCz layer exhibited higher current density than EODs employing pure PVCz and $(ppy)_2$Ir(*acac*)-doped PVCz layers, clearly indicating the electron-transporting ability of **Ir-E1**.

In the last chapter, the conclusions of the present thesis are given together with the future prospects.

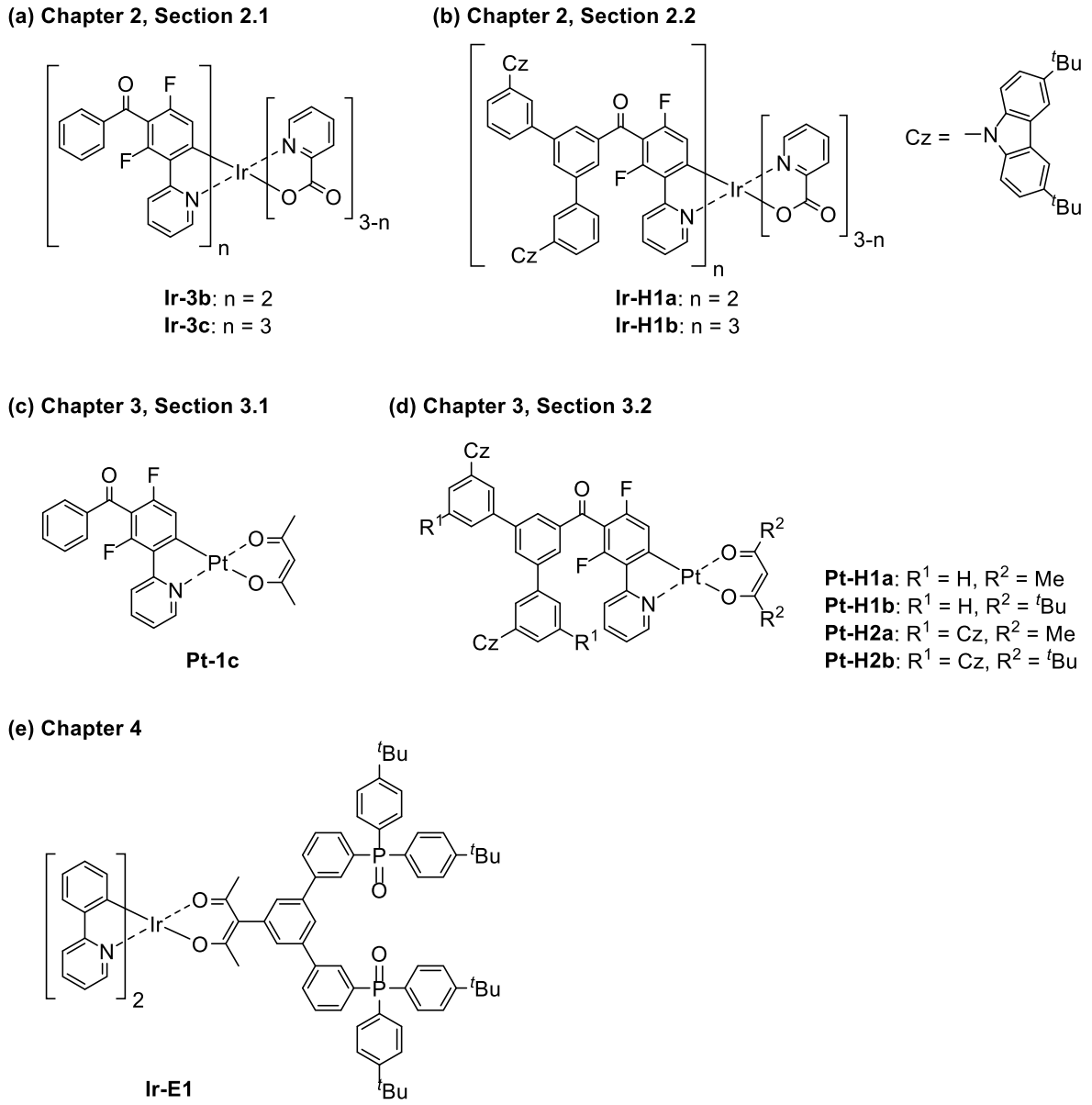

Fig. 13. Representative phosphorescent organometallic complexes developed in this thesis.

1.5. References

[1] M. Pope, H. P. Kallmann and P. Magnante, *J. Chem. Phys*., 1963, **38**, 2042−2043.

[2] W. Helfrich and W. G. Schneider, *Phys. Rev. Lett*., 1965, **14**, 229−231.

[3] P. S. Vincett, W. A. Barlow, R. A. Hann and G. G. Roberts, *Thin Solid Films*, 1982, **94**, 171−183.

[4] C. W. Tang and S. A. VanSlyke, *Appl. Phys. Lett*., 1987, **51**, 913−915.

[5] C. W. Tang, S. A. VanSlyke and C. H. Chen, *J. Appl. Phys*., 1989, **65**, 3610−3616.

[6] M. A. Baldo, D. F. O'Brien, M. E. Thompson and S. R. Forrest, *Phys. Rev. B*, 1999, **60**, 14422−14428.

[7] C. Adachi, M. A. Baldo, M. E. Thompson and S. R. Forrest, *J. Appl. Phys*., 2001, **90**, 5048−5051.

[8] S. Hoshino and H. Suzuki, *Appl. Phys. Lett*., 1996, **69**, 224−226.

[9] M. A. Baldo, D. F. O'Brien, Y. You, A. Shoustikov, S. Sibley, M. E. Thompson and S. R. Forrest, *Nature*, 1998, **395**, 151−154.

[10] A. Endo, K. Sato, K. Yoshimura, T. Kai, A. Kawada, H. Miyazaki and C. Adachi, *Appl. Phys. Lett*., 2011, **98**, 083302 (3 pages).

[11] M. A. Baldo, S. Lamansky, P. E. Burrows, M. E. Thompson and S. R. Forrest, *Appl. Phys. Lett*., 1999, **75**, 4−6.

[12] K. A. King, P. J. Spellane and R. J. Watts, *J. Am. Chem. Soc*., 1985, **107**, 1431−1432.

[13] A. B. Tamayo, B. D. Alleyne, P. I. Djurovich, S. Lamansky, I. Tsyba, N. N. Ho, R. Bau and M. E. Thompson, *J. Am. Chem. Soc*., 2003, **125**, 7377−7387.

[14] S. Lamansky, P. Djurovich, D. Murphy, F. Abdel-Razzaq, H.-E. Lee, C. Adachi, P. E. Burrows, S. R. Forrest and M. E. Thompson, *J. Am. Chem. Soc*., 2001, **123**, 4304−4312.

[15] A. F. Rausch, M. E. Thompson and H. Yersin, *J. Phys. Chem. A*, 2009, **113**, 5927−5932.

[16] H. Tsujimoto, S. Yagi, H. Asuka, Y. Inui, S. Ikawa, T. Maeda, H. Nakazumi and Y.

Sakurai, *J. Organomet. Chem*., 2010, **695**, 1972−1978.

[17] S. Ikawa, S. Yagi, T. Maeda, H. Nakazumi, H. Fujiwara and Y. Sakurai, *Dyes Pigm*., 2012, **95**, 695−705.

[18] N. Okamura, M. Miyazaki, S. Ikawa, T. Maeda, H. Nakazumi and S. Yagi, *Mol. Cryst. Liq. Cryst*., 2017, **653**, 131−136.

[19] J. Brooks, Y. Babayan, S. Lamansky, P. I. Djurovich, I. Tsyba, R. Bau and M. E. Thompson, *Inorg. Chem*., 2002, **41**, 3055−3066.

[20] V. Adamovich, J. Brooks, A. Tamayo, A. M. Alexander, P. I. Djurovich, B. W. D'Andrade, C. Adachi, S. R. Forrest and M. E. Thompson, *New J. Chem.*, 2002, **26**, 1171−1178.

[21] D. Kim and J.-L. Brédas, *J. Am. Chem. Soc*., 2009, **131**, 11371−11380.

[22] T. Shigehiro, S. Yagi, T. Maeda, H. Nakazumi, H. Fujiwara and Y. Sakurai, *J. Phys. Chem. C*, 2013, **117**, 532−542.

[23] C. Adachi, T. Tsutsui and S. Saito, *Appl. Phys. Lett*., 1989, **55**, 1489−1491.

[24] C. Adachi, T. Tsutsui and S. Saito, *Appl. Phys. Lett*., 1990, **57**, 531−533.

[25] M. Arai, K. Nakaya, O. Onitsuka, T. Inoue, M. Codama, M. Tanaka and H. Tanabe, *Synth. Met*., 1997, **91**, 21−25.

[26] G. Sakamoto, C. Adachi, T. Koyama, Y. Taniguchi, C. D. Merritt, H. Murata and Z. H. Kafafi, *Appl. Phys. Lett*., 1999, **75**, 766−768.

[27] X. Zhou, D. S. Qin, M. Pfeiffer, J. Blochwitz-Nimoth, A. Werner, J. Drechsel, B. Maennig, K. Leo, M. Bold, P. Erk and H. Hartmann, *Appl. Phys. Lett*., 2002, **81**, 4070−4072.

[28] S. Reineke, M. Thomschke, B. Lüssem and K. Leo, *Rev. Mod. Phys*., 2013, **85**, 1245−1293.

[29] N. Aizawa, Y.-J. Pu, M. Watanabe, T. Chiba, K. Ideta, N. Toyota, M. Igarashi, Y. Suzuri, H. Sasabe and J. Kido, *Nature Commun*., 2014, **5**, 5756 (7 pages).

[30] T. Wakimoto, Y. Fukuda, K. Nagayama, A. Yokoi, H. Nakada and M. Tsuchida, *IEEE Trans. Electron Devices*, 1997, **44**, 1245−1248.

[31] H. Ishii, K. Sugiyama, E. Ito and K. Seki, *Adv. Mater.*, 1999, **11**, 605−625.

[32] Y. Tao, C. Yang and J. Qin, *Chem. Soc. Rev.*, 2011, **40**, 2943−2970.

[33] M.-H. Kim, M. C. Suh, J. H. Kwon and B. D. Chin, *Thin Solid Films*, 2007, **515**, 4011−4015.

[34] J. Pina, J. Seixas de Melo, H. D. Burrows, A. P. Monkman and S. Navaratnam, *Chem. Phys. Lett.*, 2004, **400**, 441−445.

[35] J. Zhang, D. Ding, Y. Wei and H. Xu, *Chem. Sci*., 2016, **7**, 2870−2882.

[36] A. Islam, M. Rabbani, M. H. Bappy, M. A. R. Miah and N. Sakib, *2013 International Conference on Informatics, Electronics and Vision (ICIEV)*, 2013, 5 pages.

[37] R.-P. Xu, Y.-Q. Li and J.-X. Tang, *J. Mater. Chem. C*, 2016, **4**, 9116−9142.

[38] X. Gong, S. Wang, D. Moses, G. C. Bazan and A. J. Heeger, *Adv. Mater.*, 2005, **17**, 2053−2058.

[39] A. Liang, L. Ying and F. Huang, *J. Inorg. Organomet. Polym. Mater*., 2014, **24**, 905−926.

[40] S. Tokito, M. Suzuki, F. Sato, M. Kamachi and K. Shirane, *Org. Electron*., 2003, **4**, 105−111.

[41] Y.-J. Pu, N. Iguchi, N. Aizawa, H. Sasabe, K.-i. Nakayama and J. Kido, *Org. Electron*., 2011, **12**, 2103−2110.

Chapter 2

Development of Novel Blue Phosphorescent Organoiridium(III) Complexes Aimed at Fabrication of Solution-Processed Organic Light-Emitting Diodes

Section 2.1
Novel Bis- and Tris-Cyclometalated Iridium(III) Complexes Bearing a Benzoyl Group on Each Fluorinated 2-Phenylpyridinate Ligand Aimed at Development of Blue Phosphorescent Materials for OLED

2.1.1. Introduction

From the viewpoint of the development of highly efficient organic light-emitting diodes (OLED), electrophosphorescent devices have been attracting considerable attention for the last decade [1–3] because they utilize both singlet and triplet excitons to achieve as high as 100% internal quantum efficiency, four times larger than that of electrofluorescent devices [4]. As phosphorescent materials for OLED applications, organometallic complexes with a heavy metal center are reliable candidates, and organoiridium and organoplatinum complexes have been intensively developed, as demonstrated by the pioneering works of Thompson and coworkers [5–8], because the strong spin–orbit coupling caused by the organometallic frameworks facilitates the intersystem crossing from the singlet state to the triplet [11]. Especially, bis- and tris-cyclometalated iridium(III) complexes represented by $(C\text{^}N)_2\mathrm{Ir}(LX)$ and $(C\text{^}N)_3\mathrm{Ir}$ (*C^N*, 2-phenylpyridinate-type cyclometalated ligand; *LX*, anionic ancillary ligand), respectively, show efficient phosphorescence with relatively high photoluminescence (PL) quantum yields, and their emission color is easily tuned by the well-designed *C^N* ligand [1,5,6,8–10]. Although blue phosphorescent cyclometalated iridium(III) complexes are

important as RGB emitters in the fabrication of OLED-based electric devices, such as full color displays [1,3] and mercury-less illumination apparatuses [3,12–14], they are less frequently reported in comparison with green and red phosphorescent emitters [1,15–18]. This is mainly because the structural variation of the *C^N* ligand to achieve the high-lying triplet level is considerably limited.

In the case of $(C^N)_2$Ir(*LX*) and $(C^N)_3$Ir, it is well known that the introduction of electron-withdrawing substituents, such as fluorine and trifluoromethyl, gives rise to stabilization of the highest occupied molecular orbital (HOMO) to yield a wide HOMO–LUMO energy gap (LUMO; lowest unoccupied molecular orbital), as a result, achieving the high-lying triplet level [1,19–21]. For example, employing 2-(2,4-difluorophenyl)pyridinate leads to sky-blue emission in combination with a picolinate ancillary ligand [9,19,22]. This *C^N* ligand is also effective in preparing a sky-blue phosphorescent emitter based on $(C^N)_3$Ir [5]. The $(C^N)_2$Ir(*LX*)-type complex, consisting of 2-(3,5-bis(trifluoromethyl)phenyl)-pyridinate and dipivaloylmethanate, is also useful as a blue emitter to fabricate a white phosphorescent OLED [13]. Fewer examples of electron-withdrawing groups on the *C^N* ligand to obtain blue phosphorescence, however, have so far been reported, other than fluorine and fluoroalkyl substituents.

Recently, green phosphorescent $(C^N)_2$Ir(*LX*)-type complexes consisting of 5'-benzoylated 2-phenylpyridinate and acetylacetonate (*acac*) were reported, where the PL maxima are blue-shifted by *ca*. 20 nm compared with $(ppy)_2$Ir(*acac*) and $(ppy)_3$Ir (*ppy*; 2-phenylpyridinate) [23]. Thus, a benzoyl group is an effective electron-withdrawing group to obtain blue-shifted phosphorescence. Although blue-emitting organoiridium(III) complexes bearing fluoro groups as well as carbonyl groups, such as methoxycarbonyl [24] and trifluoroacetyl [9,15,24] are reported, the impact of the combination of benzoyl with other electron-withdrawing group(s) on the emission color has never been investigated with respect

to developing blue phosphorescent organoiridium complexes. Here, the author reports the synthesis and PL properties of novel bis- and tris-cyclometalated iridium(III) complexes bearing 5'-benzoylated 2-(4-fluorophenyl)- and 2-(4,6-difluorophenyl)pyridinates as *C^N* ligands. The author also reports the fabrication and electroluminescent behavior of poly(9-vinylcarbazole)-based OLEDs using these phosphorescent complexes.

2.1.2. Results and Discussion

2.1.2.1. Synthesis and Molecular Structures

The 3'-benzoylated 2-phenylpyridine derivatives, **H*C*^*N*-2** and **H*C*^*N*-3**, were newly prepared as the *C^N* ligands in accordance with Scheme 1; 2-fluoro-5-(pyridin-2-yl)benzonitrile (**2**) was obtained by the Suzuki–Miyaura cross-coupling reaction of (3-cyano-4-fluorophenyl)boronic acid with 2-iodopyridine in 82% yield, and was subjected to the addition of phenylmagnesium bromide, followed by hydrolysis, to yield **H*C*^*N*-2** in 28% yield. On the other hand, **H*C*^*N*-3** was obtained in three steps from 3-bromo-2,6-difluorobenzaldehyde. First, the starting material was subjected to the Stille coupling reaction with 2-(tributylstannyl)pyridine to obtain the phenylpyridine derivative **3** in 78% yield, which was reacted with phenylmagnesium bromide to yield the alcohol **4** in 58% yield. Finally, oxidation of **4** with pyridinium dichromate (PDC) in dichloromethane afforded **H*C*^*N*-3** in 90% yield. To obtain the referential complexes, **H*C*^*N*-1** was prepared in a similar way to the preparation of **H*C*^*N*-2**, although it was previously reported to be obtained by the Stille-type coupling reaction of (3-bromophenyl)phenylmethanone with 2-(tributylstannyl)pyridine [23]. The syntheses of the 5'-benzoyl-substituted bis- and tris-cyclometalated iridium(III) complexes are shown in Scheme 2. The prepared benzoylated 2-phenylpyridines were reacted with $IrCl_3 \bullet 3H_2O$ to obtain μ-chloro-bridged iridium(III) dimers $[(\boldsymbol{C}\text{^}\boldsymbol{N}\text{-}\boldsymbol{X})_2IrCl]_2$ (X = 1–3) as precursors. These dinuclear complexes were reacted

with acetylacetone in the presence of Na_2CO_3 to afford the corresponding bis-cyclometalated complexes, **Ir-1a** (the referential complex, reported in ref. 23), **Ir-2a**, and **Ir-3a**. The reaction of $[(\boldsymbol{C}\text{^}\boldsymbol{N}\text{-}\mathbf{3})_2\mathrm{IrCl}]_2$ with picolinic acid was also carried out under the same conditions to obtain the picolinate analogue, **Ir-3b**. The tris-cyclometalated complexes, **Ir-1c**, **Ir-2c**, and **Ir-3c**, were also prepared by the microwave-assisted reaction of the corresponding $[(\boldsymbol{C}\text{^}\boldsymbol{N}\text{-}\mathbf{X})_2\mathrm{IrCl}]_2$ with **H*C*^*N*-X** in 15–59% yields. The prepared complexes were characterized by ^{1}H NMR, ESI-TOF mass spectrometry, and IR spectroscopy, as well as elemental analyses; ^{13}C NMR spectra were also taken, except for the fluorinated compounds.

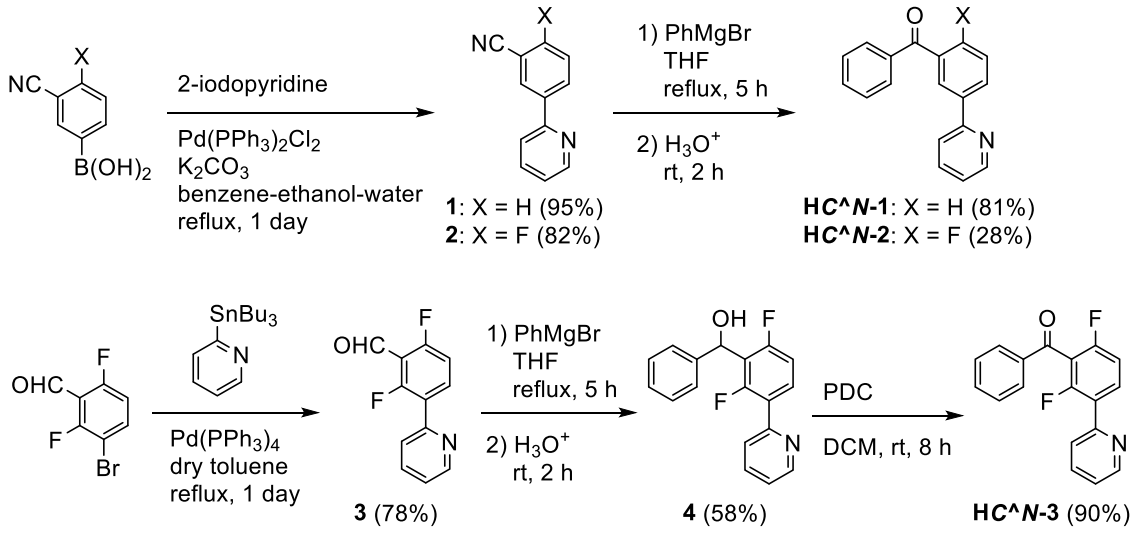

Scheme 1. Syntheses of **H*C*^*N*-1**–**3**.

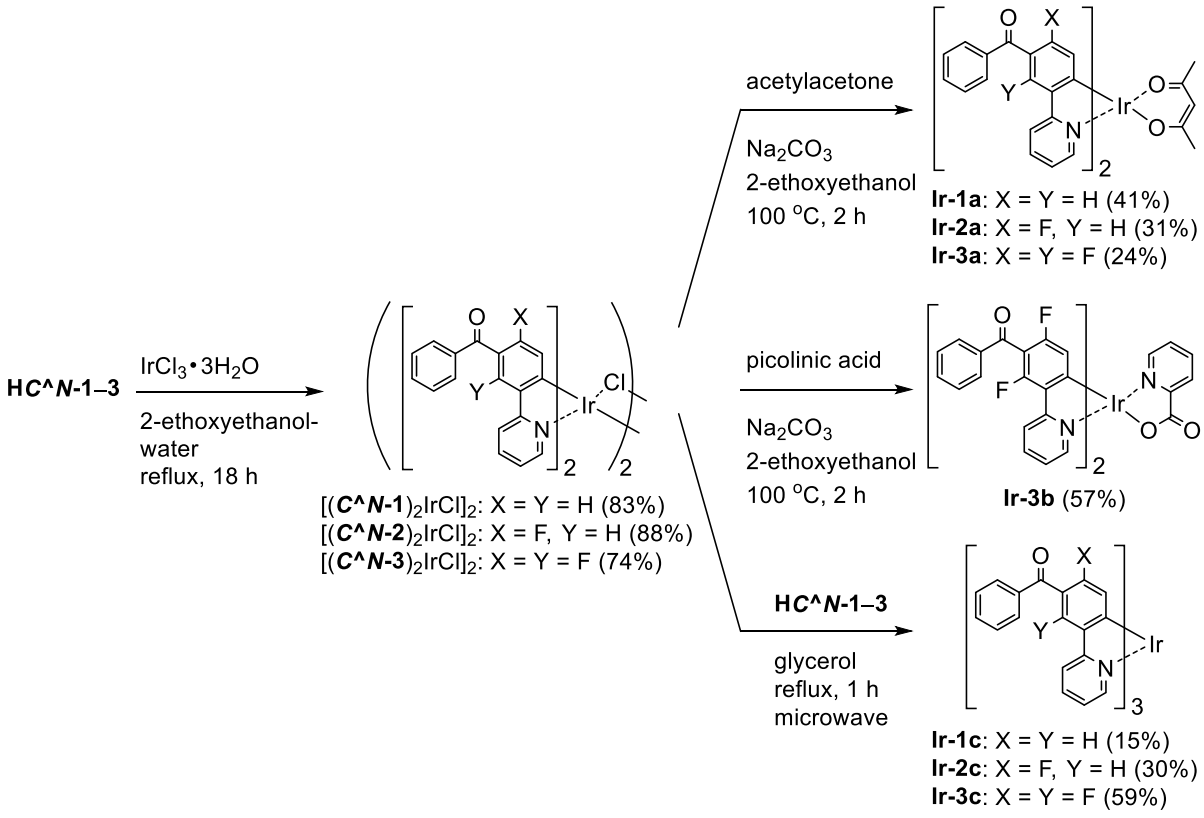

Scheme 2. Syntheses of iridium(III) complexes.

Among the developed cyclometalated iridium(III) complexes, the structures of **Ir-3a** and **Ir-3c** were characterized by X-ray crystallographic analysis, where suitable single crystals were obtained by slow diffusion of dichloromethane solutions of the complexes to hexane. Fig. 1 shows ORTEP drawings of **Ir-3a** and **Ir-3c**, and the crystal data are summarized in Table 1. The selected bond lengths and angles around the iridium center are also summarized in Tables 2 and 3. In the structure of **Ir-3a**, the ligands are arranged in a pseudo-octahedral geometry with a *cis*-*C*,*C* and *trans*-*N*,*N* configuration, as is observed for the typical bis-cyclometalated iridium(III) complexes so far reported [6,8,25]. The bond lengths are also similar to the typical heteroleptic complexes: the lengths of the Ir–N, Ir– C, and Ir–O bonds are 2.04, 1.99–2.00, and 2.13 Å, respectively. Likewise, **Ir-3c** adopts a pseudo-octahedral geometry with a facial configuration, similar to typical phosphorescent homoleptic complexes

[5,26], where the lengths of Ir–N and Ir–C bonds are 2.12–2.13 and 2.02–2.03 Å, respectively. It has been reported that the thermodynamically favored facial isomer is more emissive than the kinetically favored meridional one, and thus **Ir-3c** is expected to afford highly efficient phosphorescence [5]. For **Ir-3a** and **Ir-3c**, the carbonyl moiety in each benzoyl group is distorted at 76.0–77.6° and 60.2–87.6°, respectively, with respect to the mean plane of the neighbouring phenyl ring of the *C^N* ligand. In addition, the phenyl and carbonyl moieties in the benzoyl group are twisted at 1.7–3.3° (**Ir-3a**) and at 2.9–25.4° (**Ir-3c**) to each other. The effect of the benzoyl group on the electronic structures is discussed below.

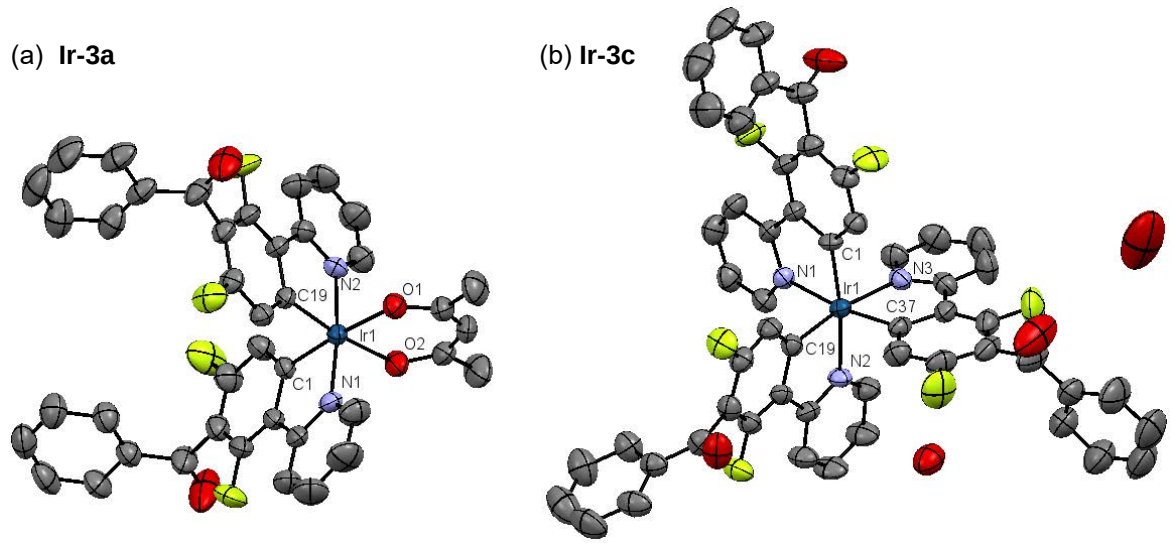

Fig. 1. ORTEP drawings of (a) **Ir-3a** and (b) **Ir-3c**•2H_2O with ellipsoids at the 50% probability level. The hydrogen atoms are omitted for clarity.

Table 1. Crystal data and structure refinement for **Ir-3a** and **Ir-3c**.

Parameter	**Ir-3a**	**Ir-3c**
Formula	$C_{41}H_{27}F_4IrN_2O_4$	$C_{54}H_{30}F_6IrN_3O_3$•$2H_2O$
Formula weight	879.89	1111.09
Crystal system	Monoclinic	Monoclinic
Space group	*C*2/*c* (#15)	$P2_1/a$ (#14)
Lattice Parameters *a* (Å)	41.393(9)	19.190 (3)
b (Å)	8.1687(14) Å	10.3544 (16)
c (Å)	23.774(5) Å	23.935 (4)
β (°)	120.926(2)	101.5280 (19)
Volume ($Å^3$)	6896(3)	4660.1 (13)
Z	8	4
Density ρ_{calc} (g cm^{-3})	1.695	1.584
μ (cm^{-1})	39.508	29.496
F_{000}	3456.00	2200.00
T (K)	293	293
No. of refractions measured	28759	36255
No. of refractions used (R_{int})	9259 (0.0265)	12611 (0.040)
R_1, (R_w)	0.0390 (0.0459)	0.0509 (0.0567)
Goodness of fit on F^2	1.067	1.088
ρ_{fin} (max/min) (e $Å^3$)	1.92 /−1.85	2.94 /−1.98

Table 2. Selected bond lengths and angles for **Ir-3a**.

Length (Å)	Ir-O1	2.131(4)
	Ir-O2	2.133(3)
	Ir-C1	1.991(6)
	Ir-N1	2.043(5)
	Ir-C19	1.995(4)
	Ir-N2	2.036(5)
Angle (°)	O1−Ir−O2	88.39(14)
	N1−Ir−C1	80.90(19)
	N2−Ir−C19	81.28(17)

Table 3. Selected bond lengths and angles for **Ir-3c**.

Length (Å)	Ir-C1	2.017(5)
	Ir-N1	2.129(4)
	Ir-C19	2.016(5)
	Ir-N2	2.119(4)
	Ir-C37	2.031(5)
	Ir-N3	2.129(4)
Angle (°)	N1−Ir−C1	79.56(18)
	N2−Ir−C19	79.4(2)
	N3−Ir−C37	78.2(2)

2.1.2.2. Light Absorption and Photoluminescent Properties

UV-vis absorption spectra of the bis- and tris-cyclometalated iridium(III) complexes were obtained in dichloromethane at rt, as shown in Fig. 2, and the spectral data are also summarized in Table 4. The absorption spectra of **Ir-1a–3a** and **Ir-3b** are shown in Fig. 2a. In the case of **Ir-1a**, intense absorption bands are observed from 250–320 nm, which are assigned to the spin-allowed ligand-center (^{1}LC, $^1\pi$–π^*) transitions at the *C^N* ligand, and the next bands at 330–420 nm are assigned to spin-allowed metal-to-ligand charge transfer (^{1}MLCT, ^{1}d–π*) transitions from the iridium core to the *C^N* ligand. As seen in the magnified spectrum, the weak shoulder-like absorption band around 475 nm with a lower molecular absorptivity is assigned to the spin-forbidden ^{3}MLCT transition [6]. Similar spectral features to **Ir-1a** are observed for the other bis-cyclometalated complexes, where the ^{3}MLCT transition bands are blue-shifted to 465, 460 and 450 nm for **Ir-2a**, **Ir-3a** and **Ir-3b**, respectively, and the absorption onsets are also blue-shifted. This clearly indicates that the lowest triplet (T_1) energy increases with an increase in the number of fluorine substituents, as well as after the replacement of the *acac* ancillary ligand with picolinate. In the case of the tris-cyclometalated complexes, the absorption spectral profiles are almost similar to those of the bis-cyclometalated complexes bearing the corresponding *C^N* ligands: the ^{1}LC (250–300 nm), ^{1}MLCT (300–410 nm), and ^{3}MLCT (>440 nm) transitions are observed from the near-ultraviolet to the neighboring visible region (Fig. 2b). As observed for the bis-cyclometalated complexes, the ^{3}MLCT transition band as well as the spectral onset is blue-shifted with an increase in the number of fluorine substituents.

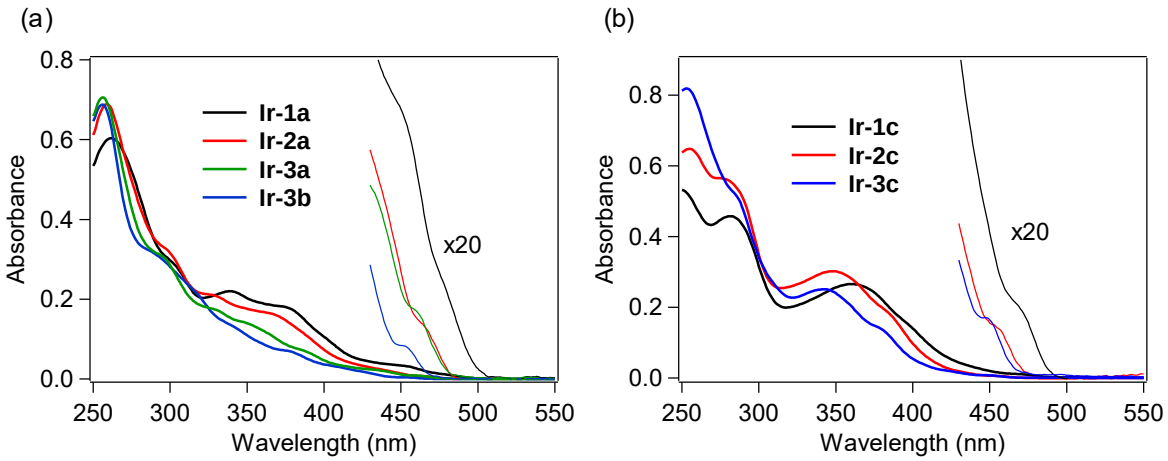

Fig. 2. UV-vis absorption spectra of (a) bis-cyclometalated and (b) tris-cyclometalated complexes in dichloromethane at rt.

Table 4. UV-vis absorption and photoluminescence data.

Compd	λ_{abs}[a] (nm) [log ε_{abs}]	λ_{PL} (nm)[b]		E_T[e] (eV)	Φ_{PL}	τ_{PL}[b,f] (μs) [χ^2]
		298 K[c]	77 K[d]			
Ir-1a	262 [4.78], 339 [4.34], 375 sh [4.26], 475 sh [3.12]	502	488, 519	2.54	0.81	1.37 [1.0]
Ir-2a	259 [4.81], 327 [4.31], 365 sh [4.21], 465 sh [2.82]	483	470, 498	2.64	0.71	1.19 [1.0]
Ir-3a	256 [4.85], 325 sh [4.25], 350 sh [4.15], 460 sh [2.93]	479	464, 504	2.67	0.80	1.01 [1.1]
Ir-3b	256 [4.84], 335 sh [4.16], 375 sh [3.85], 450 sh [2.62]	464, 492	455, 487	2.73	0.82	1.97 [1.1]
Ir-1c	282 [4.66], 360 [4.42], 395 sh [4.20], 470 sh [2.94]	487	471, 509	2.63	0.82	1.16 [1.07]
Ir-2c	255 [4.81], 274 sh [4.75], 347 [4.48], 380 sh [4.30], 455 sh [2.58]	469, 497	459, 490	2.70	0.85	1.57 [1.07]
Ir-3c	253 [4.91], 285 sh [4.71], 342 [4.40], 380 sh [4.13], 445 sh [2.88]	463, 489	451, 483	2.75	0.90	1.54 [1.11]

[a]The symbol "sh" in the parenthesis indicates a peak observed as a shoulder. [b]Excited at 390 nm. [c]Obtained in deaerated dichloromethane. [d]Obtained in glassy 2-MeTHF. [e]Determined from λ_{PL} at 77 K. [f]Monitored at shortest λ_{PL} of each complex.

The photoluminescence (PL) spectra of bis- and tris-cyclometalated iridium(III) complexes in dichloromethane at rt are shown in Fig. 3. The spectral data are summarized in Table 4, along with PL quantum yields (Φ_{PL}) and PL lifetimes (τ_{PL}). All the data were obtained for deaerated samples, which were kept away from luminescence quenching by oxygen. In the spectra of the bis-cyclometalated complexes (Fig. 3a), the λ_{PL} of **Ir-1a** was observed at 502 nm (green), and the emission band was blue-shifted with an increase in the number of fluorine substituents: **Ir-2a** and **Ir-3a** show their λ_{PL}s at 483 (bluish green) and 479 nm (bluish green), respectively. For the ***C^N*-3**-derived complexes, replacement of the *acac* ancillary ligand with picolinate gives rise to a further blue shift of 15 nm (λ_{PL} of **Ir-3b**; 464 nm), yielding sky-blue emission. Such a blue shift induced by picolinate is usually observed in typical bis-cyclometalated complexes [8,27]. The blue shifts caused by the fluorine substituents as well as the ancillary ligand replacement are comparable to the blue-shifted spectral behavior of the ^{3}MLCT absorption (*vide supra*). The Φ_{PL} values of **Ir-1a**, **Ir-2a**, **Ir-3a** and **Ir-3b** were determined as 0.81, 0.71, 0.80 and 0.82, respectively. Also, the τ_{PL}s of these complexes ranged from 1.01 to 1.97 μs, each of which was well fitted to a single-exponential decay. Fernández-Sánchez and coworkers reported (*MeOCOdfppy*)$_2$Ir(*pic*) (*MeOCOdfppy*, 2-(4,6-difluoro-5-methoxycarbonylphenyl) pyridinate; *pic*, picolinate) and (*CF$_3$COdfppy*)$_2$Ir(*pic*) (*CF$_3$COdfppy*; 2-(4,6-difluoro-5-(trifluoroacetyl)phenyl)pyridinate), which have a methoxycarbonyl and a trifluoroacetyl group, respectively, instead of the benzoyl group of **Ir-3b**. The complexes exhibited blue and deep blue PL at 463 and 459 nm, where the Φ_{PL}s are 0.44 and 0.08 in acetonitrile, respectively [24]. The λ_{PL} of **Ir-3b** is comparable to that of (*MeOCOdfppy*)$_2$Ir(*pic*) and is red-shifted by 5 nm in comparison with that of (*CF$_3$COdfppy*)$_2$Ir(*pic*). One can see that this is because the electron-withdrawing ability of a benzoyl group is comparable to that of a methoxycarbonyl group and lower than that of a trifluoroacetyl group: the Hammet substituent constants (σ_p) of benzoyl,

methoxycarbonyl and trifluoroacetyl groups are 0.43, 0.45 and 0.80, respectively [28]. On the other hand, the Φ_{PL} of **Ir-3b** is 0.94 in acetonitrile, which is much higher than that of (*MeOCOdfppy*)$_2$Ir(*pic*) and (*CF$_3$COdfppy*)$_2$Ir(*pic*). As seen in Fig. 3b, the λ_{PL}s of **Ir-1c**, **Ir-2c** and **Ir-3c** were observed at 487 (bluish green), 470 (bluish green) and 463 nm (sky blue), respectively, blue-shifted by 14−17 nm in comparison with those of the corresponding *acac*-based bis-cyclometalated complexes. These blue shifts are caused by the relatively high ligand field strength of the *C^N* ligands in comparison with the acetylacetonate and picolinate anions [29,30]. Thompson and coworkers reported that *fac*-(*dfppy*)$_3$Ir (*dfppy*; 2-(4,6-difluorophenyl)pyridinate) exhibits blue PL at 468 nm in dichloromethane at rt [5]. In the present case, the λ_{PL} of **Ir-3c** is 5 nm shorter than that of *fac*-(*dfppy*)$_3$Ir. This blue-shift is obviously brought about by the introduction of a benzoyl group to the *C^N* ligand. The Φ_{PL}s of **Ir-1c**, **Ir-2c** and **Ir-3c** were determined as 0.82, 0.85 and 0.90, respectively. Their τ_{PL}s were determined as 1.16–1.57 μs, similar to those of the corresponding bis-cyclometalated complexes. It is worthy to note that **Ir-3c** is more emissive than the representative blue phosphorescent organoiridium complexes, such as *fac*-(*dfppy*)$_3$Ir (Φ_{PL}; 0.43) [5] and bis[(4,6-difluorophenyl)pyridinato-*N*,*C*$^{2'}$]iridium(III) picolinate, FIrpic (Φ_{PL}; 0.87) [31]. To determine the T_1 energy values (E_T), the phosphorescence spectra were measured in deaerated 2-MeTHF glassy matrices at 77 K, and the spectral data are also summarized in Table 4. All of the complexes are also intensely phosphorescent in the glass solutions at 77 K, showing more structured spectral shapes. The λ_{PL}s are blue-shifted by 9−16 nm in comparison with those obtained in dichloromethane at 298 K. The E_Ts obtained from the phosphorescence spectra at 77 K are almost comparable to the spectral onsets of the absorption spectra.

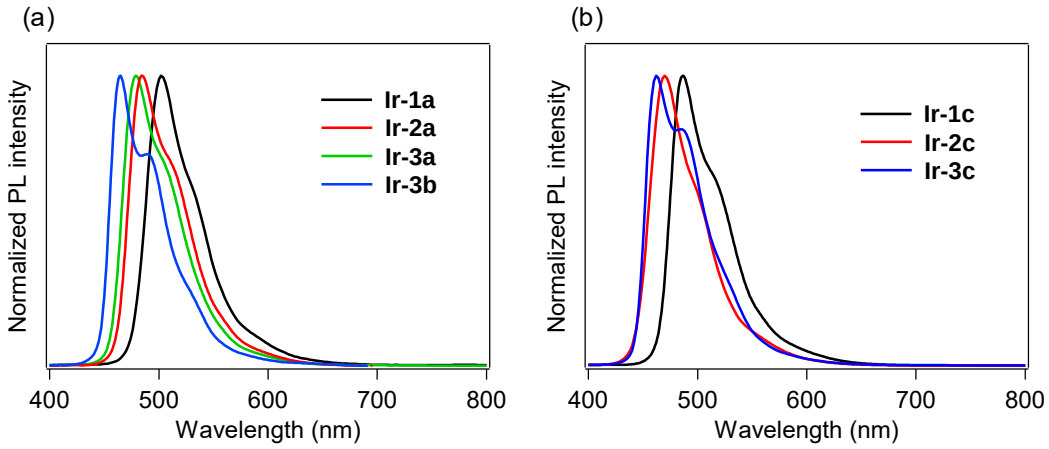

Fig. 3. Photoluminescence spectra of (a) bis- and (b) tris-cyclometalated complexes in dichloromethane at rt.

2.1.2.3. Electrochemical Properties

As the energy levels of frontier orbitals are important in optimizing the device efficiency of OLEDs, the oxidation potentials of the present organoiridium(III) complexes ($E_{1/2,\,Ox}$) *vs*. the ferrocenium/ferrocene (Fc^+/Fc) redox couple were determined by cyclic voltammetry (CV) in anhydrous acetonitrile to estimate the effect of the substituents on the HOMO energy level (E_{HOMO}). The E_{HOMO}s derived from $E_{1/2,\,Ox}$ are listed in Table 5. All the complexes exhibited pseudo-reversible oxidation cycles with $E_{1/2,\,Ox}$ in the region of 0.655–1.03 V, although they showed irreversible reduction potentials, which prevented us from determining the LUMO energy levels. For **Ir-1a**, **Ir-2a** and **Ir-3a**, the E_{HOMO} values were determined as −5.46, −5.55 and −5.67 eV, respectively, indicating that the HOMO is stabilized by an increase in the number of fluorine substituents. In addition, a benzoyl group also stabilizes the HOMO: the E_{HOMO} of $(ppy)_2Ir(acac)$ is reported as −5.2 eV [27]. For **Ir-3b**, E_{HOMO} was determined as −5.81 eV, larger in a negative direction than that of **Ir-3a** (−5.67 eV). This indicates that the replacement of the ancillary ligand by picolinate also gives rise to stabilization of the HOMO level. In the case of the tris-cyclometalated complexes, the E_{HOMO} values were determined as

−5.57, −5.73 and −5.83 eV for **Ir-1c**, **Ir-2c** and **Ir-3c**, respectively. As is seen in the bis-cyclometalated complexes, the HOMO level of the tris-cyclometalated complex is stabilized by an increase in the number of fluorine substituents. Also, it is more stabilized in comparison with those of the corresponding bis-cyclometalated complexes (*i.e.*, **Ir-1a**–**3a**).

Table 5. The calculated HOMO energy levels (E_{HOMO}) corresponding to the potentials of oxidative cyclic voltammograms.

Compd	$E_{1/2,\,Ox}$ (V) *vs*. Fc^+/Fc	$E_{HOMO}{}^a$ (eV)
Ir-1a	0.655	–5.46
Ir-2a	0.755	–5.55
Ir-3a	0.865	–5.67
Ir-3b	1.01	–5.81
Ir-1c	0.765	–5.57
Ir-2c	0.925	–5.73
Ir-3c	1.03	–5.83

[a]Calculated using the equation of $-E_{1/2,\,Ox} - 4.80$ eV.

2.1.2.4. DFT Calculations

In order to discuss the effect of benzoyl and fluorine substituents on the E_{HOMO}s, density functional theory (DFT) calculations were performed for the tris-cyclometalated complexes, using the Gaussian 09 program package [32]. The structures of **Ir-1c**, **Ir-2c** and **Ir-3c** were optimized using the B3LYP functional [33], where the crystal structure of **Ir-3c** was used as an initial structure. LanL2DZ and 6-31+G(d) basis sets were employed for iridium and the other atoms, respectively, where LanL2DZ is one of the relativistic effective core potential (RECP) basis sets and consists of relativistic effective potentials and their associated basis

sets [34]. The optimized structure and the spatial distributions of the HOMO and LUMO of **Ir-1c** are shown in Fig. 4. Those of **Ir-2c** and **Ir-3c** are similar to **Ir-1c**. The calculated energy levels of the HOMO and LUMO ($E_{HOMO,\ calcd}$ and $E_{LUMO,\ calcd}$, respectively) of these complexes are summarized in Table 6, together with the HOMO–LUMO energy gaps ($E_{g,\ calcd}$). The spatial distributions of the HOMOs and LUMOs of these complexes are almost the same as those of typical $(ppy)_3$Ir-type complexes [19,27], and the carbonyl group shows an electronic contribution to both the HOMO and LUMO, in spite of disrupted π-conjugation due to deviation from the phenylpyridine plane. The $E_{HOMO,\ calcd}$ value of each complex is comparable to the E_{HOMO} determined by CV, and an increase in the number of fluorine substituents leads to stabilization of the HOMO. Although the $E_{LUMO,\ calcd}$ is also decreased by an increase in the fluorine substituents, the $E_{HOMO,\ calcd}$ is decreased more drastically than $E_{LUMO,\ calcd}$. This indicates that the high-lying triplet state is brought about by stabilization of the HOMO.

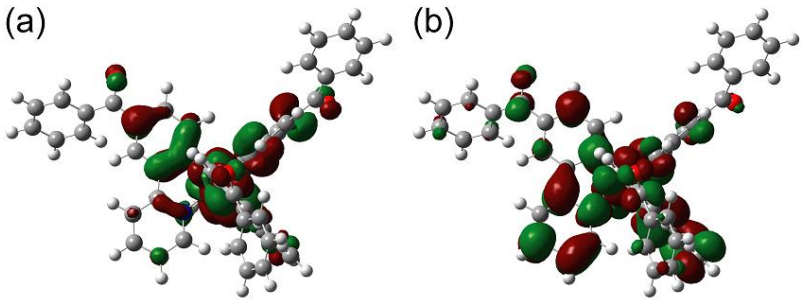

Fig. 4. Optimized geometry structure and electron configurations of (a) HOMO and (b) LUMO for **Ir-1c**.

Table 6. Calculated energy levels of the HOMO ($E_{HOMO,\ calcd}$), LUMO ($E_{LUMO,\ calcd}$) and energy gap ($E_{g,\ calcd}$).

Compd	$E_{HOMO,\ calcd}$ (eV)	$E_{LUMO,\ calcd}$ (eV)	$E_{g,\ calcd}$[a] (eV)
Ir-1c	–5.40	–1.71	3.69
Ir-2c	–5.66	–1.87	3.79
Ir-3c	–5.87	–2.00	3.87

[a] $E_{g,\ calcd} = E_{LUMO,\ calcd} - E_{HOMO,\ calcd}$.

2.1.2.5. Fabrication of Phosphorescent OLEDs

Using the developed bis- and tris-cyclometalated iridium(III) complexes as a phosphorescent dopant, the author fabricated OLEDs consisting of a poly(9-vinylcarbazole) (PVCz) emitting layer (EML), device-1. The device structure is as follows; ITO (transparent anode, 150 nm, 10 Ω per square)/poly(3,4-ethylenedioxythiophene):poly(styrene sulfonate) (PEDOT:PSS, 40 nm)/EML (100 nm)/CsF (1.0 nm)/Al (cathode, 250 nm). The EML consists of PVCz (hole-transporting host material), 1,3-bis(5-(4-(*tert*-butyl)phenyl)-1,3,4-oxadiazol-2-yl)benzene (OXD-7, electron-transporting material), and the phosphorescent dopant in a ratio of 10 : 3.0 : 0.40 (wt/wt/wt). The electroluminescence (EL) spectra of the fabricated devices are shown in Fig. 5, and the device properties are also summarized in Table 7. In the case of the bis-cyclometalated complexes, the devices exhibited EL spectra almost identical to the PL spectra of the constituent emitting dopants; the EL wavelengths (λ_{EL}) of the **Ir-1a**-, **Ir-2a**-, and **Ir-3a**-doped devices were 507, 485, and 481 nm, respectively. As for the Commission Internationale de L'éclairage (CIE) chromaticity coordinates (CIE (x, y)), the **Ir-3a**-doped device afforded a value of (0.19, 0.42). The ancillary ligand replacement in **Ir-3a** from *acac* to picolinate allowed the author to fabricate an OLED emitting further blue-shifted EL: the device doped with **Ir-3b** exhibited sky-blue EL with a λ_{EL} of 469 nm and afforded a CIE (x, y)

of (0.18, 0.34), where the value of the *y*-axis was improved in comparison with the **Ir-3a**-doped device. In terms of the device efficiency, the maximum external quantum efficiency ($\eta_{ext,\ max}$) decreased slightly with an increase in the fluorine substituents; 2.44 (@10.0 V), 2.13 (@10.0 V), and 1.90% (@9.5 V) for the **Ir-1a**-, **Ir-2a**-, and **Ir-3a**-doped devices, respectively. In addition, the ancillary ligand replacement from *acac* to picolinate gave rise to deterioration of $\eta_{ext,\ max}$ down to 1.72% (@10.5 V, the **Ir-3b**-doped device). One can see that an increase in the E_T is likely to bring about a back energy transfer to OXD-7 (E_T = 2.7 eV) [3]. In the case of the tris-cyclometalated complexes, the **Ir-3c**-doped device exhibited the most blue-shifted EL (λ_{EL}; 462 nm) among the OLEDs fabricated in this study. As expected from the results described above, the **Ir-1c**-doped device showed a better performance ($\eta_{ext,\ max}$; 2.31% @11.0 V) than the **Ir-2c**- ($\eta_{ext,\ max}$; 2.10% @10.5 V) and **Ir-3c**-doped devices ($\eta_{ext,\ max}$; 1.81% @8.0 V): the increase in the number of fluorine substituents afforded a comparable or higher E_T to facilitate the back energy transfer to OXD-7. In the **Ir-3c**-doped device, however, both the *x*- and *y*-axis values of the CIE chromaticity coordinate were improved in comparison with the **Ir-3b**-doped device, yielding a CIE (*x*, *y*) of (0.16, 0.28). This value is better than that of FIrpic (CIE (*x*, *y*) of (0.17, 0.34)), which is frequently used as a blue phosphorescent material [22].

Table 7. OLED performance of device-1.

Device	Dopant	$V_{turn\text{-}on}$ [a] (V)	L_{max} [b] (cd m^{-2}) [@V]	$\eta_{ext,\,max}$ [b] (%) [@V]	$\eta_{j,\,max}$ [b] (cd A^{-1}) [@V]	$\eta_{p,\,max}$ [b] (lm W^{-1}) [@V]	CIE (x, y) [b,c]	λ_{EL} [b,c] (nm)
1a	**Ir-1a**	4.0	8210 [14.5]	2.44 [10.0]	7.67 [10.0]	2.81 [7.5]	(0.27, 0.60)	507
1b	**Ir-2a**	4.5	6090 [14.5]	2.13 [10.0]	5.70 [10.0]	2.07 [8.0]	(0.21, 0.50)	485
1c	**Ir-3a**	5.0	6660 [14.0]	1.90 [9.5]	4.46 [9.5]	1.57 [8.0]	(0.19, 0.42)	481
1d	**Ir-3b**	6.5	1350 [15.5]	1.72 [10.5]	3.62 [10.5]	1.09 [9.5]	(0.18, 0.34)	469
1e	**Ir-1c**	5.0	7290 [15.0]	2.31 [11.0]	7.39 [10.0]	2.48 [9.0]	(0.22, 0.48)	485
1f	**Ir-2c**	5.5	3930 [16.5]	2.10 [10.5]	5.90 [10.0]	2.21 [7.0]	(0.18, 0.34)	469
1g	**Ir-3c**	4.5	1510 [13.0]	1.81 [8.0]	3.47 [8.0]	1.36 [8.0]	(0.16, 0.28)	462

[a]The voltage where the luminance more than 1 cd m^{-2} is observed. [b]The maximum values of luminance (L_{max}), external efficiency ($\eta_{ext,\,max}$), current efficiency ($\eta_{j,\,max}$), and power efficiency ($\eta_{p,\,max}$). The values in parentheses are the voltages at which they were obtained. [c]CIE chromaticity coordinates (CIE (x, y)) and EL wavelengths (λ_{EL}) obtained at the voltages where the maximum luminance was observed.

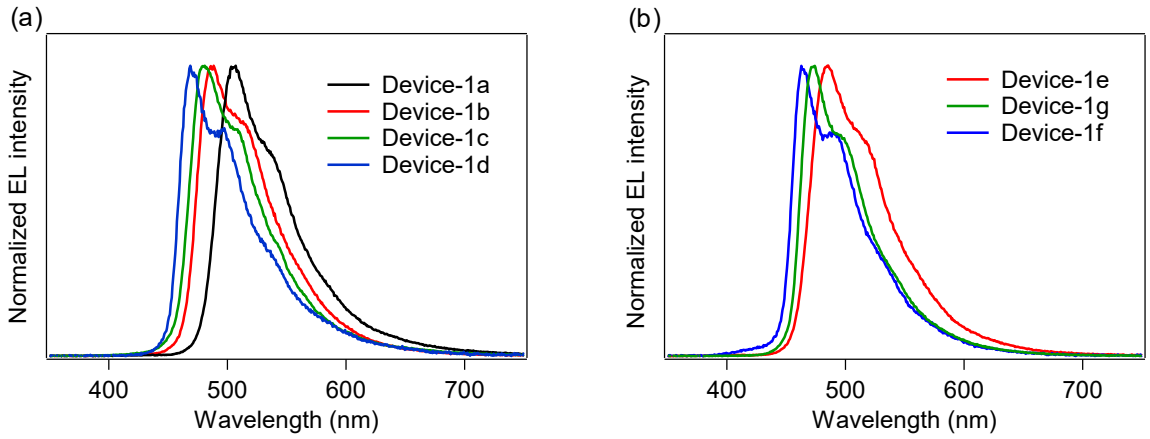

Fig. 5. EL spectra of device-1 employing (a) bis-cyclometalated and (b) tris-cyclometalated complexes at L_{max}.

In order to improve the device efficiency of blue OLEDs, solution-processed multilayer OLEDs employing **Ir-3** were fabricated (device-2), which have a so-called double-emitting layer (D-EML) structure [35]. The device structure is as follows; ITO (transparent anode, 150 nm)/PEDOT:PSS (40 nm)/EML-1 (40 nm)/EML-2 (40 nm)/CsF (1.0 nm)/Al (cathode, 250 nm), where EML-1 is **Ir-3**-doped PVCz film (PVCz : **Ir-3** = 10 : 1.0, wt/wt) and EML-2 is **Ir-3**-doped [1,1':3',1''-terphenyl]-4,4''-diylbis(diphenylphosphine oxide) (BPOPB) [36] film (BPOPB : **Ir-3** = 10 : 1.0, wt/wt). BPOPB is an electron-transporting material bearing a sufficiently high E_T of 2.79 eV [36]. The EML-2 was fabricated by spin-coating of a 2-propanol solution of **Ir-3** and BPOPB onto the EML-1, utilizing the quite moderate solubility of **Ir-3** in 2-propanol. The EL spectra and device performance of device-2 are shown in Fig. 6 and Table 8, respectively. The **Ir-3a**-doped D-EML OLED (device-2a) showed a better performance ($\eta_{ext, max}$; 6.68% @11.0 V) than device-1c discussed above. The **Ir-3b**- and **Ir-3c**-doped devices (device-2b and device-2c, respectively) also exhibited improved $\eta_{ext, max}$s of 8.55% (@9.0 V) and 7.46% (@10.0 V), respectively. Device-2b and device-2c exhibited sky-blue EL with almost identical CIE coordinates of (0.17, 0.33) and

(0.17, 0.29) to the corresponding device-1, respectively.

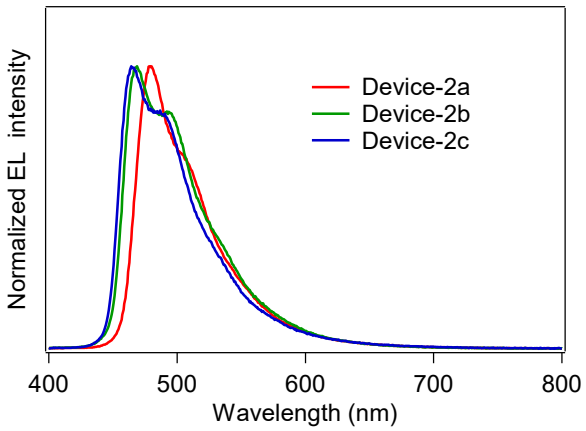

Fig. 6. EL spectra of D-EML OLEDs Device-2a–c employing **Ir-1a–c**, respectively, at L_{max}.

Table 8. OLED performance of Device-2.

Device	Dopant	$V_{turn\text{-}on}$ (V)	L_{max} (cd m^{-2}) [@V]	$\eta_{ext,\,max}$ (%) [@V]	$\eta_{j,\,max}$ (cd A^{-1}) [@V]	$\eta_{p,\,max}$ (lm W^{-1}) [@V]	CIE (x, y)	λ_{EL} (nm)
2a	**Ir-3a**	5.5	7560 [12.0]	6.68 [9.0]	15.0 [9.0]	5.23 [9.0]	(0.17, 0.40)	480
2b	**Ir-3b**	5.0	6220 [11.5]	8.55 [9.0]	17.6 [9.0]	6.15 [9.0]	(0.17, 0.33)	469
2c	**Ir-3c**	5.0	4760 [13.5]	7.46 [10.0]	13.9 [10.0]	4.36 [10.0]	(0.17, 0.29)	466

2.1.3. Conclusions

In summary, novel blue phosphorescent bis- and tris-cyclometalated iridium(III) complexes with excellent PL quantum yields were successfully developed. In a series of bis-cyclometalated complexes, the 2-(4,6-difluoro-5-benzoylphenyl)pyridinate-based complex (**Ir-3b**) exhibited the most blue-shifted PL in combination with a picolinate ancillary ligand. A PVCz-based OLED, using **Ir-3b** as an emitting dopant, exhibited sky-blue EL along with a CIE (*x*, *y*) of (0.18, 0.34). Further ligand replacement with the identical *C^N* ligand afforded a facial isomer of the homoleptic tris-cyclometalated complex (**Ir-3c**), which also exhibited sky-blue PL. This tris-cyclometalated complex was an excellent blue phosphorescent dopant for OLED application with respect to the chromaticity coordinates, where the **Ir-3b**-based device afforded a CIE (*x*, *y*) of (0.16, 0.28). Although the PVCz-based OLEDs employing OXD-7 as an electron-transporting material showed low $\eta_{ext,\ max}$ (~2%), D-EML OLEDs doped with **Ir-3** showed an improved $\eta_{ext,\ max}$ of 6.68–8.55% without any considerable changes in the CIE coordinates. From the results of electrochemical and DFT studies, it was revealed that the blue-shifted PL and EL are mainly brought about by stabilization of the HOMO. Therefore, this work clearly demonstrates that the introduction of a benzoyl substituent into a fluorinated 2-phenylpyridinate cyclometalated ligand provides an opportunity to develop blue phosphorescent organoiridium(III) complexes with improved CIE chromaticity coordinates.

2.1.4. Experimental

2.1.4.1. Syntheses and Characterizations

All chemicals used for synthesis were purchased from Sigma-Aldrich Co., Tokyo Chemical Industry Co., Ltd., and Wako Pure Chemical Industries, Ltd. and used without further purification. NMR spectra (^{1}H and ^{13}C) were obtained on a Jeol ECX400 (400 MHz for ^{1}H and 100 MHz for ^{13}C) spectrometer, using TMS as an internal standard (0.00 ppm). Electrospray ionization time-of-flight (ESI-TOF) mass spectra were measured on a Jeol JMS-T100LP. Elemental analyses were carried out on a J-Science Lab MICRO CORDER JM10 analyzer.

General procedure of synthesis of 1 and 2

To a mixture of 2-iodopyridine (0.25 g, 1.2 mmol), arylboronic acid (1.8 mmol), and $PdCl_2(PPh_3)_2$ (0.069 g, 0.098 mmol) in a solvent mixture of benzene (5 mL) and ethanol (2 mL) was added Na_2CO_{3aq} (2 M, 5 mL). Then, the mixture was heated at 80 °C for 24 h under nitrogen. After cooling, the solvent was removed on a rotary evaporator. The residue was dissolved in dichloromethane, and the solution was washed with water (50 mL × 2) and sat. brine, and then dried over anhydrous $MgSO_4$. The solvent was removed on a rotary evaporator, and the residue was purified by silica gel column chromatography using dichloromethane as eluent to obtain the target arylpyridine derivative.

3-(Pyridin-2-yl)benzonitrile (1). 95% yield. ^{1}H NMR (400 MHz, $CDCl_3$) δ 7.31 (ddd, J = 1.4, 4.8 and 7.4 Hz, 1H), 7.57 (t, J = 7.8 Hz, 1H), 7.68 (td, J = 1.4 and 7.8 Hz, 1H), 7.71−7.75 (m, 1H), 7.80 (dt, J = 1.8 and 7.8 Hz, 1H), 8.23 (td, J = 1.4 and 7.8 Hz, 1H), 8.31 (t, J = 1.4 Hz, 1H), 8.70−8.73 (m, 1H). This compound has been reported [37].

2-Fluoro-5-(pyridin-2-yl)benzonitrile (2). 82% yield. ^{1}H NMR (400 MHz, $CDCl_3$) δ 7.28−7.34 (m, 2H), 7.69 (d, J = 8.2 Hz, 1H), 7.80 (dt, J = 1.8 and 7.3 Hz, 1H), 8.22−8.27 (m, 1H), 8.30 (dd, J = 2.3 and 6.0 Hz, 1H), 8.70 (d, J = 5.0 Hz, 1H). IR (KBr, cm^{-1}) 471, 735, 777, 843, 906, 1117, 1250, 1435, 1472, 1504, 2223. ESI-TOF MS: m/z $[M + H]^+$ calcd for $C_{12}H_8FN_2$: 199.07; found: 199.07. Anal. calcd for $C_{12}H_7FN_2$: C, 72.72; H, 3.56; N, 14.13. Found: C, 72.98; H, 3.65; N, 14.11.

Synthesis of 2,6-difluoro-3-(pyridin-2-yl)benzaldehyde (3)

A mixture of 3-bromo-2,6-difluorobenzaldehyde (0.442 g, 2.03 mmol) and $Pd(PPh_3)_4$ (0.121 g, 0.104 mmol) in dry toluene (10 mL) was heated up to 80 °C, then 2-(tributylstannyl)pyridine (0.884 g, 2.40 mmol) was added. The mixture was refluxed for 24 h. After the solution was cooled to rt, the reaction mixture was quenched with a saturated aqueous KF solution (10 mL). The solution was dissolved in dichloromethane (100 mL), washed with water (50 mL × 2) and sat. brine (100 mL), and then dried over anhydrous $MgSO_4$. The solvent was removed on a rotary evaporator, and the residue was purified by silica gel column chromatography using ethyl acetate/hexane (2/3, v/v) as eluent to afford a white solid of **3** (0.346 g, 1.59 mmol, 78%). ^{1}H NMR (400 MHz, $CDCl_3$) δ 7.13 (dt, J = 1.4 and 9.2 Hz, 1H), 7.32 (q, J = 4.6 Hz, 1H), 7.78−7.81 (m, 2H), 8.29 (td, J = 6.4 and 8.7 Hz, 1H), 8.74 (td, J = 1.4 and 5.0 Hz, 1H), 10.44 (s, 1H). IR (KBr, cm^{-1}) 501, 679, 756, 847, 1227, 1296, 1589, 1643. ESI-TOF MS: m/z $[M + H]^+$ calcd for $C_{12}H_7F_2NO$: 220.06; found: 220.07. Anal. calcd for $C_{12}H_7F_2NO$: C, 65.76; H, 3.22; N, 6.39. Found: C, 65.62; H, 3.50; N, 6.30.

General procedure of synthesis of H*C*^*N*-1, H*C*^*N*-2, and 4

A solution of phenylmagnesium bromide was prepared by dropwise addition of bromobenzene (1.57 g, 10 mmol) in 15 mL of dry THF *via* a dropping funnel to magnesium

turnings (0.323 g, 13.3 mmol) suspended in dry THF (5 mL) under N_2 at rt, where vigorous stirring was essential. The obtained solution of the Grignard reagent (12 mL) was added slowly to a solution of **1**–**3** (2 mmol) in dry THF (4 mL), and then the reaction mixture was heated at reflux for 5 h. After cooling, 1 M H_2SO_4 (10 mL) was added, and the obtained mixture was stirred at rt for 2 h, followed by neutralization using a saturated aqueous solution of $NaHCO_3$. After the mixture was concentrated on a rotary evaporator, dichloromethane (50 mL) was added to the residual solution. This mixture was vigorously shaken in a separation funnel, and the organic layer was separated, washed with water (50 mL × 2) and sat. brine, and then dried over anhydrous $MgSO_4$. The solvent was removed on a rotary evaporator, and the residue was purified by silica gel column chromatography using ethyl acetate/hexane (1/3, v/v) to obtain the product.

Phenyl(3-(pyridin-2-yl)phenyl)methanone (HC^*N*-1). 81% yield. ^{1}H NMR (400 MHz, $CDCl_3$) δ 7.22−7.29 (m, 1H), 7.49 (t, J = 7.6 Hz, 2H), 7.58−7.62 (m, 2H), 7.75−7.78 (m, 2H), 7.81−7.86 (m, 3H), 8.26 (td, J = 1.4 and 7.8 Hz, 1H), 8.39 (t, J = 1.8 Hz, 1H), 8.69 (d, J = 5.0, 1H). This compound has been reported [23].

(2-Fluoro-5-(pyridin-2-yl)phenyl)(phenyl)methanone (HC^*N*-2). 28% yield. ^{1}H NMR (400 MHz, $CDCl_3$) δ 7.22−7.29 (m, 2H, masked by $CHCl_3$), 7.48 (t, J = 7.7 Hz, 2H), 7.60 (tt, J = 1.4 and 7.3 Hz, 1H), 7.69−7.79 (m, 2H), 7.87 (d, J = 8.2 Hz, 2H), 8.15 (dd, J = 2.5 and 6.6 Hz, 1H), 8.18−8.23 (m, 1H), 8.65−8.69 (m, 1H). IR (KBr, cm^{-1}) 602, 756, 849, 1157, 1250, 1312, 1412, 1504, 1597, 1659. ESI-TOF MS: m/z $[M + Na]^+$ calcd for $C_{18}H_{12}FNNaO$: 300.08; found: 300.07. Anal. calcd for $C_{18}H_{12}FNO$: C, 77.97; H, 4.36; N, 5.05. Found: C, 77.79; H, 4.35; N, 5.06.

(2,6-Difluoro-3-(pyridin-2-yl)phenyl)(phenyl)methanol (4). 74% yield. ^{1}H NMR (400 MHz, $CDCl_3$) δ 2.91 (td, J = 2.3 and 9.2 Hz, 1H), 6.33 (d, J = 8.7 Hz, 1H), 7.03 (dt, J = 1.4 and 9.2

Hz, 1H), 7.23−7.30 (m, 2H, masked by $CHCl_3$), 7.32−7.37 (m, 2H), 7.42 (d, *J* = 7.3 Hz, 2H), 7.67−7.76 (m, 2H), 7.92 (td, *J* = 6.4 and 8.7 Hz, 1H), 8.70 (td, *J* = 1.4 and 4.6 Hz, 1H). IR (KBr, cm^{-1}) 1026, 1177, 1207, 1412, 1435, 1466, 1589, 3024, 3059, 3232. ESI-TOF MS: *m*/*z* $[M + H]^+$ calcd for $C_{18}H_{13}F_2NO$: 298.10; found: 298.10. Anal. calcd for $C_{18}H_{13}F_2NO$: C, 72.72; H, 4.41; N, 4.71. Found: C, 72.52; H, 4.54; N, 4.59.

Synthesis of (2,6-difluoro-3-(pyridin-2-yl)phenyl)(phenyl)methanone (H*C*^*N*-3)

To a solution of **4** (0.243 g, 0.820 mmol) in dichloromethane (40 mL) was added a 4 Å molecular sieve (0.832 g) and pyridinium dichromate (0.539 g, 1.45 mmol) at rt. The reaction mixture was stirred at rt for 8 h, then the suspension was filtered over a Celite® pad, and the solution was evaporated to dryness. The residue was dissolved in dichloromethane (100 mL), and the solution was washed with water (50 mL × 2) and sat. brine (100 mL), and then dried over anhydrous $MgSO_4$. The solvent was removed on a rotary evaporator, and the residue was purified by silica gel column chromatography using ethyl acetate/chloroform (1/10, v/v) as eluent to afford a pale yellow oil, **H*C*^*N*-3** (0.217 g, 0.735 mmol, 90%). ^1H NMR (400 MHz, $CDCl_3$) δ 7.10−7.16 (m, 1H), 7.24−7.30 (m, 1H, masked by $CHCl_3$), 7.49 (t, *J* = 7.7 Hz, 2H), 7.62 (t, *J* = 7.7 Hz, 1H), 7.72−7.75 (m, 2H), 7.90 (d, *J* = 7.7 Hz, 2H), 8.16 (td, *J* = 6.8 and 8.6 Hz, 1H), 8.72 (d, *J* = 4.5 Hz, 1H). IR (KBr, cm^{-1}) 764, 1065, 1126, 1258, 1319, 1582, 1666, 3063. ESI-TOF MS: *m*/*z* $[M + Na]^+$ calcd for $C_{18}H_{11}F_2NNaO$: 318.07; found: 318.07. Anal. calcd for $C_{18}H_{11}F_2N_2O$: C, 73.22; H, 3.75; N, 4.74. Found: C, 73.21; H, 3.94; N, 4.77.

General procedure of synthesis of μ-chloro-bridged iridium(III) dimers $[(C^N\text{-}X)_2IrCl]_2$

The μ-chloro-bridged iridium(III) dimers $[(C^N\text{-}X)_2IrCl]_2$ (**X** = **1**–**3**) were prepared according to the conventional procedure [6]. To a solution of the cyclometalated ligand (H*C*^*N*-**X**, 2.5 mmol) in 2-ethoxyethanol (50 mL) was added a solution of $IrCl_3•3H_2O$ (1.2

mmol) in water (50 mL), and the mixture was heated at 100 °C in an oil bath for 18 h. After cooling, water (100 mL) was added, and the obtained precipitate was collected by filtration and washed with ethanol (20 mL) and hexane (20 mL) to afford $[(\boldsymbol{C}\text{^}\boldsymbol{N}\text{-}\mathbf{X})_2\mathrm{IrCl}]_2$ in 83, 88 and 74% yields for X = 1, 2 and 3, respectively. The obtained materials were highly insoluble, and thus were used in the next reaction without further purification in accordance with conventional procedures.

General procedure of synthesis of bis-cyclometalated complexes

A mixture of $[(\boldsymbol{C}\text{^}\boldsymbol{N}\text{-}\mathbf{X})_2\mathrm{IrCl}]_2$ (0.10 mmol), acetylacetone or picolinic acid (0.40 mmol), and Na_2CO_3 (0.18 g, 1.7 mmol) in 2-ethoxyethanol (30 mL) was heated at 100 °C under nitrogen for 2 h. After cooling, the solvent was removed on a rotary evaporator. The residue was dissolved in dichloromethane, and the solution was washed with water (20 mL × 2) and sat. brine, and dried over anhydrous Na_2SO_4. The solvent was removed on a rotary evaporator, and the residue was purified by alumina column chromatography using dichloromethane as eluent. Further purification was carried out by recrystallization from chloroform-hexane or dichloromethane-hexane.

Bis[2-(5-benzoylphenyl)pyridinato-*N*,*C*$^{2'}$]iridium(III) acetylacetonate (Ir-1a). 41% yield. ^{1}H NMR (400 MHz, $CDCl_3$) δ 1.74 (s, 6H), 5.33 (s, 1H), 6.42 (d, J = 7.8 Hz, 2H), 7.06 (dd, J = 1.9 and 7.8 Hz, 2H), 7.43–7.49 (m, 6H), 7.57 (tt, J = 1.5 and 7.6 Hz, 2H), 7.67–7.70 (m, 4H), 8.01 (td, J = 1.5 and 7.8 Hz, 2H), 8.13 (d, J = 1.8 Hz, 2H), 8.20 (d, J = 8.2 Hz, 2H), 8.64 (d, J = 5.0 Hz, 2H). This compound has been reported [23].

Bis[2-(4-fluoro-5-benzoylphenyl)pyridinato-*N*,*C*$^{2'}$]iridium(III) acetylacetonate (Ir-2a). 31% yield. ^{1}H NMR (400 MHz, acetone-d_6) δ 1.78 (s, 6H), 5.36 (s, 1H), 5.96 (d, J = 11.0 Hz, 2H), 7.45–7.50 (m, 6H), 7.59 (tt, J = 7.8 Hz, 2H), 7.71–7.76 (m, 4H), 7.99 (d, J = 7.3 Hz, 2H),

8.03 (dt, J = 1.4 and 7.8 Hz, 2H), 8.22 (d, J = 8.2 Hz, 2H), 8.46 (dd, J = 0.9 and 5.5 Hz, 2H). IR (KBr, cm^{-1}) 611, 762, 851, 1032, 1155, 1225, 1259, 1396, 1518, 1597, 1647. ESI-TOF MS: m/z $[M + Na]^+$ calcd for $C_{41}H_{29}F_2IrN_2NaO_4$: 867.16; found: 867.16. Anal. calcd for $C_{41}H_{29}F_2IrN_2O_4$: C, 58.35; H, 3.46; N, 3.32. Found: C, 58.22; H, 3.62; N, 3.28.

Bis[2-(4,6-difluoro-5-benzoylphenyl)pyridinato-*N*,*C*$^{2'}$]iridium(III) acetylacetonate (Ir-3a). 24% yield. ^{1}H NMR (400 MHz, acetone-d_6) δ 1.79 (s, 6H), 5.39 (s, 1H), 5.88 (d, J = 9.2 Hz, 2H), 7.49–7.56 (m, 6H), 7.66 (tt, J = 1.4 and 7.3 Hz, 2H), 7.84 (d, J = 7.3 Hz, 4H), 8.07 (dt, J = 1.4 and 7.9 Hz, 2H), 8.28 (d, J = 8.2 Hz, 2H), 8.63 (dd, J = 0.9 and 6.0 Hz, 2H). IR (KBr, cm^{-1}) 673, 706, 733, 752, 773, 945, 1252, 1277, 1396, 1472, 1514, 1578, 1647. ESI-TOF MS: m/z $[M + Na]^+$ calcd for $C_{41}H_{27}F_4IrN_2NaO_4$: 903.14; found: 903.10. Anal. calcd for $C_{41}H_{27}F_4IrN_2O_4$: C, 55.97; H, 3.09; N, 3.18. Found: C, 55.84; H, 3.25; N, 3.29.

Bis[2-(4,6-difluoro-5-benzoylphenyl)pyridinato-*N*,*C*$^{2'}$]iridium(III) picolinate (Ir-3b). 40% yield. ^{1}H NMR (400 MHz, CD_2Cl_2) δ 5.80 (d, J = 9.2 Hz, 1H), 6.01 (d, J = 9.2 Hz, 1H), 7.07 (ddd, J = 1.4, 5.9 and 7.6 Hz, 1H), 7.26 (ddd, J = 1.4, 5.9 and 7.3 Hz, 1H), 7.43–7.53 (m, 6H), 7.57–7.64 (m, 2H), 7.77–7.89 (m, 7H), 7.99 (dt, J = 1.4 and 7.6 Hz, 1H), 8.22 (d, J = 8.2 Hz, 1H), 8.25–8.32 (m, 2H), 8.74 (dd, J = 0.9 and 6.0 Hz, 1H). IR (KBr, cm^{-1}) 766, 1065, 1128, 1169, 1269, 1312, 1325, 1398, 1474, 1514, 1562, 1580, 1659. ESI-TOF MS: m/z $[M + Na]^+$ calcd for $C_{42}H_{24}F_4IrN_3NaO_4$: 926.12; found: 926.10. Anal. calcd for $C_{42}H_{24}F_4IrN_3O_4$: C, 55.87; H, 2.68; N, 4.65. Found: C, 55.49; H, 2.88; N, 4.53.

General procedure of synthesis of tris-cyclometalated complexes

In a 50 mL round-bottom flask, a mixture of $[(\boldsymbol{C}\text{^}\boldsymbol{N}\text{-}\mathbf{X})_2IrCl]_2$ (0.050 mmol) and **H*C*^*N*-X** (0.5 mmol) in glycerol (30 mL) was added. This flask was set up in a J-Science Lab GM•IC Microwave Applicator, and irradiated with microwaves (2450 MHz, 300 W), and the

suspension was refluxed for 1 h. After cooling, the reaction mixture was added to 100 mL of 3% $NaCl_{aq}$. The resultant suspension was extracted with ethyl acetate/hexane (1/1, v/v), and dried over anhydrous Na_2SO_4. The solvent was removed on a rotary evaporator, and the residue was purified by silica gel column chromatography using ethyl acetate/hexane (2/1, v/v) as eluent. Further purification was carried out by recrystallization from chloroform-hexane or dichloromethane-hexane.

***fac*-Tris[2-(5-benzoylphenyl)pyridinato-*N*,$C^{2'}$]iridium(III) (Ir-1c)**. 15% yield. ^{1}H NMR (400 MHz, $CDCl_3$) δ 6.95 (d, J = 8.2 Hz, 3H), 7.01 (ddd, J = 0.9, 5.7 and 7.0 Hz, 3H), 7.21 (dd, J = 1.8 and 7.7 Hz, 3H), 7.42 (t, J = 7.5 Hz, 6H), 7.48–7.57 (m, 6H) , 7.69–7.78 (m, 9H), 8.05 (d, J = 8.2 Hz, 3H), 8.27 (d, J = 1.4 Hz, 3H). ^{13}C NMR (100 MHz, $CDCl_3$) δ 119.72, 122.96, 125.28, 128.03, 129.70, 130.21, 131.50, 132.32, 136.43, 137.07, 138.73, 144.55, 147.12, 165.31, 170.50, 196.89. IR (KBr, cm^{-1}) 708, 752, 773, 945, 1254, 1275, 1396, 1471, 1516, 1578, 1647. ESI-TOF MS: m/z $[M + Na]^+$ calcd for $C_{54}H_{36}IrN_3NaO_3$; 990.23; found: 990.23. Anal. calcd for $C_{54}H_{36}IrN_3O_3$: C, 67.06; H, 3.75; N, 4.34. Found: C, 67.12; H, 3.45; N, 4.57.

***fac*-Tris[2-(5-benzoyl-4-fluorophenyl)pyridinato-*N*,$C^{2'}$]iridium(III) (Ir-2c)**. 30% yield. ^{1}H NMR (400 MHz, $CDCl_3$) δ 6.62 (d, J = 11.5 Hz, 3H), 7.03 (t, J = 5.9 Hz, 3H), 7.43 (t, J = 7.8 Hz, 6H), 7.49–7.56 (m, 6H), 7.75 (t, J = 8.0 Hz, 3H), 7.82 (d, J = 7.8 Hz, 6H), 7.97 (d, J = 8.2 Hz, 3H), 8.02 (d, J = 6.9 Hz, 3H). IR (KBr, cm^{-1}) 766, 1065, 1128, 1169, 1269, 1325, 1398, 1514, 1580, 1659. ESI-TOF MS: m/z $[M + Na]^+$ calcd for $C_{54}H_{33}F_3IrN_3NaO_3$: 1044.20; found: 1044.21. Anal. calcd for $C_{54}H_{33}F_3IrN_3O_3$: C, 68.52; H, 3.26; N, 4.12. Found: C, 68.50; H, 3.45; N, 3.89.

***fac*-Tris[2-(5-benzoyl-4,6-difluorophenyl)pyridinato-*N*,$C^{2'}$]iridium(III) (Ir-3c)**. 59% yield. ^{1}H NMR (400 MHz, CD_2Cl_2) δ 6.52 (d, J = 9.6 Hz, 3H), 7.07 (t, J = 6.6 Hz, 3H), 7.45 (t, J =

7.8 Hz, 6H), 7.53–7.61 (m, 6H), 7.79 (t, J = 7.8 Hz, 3H), 7.86 (d, J = 7.8 Hz, 6H), 8.32 (d, J = 9.2 Hz, 3H). IR (KBr, cm^{-1}) 708, 754, 947, 1016, 1030, 1167, 1258, 1271, 1317, 1404, 1474, 1531, 1599, 1666, 3061. ESI-TOF MS: m/z $[M + Na]^+$ calcd for $C_{54}H_{30}F_6IrN_3NaO_3$: 1098.17; found: 1098.18. Anal. calcd for $C_{54}H_{30}F_6IrN_3O_3$: C, 60.33; H, 2.81; N, 3.91. Found: C, 60.63; H, 3.21; N, 4.01.

2.1.4.2. X-Ray Crystallography

Diffraction data for **Ir-3a** and **Ir-3c** were collected on a Rigaku AFC-7 Mercury CCD diffractometer, using graphite monochromated Mo-Kα radiation (λ = 0.71075 Å). The cell parameters were collected at a temperature of 20 ± 1 °C to maximum 2θ values of 61.1° and 61.6° for **Ir-3a** and **Ir-3c**, respectively. The structures were solved by direct methods using the SHELX97 [38] and the SIR92 [39] programs for **Ir-3a** and **Ir-3c**, respectively, and expanded using Fourier techniques on the DIRDIF99 [40] program. All calculations were performed using the Crystal Structure 4.0 [41] and Crystal Structure 3.8 [42] software packages for **Ir-3a** and **Ir-3c**, respectively. The crystal data and refinement details of the crystal structure determination are given in Table 1.

2.1.4.3. Spectroscopic Measurements

UV-vis absorption spectra were measured on a Shimadzu UV-3600 spectrophotometer. PL spectra were measured on a Horiba Jobin Yvon Fluorolog-3 spectrophotometer. Phosphorescent spectra were measured for samples in a 2-methyltetrahydrofuran glass matrix at 77 K on a Jasco FP-6600 spectrometer equipped with a Jasco PMU-183 phosphorescence measurement base unit. τ_{PL}s were obtained on a Horiba Jobin Yvon FluoroCube spectroanalyzer using a 390 nm nanosecond-order LED light source. Φ_{PL}s were obtained on a Hamamatsu Photonics C9920 PL quantum yield measurement system using an excitation

wavelength of 390 nm. Except for UV-vis absorption spectroscopy, the sample solutions were deaerated by N_2 bubbling, followed by complete sealing, and the analyses were carried out just after preparation of the samples. For the PL measurement, FIrpic, as a referential blue phosphorescent organoiridium(III) complex, was purchased from Luminescence Technology Corp. and used without further purification.

2.1.4.4. Electrochemical Properties

Cyclic voltammograms of the organoiridium(III) complexes were recorded on a Hokuto Denko HZ-5000 electrochemical measurement system at a scanning rate of 100 mV s^{-1}. The measurements were performed in deaerated acetonitrile, where 0.1 M tetrabutylammonium perchlorate was used as a supporting electrolyte at room temperature. The potentials were recorded relative to an $Ag/AgNO_3$ (0.1 M) reference electrode with a Pt wire being used for both working and counter electrodes. An oxidation potential ($E_{1/2,\,Ox}$) was determined using the Fc^+/Fc redox couple as an external standard (0.000 V).

2.1.4.5. Fabrication of OLEDs

For fabrication of OLEDs, PVCz (M_w = 25000−50000) was purchased from Sigma-Aldrich Co., and used after purification by reprecipitation from THF to methanol. PEDOT:PSS (Clevios P CH 8000) and OXD-7 were purchased from Heraeus GmbH and Luminescence Technology Corp., respectively. BPOPB was prepared according to a literature report [36]. Cesium fluoride and aluminum wires were purchased from Wako Pure Chemical Industries, Ltd. and the Nilaco Co., respectively.

Fabrication of device-1. A pre-patterned ITO glass substrate as an anode was routinely cleaned by ultrasonic treatment in an aqueous detergent solution, water, acetone, chloroform, hexane and 2-propanol. PEDOT:PSS (40 nm) was spin-coated onto an ITO layer pretreated

with UV-O_3 and then dried at 115 °C for 1 h. For fabrication of an EML, a mixture of PVCz, OXD-7, and an organoiridium(III) complex in dry toluene (PVCz; 10 mg/0.7 mL of toluene) was filtered through a 0.2 μm Millex-FG filter (Millipore). The obtained stock solution was then spin-coated onto the PEDOT:PSS layer under an argon atmosphere. Thereafter, cesium fluoride (1.0 nm) and aluminum (250 nm) layers were successively embedded on the EML by vacuum deposition with a base pressure of *ca*. 1×10^{-4} Pa. Finally, the device was covered with a glass cap and encapsulated with a UV-curing epoxy resin under a dry argon atmosphere to keep oxygen and moisture away from the device. The emitting area was 10 mm^2 (2 mm × 5 mm). The device fabrication was carried out in a glovebox filled with dry argon, except for the preparation of the PEDOT:PSS layer.

Fabrication of device-2. A PEDOT:PSS layer (40 nm) was fabricated on an ITO glass substrate using the same method as for device-1. For fabrication of an EML-1, a mixture of PVCz and an organoiridium(III) complex in dry toluene (PVCz; 6.4 mg/0.7 mL of toluene) was filtered through a 0.2 μm Millex-FG filter (Millipore). The obtained stock solution was then spin-coated onto the PEDOT:PSS layer under an argon atmosphere. Then, for fabrication of an EML-2, a mixture of BPOPB and an organoiridium(III) complex in dry 2-propanol (BPOPB; 4.1 mg/0.7 mL of 2-propanol) was filtered through a 0.2 μm Millex-FG filter (Millipore). The obtained stock solution was then spin-coated onto the EML-1 under an argon atmosphere. Thereafter, cesium fluoride (1.0 nm) and aluminum (250 nm) layers were embedded, and then the device was covered with a glass cap in the same way as device-1.

2.1.5. Notes and References

[1] H. Xu, R. Chen, Q. Sun, W. Lai, Q. Su, W. Huang and X. Liu, *Chem. Soc. Rev*., 2014, **43**, 3259−3302.

[2] Y. Chi and P. T. Chou, *Chem. Soc. Rev*., 2010, **39**, 638−655.

[3] Y. Tao, C. Yang and J. Qin, *Chem. Soc. Rev*., 2011, **40**, 2943−2970.

[4] C. Adachi, M. A. Baldo, M. E. Thompson and S. R. Forrest, *J. Appl. Phys*., 2001, **90**, 5048−5051.

[5] A. B. Tamayo, B. D. Alleyne, P. I. Djurovich, S. Lamansky, I. Tsyba, N. N. Ho, R. Bau and M. E. Thompson, *J. Am. Chem. Soc*., 2003, **125**, 7377−7387.

[6] S. Lamansky, P. Djurovich, D. Murphy, F. Abdel-Razzaq, H.-E. Lee, C. Adachi, P. E. Burrows, S. R. Forrest and M. E. Thompson, *J. Am. Chem. Soc*., 2001, **123**, 4304−4312.

[7] J. Brooks, Y. Babayan, S. Lamansky, P. I. Djurovich, I. Tsyba, R. Bau and M. E. Thompson, *Inorg. Chem*., 2002, **41**, 3055−3066.

[8] S. Lamansky, P. Djurovich, D. Murphy, F. Abdel-Razzaq, R. Kwong, I. Tsyba, M. Bortz, B. Mui, R. Bau and M. E. Thompson, *Inorg. Chem*., 2001, **40**, 1704−1711.

[9] X. Yang, G. Zhou and W.-Y. Wong, *Chem. Soc. Rev*., 2015, **44**, 8484−8575.

[10] J. Zhao, Y. Yu, X. Yang, X. Yan, H. Zhang, X. Xu, G. Zhou, Z. Wu, Y. Ren and W.-Y. Wong, *ACS Appl. Mater. Interfaces*, 2015, **7**, 24703−24714.

[11] S. Koseki, N.-O. Kamata, T. Asada, S. Yagi, H. Nakazumi and T. Matsushita, *J. Phys. Chem. C*, 2013, **117**, 5314−5327.

[12] G. M. Farinola and R. Ragni, *Chem. Soc. Rev*., 2011, **40**, 3467−3482.

[13] H. Tsujimoto, S. Yagi, S. Ikawa, H. Asuka, T. Maeda, H. Nakazumi and Y. Sakurai, *J. Jpn. Soc. Colour Mater.*, 2010, **83**, 207–214.

[14] S. Ikawa, S. Yagi, T. Maeda, H. Nakazumi and Y. Sakurai, *J. Lumin*., 2014, **155**, 368−373.

[15] S. Lee, S. O. Kim, H. Shin, H. J. Yun, K. Yang, S. K. Kwon, J. J. Kim and Y. H. Kim, *J. Am. Chem. Soc*., 2013, **135**, 14321−14328.

[16] S. J. Lee, K. M. Park, K. Yang and Y. Kang, *Inorg. Chem*., 2009, **48**, 1030−1037.

[17] C.-H. Yang, S.-W. Li, Y. Chi, Y.-M. Cheng, Y.-S. Yeh, P.-T. Chou, G.-H. Lee, C.-H. Wang and C.-F. Shu, *Inorg. Chem*., 2005, **44**, 7770−7780.

[18] S.-J. Yeh, C.-T. Chen, Y.-H. Song, Y. Chi and M.-H. Ho, *J. Soc. Inf. Disp*., 2005, **13**, 857−862.

[19] N. G. Park, G. C. Choi, Y. H. Lee and Y. S. Kim, *Curr. Appl. Phys*., 2006, **6**, 620−626.

[20] V. V. Grushin, N. Herron, D. D. LeCloux, W. J. Marshall, V. A. Petrov and Y. Wang, *Chem. Commun*., 2001, 1494−1495.

[21] H.-J. Seo, K.-M. Yoo, M. Song, J. S. Park, S.-H. Jin, Y. I. Kim and J.-J. Kim, *Org. Electron*., 2010, **11**, 564−572.

[22] S. Tokito, T. Iijima, Y. Suzuri, H. Kita, T. Tsuzuki and F. Sato, *Appl. Phys. Lett*., 2003, **83**, 569−571.

[23] K. H. Lee, J. S. Hwang, D. H. Chae, S. J. Lee, Y. K. Kim and S. S. Yoon, *Mol. Cryst. Liq. Cryst.*, 2012, **563**, 185−194.

[24] M. Marín-Suárez, B. F. E. Curchod, I. Tavernelli, U. Rothlisberger, R. Scopelliti, I. Jung, D. D. Censo, M. Grätzel, J. F. Fernández-Sánchez, A. Fernández-Gutiérrez, M. K. Nazeeruddin and E. Baranoff, *Chem. Mater*., 2012, **24**, 2330−2338.

[25] S. Ikawa, S. Yagi, T. Maeda, H. Nakazumi, H. Fujiwara and Y. Sakurai, *Dyes Pigm*., 2012, **95**, 695−705.

[26] S. Ikawa, S. Yagi, T. Maeda, H. Nakazumi, H. Fujiwara, S. Koseki and Y. Sakurai, *Inorg. Chem. Commun.*, 2013, **38**, 14−19.

[27] J. Frey, B. F. Curchod, R. Scopelliti, I. Tavernelli, U. Rothlisberger, M. K. Nazeeruddin and E. Baranoff, *Dalton Trans*., 2014, **43**, 5667−5679.

[28] C. Hansch, A. Leo and R. W. Taft, *Chem. Rev*., 1991, **91**, 165−195.

[29] R. Wang, D. Liu, R. Zhang, L. Deng and J. Li, *J. Mater. Chem*., 2012, **22**, 1411−1417.

[30] G.-J. Zhou, W.-Y. Wong, B. Yao, Z. Xie and L. Wang, *J. Mater. Chem*., 2008, **18**, 1799.

[31] Measured for a commercially available sample of FIrpic in deaerated dichloromethane.

[32] M. J. Frisch, G. W. Trucks, H. B. Schlegel, G. E. Scuseria, M. A. Robb, J. R. Cheeseman, G. Scalmani, V. Barone, B. Mennucci, G. A. Petersson, H. Nakatsuji, M. Caricato, X. Li, H. P. Hratchian, A. F. Izmaylov, J. Bloino, G. Zheng, J. L. Sonnenberg, M. Hada, M. Ehara, K. Toyota, R. Fukuda, J. Hasegawa, M. Ishida, T. Nakajima, Y. Honda, O. Kitao, H. Nakai, T. Vreven, J. A. Montgomery Jr, J. E. Peralta, F. Ogliaro, M. J. Bearpark, J. Heyd, E. N. Brothers, K. N. Kudin, V. N. Staroverov, R. Kobayashi, J. Normand, K. Raghavachari, A. P. Rendell, J. C. Burant, S. S. Iyengar, J. Tomasi, M. Cossi, N. Rega, N. J. Millam, M. Klene, J. E. Knox, J. B. Cross, V. Bakken, C. Adamo, J. Jaramillo, R. Gomperts, R. E. Stratmann, O. Yazyev, A. J. Austin, R. Cammi, C. Pomelli, J. W. Ochterski, R. L. Martin, K. Morokuma, V. G. Zakrzewski, G. A. Voth, P. Salvador, J. J. Dannenberg, S. Dapprich, A. D. Daniels, Ö. Farkas, J. B. Foresman, J. V. Ortiz, J. Cioslowski and D. J. Fox, *Gaussian 09*, Gaussian, Inc., Wallingford, CT, 2009.

[33] A. D. Becke, *J. Chem. Phys*., 1993, **98**, 5648−5652.

[34] S. Chiodo, N. Russo and E. Sicilia, *J. Chem. Phys*., 2006, **125**, 104107 (8 pages).

[35] X. Zhou, D. S. Qin, M. Pfeiffer, J. Blochwitz-Nimoth, A. Werner, J. Drechsel, B. Maennig and K. Leo, *Appl. Phys. Lett*., 2002, **81**, 4070−4072.

[36] N. Aizawa, Y.-J. Pu, M. Watanabe, T. Chiba, K. Ideta, N. Toyota, M. Igarashi, Y. Suzuri, H. Sasabe and J. Kido, *Nat. Commun*., 2014, **5**, 5756 (7 pages).

[37] M. R. Luzung, J. S. Patel and J. Yin, *J. Org. Chem*., 2010, **75**, 8330−8332.

[38] G. M. Sheldrick, *Acta Crystallogr., Sect. A: Found. Crystallogr.*, 2008, **64**, 112−122.

[39] A. Altomare, G. Cascarano, C. Giacovazzo, A. Guagliardi, M. C. Burla, G. Polidori and

M. Camalli, *J. Appl. Crystallogr*., 1994, **27**, 435−436.

[40] P. T. Beurskens, G. Admiraal, G. Beuskens, W. P. Bosman, R. D. Gelder, R. Israel and J. M. M. Smits, *The DIRDIF-99 program system; technical report of crystallography laboratory*, University of Nijimegen, Nijimegen, The Netherlands, 1999.

[41] *CrystalStructure. Version 4.0*, Rigaku Corporation, Tokyo, Japan, 2010.

[42] *CrystalStructure. Version 3.8*, Rigaku Corporation, Tokyo, Japan, 2006.

Chapter 2

Section 2.2

Sky-Blue Phosphorescence from Bis- and Tris-Cyclometalated Iridium(III) Complexes Bearing Carbazole-Based Dendrons: Fabrication of Non-Doped Multilayer Organic Light-Emitting Diodes by Solution Processing

2.2.1. Introduction

Phosphorescent cyclometalated iridium(III) complexes are often used as emitters for organic light-emitting diodes (OLED) because they allow us to obtain excellent internal quantum efficiencies (η_{int}) up to 100% due to superiority in spin statics to fluorescent OLEDs [1–13]. Recently, solution-processable non-doped OLEDs whose emitting layer (EML) consists of a charge carrier transporting emitter have been enthusiastically developed not only to avoid incompatibility (*i.e.*, phase separation) between the charge carrier transporting host and the emitting dopant in EML but also to simplify the device fabrication process [14–23]. In this regard, phosphorescent iridium(III) complexes with hole- and/or electron-transporting dendrons have been developed, which show the ability to suppress aggregate formation between the luminescent cores [3,5,14,16–21,24–29]. However, few blue phosphorescent ones have been reported although they are important as emitters of one of the RGB primary colors [19,20,26,28]. Wang and co-workers recently reported a sky-blue phosphorescent tris-cyclometalated iridium(III) complex bearing carbazole-based dendrons, where they fabricated a nondoped OLED employing the dendrimer as EML. With the help of a vacuum-deposited electron-transporting layer (ETL), the non-doped device showed an excellent maximum external quantum efficiency ($\eta_{ext,\ max}$) of 15.3% [20]. However, few

examples of efficient non-doped OLEDs in which all organic layers were fabricated by solution processing have so far been reported [22,23]. To achieve high η_{int}, an organic multilayer structure consisting of a stack of the hole-injection layer (HIL)/hole-transporting layer (HTL)/EML/ETL is required from the viewpoint of the electron–hole charge balance factor (γ), and such a device structure is generally fabricated by vacuum deposition methods [30–32]. Recently Pu and co-workers reported the fabrication of highly efficient multilayer OLEDs by the spin-coating technique aimed at low cost device production, utilizing orthogonal solvents for preparation of the successively stacked emitting layers [33]. Besides their sophisticated devices, several types of multilayer structures have so far been fabricated by solution processing; for example, HIL/doped EML/ETL [34–36], HIL/non-doped EML/ETL [15] and HIL/HTL/doped EML/ETL [33,37,38]. However, an OLED with a HIL/HTL/non-doped EML/ETL stacked structure fully fabricated by solution processing has never been reported. In this study, the author has designed novel blue phosphorescent bis- and tris-cyclometalated iridium(III) complexes bearing carbazole-appended dendrons **Ir-H1a** and **Ir-H1b** (Fig. 1) whose luminescent cores are based on the excellent sky-blue phosphorescent iridium(III) complexes discussed in Section 2.1, namely, **Ir-3b** and **Ir-3c**, respectively (Fig. 1) [11]. The dendron bearing *m*-phenylene linkages with the π-conjugation partially disconnected is adopted to keep its triplet level higher than those of the blue luminescent cores [39]. In addition, attachment of *tert*-butyl groups at the peripheries of the dendrons affords high liposolubility and insolubility in alcohol, and thus such properties should allow us to fabricate a solution-processed multi-stacked structure by using an apolar solvent and alcohol as orthogonal solvents. Here the author reports the synthesis and photoluminescence (PL) properties of **Ir-H1**, and also demonstrate the fabrication of a non-doped multilayer OLED by solution processing.

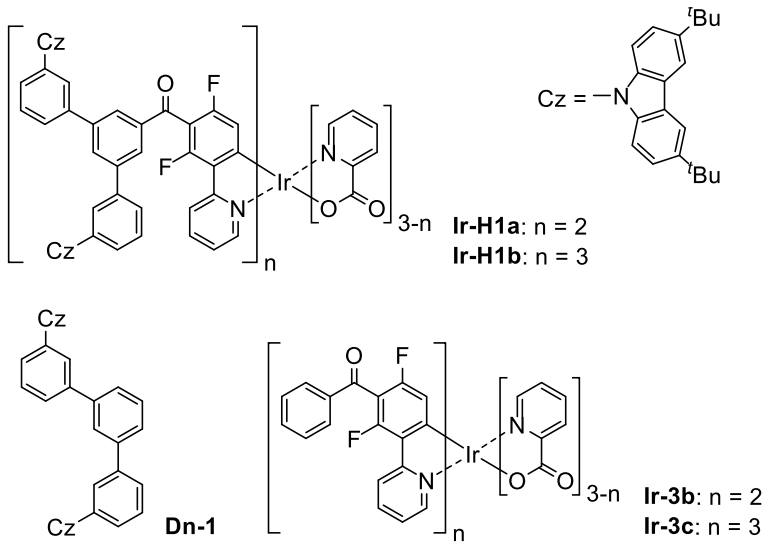

Fig. 1. Chemical structures of **Ir-H1a**, **Ir-H1b**, **Ir-3b**, **Ir-3c** and **Dn-1**.

2.2.2. Results and Discussion

2.2.2.1. Synthesis and Characterization

The total synthetic scheme of **Ir-H1** is shown in Scheme 1. The carbazole-appended 2-phenylpyridine derivative **H*C*^*N*-H1** corresponding to the cyclometalated ligand was synthesized through three steps from the reported aldehyde **3**. First, the Grignard reaction of (3,5-dibromophenyl)magnesium bromide [40] with 2,6-difluoro-3-(pyridin-2-yl)benzaldehyde (**3**) [11] afforded a dibromofunctionalized 2-phenylpyridine derivative **5** in 56% yield, which was oxidized by pyridinium dichromate (PDC) to obtain a benzophenone derivative **6** in 78% yield. The Suzuki–Miyaura cross coupling reaction of **6** and (3,6-di-*tert*-butylcarbazol-9-yl)phenyl boronic acid pinacol ester (**7**) [39] yielded **H*C*^*N*-H1** in 74% yield, which was reacted with iridium(III) chloride trihydrate to obtain the corresponding μ-chloro-bridged iridium(III) dinuclear complex $[(\boldsymbol{C}\text{^}\boldsymbol{N}\text{-}\mathbf{H1})_2\mathrm{Ir}(\mu\text{-Cl})]_2$ in 98% yield. The dendritic bis- and tris-cyclometalated iridium(III) complexes **Ir-H1a** and **Ir-H1b** were synthesized from $[(\boldsymbol{C}\text{^}\boldsymbol{N}\text{-}\mathbf{H1})_2\mathrm{Ir}(\mu\text{-Cl})]_2$ through ligand exchange with picolinate and ***C*^*N*-H1** in the yields of 30 and 23%, respectively, both of which were well characterized by

^{1}H and ^{19}F NMR, MALDI TOF-MS and elemental analysis. According to the ^{1}H and ^{19}F NMR spectra, **Ir-H1b** has a highly symmetrical structure in which the three cyclometalated ligands are magnetically equivalent. Thus, **Ir-H1b** was obtained as a facial isomer which generally shows a higher PL quantum yield (Φ_{PL}) than the meridional isomer [9]. The carbazole dimer **Dn-1** (Fig. 1) was also synthesized by the Suzuki–Miyaura coupling reaction of the boronic ester **7** and 1,3-diiodobenzene as a model compound of the dendron of **Ir-H1**.

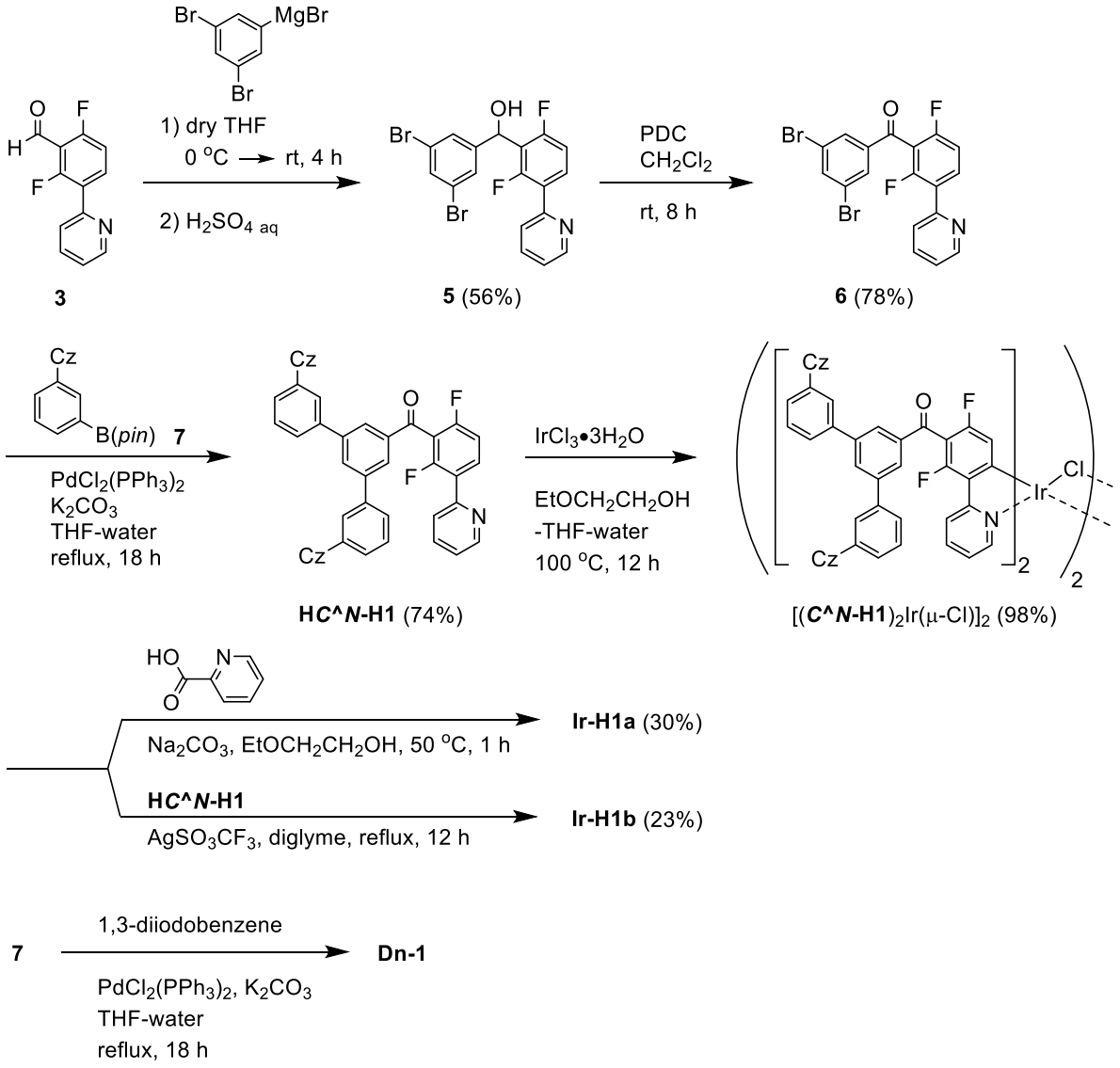

Scheme 1. Syntheses of **Ir-H1** and **Dn-1**. The ligand *pin* corresponds to pinacolate. The structure of Cz is represented in Fig. 1.

2.2.2.2. UV-Vis Absorption and Photoluminescence Properties

UV-vis absorption spectra of the dendritic complexes **Ir-H1a** and **Ir-H1b** in dichloromethane (10 μM) are shown in Fig. 2, along with the spectra of the referential core complexes **Ir-3b** and **Ir-3c** and the dendron model compound **Dn-1**. The spectral data of these compounds are also summarized in Table 1. In **Ir-H1**, characteristic absorption peaks were observed at *ca*. 290, *ca*. 330, and *ca*. 345 nm, almost identical to those of **Dn-1**. Thus, these are assigned to the π–π^* transition at the carbazole-based dendron chromophores [41]. As observed in **Ir-3b** and **Ir-3c**, **Ir-H1** showed broad absorption shoulder bands at *ca*. 370–390 nm assignable to spin-allowed metal-to-ligand charge transfer (^{1}MLCT) transitions at their cores, and the next weak shoulder bands at *ca*. 450 nm are assigned to the spin-forbidden ^{3}MLCT transitions [11].

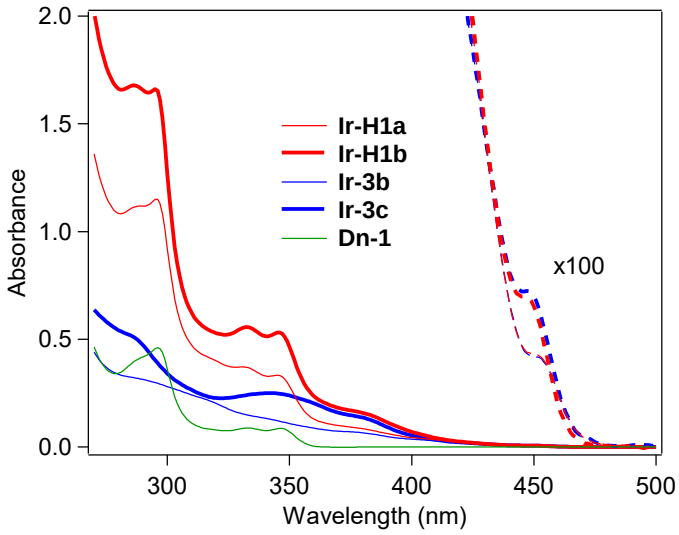

Fig. 2. UV-vis absorption spectra of **Ir-H1a**, **Ir-H1b**, **Ir-3b, Ir-3c**, and **Dn-1** in dichloromethane (10 μM). Dotted lines are the spectra magnified a hundred times.

Table 1. UV-vis absorption and PL properties of **Ir-H1a**, **Ir-H1b**, **Ir-3b**, **Ir-3c** and **Dn-1**.

Compd	CH_2Cl_2 solution (10 μM)				Neat film (80 nm)	
	λ_{abs}[a] (nm) [log (ε_{abs}[b] /(M^{-1} cm^{-1}))]	λ_{PL}[c] (nm)	Φ_{PL}[d]	τ_{PL}[e] (μs)	λ_{PL}[a] (nm)	Φ_{PL}[d]
Ir-H1a	289 [5.05], 296 [5.06], 330 [4.57], 345 [4.52], 370 sh [4.00], 448 sh [2.58]	464, 491	0.78	1.78	470, 493	0.33
Ir-H1b	286 [5.22], 295 [5.22], 332 [4.75], 346 [4.72], 370 sh [4.26], 445 sh [2.84]	460, 488	0.80	1.48	463, 488	0.25
Ir-3b	335 sh [4.16], 375 sh [3.85], 450 sh [2.62][f]	464, 492[f]	0.82[f]	1.97[f]	499	0.47
Ir-3b	285 sh [4.71], 342 [4.40], 380 sh [4.13], 445 sh [2.88][f]	463, 489[f]	0.90[f]	1.54[f]	490	0.21
Dn-1	290 sh [4.62], 296 [4.66], 333 [3.95], 346 [3.94]	356, 373	0.070	---[g]	---[g]	---[g]

[a]Absorption wavelength where the symbol "sh" indicates a peak observed as a shoulder. [b]Molar absorption coefficient. [c]PL wavelength. [d]PL quantum yield. [e]PL lifetime detecterd at the shortest λ_{PL} of each complexes where the χ^2 value was 1.03−1.14.[f]Reported values in Ref. 11. [g]Not measured.

PL spectra of **Ir-H1a** and **Ir-H1b** in deaerated dichloromethane (10 μM) at rt are shown in Fig. 3a and b, respectively. The PL properties of **Ir-H1** are also shown in Table 1, accompanied by the data of **Ir-3b**, **Ir-3c** and **Dn-1**. The complexes **Ir-H1a** and **Ir-H1b** exhibited sky-blue PL (PL wavelength (λ_{PL}); 464 and 460 nm, respectively). The relatively long PL lifetimes (τ_{PL}; 1.78 and 1.48 μs, respectively) clearly show the observed emission is based on phosphorescence. The PL spectra were identical to those of the referential core complexes (Fig. 3c and d). The Φ_{PL}s of **Ir-H1a** and **Ir-H1b** were 0.78 and 0.80, respectively, which were still excellent although they were slightly lower than those of **Ir-3b** (0.82) and **Ir-3c** (0.90). This indicates that the triplet level of the dendron moiety is higher than that of the luminescent core and that the triplet exciton generated at the core is not trapped by the dendrons. In fact, the triplet energy (E_T) of **Dn-1** was estimated as 2.82 eV from the phosphorescence spectrum in glassy 2-methyltetrahydrofuran at 77 K, which is higher than those of **Ir-H1a** and **Ir-H1b** (2.67 and 2.70 eV, respectively).

Next, the PL spectra of the neat films of **Ir-H1a** and **Ir-H1b** were recorded, which are also shown in Fig. 3a and b, respectively. Sky-blue emission was observed for **Ir-H1a** (λ_{PL}; 470 nm) even in the neat film state, although the Φ_{PL} decreased to 0.33 in comparison with that in dichloromethane. On the other hand, **Ir-3b** showed aggregate-based green emission at 499 nm (Fig. 3c). An **Ir-3b**–**Dn-1** blended film, which included **Ir-3b** and **Dn-1** at the same core–dendron ratio as **Ir-H1a** (1 : 2, mol/mol), still showed aggregate-based emission similar to the neat film of **Ir-3b** (Fig. 3c). This clearly indicates that the dendrons connected to the cyclometalated ligands efficiently suppress aggregate formation. The tris-cyclometalated complex **Ir-H1b** also showed monomer-based emission in the film state (λ_{PL}, 464 nm; Φ_{PL}, 0.25) with almost the same PL spectrum as that in dichloromethane (Fig. 3b), whereas the neat film of **Ir-3c** and the **Ir-3c**–**Dn-1** (1 : 3, mol/mol) blended film exhibited aggregation-based emission (Fig. 3d), as seen in the **Ir-3b** and **Ir-3b**–**Dn-1** films. Therefore,

the luminescent core of **Ir-H1** is effectively isolated by the carbazole-based dendrons.

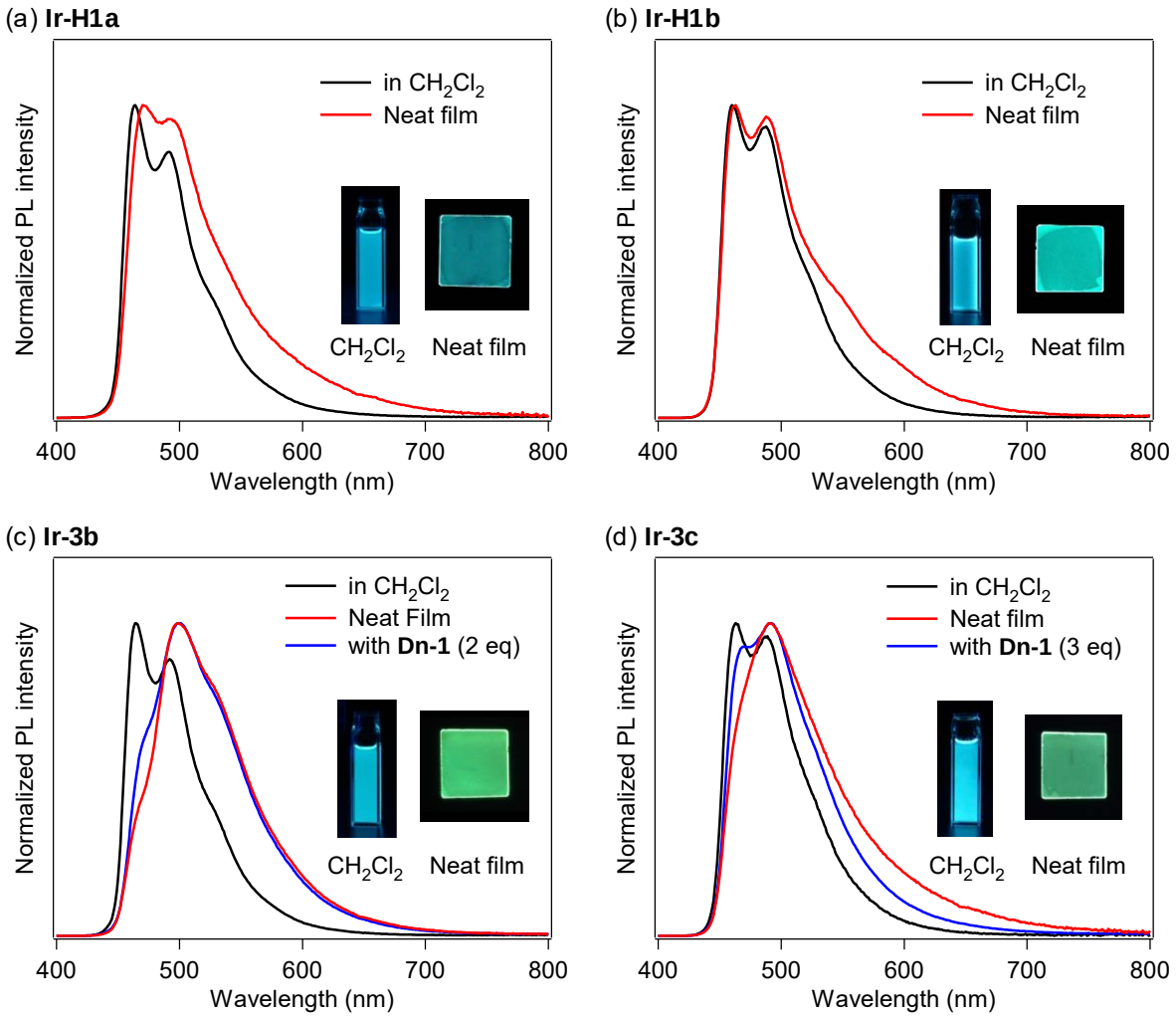

Fig. 3. PL spectra (λ_{ex}; 390 nm) of (a) **Ir-H1a** (a CH_2Cl_2 solution and a neat thin film), (b) **Ir-H1b** (a CH_2Cl_2 solution and a neat thin film), (c) **Ir-3b** (a CH_2Cl_2 solution, a neat thin film and a blended film with **Dn-1** (2 eq.)), and (d) **Ir-3c** (a CH_2Cl_2 solution, a neat thin film and a blended film with **Dn-1** (3 eq.)). The spectra of the neat thin films were measured under N_2 flow (rt). The photographs of the emitting solutions and neat films are also shown in the figures.

To obtain high performance OLEDs, it is necessary that excitons generated at the dendrons are efficiently transferred to the luminescent core [14,24,27,29], and thus the energy transfer in **Ir-H1** was investigated, where **Ir-3b**–**Dn-1** and **Ir-3c**–**Dn-1** mixed dopants were employed as references. To reduce the intermolecular excitonic interaction, the dopants were doped into poly(methyl methacrylate) (PMMA) films. First, the UV-vis absorption spectrum of the **Ir-3b**–**Dn-1** and **Ir-3c**–**Dn-1** co-doped films were obtained, and the excitation wavelength (λ_{ex}) of the dendron was determined. The appropriate λ_{ex} was 290 nm because **Dn-1** strongly absorbed the 290 nm light and **Ir-3b** and **Ir-3c** did not show strong absorption at 290 nm (see Fig. 2). As shown in Fig. 4, the film co-doped with **Ir-3b** and **Dn-1** (10 and 20 μmol g^{-1}, respectively) exhibited emission from both **Ir-3b** (λ_{PL}; 464 nm) and **Dn-1** (λ_{PL}; 354 nm) when excited at 290 nm. On the other hand, the **Ir-H1a**-doped film (10 μmol g^{-1}) exclusively exhibited emission from the luminescent core (λ_{PL}; 466 nm), and emission from the dendrons was efficiently quenched [24,27,29]. In addition, the shape of the excitation spectrum of **Ir-H1a** was almost identical to that of its absorption spectrum (Fig. 5), although the intensity around 290 nm, assignable to the absorption of the dendrons, was slightly reduced by *ca*. 16% in comparison with the absorption spectrum. Thus the emission was obtained from the luminescent core even when the excitons were generated on the dendrons [14]. These results indicate the efficient energy transfer from the dendrons to the core of **Ir-H1a**. In the case of **Ir-H1b**, similar spectral behaviour to **Ir-H1a** was obtained, showing that efficient energy transfer occurs from the dendrons to the luminescent core.

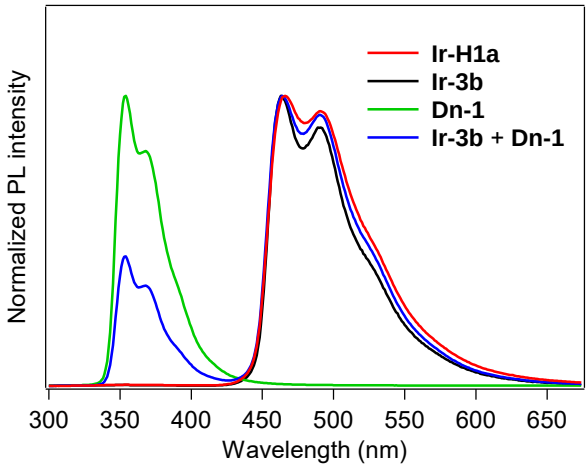

Fig. 4. PL spectra (λ_{ex}; 290 nm) of PMMA films doped with **Ir-H1a** (10 μmol g^{-1}), **Ir-3b** (10 μmol g^{-1}), **Dn-1** (20 μmol g^{-1}), and **Ir-3b** + **Dn-1** (10 and 20 μmol g^{-1}, respectively).

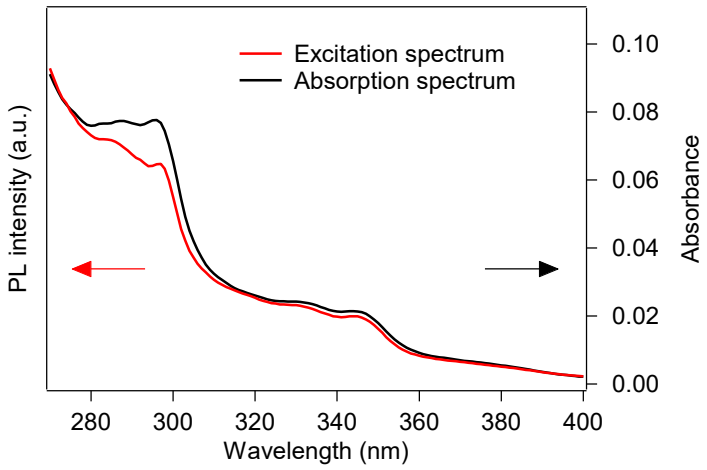

Fig. 5. UV-vis absorption and excitation spectra (λ_{PL}; 466 nm) of the PMMA film doped with **Ir-H1a** (10 μmol g^{-1}).

2.2.2.3. Electrochemical Properties

The oxidation and reduction potentials of **Ir-H1a**, **Ir-H1a**, **Ir-3b**, **Ir-3c**, and **Dn-1** were determined by cyclic voltammetry in dichloromethane and *N*,*N*-dimethylformamide, respectively, where the oxidation potentials of **Ir-3b** and **Ir-3c** have already been reported [11]. All the compounds exhibited pseudo-reversible oxidation and reduction cycles (Fig. 6 and 7). The energy levels of HOMO and LUMO (E_{HOMO} and E_{LUMO}, respectively) were calculated from their half-wave potentials by comparing with that of the ferrocenium/ferrocene (Fc^+/Fc) redox cycle (E_{HOMO}; −4.80 eV), and are summarized in Table 2. The E_{HOMO}s of **Ir-H1a** and **Ir-H1b** are −5.56 eV, which is higher than that of **Ir-3b** and **Ir-3c** (*ca*. −5.8 eV) and almost identical to that of **Dn-1** (−5.53 eV). The E_{LUMO}s of **Ir-H1a** (−2.66 eV) and **Ir-H1b** (−2.64 eV) are identical to that of **Ir-3b** and **Ir-3c** (*ca*. −2.6 eV) [11]. This result indicates that the HOMO and LUMO of **Ir-H1** are localized on the dendrons and the luminescent core, respectively. Thus injected holes should be transported to the cathode side of EML through the dendron of **Ir-H1**. We tried to obtain the oxidation potentials for the luminescent cores of **Ir-H1a** and **Ir-H1b** by sweeping at higher voltage, and irreversible second oxidation cycles were obtained (onset potential: 1.08 V for **Ir-H1a**, *vs*. Fc^+/Fc).

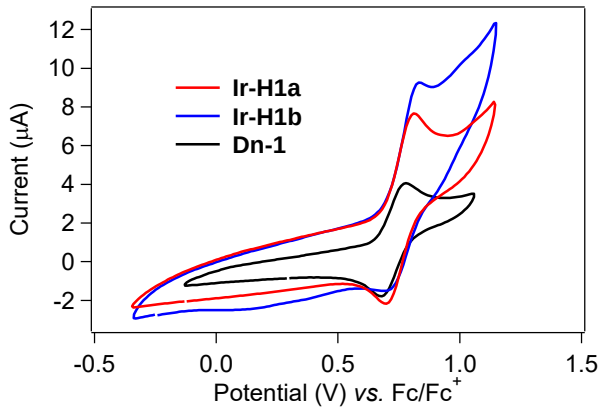

Fig. 6. Cyclic voltammograms of **Ir-H1** and **Dn-1** in dichloromethane (0.50 mM) for oxidation potentials.

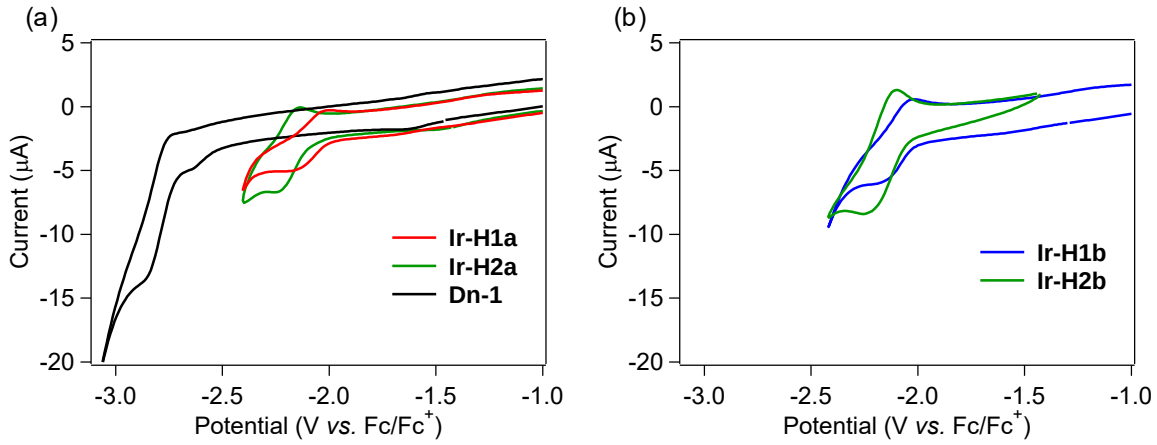

Fig. 7. Cyclic voltammograms of (a) **Ir-H1a** (1.0 mM), **Ir-3b** (1.0 mM) and **Dn-1** (3.0 mM) (b) **Ir-H1b** (1.0 mM) and **Ir-3c** (1.0 mM) in deaerated DMF for reduction potentials.

Table 2. Electrochemical properties and the calculated E_{HOMO}s and E_{LUMO}s of **Ir-H1a**, **Ir-H1b**, **Ir-3b**, **Ir-3c** and **Dn-1**.

Compd	$E_{1/2,\,Ox}$ (V) *vs.* Fc^+/Fc	$E_{1/2,\,Red}$ (V) *vs.* Fc^+/Fc	E_{HOMO}[b] (eV)	E_{LUMO}[c] (eV)
Ir-H1a	0.76	−2.14	−5.56	-2.66
Ir-H1b	0.76	−2.16	−5.56	-2.64
Ir-3b	0.94[a]	−2.21[a]	−5.74	-2.59
Ir-3c	1.03[a]	−2.19[a]	−5.83	-2.61
Dn-1	0.73	−2.85	−5.53	-1.95

[a]Reported value in Ref. 11. [b]E_{HOMO} [eV] = −($E_{1/2,ox}$ + 4.80). [c]E_{LUMO} [eV] = −($E_{1/2,red}$ + 4.80).

2.2.2.4. Thermal Properties

Thermogravimetric (TG) and differential scanning calorimetric (DSC) analyses are carried out for the dendritic complexes **Ir-H1a** and **Ir-H1b**. The TG and DSC heating curves are shown in Fig. 8a and b, respectively, and TG curves of the reference core complexes **Ir-3b** and **Ir-3c** are also shown in Fig. 8a. In the TG profiles, the 1 wt% decomposition

temperatures ($T_d^{1\%}$) of **Ir-H1a** and **Ir-H1b** were 372 and 446 °C, showing they exhibited a considerably higher stability than **Ir-3b** and **Ir-3c** ($T_d^{1\%}$; 331 and 340 °C, respectively). According to the DSC thermograms, **Ir-H1a** and **Ir-H1b** showed a baseline shift with an associated endothermic peak at around 270 °C, which is assignable to the glass transition with enthalpy relaxation [42], and no exothermic peaks for crystallization were observed. Many of the reported dendrimer-type organoiridium(III) complexes have lower glass transition temperatures (T_g) around 100 °C, and only a few examples of high T_gs (> 270 °C) are reported [19,20,26,28]. Thus, the present dendrimers form very stable amorphous glassy states. It is conceivable that the structurally hindered dendritic structure including the twisted aromatic local structures should enhance the amorphous stability as well as thermal stability [43].

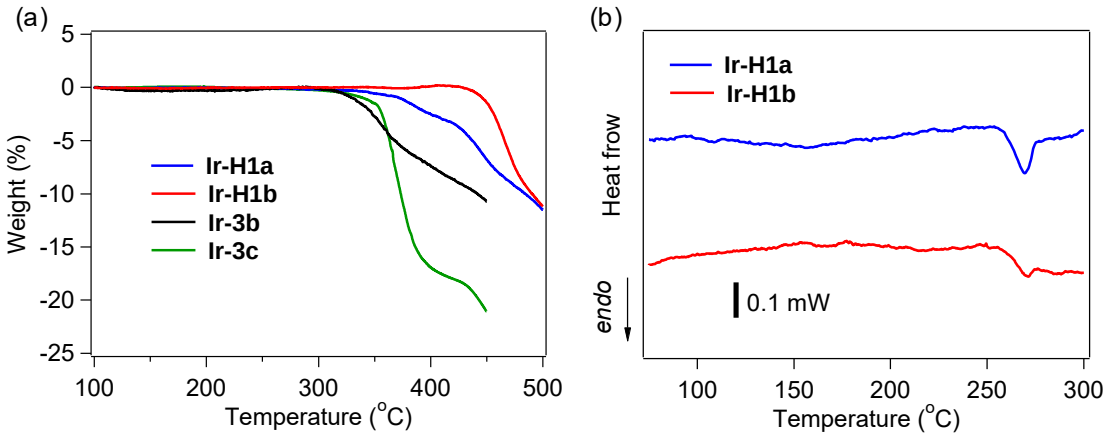

Fig. 8. (a) TG curves of **Ir-H1a**, **Ir-H1b**, **Ir-3b**, **Ir-3c**, and (b) DSC heating curves of **Ir-H1** under N_2 flow. The heating rate and the sample size were 10 K min^{-1} and *ca*. 2 mg, respectively.

2.2.2.5. OLED Fabrication

The author fabricated solution-processed OLEDs whose device structure is ITO (150 nm, anode)/PEDOT:PSS (40 nm)/*X*/CsF (1 nm)/Al (250 nm, cathode). The component *X* represents a single layer or multi-stacked layers. First, simple non-doped OLEDs Device-1a and Device-1b employing the dendritic complexes **Ir-H1a** and **Ir-H1b**, respectively, were fabricated (*X* = **Ir-H1** (80 nm)). As referential OLEDs employing the benchmark sky-blue emitter bis[(4,6-difuorophenyl)pyridinato-*N*,$C^{2'}$]iridium(III) picolinate (FIrpic) [44], Device-1c (*X* = FIrpic (80 nm)) and Device-1c' (*X* = FIrpic : **Dn-1** (1 : 2, mol/mol, 80 nm)), were also fabricated. The device performances are summarized in Table 3. Device-1a and Device-1b showed current density–voltage–luminance (*J*–*V*–*L*) curves with threshold voltages (Fig. 9), characteristic of semiconductive devices, and gave sky-blue EL with maximum luminances (L_{max}) of 1700 and 1600 cd m^{-2} at 17.0 V, respectively. The $\eta_{ext,\ max}$s were relatively low; 0.953 (@12.0 V) and 0.498% (@13.5 V), respectively. The EL spectra of the devices (Fig. 10) were roughly identical to the PL spectra of **Ir-H1a** and **Ir-H1b** (Fig. 3a and b), respectively. The CIE chromaticity coordinate of EL from Device-1a was (0.21, 0.36), which was more greenish than that of the reported OLED doped with the corresponding luminescent core **Ir-3b** (CIE; (0.18, 0.34)) [11]. On the other hand, that from Device-1b was (0.16, 0.27), which was identical to that of the reported OLED doped with **Ir-3c** [11]. The referential OLEDs Device-1c and Device-1c' employing FIrpic showed comparable L_{max} and η_{ext} to Device-1a and Device-1b, showing more greenish EL with CIE chromaticity coordinates of (0.24, 0.43) and (0.17, 0.36), respectively.

Table 3. Device performance of Device-1−3 with the device structure of ITO/PEDOT:PSS/*X*/CsF/Al.

OLED	*X*	L_{max} (cd m^{-2}) [@V]	$V_{turn\text{-}on}$[a] (V)	$\eta_{j,\,max}$[b] (cd A^{-1}) [@V]	$\eta_{p,\,max}$[b] (lm W^{-1}) [@V]	$\eta_{ext,\,max}$ (%) [@V]	γ[c]	CIE (x, y)[d]
Device-1a	**Ir-H1a**	1700 [17.0]	5.5	1.99 [12.0]	0.542 [9.5]	0.953 [12.0]	0.14	(0.21, 0.36)
Device-1b	**Ir-H1b**	1600 [17.0]	7.5	0.886 [13.5]	0.222 [11.5]	0.498 [13.5]	0.10	(0.16, 0.27)
Device-1c	FIrpic	1200 [11.0]	5.0	1.49 [6.0]	0.778 [6.0]	0.614 [6.0]	0.18	(0.24, 0.43)
Device-1c’	FIrpic:**Dn-1**	1200 [14.0]	7.0	2.23 [12.0]	0.620 [10.0]	1.04 [12.0]	0.083	(0.17, 0.36)
Device-2a	**Ir-H1a**:DPEPO	3000 [21.0]	7.5	8.66 [16.0]	2.02 [12.5]	4.62 [16.0]	0.47	(0.16, 0.29)
Device-2b	**Ir-H1b**:DPEPO	4300 [18.5]	6.0	6.38 [12.5]	1.65 [12.0]	3.48 [12.5]	0.28	(0.16, 0.27)
Device-2c	FIrpic:**Dn-1**:DPEPO	4500 [21.5]	8.5	7.01 [15.0]	1.57 [13.5]	3.34 [15.0]	0.18	(0.16, 0.34)
Device-3a	PVCz/**Ir-H1a**/BPOPB	2700 [14.0]	5.5	11.8 [9.5]	4.16 [7.5]	5.72 [9.5]	0.86	(0.18, 0.34)
Device-3b	PVCz/**Ir-H1b**/BPOPB	3100 [18.0]	9.5	8.52 [14.0]	1.98 [13.5]	4.72 [14.0]	0.94	(0.16, 0.28)

[a] The voltage where a luminance of more than 1 cd m^{-2} is observed. [b] The maximum values of current efficiency ($\eta_{j,\,max}$) and power efficiency ($\eta_{p,\,max}$). [c] Estimated value from the Φ_{PL} of each EML (Table 4). [d] Obtained at the voltage where the luminance of 1000 cd m^{-2} was observed.

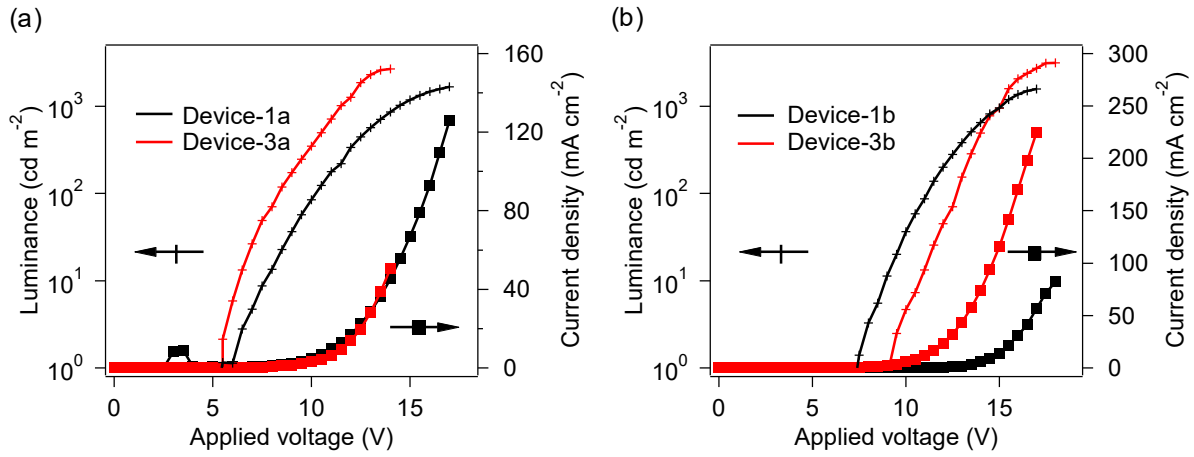

Fig. 9. *J-V-L* curves of (a) Device-1a and Device-3a and (b) Device-1b and Device-3b.

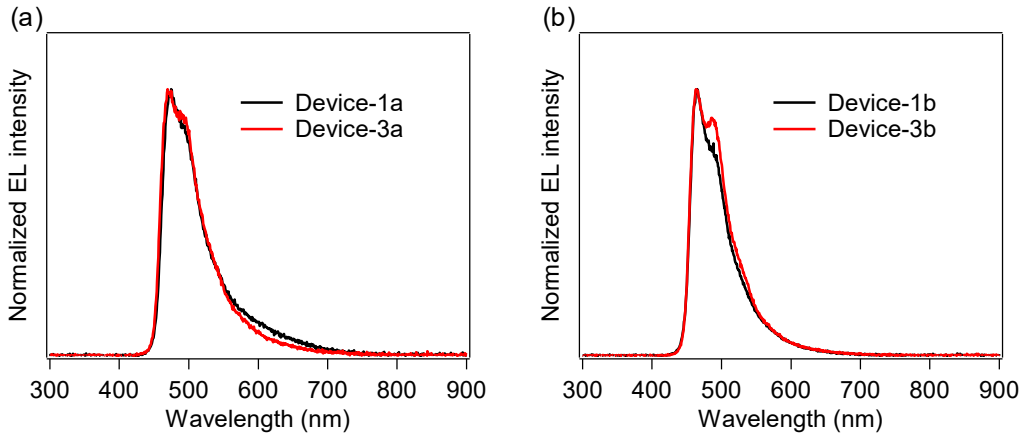

Fig. 10. EL spectra of (a) Device-1a and Device-3a and (b) Device-1b and Device-3b when the luminance is *ca*. 1000 cd m^{-2}.

Next, **Ir-H1** was doped into bis(2-(diphenylphosphino)phenyl)ether oxide (DPEPO), an electron-transporting host material with a high E_T of 3.00 eV [45]. Device-2a (*X* = **Ir-H1a**:DPEPO (1 : 5, mol/mol, 80 nm)), Device-2b (*X* = **Ir-H1b**:DPEPO (1 : 5, mol/mol, 80 nm)) and the referential OLED Device-2c (*X* = FIrpic:**Dn-1**:DPEPO (1: 2 : 5, mol/mol/mol, 80 nm)) were fabricated. The L_{max} and $\eta_{ext,\,max}$ of Device-2a were improved to 3000 cd m^{-2} (@21.0 V) and 4.62% (@16.0 V), respectively, compared with Device-1a. Supposing that the light extraction efficiency (η_{ex}) and the exciton formation efficiency resulting in radiative

transitions (η_{ph}) are 0.20 and 1.0, respectively, the electron–hole charge balance factor γ of Device-2a was estimated to be 0.47, according to the following eqn (1) [1,2]:

$$\gamma = \eta_{ext} / (\eta_{ex} \times \Phi_{PL} \times \eta_{ph}) \qquad (1)$$

where the Φ_{PL} was assumed as that of the **Ir-H1a** : DPEPO (1 : 5, mol/mol) mixed film (Φ_{PL}; 0.49, Table 4). The obtained γ was larger than that of Device-1a (γ; 0.14), indicating that doping the hole-transporting emitter **Ir-H1a** into the electron-transporting host DPEPO improved the hole–electron ratio in the EML. In the case of Device-2b employing **Ir-H1b**, the $\eta_{ext, max}$ was 3.48% (@12.5 V) and the γ was improved to 0.28, which was estimated by using the Φ_{PL} (0.63) of the **Ir-H1b** : DPEPO (1 : 5, mol/mol) mixed film. The $\eta_{ext, max}$ of Device-2c employing FIrpic was also improved to 3.34% (@15.0 V), and the value was slightly lower than those of Device-2a and Device-2b.

Table 4. PL quantum yields of films under a nitrogen atmosphere (film thickness, 80 nm; excitation wavelength, 390 nm).

Film	Φ_{PL}
Ir-H1a	0.33
Ir-H1b	0.25
FIrpic	0.17
FIrpic + **Dn-1** (1:2, mol/mol)	0.63
Ir-H1a + DPEPO (1:5, mol/mol)	0.49
Ir-H1b + DPEPO (1:5, mol/mol)	0.63
FIrpic + **Dn-1** + DPEPO (1:2:5, mol/mol)	0.94

As hydrophobic *tert*-butyl groups are placed on the periphery, **Ir-H1** exhibits good solubility in cyclohexane (solubility; higher than 3.0 mg mL^{-1}) and insolubility in 2-propanol. The thickness of the neat film of **Ir-H1** (30 nm) hardly decreased (< 1 nm) after its surface was rinsed with 2-propanol. Thus, the non-doped multilayer OLED employing the neat film of **Ir-H1** as EML was fabricated by using cyclohexane and 2-propanol as orthogonal solvents. Therein poly(9-vinylcarbazole) (PVCz) [46,47] and [1,1':3',1''-terphenyl]-4,4''-diylbis(diphenylphosphine oxide) (BPOPB) [33] were used as the HTL and ETL, respectively, and the device is represented as Device-3 (*X* = PVCz (25 nm)/**Ir-H1** (30 nm)/BPOPB (55 nm)). As shown in Fig. 11, this device structure is expected to give efficient charge recombination in the **Ir-H1** layer because the PVCz and BPOPB layers also act as electron- and hole-blocking layers, respectively. All the organic layers were formed by solution processing: a water/2-propanol (1 : 1, v/v) solution of PEDOT:PSS, a toluene solution of PVCz, a cyclohexane solution of **Ir-H1**, and a 2-propanol solution of BPOPB were sequentially spin-coated on an ITO glass substrate, followed by vacuum deposition of cesium fluoride and aluminium to fabricate the cathode. The EL spectra and *J–V–L* curves are shown in Fig. 9 and 10, respectively. Device-3a, employing the neat film of **Ir-H1a** as its EML, showed sky-blue EL with L_{max} of 2700 cd m^{-2} (@14.0 V) and $\eta_{ext,\,max}$ of 5.72% (@9.5 V). The estimated γ of 0.86 was much larger than that of Device-1a (γ; 0.14), indicating that efficient charge recombination occurs in the **Ir-H1a** layer due to the appropriate multi-layered structure. Interestingly, the CIE chromaticity coordinate of EL was also improved to (0.18, 0.34) compared with Device-1a, which is the same as that of the reported OLED doped with **Ir-2a** [11]. Device-1b employing **Ir-H1b** also showed sky-blue EL with L_{max} of 3100 cd m^{-2} (@18.0 V), $\eta_{ext,\,max}$ of 4.72% (@14.0 V), and the CIE coordinates of (0.16, 0.27) and achieved the excellent γ of 0.94, much larger than that of Device-1b (γ; 0.10). Note that FIrpic is insoluble in cyclohexane (solubility; < 0.01 mg mL^{-1}) and soluble in 2-propanol (solubility;

>1 mg mL^{-1}) in contrast to **Ir-H1**. Thus this type of multilayer OLED employing FIrpic cannot be fabricated.

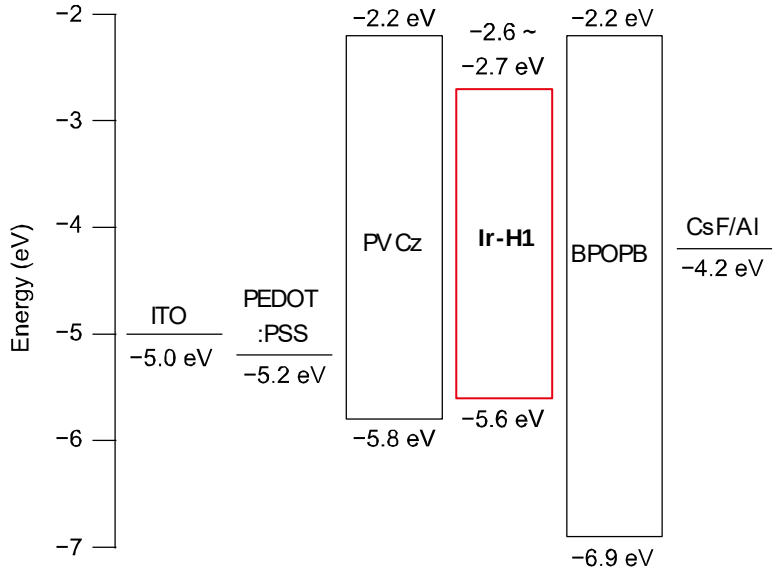

Fig. 11. Energy diagram of Device-3. The highest energy levels of the valence bands of ITO, PEDOT:PSS and Al are reported values [33]. E_{HOMO}s and E_{LUMO}s of PVCz [43], and BPOPB [12] are reported values.

2.2.3. Conclusions

In summary, novel bis- and tris-cyclometalated iridium(III) complexes bearing carbazole-appended dendrons were developed for solution-processed, non-doped phosphorescent OLEDs. These dendritic complexes exhibited sky-blue phosphorescence from their luminescent cores with excellent PL quantum yields (*ca.* 0.80) in deaerated dichloromethane. They still exhibited core-based sky-blue PL even in the film state, although the neat film of the referential core complexes showed aggregate-based PL spectra in the red-shifted region. This clearly shows that the sterically hindered dendrons are effective in suppressing the aggregate formation. In addition, the dendrons played a crucial role in efficient excitation energy transfer to the luminescent core. Non-doped multilayer OLEDs

employing the neat film of **Ir-H1** as EML were successfully fabricated by solution processing, utilizing the solubility of **Ir-H1** in orthogonal solvents such as cyclohexane and 2-propanol. The obtained devices showed an excellent electron–hole charge balance factor of *ca*. 0.9. Therefore, as we demonstrated, liposoluble and alcohol-insoluble dendritic phosphorescent complexes have great potential for high performance non-doped OLEDs with multi-stacked structures.

2.2.4. Experimental Section

2.2.4.1. General Procedures

2,6-Difluoro-3-pyridin-2-yl-benzaldehyde (**3**), bis[2-(4,6-difuoro-5-benzoylphenyl)-pyridinato-*N*,$C^{2'}$]iridium(III) picolinate (**Ir-3b**), *fac*-tris[2-(5-benzoyl-4,6-difuorophenyl)-pyridinato-*N*,$C^{2'}$]iridium(III) (**Ir-3c**) were synthesized according to Section 2.1. 9,9'-(5-(4,4,5,5-Tetramethyl-1,3,2-dioxaborolan-2-yl)-1,3-phenylene)bis(3,6-ditert-butyl-9*H*-carbazole) (**7**) [39], bis(2-(diphenylphosphino)phenyl)ether oxide (DPEPO) [48], and [1,1':3',1''-terphenyl]-4,4''-diylbis(diphenylphosphine oxide) (BPOPB) [33] were prepared as reported in the literature. Bis[(4,6-difuorophenyl)pyridinato-*N*,$C^{2'}$]iridium(III) picolinate (FIrpic) was purchased from Luminescence Technology Corp. The other starting materials and reagents were used as obtained from Wako Pure Chemical Industries, Ltd, Tokyo Chemical Industry Co., Ltd, Sigma-Aldrich Co. LLC., or Kanto Chemical Co., Inc. ^{1}H NMR (400 MHz), ^{13}C NMR (100 MHz), and ^{19}F NMR (376 MHz) spectra were obtained on a Jeol ECS-400 or a Jeol ECX-400 spectrometer, using TMS (0.00 ppm) as an internal standard for ^{1}H and ^{13}C NMR and $CFCl_3$ (0.00 ppm) as an external standard for ^{19}F NMR. Matrix assisted laser desorption/ionization time-of-flight (MALDI-TOF) mass spectra were recorded on a Shimadzu-Kratos AXIMA-CFR PLUS TOF mass spectrometer, using a-cyano-4-hydroxycinnamic acid as a matrix. Elemental analyses were carried out on a

J-Science MICRO CORDER JM10 analyser.

2.2.4.2. Syntheses and Characterizations

Synthesis of (3,5-dibromophenyl)(2,6-difluoro-3-(pyridin-2-yl)phenyl)methanol (5)

A solution of 3,5-dibromophenylmagnesium bromide was prepared by dropwise addition of a solution of 1,3,5-tribromobenzene (3.15 g, 10.0 mmol) in dry THF (15 mL) *via* a dropping funnel to a suspension of magnesium turnings (0.261 g, 10.9 mmol) in dry THF (5 mL) at rt under a nitrogen atmosphere followed by vigorous stirring for 2 hours. The obtained solution of the Grignard reagent (4.4 mL) was added dropwise to a solution of the benzaldehyde derivative **3** (0.438 g, 2.00 mmol) in dry THF (4 mL) at 0 °C, and then the reaction mixture was stirred at rt for 4 hours under a nitrogen atmosphere. After the reaction was completed, 1 M H_2SO_4 (5 mL) was added to the reaction mixture, and the obtained mixture was neutralized using a saturated aqueous solution of $NaHCO_3$. Then the organic layer was separated and the solvent was removed on a rotary evaporator. The residue was dissolved in chloroform (50 mL), and the obtained solution was washed with water (50 mL × 2) and sat. brine (50 mL), and then dried over anhydrous $MgSO_4$. The solvent was removed on a rotary evaporator, and the residue was purified by the silica gel column chromatography using ethyl acetate/hexane (1 : 2, v/v) as eluent to afford a white solid of **5** (0.509 g, 1.12 mmol, 56%). m.p. 176 °C. ^{1}H NMR (400 MHz, $CDCl_3$) δ 3.15 (d, J = 7.3 Hz, 1H), 6.24 (d, J = 7.3Hz, 1H), 7.04 (td, J = 9.2 and 1.4 Hz, 1H), 7.28 (ddd, J = 7.3, 4.8 and 1.4 Hz, 1H), 7.50 (s, 2H), 7.57 (t, J = 1.8 Hz, 1H), 7.69 (dt, J = 8.2 and 1.4 Hz, 1H), 7.76 (td, J = 8.2 and 1.8 Hz, 1H), 7.94 (td, J = 8.9 and 6.4 Hz, 1H), 8.71 (ddd, J = 4.8, 1.8 and 0.9 Hz, 1H). ^{19}F NMR (376 MHz, $CDCl_3$) δ 117.9, 113.2. MALDI-TOF MS: m/z $[M + H]^+$ calcd for $C_{18}H_{12}Br_2F_2NO$ 456; found 456. Anal. calcd for $C_{18}H_{11}Br_2F_2NO$: C, 47.51; H, 2.44;N, 3.08. Found: C, 47.77; H, 2.67; N, 2.96.

Synthesis of (3,5-dibromophenyl)(2,6-difluoro-3-(pyridin-2-yl)phenyl)methanone (6)

A mixture of **5** (0.321 g, 0.705 mmol), pyridinium dichromate (PDC, 0.465 g, 2.16 mmol) and 4 Å molecular sieves (0.819 g) in dichloromethane (40 mL) was stirred at rt for 8 h. Then the suspension was filtered, and the solution was washed with water (50 mL × 2) and sat. brine (50 mL), and then dried over anhydrous $MgSO_4$. The solvent was removed on a rotary evaporator, and the residue was purified by silica gel column chromatography using chloroform as eluent to afford a white solid of **6** (0.251 g, 0.554 mmol, 78%). m.p. 126 °C. ^{1}H NMR (400 MHz, $CDCl_3$) δ 7.13–7.19 (m, 1H), 7.29 (ddd, J = 6.68, 4.53 and 1.81 Hz, 1H), 7.71–7.78 (m, 2H), 7.89–7.93 (m, 3H), 8.21 (td, J = 8.83 and 6.80 Hz, 1H), 8.72 (dt, J = 4.53 and 1.36 Hz, 1H). ^{19}F NMR (376 MHz, $CDCl_3$) δ 115.2, 110.3. MALDI-TOF MS: m/z $[M + H]^+$ calcd for $C_{18}H_{10}Br_2F_2NO$ 454; found 454. Anal. calcd for $C_{18}H_9Br_2F_2NO$: C, 47.72; H, 2.00; N, 3.09. Found: C, 47.76; H, 2.08; N, 3.03.

Synthesis of (3,3''-bis(3,6-di-*tert*-butyl-9*H*-carbazol-9-yl)-[1,1':3',1''-terphenyl]-5'-yl)-(2,6-difluoro-3-(pyridin-2-yl)phenyl)methanone (H*C*^*N*-H1)

A mixture of **6** (0.483 g, 1.07 mmol), the boronic ester **7** (1.13 g, 2.35 mmol), bis(triphenylphosphine)palladium(II) dichloride (0.0834 g, 0.119 mmol) and potassiumcarbonate (4.94 g, 35.6mmol) in a nitrogen-bubbled solvent mixture of THF (18 mL) and water (18 mL) was stirred at reflux for 18 h under a nitrogen atmosphere. After cooling, the organic layer was separated, and the solvent was removed on a rotary evaporator. The residue was dissolved in chloroform (50 mL), and the solution was washed with water (50 mL × 2) and sat. brine (50 mL), and then dried over anhydrous $MgSO_4$. The solvent was removed on a rotary evaporator, and the residue was purified by silica gel column chromatography using chloroform/hexane (2 : 1, v/v) as eluent to afford a white solid. Then the solid was suspended in refluxed hexane, and vacuum filtration of the suspension gave a

white solid of **H*C*^*N*-H1** (0.795 g, 0.793 mmol, 74%). m.p. 263 °C. ^{1}H NMR (400 MHz, $CDCl_3$) δ 1.44 (s, 36H), 7.14 (t, J = 8.4 Hz, 1H), 7.21–7.24 (masked by $CHCl_3$, 1H), 7.36 (d, J = 8.6 Hz, 4H), 7.43 (dd, J = 8.6 and 1.8 Hz, 4H), 7.56–7.61 (m, 2H), 7.63–7.74 (m, 6H), 7.82 (s, 2H), 8.09–8.24 (m, 8H), 8.69 (d, J = 4.53 Hz, 1H). ^{19}F NMR (376 MHz, $CDCl_3$) δ 115.2, 110.3. MALDI-TOF MS: m/z [M]+ calcd for $C_{70}H_{65}F_2N_3O$ 1002; found 1002. Anal. calcd for $C_{70}H_{65}F_2N_3O$: C, 83.88; H, 6.54; N, 4.19. Found: C, 84.12; H, 6.57; N, 3.87.

Synthesis of the μ-chloro-bridged iridium(III) dimer [(*C*^*N*-H1)$_2$Ir(μ-Cl)]$_2$

A mixture of **H*C*^*N*-H1** (301 mg, 0.301 mmol) and IrCl•3H_2O (53.7 mg, 0.152 mmol) in a water/THF/2-ethoxyethanol mixed solvent (1 : 5 : 10, v/v/v, 24 mL) was stirred at 100 °C for 12 hours. After cooling, the reaction mixture was concentrated on a rotary evaporator, and addition of methanol gave rise to precipitation of the μ-chloro-bridged iridium(III) dimer [(***C*^*N*-H1**)$_2$Ir(μ-Cl)]$_2$ (328 mg, 0.0735 mmol, 98%), which was collected by filtration. It was used in the next reaction without further purification, because it was difficult to purify by column chromatography due to instability in silica gel.

Synthesis of bis[2-(5-(3,3”-bis(3,6-di-*tert*-butyl-9*H*-carbazol-9-yl)-[1,1’:3’,1”-terphenyl]-5’-carbonyl)-4,6-difluorophenyl)pyridinato-*N*,*C*$^{2'}$]iridium(III) picolinate (Ir-H1a)

A mixture of [(***C*^*N*-H1**)$_2$Ir-(μ-Cl)]$_2$ (280 mg, 0.062 mmol), picolinic acid (17 mg, 0.14 mmol) and sodium carbonate (151 mg, 1.42 mmol) in 2-ethoxyethanol (29 mL) was stirred at 50 °C for 1 hour. After cooling, the solvent was removed on a rotary evaporator. The residue was dissolved in chloroform (30 mL) and the solution was washed with water (30 mL × 2) and sat. brine (30 mL), and then dried over anhydrous Na_2SO_4. The solvent was removed on a rotary evaporator, and the residue was purified by silica gel column chromatography using dichloromethane/ethyl acetate (10 : 1, v/v) as eluent and then by silica gel preparative TLC

using dichloromethane/ethyl acetate (10 : 1, v/v) as eluent. Further purification by recrystallization from dichloromethane/methanol gave a yellow solid of **Ir-H1a** (85 mg, 0.037 mmol, 30%). m.p. 310 °C. ^{1}H NMR (400 MHz, CDCl3) δ 1.42 (s, 36H), 1.43 (s, 36H), 5.75 (d, J = 9.1Hz, 1H), 5.98 (d, J = 8.6 Hz, 1H), 6.98 Hz (m, 2H), 7.19 (m, 1H), 7.32–7.45 (m, 17H), 7.50–7.68 (m, 14H), 7.72–7.84 (m, 6H), 7.99 (t, J = 1.6 Hz, 1H), 8.05 (t, J = 1.6 Hz, 1H), 8.08–8.16 (m, 12H), 8.24 (d, J = 7.7 Hz, 2H), 8.30 (d, J = 9.5 Hz, 1H), 8.75 (d, J = 4.5 Hz, 1H). ^{19}F NMR (376 MHz, $CDCl_3$) δ 112.4, 111.9, 108.4, 107.5. MALDI-TOF MS: m/z $[M]^+$ calcd for $C_{146}H_{132}F_4IrN_7O_4$ 2316; found 2316. Anal. calcd for $C_{146}H_{132}F_4IrN_7O_4$: C, 75.69; H, 5.74; N, 4.23. Found: C, 75.82; H, 5.56; N, 4.31.

Synthesis of *fac*-tris[2-(5-(3,3”-bis(3,6-di-*tert*-butyl-9*H*-carbazol-9-yl)-[1,1’:3’,1”-terphenyl]-5’-carbonyl)-4,6-difluorophenyl)pyridinato-*N*,$C^{2'}$]iridium(III) (Ir-H1b)

A mixture of $[(\boldsymbol{C}\text{^}\boldsymbol{N}\text{-H1})_2Ir(\mu\text{-Cl})]_2$ (200 mg, 0.0449 mmol), **HC^*N*-H1** (115 mg, 0.114 mmol) and silver(I) triflate (37.6 mg, 0.144 mmol) in diglyme (10 mL) was stirred at 170 °C for 12 hours in the dark. After cooling, the solvent was removed under reduced pressure. The residue was dissolved in chloroform (30 mL) and the solution was washed with water (30 mL × 2) and sat. brine (30 mL), and then dried over anhydrous Na_2SO_4. The solvent was removed on a rotary evaporator, and the residue was purified by silica gel column chromatography using chloroform/hexane (2 : 1, v/v) as eluent. Further purification by recrystallization from dichloromethane/methanol gave a yellow solid of **Ir-H1b** (32.3 mg, 0.010 mmol, 23%). m.p. 310 °C. ^{1}H NMR (400 MHz, $CDCl_3$) δ 1.43 (s, 108H), 6.51 (d, J = 9.5 Hz, 3H), 6.66 (t, J = 6.8 Hz, 3H), 7.27–7.45 (m, 30H), 7.48 (d, J = 7.7 Hz, 6H), 7.56 (t, J = 7.7 Hz, 6H), 7.62 (d, J = 7.7 Hz, 6H), 7.77 (s, 6H), 8.01 (s, 3H), 8.10 (d, J = 1.36 Hz, 18H), 8.21 (d, J = 10.4 Hz, 3H). ^{19}F NMR (376 MHz, $CDCl_3$) δ 112.4, 108.2. MALDI-TOF MS: m/z $[M]^+$ calcd for $C_{210}H_{192}F_6IrN_9O_3$ 3196; found 3196. Anal. calcd for $C_{210}H_{192}F_6IrN_9O_3$: C, 78.92; H, 6.06; N,

3.94. Found: C, 78.74; H, 6.11; N, 3.85.

Synthesis of 3,3”-bis(3,6-di-*tert*-butyl-9*H*-carbazol-9-yl)-1,1’:3’,1”-terphenyl (Dn-1)

A mixture of **7** (0.521 g, 1.08 mmol), 1,3-diiodobenzene (0.163 g, 0.494 mmol), bis(triphenylphosphine)palladium(II) dichloride (0.0474 g, 0.0675 mmol) and potassium carbonate (2.40 g, 17.4 mmol) in nitrogen-bubbled THF (17 mL) and water (17 mL) was stirred at reflux for 18 h under a nitrogen atmosphere. After cooling, the organic layer was separated and the aqueous layer was extracted with ethyl acetate (50 mL), and the combined organic solution was dried over anhydrous Na_2SO_4. The solvent was removed on a rotary evaporator, and the residue was purified twice by silica gel column chromatography using dichloromethane/hexane (2 : 1 and then 1 : 2, v/v) as eluent to afford a white solid of **Dn-1** (0.175 g, 0.223 mmol, 45%). m.p. 186 °C. ^{1}H NMR (400 MHz, CDCl3) δ 1.46 (s, 36H), 7.40 (d, J = 8.7 Hz, 4H), 7.46 (dd, J = 8.7 and 1.8 Hz, 4H), 7.51–7.58 (m, 3H), 7.62–7.75 (m, 6H), 7.84 (t, J = 1.8 Hz, 2H), 7.88 (t, J = 1.8 Hz, 1H), 8.14 (d, J = 1.4 Hz, 4H). ^{13}C NMR (100 MHz, CDCl3) δ 32.2, 34.9, 109.3, 116.4, 123.5, 123.8, 125.6, 125.8, 125.9, 126.3, 126.7, 129.7, 130.4, 138.9, 139.3, 141.2, 142.9, 143.0. MALDI-TOF MS: m/z $[M]^+$ calcd for $C_{58}H_{60}N_2$ 784; found 784. Anal. calcd for $C_{58}H_{60}N_2$: C, 88.73; H, 7.70;N, 3.57. Found: C, 88.81; H, 7.63; N, 3.59.

2.2.4.3. Characterization of Photophysical, Electrochemical and Thermal Properties

UV-vis absorption spectra were recorded on a Shimadzu UV-3600 spectrophotometer, using a quartz cell for solutions or a quartz plate for thin films. Photoluminescence (PL) and excitation spectra were recorded on a Horiba Jobin Yvon Fluorolog-3 spectrophotometer. Phosphorescence spectra were recorded at 77 K on the same spectrometer with a VT CBL-LR/RM12 Dewar adapter using 2-methyltetrahydrofuran as a matrix after the deaeration

through three-time freeze–pump–thaw cycling. PL lifetimes were obtained on a Horiba Jobin Yvon FluoroCube spectroanalyzer using a 390 nm nanosecond-order LED light source. PL quantum yields were obtained on a Hamamatsu Photonics C9920 PL quantum yield measurement system. The sample solutions for the spectroscopic measurements were deaerated by nitrogen bubbling followed by complete sealing, and the analyses were carried out just after preparation of the samples. For thin films, the spectroscopic measurements were carried out under a nitrogen atmosphere. The cyclic voltammogram was measured on a Hokuto Denko HZ-5000 potentiostat for dichloromethane (0.50 mM, for oxidation) and *N*,*N*-dimethylformamide (1.0 mM, for reduction) solutions containing tetrabutylammonium perchlorate (0.10 M) as a supporting electrolyte at a scan rate of 100 mV s^{-1}. Platinum wire was used as the working and the counter electrodes, and silver wire in contact with $AgNO_3$ (0.1 M in acetonitrile) was used as the reference electrode. The potential value was recorded relative to the oxidation of ferrocene, which was added to the electrolyte as an external standard. Thermogravimetry (TG) analysis and differential scanning calorimetry (DSC) were performed on a Rigaku Thermo Plus EVO TG 8120 and a Termo-5-Plus EVO DSC 823 analyser, respectively, under a nitrogen atmosphere using aluminum oxide as blank correction. The heating rates were 10 K min^{-1}.

2.2.4.4. Fabrication and Evaluation of OLEDs

A pre-patterned ITO (150 nm thickness with sheet resistance of *ca*. 10 Ω per square, Sanyo Vacuum Industries Co., Ltd) glass substrate was cleaned with an ultrasonic cleaner using a detergent and solvents, and then treated with UV-O_3. Poly(ethylenedioxy-3,4-thiophene): poly(styrene sulfonate) (PEDOT:PSS, Heraeus Clevios P VP CH8000) was spin-coated onto the ITO layer and then dried at 120 °C for an hour. In the cases of Device-1 and Device-2, a solution of **Ir-H1** or FIrpic (mixed with DPEPO) in chloroform (*ca*. 15 mg mL^{-1}) was filtered

through a 0.2 μm Millex-FG filter and spin-coated onto the PEDOT:PSS layer under an argon atmosphere. In the case of Device-3, a solution of PVCz (M_w = 25 000–50 000, purchased from Aldrich) in dry toluene (5.9 mg mL^{-1}) was filtered through a 0.2 μm Millex-FG filter (Millipore Co.). The obtained solution was subjected to spin-coating onto the PEDOT:PSS layer under an argon atmosphere, and the prepared films were dried at 120 °C for an hour. Thereafter a solution of **Ir-H1** in cyclohexane (3.8 and 3.2 mg mL^{-1} for **Ir-H1a** and **Ir-H1b**, respectively) was filtered through a 0.2 μm Millex-FG filter and spin-coated onto the PVCz layer under an argon atmosphere. The prepared films were dried at 100 °C for 30 minutes. Next, a solution of BPOPB in 2-propanol (7.0 mg mL^{-1}) was filtered through a 0.2 μm Millex-FG filter and spin-coated onto the **Ir-H1** layer under an argon atmosphere. The prepared films were dried at 80 °C for 10 minutes. Next, cesium fluoride (purchased from Alfa Aesar) and aluminum (purchased from The Niraco Corporation) layers were successively embedded by vacuum deposition. Finally, the device was covered with a glass cap and encapsulated with a UV-curing epoxy resin under a dry argon atmosphere to keep oxygen and moisture away. The area of the emitting part was adjusted to 10 mm^2 (2 mm × 5 mm). The device fabrication was carried out in a glove box filled with dry argon, except for the preparation of the PEDOT:PSS layer. The OLED performance was conducted at room temperature, using a Hamamatsu Photonics C-9920-11 organic EL device evaluating system.

2.2.5. References

[1] C. Adachi, M. A. Baldo, M. E. Thompson and S. R. Forrest, *J. Appl. Phys*., 2001, **90**, 5048−5051.

[2] M. A. Baldo, D. F. O'Brien, Y. You, A. Shoustikov, S. Sibley, M. E. Thompson and S. R. Forrest, *Nature*, 1998, **395**, 151−154.

[3] X. Yang, G. Zhou and W. Y. Wong, *Chem. Soc. Rev*., 2015, **44**, 8484−8575.

[4] Y. Chi and P.-T. Chou, *Chem. Soc. Rev*., 2010, **39**, 638−655.

[5] H. Xu, R. Chen, Q. Sun, W. Lai, Q. Su, W. Huang and X. Liu, *Chem. Soc. Rev*., 2014, **43**, 3259−3302.

[6] C.-L. Ho and W.-Y. Wong, *New J. Chem*., 2013, **37**, 1665−1683.

[7] C.-H. Yang, S.-W. Li, Y. Chi, Y.-M. Cheng, Y.-S. Yeh, P.-T. Chou, G.-H. Lee, C.-H. Wang and C.-F. Shu, *Inorg. Chem*., 2005, **44**, 7770−7780.

[8] S. Lamansky, P. Djurovich, D. Murphy, F. Abdel-Razzaq, H.-E. Lee, C. Adachi, P. E. Burrows, S. R. Forrest and M. E. Thompson, *J. Am. Chem. Soc*., 2001, **123**, 4304−4312.

[9] A. B. Tamayo, B. D. Alleyne, P. I. Djurovich, S. Lamansky, I. Tsyba, N. N. Ho, R. Bau and M. E. Thompson, *J. Am. Chem. Soc*., 2003, **125**, 7377−7387.

[10] S. J. Lee, K.-M. Park, K. Yang and Y. Kang, *Inorg. Chem*., 2009, **48**, 1030−1037.

[11] N. Okamura, T. Nakamura, S. Yagi, T. Maeda, H. Nakazumi, H. Fujiwara and S. Koseki, *RSC Adv*., 2016, **6**, 51435−51445.

[12] N. Okamura, K. Ishiguro, T. Maeda and S. Yagi, *Chem. Lett*., 2017, **46**, 1086−1089.

[13] M. L. P. Reddy and K. S. Bejoymohandas, *J. Photochem. Photobiol., C*, 2016, **29**, 29−47.

[14] J. Pan, W. Zhu, S. Li, W. Zeng, Y. Cao and H. Tian, *Polymer*, 2005, **46**, 7658−7669.

[15] Z. Zhong, S. Zhao, J. Pei, J. Wang, L. Ying, J. Peng and Y. Cao, *ACS Appl. Mater. Interfaces*, 2016, **8**, 20237−20242.

[16] T. Qin, J. Ding, L. Wang, M. Baumgarten, G. Zhou and K. Müllen, *J. Am. Chem. Soc*., 2009, **131**, 14329–14336.

[17] K. M. Jung, T. W. Lee, K. H. Kim, M. J. Cho, J.-I. Jin and D. H. Choi, *Chem. Lett*., 2009, **38**, 314−315.

[18] Y.-J. Pu, N. Iguchi, N. Aizawa, H. Sasabe, K.-i. Nakayama and J. Kido, *Org. Electron*., 2011, **12**, 2103−2110.

[19] S.-C. Lo, R. E. Harding, C. P. Shipley, S. G. Stevenson, P. L. Burn and I. D. W. Samuel, *J. Am. Chem. Soc*., 2009, **131**, 16681−16688.

[20] D. Xia, B.Wang, B. Chen, S.Wang, B. Zhang, J. Ding, L.Wang, X. Jing and F. Wang, *Angew. Chem., Int. Ed*., 2014, **53**, 1048−1052.

[21] A. Liang, L. Ying and F. Huang, *J. Inorg. Organomet. Polym. Mater*., 2014, **24**, 905−926.

[22] H. Zhen, C. Luo, W. Yang, W. Song, B. Du, J. Jiang, C. Jiang, Y. Zhang and Y. Cao, *Macromolecules*, 2006, **39**, 1693–1700.

[23] M. Suzuki, S. Tokito, F. Sato, T. Igarashi, K. Kondo, T. Koyama and T. Yamaguchi, *Appl. Phys. Lett*., 2005, **86**, 103507 (3 pages).

[24] T. Sato, D.-L. Jiang and T. Aida, *J. Am. Chem. Soc*., 1999, **121**, 10658−10659.

[25] A. W. Freeman, S. C. Koene, P. R. L. Malenfant, M. E. Thompson and J. M. J. Fréchet, *J. Am. Chem. Soc*., 2000, **122**, 12385−12386.

[26] S. C. Lo, G. J. Richards, J. P. J. Markham, E. B. Namdas, S. Sharma, P. L. Burn and I. D. W. Samuel, *Adv. Funct. Mater*., 2005, **15**, 1451−1458.

[27] T.-H. Kwon,M.K.Kim, J. Kwon,D.-Y. Shin, S. J. Park,C.-L. Lee, J.-J. Kim and J.-I. Hong, *Chem. Mater*., 2007, **19**, 3673−3680.

[28] S.-C. Lo, R. N. Bera, R. E. Harding, P. L. Burn and I. D. W. Samuel, *Adv. Funct. Mater*., 2008, **18**, 3080−3090.

[29] Y.-J. Cho, K.-R. Wee, H.-J. Son, D. W. Cho and S. O. Kang, *Phys. Chem. Chem. Phys.*, 2014, **16**, 4510−4521.

[30] C.W. Tang and S. A. VanSlyke, *Appl. Phys. Lett*., 1987, **51**, 913−915.

[31] J. Kido, M. Kimura and K. Nagai, Science, 1995, **267**, 1332−1334.

[32] X. Qiao, Y. Tao, Q. Wang, D. Ma, C. Yang, L. Wang, J. Qin and F. Wang, *J. Appl. Phys*., 2010, **108**, 034508−034508.

[33] N. Aizawa, Y. J. Pu, M. Watanabe, T. Chiba, K. Ideta, N. Toyota, M. Igarashi, Y. Suzuri, H. Sasabe and J. Kido, *Nat. Commun*., 2014, **5**, 5756 (7 pages).

[34] F. Huang, P.-I. Shih, C.-F. Shu, Y. Chi and A. K. Y. Jen, *Adv. Mater.*, 2009, **21**, 361−365.

[35] T. Ye, S. Shao, J. Chen, L. Wang and D. Ma, *ACS Appl. Mater. Interfaces*, 2011, **3**, 410−416.

[36] T. Earmme and S. A. Jenekhe, *Adv. Funct. Mater*., 2012, **22**, 5126−5136.

[37] X. Gong, S. Wang, D. Moses, G. C. Bazan and A. J. Heeger, *Adv. Mater*., 2005, **17**, 2053−2058.

[38] K. S. Yook, S. E. Jang, S. O. Jeon and J. Y. Lee, *Adv. Mater*., 2010, **22**, 4479−0000.

[39] N. Okamura, H. Funagoshi, S. Ikawa, S. Yagi, T. Maeda and H. Nakazumi, *Mol. Cryst. Liq. Cryst*., 2015, **621**, 59−63.

[40] C. Matera, M. Quadri, M. Sciaccaluga, D. Y. Pomé, F. Fasoli, M. De Amici, S. Fucile, C. Gotti, C. Dallanoce and G. Grazioso, *Eur. J. Med. Chem*., 2016, **108**, 392–405.

[41] G. E. Johnson, *J. Phys. Chem*., 1974, **78**, 1512−1521.

[42] B. Sarti and M. Scandola, *Biomaterials*, 1995, **16**, 785−792.

[43] J. Bettenhausen and P. Strohriegl, *Adv. Mater*., 1996, **8**, 507−510.

[44] S. Tokito, T. Iijima, Y. Suzuri, H. Kita, T. Tsuzuki and F. Sato, *Appl. Phys. Lett*., 2003, **83**, 569−571.

[45] Q. Zhang, T. Komino, S. Huang, S. Matsunami, K. Goushi and C. Adachi, *Adv. Funct.*

Mater., 2012, **22**, 2327−2336.

[46] Y. Moon-Jae and T. Tetsuo, *Jpn. J. Appl. Phys*., 2000, **39**, L828−L829.

[47] M.-H. Kim, M. C. Suh, J. H. Kwon and B. D. Chin, *Thin Solid Films*, 2007, **515**, 4011−4015.

[48] Y. Li, L.-Q. Lu, S. Das, S. Pisiewicz, K. Junge and M. Beller, *J. Am. Chem. Soc*., 2012, **134**, 18325−18329.

Chapter 3

Development of Novel Phosphorescent Organoplatinum(II) Complexes Aimed at Fabrication of White Organic Light-Emitting Diodes

Section 3.1
Photokinetic Study on Remarkable Excimer Phosphorescence from Heteroleptic Cyclometalated Platinum(II) Complexes Bearing a Benzoylated 2-Phenylpyridinate Ligand

3.1.1. Introduction

Organic light-emitting diodes (OLEDs) have been attracting much attention due to their applicability to flat-panel displays, illumination devices, electronic papers, and so on [1–4]. In OLEDs, the excitons of an emitting material generated by charge recombination are divided into singlet and triplet states at a ratio of 1 : 3 according to the spin statistics theorem. Thus, when a fluorescent emitter is used, the device can achieve an internal quantum efficiency (η_{int}) of at most 25%. On the other hand, phosphorescent emitters can achieve η_{int} as high as 100% in theory, taking account of the intersystem crossing (ISC) from the singlet excited state to the triplet state [1–7]. Hence, organometallic compounds including platinum(II) [2,7–26] and iridium(III) [27–33] have been enthusiastically developed as phosphorescent emitters because the strong spin–orbit coupling due to the heavy metal center facilitates the ISC to provide efficient phosphorescence under ambient conditions. Actually, high current efficiencies of more than 50 cd A^{-1} have been achieved by employing phosphorescent platinum(II) complexes [34,35].

Heteroleptic cyclometalated platinum(II) complexes, consisting of 2-phenylpyridinate

cyclometalated (*C^N*) and β-diketonate ancillary (*O^O*) ligands, adopt four-coordinated square-planar structures that enhance intermolecular interactions to yield excimer phosphorescence emerging in longer wavelength regions along with the monomer one [2,8,15,17,22,24,36]. In the case of the blue phosphorescent complex such as (*dfppy*)Pt(*acac*) (*dfppy*, 2-(4,6-difluorophenyl)pyridinate-*N*,$C^{2'}$; *acac*, acetylacetonate), an optimized balance of monomer and excimer emissions yielded a broadened electroluminescence (EL) spectrum covering the whole visible region, and it allows us to fabricate a white OLED using this complex as a single emitting dopant [8]. This type of white OLED is important for potential application in the low-cost and facile fabrication of room lighting and backlights of displays because precise tuning of the balance of primary color emitting materials is avoided and a smaller amount of emitter is consumed [2]. From this viewpoint, a variety of cyclometalated platinum(II) complexes showing excimer emission have so far been developed [2,8,11,14,16–18,24,26,37,38]. Recently, we also reported a heteroleptic cyclometalated platinum(II) complex consisting of dibenzo[*b*,*d*]furan-2-ylpyridinate-*N*,$C^{2'}$ and 1,3-bis(3,4-dibutoxyphenyl)propane-1,3-dionate as cyclometalated and ancillary ligands, respectively, which showed remarkable excimer emission in polymer matrices due to its expanded π-planes of the ligands enhancing the intermolecular interaction [17]. However, there are few reports of the structure–function relationships and photokinetic features of excimer emission of cyclometalated platinum(II) complexes [14,17,24]. Upon development of excimer-emissive complexes, it has been extensively discussed how intensely the excimer emission emerges relative to that of the monomer [11,14,17,18,24]. To discuss how the excimer emission is generated, the photokinetic analysis on the basis of the structural factors is of particular importance. In this regard, Shinozaki and coworkers estimated the excimer and excited trimer formation rate constants of tridentate cyclometalated platinum(II) complexes by analysing their photoluminescence (PL) decays [39]. However, the excimer formation

kinetics of (*C^N*)Pt(*O^O*)-type complexes has not been sufficiently discussed, although the kinetic aspects of the excimer emission of this type of organoplatinum(II) complexes should provide valuable insights to manage their electroluminescence behavior in OLED applications.

To obtain white luminescence through the optimized balance of the monomer and excimer emissions from a (*C^N*)Pt(*O^O*)-type complex, ligand design to yield monomer emission in the blue region is essential [14]. As discussed in Section 2.1, the author reported bis- and tris-cyclometalated iridium(III) complexes bearing benzoylated *dfppy* ligands [33]. The introduction of a benzoyl group to the 5'-position of each *dfppy* ligand is effective to obtain a more blue-shifted PL wavelength (λ_{PL}) than those of the corresponding *dfppy*-based complexes. In particular, tris[2-(5-benzoyl-4,6-difluorophenyl)pyridinate-*N*,$C^{2'}$]iridium(III) exhibited blue PL at 463 nm with an excellent PL quantum yield (Φ_{PL}) of 0.90 in deaerated dichloromethane (10 μM) at rt. Taking into consideration that the impact of the cyclometalated ligand on λ_{PL} is comparable between organoiridium(III) and organoplatinum(II) complexes, the benzoylated *dfppy* ligand should be a good candidate to obtain (*C^N*)Pt(*O^O*)-type complexes emitting in the blue region. Here, the author reports novel cyclometalated platinum(II) complexes **Pt-1a**–**c** (Fig. 1) bearing the 5'-benzoylated 2-phenylpyridinate (*ppy*) ligands with or without fluorine substituent(s), and their excimer phosphorescence behaviors are investigated in detail, especially focusing on the impacts of the introduced substituents on the radiative excimer formation. The author investigates the photokinetics of these complexes to clarify how the excimer formation is facilitated. In addition, the fabrication of a white OLED employing **Pt-1c** as a single emitting dopant is demonstrated.

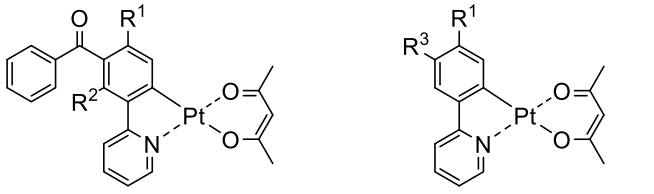

Pt-1a: $R^1 = R^2 = H$
Pt-1b: $R^1 = F$, $R^2 = H$
Pt-1c: $R^1 = R^2 = F$

Pt-2a: $R^1 = R^3 = H$
Pt-2b: $R^1 = COPh$, $R^3 = H$
Pt-2c: $R^1 = H$, $R^3 = COCH_3$
Pt-2d: $R^1 = H$, $R^3 = F$

Fig. 1. Structures of platinum(II) complex **Pt-1** bearing a benzoyl group on the 5'-position of its 2-phenylpyridinate ligand and its reference complex **Pt-2**.

3.1.2. Results and Discussion

3.1.2.1. Synthesis and Molecular Structures of Pt-1a–c

The novel benzoylated platinum(II) complexes **Pt-1a**–**c** were synthesized according to Scheme 1. The 5'-benzoylated 2-phenylpyridine derivatives **HC^*N*-1**–**3** were reacted with potassium tetrachloridoplatinate to afford the corresponding mononuclear complexes (***C*^*N*-X**)PtCl(**HC*^*N*-X**) (**X** = **1**–**3**) in 69–86% yields, which were subjected to the ligand exchange reaction to yield **Pt-1a–c** in 29, 30 and 65% yields, respectively. The author found that recrystallization from hot ethyl acetate solution afforded highly pure **Pt-1a**–**c**. The low synthetic yields of **Pt-1a** and **Pt-1b** were due to their relatively high solubility in ethyl acetate at rt. On the other hand, **Pt-1c** was obtained in a higher yield because of its lower solubility in ethyl acetate at ambient temperature. Reference complexes **Pt-2b**–**d** were also synthesized in the same procedure.

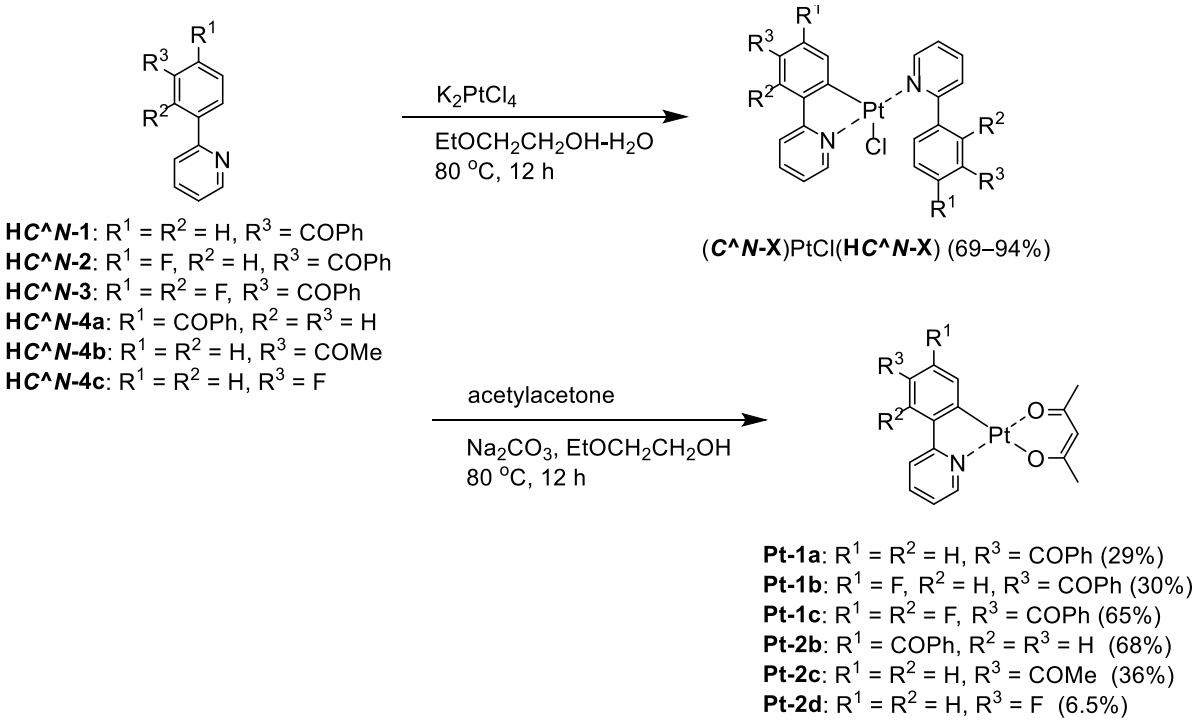

Scheme 1. Synthesis of **Pt-1a**–**c** and **Pt-2b**–**d**.

Molecular structures of **Pt-1a**–**c** were characterized by X-ray crystallography using their single crystals. The ORTEP drawings of **Pt-1a**–**c** are shown in Fig. 2, and the crystal data are summarized in Table 1. As seen in typical heteroleptic cyclometalated platinum(II) complexes so far reported, **Pt-1a**–**c** adopt a four-coordinated square-planar coordination geometry [9,10,17,23,40–43]. The mean plane deviations of a mean plane consisting of the (*ppy*)Pt(*acac*) skeleton except the benzoyl group and the hydrogen atoms were 0.044, 0.015, and 0.021 Å for **Pt-1a**, **Pt-1b**, and **Pt-1c**, respectively, suggesting their quite high planarities. In **Pt-1a**, the bond lengths of Pt–C^a, Pt–N, Pt–O^a, and Pt–O^b were 1.965, 1.988, 1.997, and 2.09 Å, respectively, and the angles of N–Pt–C^a, C^a–Pt–O^a, O^a–Pt–O^b, and O^b–Pt–N were 81.71°, 92.81°, 92.31°, and 93.31°, respectively. The bond lengths and angles of **Pt-1a** are similar to those of **Pt-1b**, **Pt-1c**, and other reported platinum(II) complexes [9,10,41,43].The benzoyl groups of **Pt-1a**–**c** were distorted with respect to the mean plane of the *ppy* skeleton: the angles between the *ppy* mean plane and a mean plane of the phenyl group in the benzoyl

group were 64.91°, 61.31° and 69.11° for **Pt-1a**–**c**, respectively. The π-stacking distances between neighbor molecules were 3.39, 3.46 and 3.41 Å in the crystals of **Pt-1a**–**c**, respectively, indicating their strong π–π interactions essential to excimer formation [36].

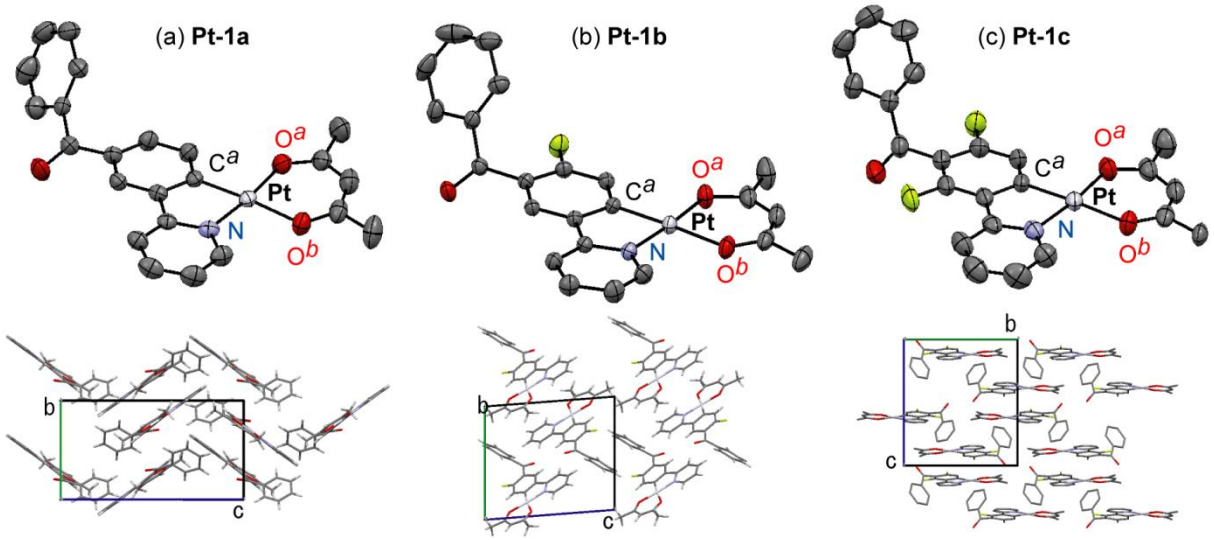

Fig. 2. ORTEP drawings and crystal packings of (a) **Pt-1a**, (b) **Pt-1b**, and (c) **Pt-1c**. The hydrogen atoms are omitted for clarity, and the thermal ellipsoids are presented at the 50% probability level.

Table 1. Crystallographic data for **Pt-1a**−**c**.

	Pt-1a	**Pt-1b**	**Pt-1c**
Empirical Formula	$C_{23}H_{19}NO_3Pt$	$C_{23}H_{18}FNO_3Pt$	$C_{23}H_{17}F_2NO_3Pt$
Formula Weight	552.50	570.49	588.48
T (K)	298	293	293
Color, habit	yellow, prism	yellow, prism	yellow, block
Size, mm	0.50 × 0.40 × 0.20	0.50 × 0.30 × 0.30	0.40 × 0.40 × 0.30
Crystal system	monoclinic	triclinic	monoclinic
Lattice Type	Primitive	Primitive	Primitive
Space group	*P*21/*c* (#14)	*P*-1 (#2)	*P*21/*c* (#14)
a (Å)	14.133(2)	6.9367(11)	11.922(3)
b (Å)	8.6154(13)	11.512(2)	12.312(2)
c (Å)	16.031(2)	13.017(3)	14.055(3)
α (°)	90	81.915(9)	90
β (°)	94.639(2)	76.395(9)	103.866(3)
γ (°)	90	72.742(9)	90
V (Å^3)	1945.5(5)	962.0(3)	2002.9(7)
Z	4	2	4
D_{calc} (g cm^{-3})	1.886	1.969	1.951
F_{000}	1064.00	548.00	1128.00
μ (MoKα) (cm^{-1})	72.072	72.983	70.207
$2\theta_{max}$ (º)	61.5	61.2	61.3
Total reflections	16271	8152	17067
Unique reflections	5269	4902	5540
Reflection/Parameter Ratio	16.10	16.41	15.00
R ($I > 3.00\sigma(I)$)[a]	0.0339	0.0274	0.0353
R_w ($I > 3.00\sigma(I)$)[b]	0.0369	0.0306	0.0431
Goodness of Fit Indicator	1.073	1.061	1.069
Max. and min. peak in Final Diff. Map (e Å^{-3})	2.43 and –1.84	1.72 and –1.39	1.36 and –1.83

[a] $R = \Sigma \, ||Fo| - |Fc|| \, / \, \Sigma \, |Fo|$, [b] $R_w = [\, \Sigma \, w \, (|Fo| - |Fc|)^2 \, / \, \Sigma \, w \, Fo^2]^{1/2}$

3.1.2.2. Photoluminescence Properties

PL spectra of **Pt-1a**–**c** in deaerated dichloromethane (10 μM) at rt are shown in Fig. 3, and the spectral and photophysical data are summarized in Table 2. All the complexes showed PL lifetimes in a micro-second or a sub-micro-second order ranging from 0.295 to 1.37 μs, indicating that the observed emission is phosphorescence. **Pt-1a** exhibits bluish green PL with a spectrum that has two peaks at 479 and 513 nm and two shoulders at *ca*. 550 and *ca*. 600 nm. This type of spectral shape is characteristic of the monomer emission of (*C^N*)Pt(*O^O*)-type complexes[9,13,15,17,24]. The lowest energy emission peak was blue-shifted by 5 nm in comparison with the unsubstituted complex **Pt-2a** (λ_{PL}; 484 nm in dichloromethane [44], Fig. 1). Thus, the introduction of the benzoyl group is actually effective in inducing a blue shift of PL. The fluorinated complexes **Pt-1b** and **Pt-1c** exhibited greenish blue PL with the lowest energy emission peaks of 469 and 465 nm, respectively, further blue-shifted in comparison with **Pt-1a**. Thompson and co-workers reported that the λ_{PL} of (*dfppy*)Pt(*acac*) was 466 nm in 2-methyltetrahydrofuran (Φ_{PL}; 0.02) [9], and it also shows the same λ_{PL} in dichloromethane [44]. Thus, the combination of benzoyl and fluorine substituents is slightly effective in inducing a blue shift of λ_{PL}. The Φ_{PL} decreased according to the increase in the number of fluorine substituents: the Φ_{PL}s of **Pt-1a**–**c** were 0.28, 0.13 and 0.063, respectively. One might see that this is due to facilitation of the non-radiative relaxation process in accordance with the increase in the lowest triplet energy, as previously reported for (*C^N*)Pt(*O^O*)-type complexes [9]. The radiative rate constant (k_r) and non-radiative rate constant (k_{nr}) of **Pt-1a**–**c** were calculated from their Φ_{PL} s and τ_{PL}s according to the following eqn (1) and (2):

$$k_r = \Phi_{PL}/\tau_{PL} \qquad (1)$$

$$k_{nr} = (1-\Phi_{PL})/\tau_{PL} \qquad (2)$$

Almost similar k_rs (0.13–0.21 μs^{-1}) are obtained for **Pt-1a**–**c**, whereas k_{nr} increases with the

increase in the number of introduced fluoro groups (0.53, 0.84, and 3.18 μs^{-1}, respectively). This result clearly shows that the increase in the lowest triplet energy gives rise to facilitation of the nonradiative decay process.

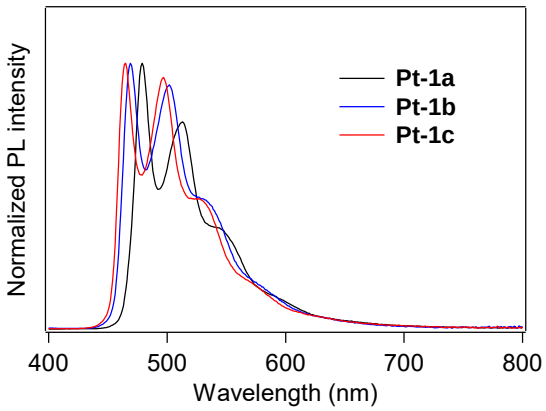

Fig. 3. PL spectra of **Pt-1a**–**c** in deaerated dichloromethane (10 μM, rt).

Table 2. PL properties of **Pt-1a**–**c** in deaerated dichloromethane (10 μM, rt), where the excited wavelength was 390 nm.

Compd	λ_{PL} (nm)	Φ_{PL}	τ_{PL} [a] (μs)	k_r (μs^{-1})	k_{nr} (μs^{-1})
Pt-1a	479, 513	0.28	1.37	0.20	0.53
Pt-1b	469, 502	0.13	1.03	0.13	0.84
Pt-1c	465, 497	0.063	0.295	0.21	3.18

[a] Detected at the shortest λ_{PL}. The value of χ^2 was 1.0–1.1.

Fig. 4 shows the PL spectra of PMMA films doped with **Pt-1a**–**c**, where the doping levels were varied as 0.050, 0.10, and 0.20 mmol g^{-1}, approximately corresponding to 3, 5, and 10 wt%, respectively. The PL spectral and photophysical data of the doped PMMA films are summarized in Table 3. The PMMA film doped with 0.050 mmol g^{-1} of **Pt-1a** showed an almost identical PL spectrum to that in dichloromethane. As the doping level of **Pt-1a** increased, a new emission band appeared at *ca*. 600 nm with increasing intensities (Fig. 4a), assignable to excimer emission because the spectral shape of the UV-vis absorption spectrum of **Pt-1a** in the PMMA film is identical regardless of the doping level (Fig. 5) [17,45]. In addition, the PMMA film at the doping level of 0.20 mmol g^{-1} showed the excitation spectrum detected at the excimer emission band to be identical to the spectra detected at the monomer ones. If the new emission band originates from an excited aggregate, a new absorption band such as a metal–metal-to-ligand charge transfer transition band should appear at the longer wavelength region [46]. On the other hand, emissive excimer molecules do not show any absorption bands in their steady-state absorption spectra because they form the dimeric structure only in the excited state [45]. In addition, the significantly broad spectral shape of the new emission band is characteristic of the excimer: in general, the excimer emission shows a broad structureless band generated by a radiative relaxation process of the excimer to a dissociated ground state [47]. Therefore, the new emission band of **Pt-1a** is not aggregate-based emission but excimer emission. For **Pt-1b** and **Pt-1c**, remarkable excimer emission was also observed at *ca*. 600 nm as the doping level increased. Obviously, the excimer emission was enhanced in comparison with **Pt-1a** with the increase in the number of introduced fluoro groups. The Φ_{PL} of **Pt-1a** in the PMMA film at the doping level of 0.050 mmol g^{-1} was 0.62, which was much higher than that in dichloromethane. It has been reported that the triplet metal-centered (^{3}MC) states of (*C^N*)Pt(*O^O*)-type complexes adopt highly distorted structures [48,49], and thus non-radiative relaxation is facilitated through the ^{3}MC

state. On the other hand, the non-radiative decay through structural relaxation should be suppressed in rigid media. This should be the reason why **Pt-1a** is highly emissive in the PMMA film. This is also the case with **Pt-1b** and **Pt-1c**, with Φ_{PL} s of 0.45 and 0.51 at a doping level of 0.050 mmol g^{-1}, respectively. In this regard, the Φ_{PL} is not drastically changed in the range of the doping level of 0.050–0.20 mmol g^{-1} for each of **Pt-1a**–**c**, with values of 0.40–0.62, 0.45–0.47, and 0.51–0.62 for **Pt-1a**–**c**, respectively. That is, the present complexes are still emissive even when remarkable excimer formation occurs, although excimer emission is often associated with concentration quenching [17,24,45,50]. In particular, **Pt-1c** shows a relatively high Φ_{PL} of 0.53 at a doping level of 0.20 mmol g^{-1}, where the relative intensity of the excimer emission is more than three times as high as that of the monomer emission.

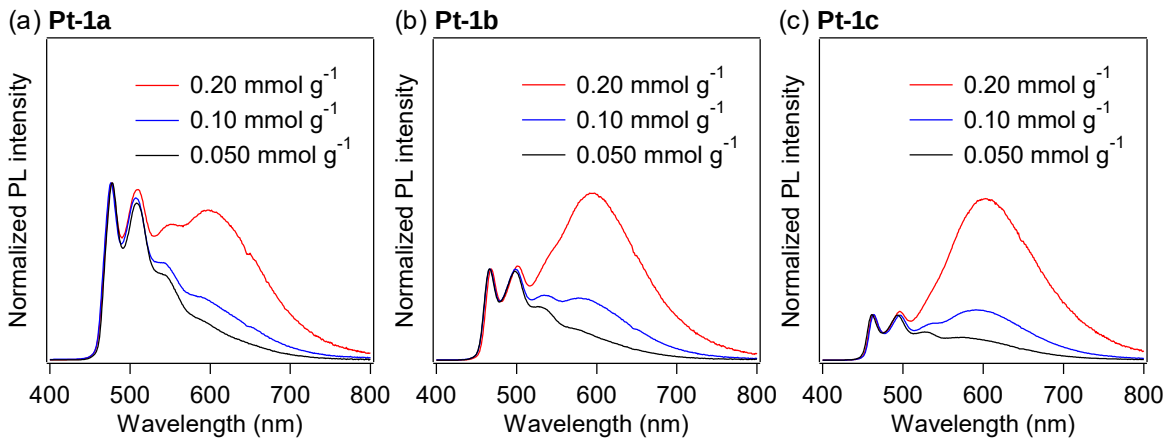

Fig. 4. PL spectra of PMMA films doped with (a) **Pt-1a**, (b) **Pt-1b** and (c) **Pt-1c** at rt under a nitrogen atmosphere.

Table 3. PL properties of **Pt-1** in PMMA film under a nitrogen atmosphere, where the excited wavelength was 390 nm.

Compd	doping level (mmol g^{-1})	λ_{PL} (nm)	Φ_{PL}
Pt-1a	0.050	478, 508	0.62
	0.10	476, 507, 583	0.40
	0.20	477, 510, 576	0.47
Pt-1b	0.050	466, 498	0.45
	0.10	467, 498, 534, 577	0.47
	0.20	468, 501, 597	0.46
Pt-1c	0.050	461, 493, 527, 572	0.51
	0.10	464, 497, 539, 591	0.62
	0.20	463, 496, 603	0.53

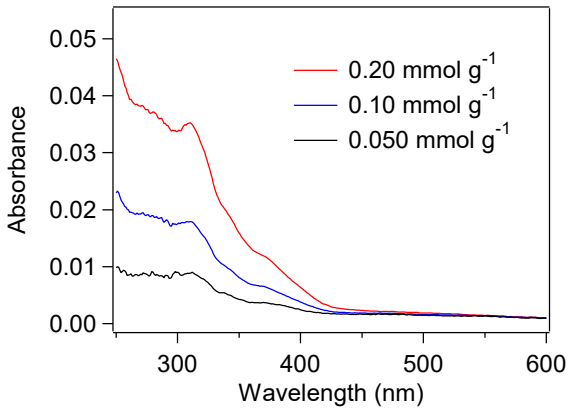

Fig. 5. UV-vis absorption spectra of **Pt-1a** in PMMA at varying doping levels.

In order to investigate the substituent effect of the benzoyl group on the excimer emission, the PL spectra of **Pt-1a** were compared with those of the reference complexes **Pt-2a**–**d**: **Pt-2a** has no substituent on the cyclometalated ligand, and **Pt-2b**, **Pt-2c**, and **Pt-2d** have a 4'-benzoyl, a 5'-acetyl, and a 5'-fluoro group, respectively. The PL spectra of **Pt-2a**–**d** in dichloromethane (10 μM) and in PMMA film (0.20 mmol g^{-1}) are shown in Fig. 6. For **Pt-2a** and **Pt-2b**, almost the same PL spectra were obtained in both dichloromethane and PMMA (Fig. 6a and b). This clearly shows that the remarkable excimer emission of **Pt-1a** is brought about by the substituent effect of the 5'-benzoyl group, and the substituted position is also important. In the case of **Pt-2c**, remarkable excimer emission was obtained in the PMMA film, the spectrum of which was very similar to that of **Pt-1a** although the excimer-to-monomer emission ratio was somewhat smaller than that of **Pt-1a** (Fig. 6c). This indicates that the remarkable excimer emission of **Pt-1a** is not based on π-extension by introduction of the benzoyl group, but predominantly on the electronic effect of the carbonyl moiety. In fact, the phenyl group of the benzoyl group is distorted with respect to the *ppy* mean plane as discussed in the X-ray crystallography section (Fig. 1), and thus the benzoylated cyclometalated ligand does not facilitate the intramolecular stacking interaction. Although **Pt-2d** showed a new emission band at *ca*. 600 nm, its intensity was quite modest in comparison with the monomer emission. Therefore, not all electron-withdrawing groups at the 5'-position facilitate remarkable excimer emission. Further investigation was carried out for the effect of combination of the benzoyl and fluoro groups, and the PL spectra of poly(9-vinylcarbazole) films doped with **Pt-1c** and (*dfppy*)Pt(*acac*) were measured. In this case, as (*dfppy*)Pt(*acac*) is not compatible with PMMA, poly(9-vinylcarbazole) was used as a matrix polymer. The excimer-to-monomer emission ratio of **Pt-1c** is much higher than that of (*dfppy*)Pt(*acac*) (Fig. 7). Thus the introduction of the benzoyl group to the fluorinated *ppy* ligand is effective to obtain considerably enhanced excimer emission.

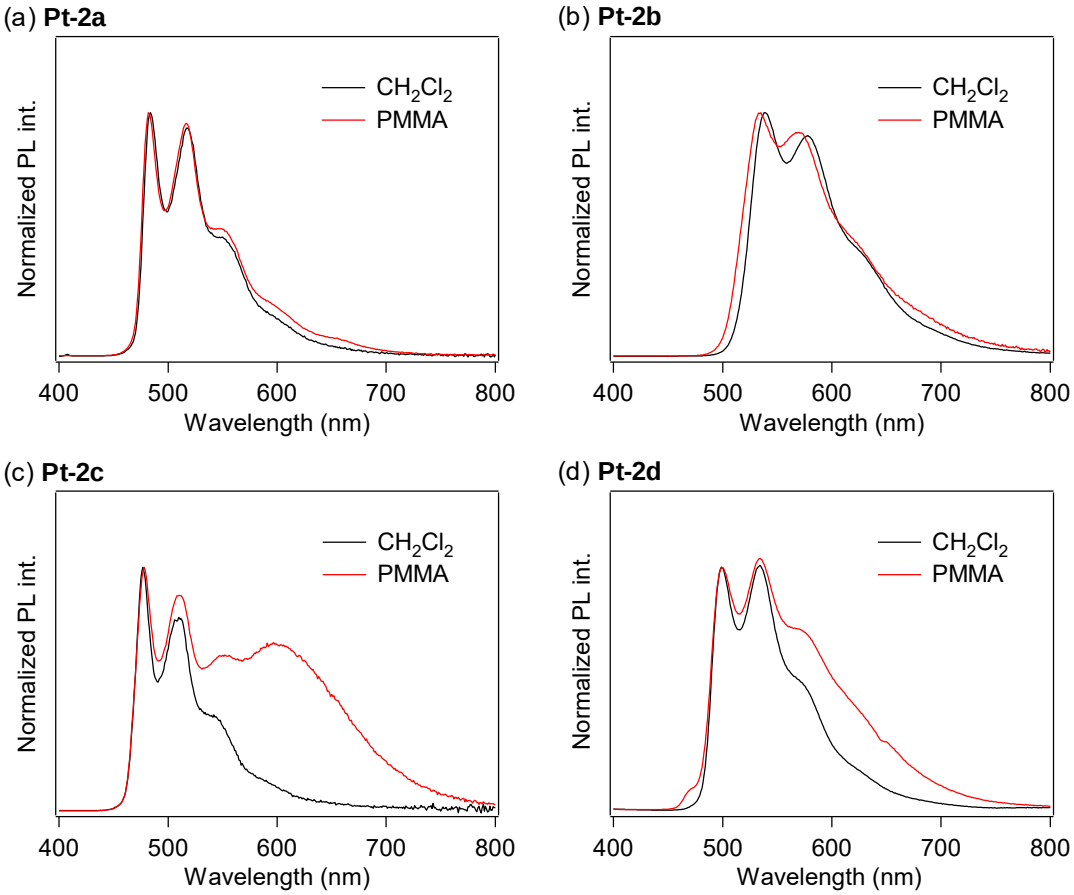

Fig. 6. PL spectra of (a) **Pt-2a**, (b) **Pt-2b**, (c) **Pt-2c** and (d) **Pt-2d** in dichloromethane (10 μM) and PMMA films (0.20 mmol g^{-1}) under deaerated conditions.

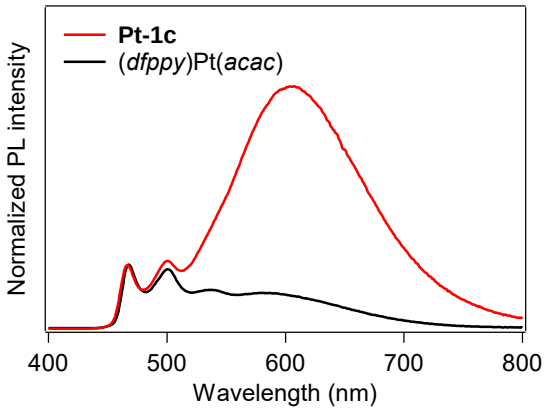

Fig. 7. PL spectra of **Pt-1c** and (*dfppy*)Pt(*acac*) in PVCz film (0.50 mmol g^{-1}) under a nitrogen atmosphere.

3.1.2.3. Photokinetic Studies

To investigate how the benzoylated cyclometalated ligand facilitates the excimer emission, we carried out the kinetic analysis of the PL decay process. Birks showed a general kinetic scheme for excimer formation and decay as shown in Scheme 2, where M, M^*, and D^* are a ground-state monomer, an excited monomer, and an excimer, respectively [51]. k_{rM} and k_{rD} are the radiative rate constants for M^* and D^*, respectively, and k_{iM} and k_{iD} are the nonradiative rate constants for M^* and D^*, respectively. k_{DM} is the second-order rate constant for excimer formation, and k_{MD} is the first-order rate constant for the regeneration of M^* from D^*. Eqn (3) and (4) represent the PL intensities of monomer emission ($I_M(t)$) and excimer emission ($I_D(t)$) at the time t in accordance with this kinetic model:

$$I_{\mathrm{M}}(t) = k_{\mathrm{rM}}[\mathrm{M}^*] = \frac{k_{\mathrm{rM}}[\mathrm{M}^*]_0(\lambda_2 - X)}{\lambda_2 - \lambda_1}\left(e^{-\lambda_1 t} + Ae^{-\lambda_2 t}\right) \quad (3)$$

$$I_{\mathrm{D}}(t) = k_{\mathrm{rD}}[\mathrm{D}^*] = \frac{k_{\mathrm{rD}}[\mathrm{M}^*]_0 k_{\mathrm{DM}}[\mathrm{M}]}{\lambda_2 - \lambda_1}\left(e^{-\lambda_1 t} - e^{-\lambda_2 t}\right) \quad (4)$$

where k_M, k_D, λ_1, λ_2, and A are defined by eqn (5)–(8) (the minus (plus) sign corresponds to λ_1 (λ_2) in eqn (7));

$$k_{\mathrm{M}} = k_{\mathrm{rM}} + k_{\mathrm{iM}} \quad (5)$$

$$k_{\mathrm{D}} = k_{\mathrm{rD}} + k_{\mathrm{iD}} \quad (6)$$

$$\lambda_{1,2} = \frac{X + Y \mp \sqrt{(Y - X)^2 + 4k_{\mathrm{MD}}k_{\mathrm{DM}}[\mathrm{M}]}}{2} \quad (7)$$

$$A = \frac{(X - \lambda_1)}{(\lambda_2 - X)} \quad (8)$$

with

$$X = k_{\mathrm{M}} + k_{\mathrm{DM}} \quad (9)$$

and

$$Y = k_{\mathrm{D}} + k_{\mathrm{MD}} \qquad (10)$$

Under the initial conditions of $[\mathrm{M}^*] = [\mathrm{M}^*]_0$ and $[\mathrm{D}^*] = 0$ at $t = 0$, suppose that the number of M^* generated by photoexcitation is much smaller than that of M and the concentration change of M is ignorable ([M]; constant). In general, the PL decay profiles of both monomer and excimer emissions should be doubly exponential as represented by eqn (3) and (4) when the excimer formation reaction is reversible ($k_{\mathrm{MD}} > 0$) [52]. However, when the excimer formation process is irreversible ($k_{\mathrm{MD}} = 0$), eqn (3) and (4) are represented by eqn (11) and (12), respectively:

$$I_{\mathrm{M}}(t) = k_{\mathrm{rM}}[\mathrm{M}^*]_0 e^{-(k_{\mathrm{M}} + k_{\mathrm{DM}}[\mathrm{M}])t} \qquad (11)$$

$$I_{\mathrm{D}}(t) = \frac{k_{\mathrm{rD}} k_{\mathrm{DM}}[\mathrm{M}][\mathrm{M}^*]_0}{k_{\mathrm{D}} - k_{\mathrm{M}} - k_{\mathrm{DM}}[\mathrm{M}]} \left(e^{-(k_{\mathrm{M}} + k_{\mathrm{DM}}[\mathrm{M}])t} - e^{-k_{\mathrm{D}} t} \right) \qquad (12)$$

Therefore, the PL decay profiles of monomer and excimer emissions should be singly and doubly exponential, respectively, in the case of the irreversible excimer formation.

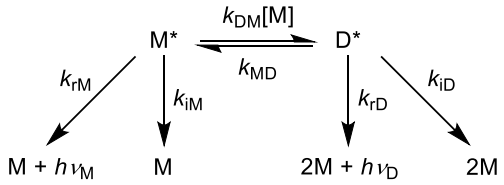

Scheme 2. The general mechanism of excimer formation and monomer ($h\nu_{\mathrm{M}}$) and excimer emissions ($h\nu_{\mathrm{D}}$).

The investigation of the kinetics of the excimer emission is more favorable in solution than in PMMA film because the diffusion rate of molecules in PMMA is low [53] and thus competes with the excimer formation rate. So the PL decay profiles of **Pt-1a** were obtained in dichloromethane at varying concentrations from 10 μM to 1.0 mM (Fig. 8). The excimer emission was observed at *ca*. 650 nm in dichloromethane when the concentration was more than 100 μM. In Fig. 8a and 8b, the PL decay profiles of monomer emission (479 nm) and excimer emission (650 nm) are shown, respectively. The decays of both monomer and excimer emissions were accelerated as the concentration increased. The decay profiles of monomer emission were singly exponential at any investigated concentration. On the other hand, those of excimer emission were doubly exponential, showing rise- and decay-type curves. These results correspond to the decay profiles represented by eqn (11) and (12). The decay profiles of monomer emission were well fitted at any concentration to the singly exponential decay (*i.e*., eqn (13)) with χ^2 values less than 1.1, where the fitting parameters a_M, τ_M and b_M are the coefficient (> 0), the lifetime, and the background intensity, respectively, for monomer emission:

$$I_M(t) = a_M \exp\left(-\frac{t}{\tau_M}\right) + b_M \qquad (13)$$

Next, the decay profiles of excimer emission were also well fitted to doubly exponential eqn (14) with χ^2 values less than 1.2, where the fitting parameters a_D, τ_{D1}, τ_{D2}, and b_D are the coefficient (> 0), the lifetime of the positive component, the lifetime of the negative component, and the background intensity, respectively, for excimer emission:

$$I_D(t) = a_D \left[\exp\left(-\frac{t}{\tau_{D1}}\right) - \exp\left(-\frac{t}{\tau_{D2}}\right)\right] + b_D \qquad (14)$$

The obtained τ_M, τ_{D1}, and τ_{D2} are summarized in Table 4. Fig. 8d shows the plots of τ_M^{-1} against the concentration of the prepared solution, *i.e*. [M]. τ_M^{-1} had a good linear relationship

to [M] with an R^2 value of 0.998. This indicates that the decay profiles of monomer emission of **Pt-1a** obey eqn (11) at any investigated concentration, and thus ${\tau_M}^{-1}$ is represented using eqn (15) according to eqn (11) and (13):

$${\tau_M}^{-1} = k_M + k_{DM}[M] \qquad (15)$$

Therefore, the intercept and slope of the approximate line correspond to the k_M and the k_{DM}, respectively, which were provided as 6.8×10^5 s^{-1} and 2.2×10^9 M^{-1} s^{-1}, respectively. The τ_{D1}s were almost identical to the τ_Ms at the same concentrations as shown in Table 4. The τ_{D2}s were *ca*. 0.2 μs and independent of the concentration. These results show that the decay profiles of excimer emission of **Pt-1a** obey eqn (12) and the k_D (= ${\tau_{D2}}^{-1}$) was 4.8×10^6 s^{-1} [54]. Therefore, the experimental results are consistent with eqn (11) and (12), indicating that the present excimer emission behavior includes the irreversible or pseudo-irreversible excimer formation reaction. On the other hand, Shinozaki and co-workers reported that tridentate cyclometalated platinum(II) complexes showed the reversible process of excimer and excited trimer formation, although the values of k_{DM}s ($2.8–4.5 \times 10^9$ M^{-1} s^{-1}) were similar to that of **Pt-1a** [39]. Next, radiative and non-radiative decay rate constants of M^* and D^* are investigated. It was supposed that the k_{rM} is the same as k_r obtained at a concentration of 10 μM; 2.0×10^5 s^{-1} (Table 2). Then the k_{iM} was determined as 4.8×10^5 s^{-1} according to eqn (5). The ratio of the excimer-to-monomer emission intensity (I_D/I_M) is represented using eqn (16) [51].

$$\frac{I_D}{I_M} = \frac{k_{rD}\, k_{DM}\, [M]}{k_{rM}\, k_D} \qquad (16)$$

I_D/I_M was 1.4 at a concentration of 0.60 mM, which was determined from the relative areas obtained by the deconvolution of the PL spectrum. k_{rD} was estimated at 1.0×10^6 s^{-1} from these values, and k_{iD} was estimated at 3.9×10^6 s^{-1} according to eqn (6). From the above, the

rate constants for **Pt-1a** were fully characterized and they are summarized in Table 5.

The unsubstituted complex **Pt-2a** also showed similar behavior to **Pt-1a**, which also exhibited excimer emission at around 650 nm. The plots of τ_M^{-1} against concentration for **Pt-2a** are also shown in Fig. 8d, and the obtained rate constants for **Pt-2a** are also summarized in Table 5. The k_{DM} of **Pt-2a** was 0.50×10^9 M^{-1} s^{-1}, a quarter of that of **Pt-1a**. This result indicates that introduction of the benzoyl group facilitates the excimer formation reaction.

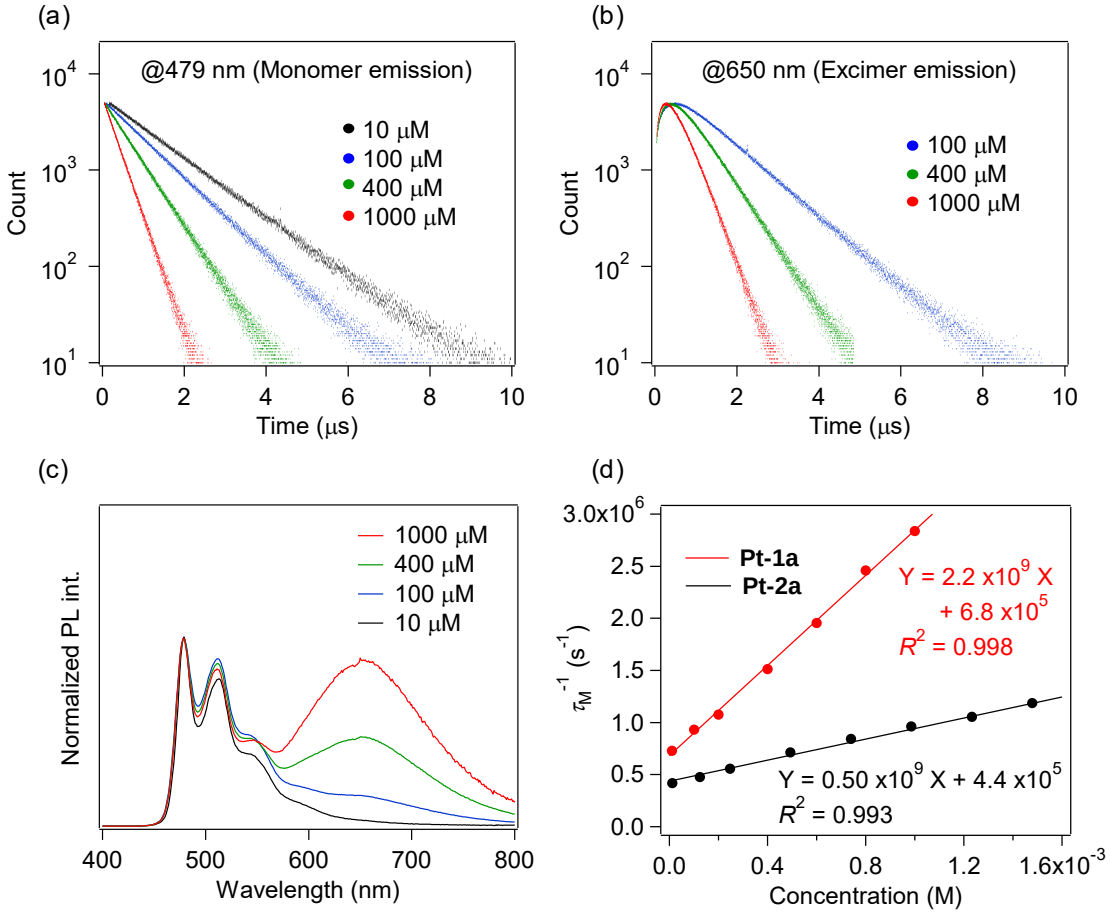

Fig. 8. PL decay profiles detected at (a) 479 nm (monomer emission) and (b) 650 nm (excimer emission) for **Pt-1a**, (c) PL spectra of **Pt-1a**, and (d) plots and approximate lines of τ_M^{-1} against concentration for **Pt-1a** and **Pt-2a** in dichloromethane at rt. All samples were excited at 390 nm.

Table 4. Fitted values of τ_M, τ_{D1} and τ_{D2} of **Pt-1a**.

[M] (mM)	τ_M (μs)	τ_{D1} (μs)	τ_{D2} (μs)
0.010	1.4	---[a]	---[a]
0.10	1.1	---[a]	---[a]
0.20	0.93	---[a]	---[a]
0.40	0.66	---[a]	---[a]
0.60	0.51	0.53	0.22
0.80	0.41	0.42	0.20
1.0	0.35	0.38	0.20

[a]Not determined due to weak excimer emission.

Table 5. The rate constants for **Pt-1a** and **Pt-2a**.

	Pt-1a	**Pt-2a**
k_{DM} (10^9 M^{-1} s^{-1})	2.2	0.50
k_M (10^5 s^{-1})	6.8	4.4
k_{rM} (10^5 s^{-1})[a]	2.0	2.1
k_{iM} (10^5 s^{-1})	4.8	2.9
k_D (10^6 s^{-1})	4.9	6.4
k_{rD} (10^6 s^{-1})[b]	1.0	5.2
k_{iD} (10^6 s^{-1})[b]	3.9	1.2

[a]The k_r at 10 μM. [b]Calculated using the PL spectrum at 0.60 mM.

3.1.2.4. Electroluminescence Properties

From the PL properties investigated above, **Pt-1c** is the best white emitter among **Pt-1a–c** because it exhibits the most blue-shifted monomer emission and remarkable excimer emission suitable to obtain emission covering the whole visible region. Therefore, we fabricated an OLED employing **Pt-1c**, where the device structure is as follows: ITO (150 nm, anode)/F4TCNQ (3 nm)/NPB (50 nm)/TAPC (15 nm)/mCP:**Pt-1c** (30 nm)/TPBi (15 nm)/Alq_3 (20 nm)/LiF (1.5 nm)/Al (100 nm, cathode), where F4TCNQ, NPB, TAPC, mCP, TPBi and Alq_3 are 2,3,5,6-Tetrafluoro-7,7,8,8-tetracyanoquinodimethane, *N*,*N*'-di(1-naphthyl)-*N*,*N*'-diphenyl(1,10-biphenyl)-4,4'-diamine, 4,4'-cyclohexylidenebis[*N*,*N*-bis(4-methylphenyl)-benzenamine], 1,3,5-tris(1-phenyl-1*H*-benzimidazol-2-yl)benzene and tris(8-hydroxy-quinolinato)aluminium, respectively, and the doping level of **Pt-1c** was 15 wt%. The electroluminescence (EL) spectrum at the maximum luminance (L_{max}) and the photograph of the emitting device are shown in Fig. 9. The device exhibited pseudo-white EL with the Commission internationale de L'éclairage (CIE) chromaticity coordinates of (0.42, 0.42) and a correlated color temperature of 3430 K at the L_{max}, and the EL spectrum covered the visible region from 460 to over 700 nm due to the combination of monomer and excimer emissions, as shown in Fig. 9a. The EL was obtained at more than 4.0 V, and the maximum values of luminance, current efficiency and power efficiency were 11500 cd m^{-2} (at 8.8 V), 16.0 cd A^{-1} (at 7.8 V) and 6.68 lm W^{-1} (at 7.4 V). We also fabricated some OLEDs bearing an emitting layer doped with 2–10% of **Pt-1c** [55]. The EL colour changed from sky-blue to pseudo-white as the doping level increased just like the PL of the doped PMMA films.

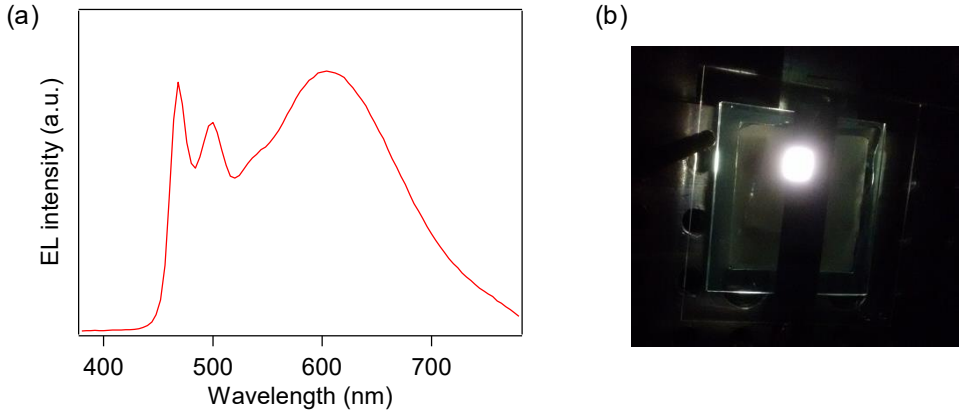

Fig. 9. (a) The EL spectrum at the L_{max} and (b) the photograph of the device employing **Pt-1c**.

3.1.3. Conclusions

In conclusion, the author found that (*ppy*)Pt(*acac*)-type complexes, **Pt-1a**–**c**, bearing a benzoyl group at the 5'-position of the *ppy* ligand exhibit remarkable excimer emission at *ca*. 600 nm in PMMA film along with monomer emission at 461–478 nm. The X-ray structural analysis revealed the distortion of the benzoyl group from the *ppy* skeleton, and that the enhancement of excimer emission is not due to π-extension of the cyclometalated ligand by introduction of the benzoyl group, but likely due to an electronic effect caused by the carbonyl moiety of the benzoyl group. The kinetic analysis of PL decays of **Pt-1a** revealed that excimer formation from the excited and ground state monomers was an irreversible or a pseudo-irreversible process. From the comparison with the analysis for the reference unsubstituted complex, the excimer formation is obviously facilitated, indicating that the introduced benzoyl group plays a crucial role in the formation of the radiative excimer. The author also found that the introduction of additional fluoro group(s) together with the benzoyl group gives rise to enhancement of excimer emission. In particular, the 2-(5-benzoyl-4,6-difluorophenyl)pyridinate-based complex exhibited considerably enhanced excimer emission at *ca*. 600 nm along with greenish blue monomer emission when doped into PMMA film at the doping level of 0.20 mmol g^{-1}. Using this excimer–emissive complex as a

single emitting dopant, a pseudo-white OLED with CIE chromaticity coordinates of (0.42, 0.42) was successfully fabricated, showing the maximum luminance of 11500 cd m^{-2} and the maximum current efficiency of 16.0 cd A^{-1}. Although the electronic effect of the benzoyl group on excimer emission enhancement is still not clarified at this point, we believe that it is important to elucidate such a substituent effect towards the molecular design to control the excimer behavior of phosphorescent organometallic complexes.

3.1.4. Experimental Section

3.1.4.1. General Procedures

The starting material **HC^N-1**−**3** were synthesized as reported in Section 2.1. **HC^N-4a**, [31] **HC^N-4b** [56] and **HC^N-4c** [57], and the reference platinum(II) complexes (*dfppy*)Pt(*acac*) [9] and **Pt-2a** [9] were prepared according to the literatures. The other reagents were used as obtained from Wako Pure Chemical, Tokyo Chemical Industry, Sigma-Aldrich, or Kanto Chemical. ^{1}H NMR (400 MHz) and ^{13}C NMR (100 MHz) spectra were obtained on a Jeol ECS-400 or a Jeol ECX-400 spectrometer, using TMS (0.00 ppm) as an internal standard. ^{19}F NMR spectra were obtained on a Jeol ECX-400 (376 MHz) or a Varian-500 (470 MHz) spectrometer, using $CFCl_3$ (0.00 ppm) as an external standard. Laser desorption/ionization time-of-flight (LDI-TOF) mass spectra were measured on a Shimadzu-Kratos AXIMA-CFR PLUS TOF mass spectrometer. Elemental analyses were carried out on a J-Science MICRO CORDER JM10 analyzer.

3.1.4.2. Syntheses and Characterizations

General procedure for synthesis of a precursor (*C^N*-X)PtCl(H*C^N*-X)

These compounds were prepared according to the conventional procedure [58,59]. A mixture of 2-phenylpyridine derivative **HC^N-X** (**X** = **1**−**3**, **4a**, **4b**, or **4c**, 1.50 mmol) and

potassium tetrachloridoplatinate (0.754 mmol) in a mixture of 2-ethoxyethanol and water (3:1, v/v, 33 mL) was stirred at 80 °C for 12 hours. After cooling, the reaction mixture was concentrated on a rotary evaporator, and then the residue was dissolved in dichloromethane (50 mL) and washed with 10% $NaCl_{aq}$ (50 mL × 2). The organic solution was dried over anhydrous sodium sulfate and it was concentrated on a rotary evaporator. Hexane was added to the concentrated solution to afford a yellow solid of (***C*^*N*-X**)PtCl(**H*C*^*N*-X**) (**X** = **1**−**3**, **4a**, **4b**, and **4c**; 69, 84, 86, 85, 94%, and 71%, respectively). These materials were used in the next reaction without further purification.

General procedure for synthesis of the platinum(II) complexes Pt-1a−c and Pt-2b−d

A mixture of (***C*^*N*-X**)PtCl(**H*C*^*N*-X**) (**X** = **1**−**3**, **4a**, **4b**, and **4c**, 1.72 mmol), acetylacetone (0.873 g, 8.72 mmol), and sodium carbonate (1.80 g, 17.0 mmol) in 2-ethoxyethanol (34 mL) was stirred at 80 °C for 12 hours. After cooling, the reaction mixture was concentrated on a rotary evaporator. Then the residue was dissolved in dichloromethane (100 mL) and washed with 10% $NaCl_{aq}$ (100 mL × 2). The organic solution was dried over anhydrous sodium sulfate and evaporated to dryness. The residue was purified by silica gel column chromatography using chloroform as eluent. Further purification by recrystallization from ethyl acetate or acetonitrile gave a yellow solid of **Pt-1a**−**c** or **Pt-2b**−**d**.

Pt-1a. 29% yield. ^{1}H NMR (400 MHz, CD_2Cl_2) δ 2.00 (s, 3H), 2.02 (s, 3H), 5.52 (s, 1H), 7.20 (ddd, J = 7.3, 5.9 and 1.4 Hz, 1H), 7.46−7.51 (m, 2H), 7.54 (dd, J = 8.2 and 1.8 Hz, 1H), 7.58 (tt, J = 7.3 and 1.4 Hz, 1H), 7.67−7.74 (m, *2*H), 7.75−7.79 (m, 2H), 7.86 (ddd, J = 7.7, 7.3 and 1.8 Hz, 1H), 7.94 (d, J = 1.8 Hz, 1H), 9.02 (ddd, J = 5.9, 0.9 and 0.9 Hz, 1H). ^{13}C NMR (100 MHz, $CDCl_3$) δ 27.19, 28.31, 102.73, 119.00, 122.00, 124.47, 128.27, 129.94, 130.18, 131.60, 131.96, 133.08, 138.57, 138.63, 145.30, 147.50, 147.72, 167.31, 184.56, 186.22, 196.82. LDI-TOF MS: m/z $[M]^+$ calcd for $C_{23}H_{19}NO_3Pt$: 552; found: 552. Anal. calcd for

$C_{23}H_{19}NO_3Pt$: C, 50.00; H, 3.47; N, 2.54. Found: C, 49.92; H, 3.68; N, 2.52.

Pt-1b. 30% yield. ^{1}H NMR (400 MHz, $CDCl_3$) δ 2.03 (s, 3H), 2.04 (s, 3H), 5.52 (s, 1H), 7.18 (ddd, J = 7.3, 6.0 and 1.4 Hz, 1H), 7.36 (d, J = 11.0 Hz, 1H), 7.43−7.49 (m, 2H), 7.58 (tt, J = 7.3 and 1.4 Hz, 1H), 7.62 (d, J = 7.8 Hz, 1H), 7.76 (d, J = 6.9 Hz, 1H), 7.82−7.87 (m, 3H), 9.01 (dd, J = 6.0 and 0.9 Hz, 1H). ^{19}F NMR (376 MHz, $CDCl_3$) δ −105.37 (1F). LDI-TOF MS: m/z $[M]^+$ calcd for $C_{23}H_{18}FNO_3Pt$: 570; found: 570. Anal. calcd for $C_{23}H_{18}FNO_3Pt$: C, 48.42; H, 3.18; N, 2.46. Found: C, 48.49; H, 3.22; N, 2.55.

Pt-1c. 65% yield. ^{1}H NMR (400 MHz, CD_2Cl_2) δ 2.01 (s, 3H), 2.03 (s, 3H), 5.53 (s, 1H), 7.18−7.24 (m, 2H), 7.45−7.50 (m, 2H), 7.61 (tt, J = 7.3 and 1.4 Hz, 1H), 7.84−7.90 (m, 3H), 7.93 (d, J = 8.2 Hz, 1H), 9.04 (ddd, J = 5.9, 0.9 and 0.9 Hz, 1H). ^{19}F NMR (376 MHz, $CDCl_3$) δ −114.84 (1F), −107.49 (1F). LDI-TOF MS: m/z $[M]^+$ calcd for $C_{23}H_{17}F_2NO_3Pt$: 588; found: 588. Anal. calcd for $C_{23}H_{17}F_2NO_3Pt$: C, 46.94; H, 2.91; N, 2.38. Found: C, 47.15; H, 3.15; N, 2.36.

Pt-2b. 68% yield. ^{1}H NMR (400 MHz, $CDCl_3$) δ 1.89 (s, 3H), 2.01 (s, 3H), 5.46 (s, 1H), 7.20 (ddd, J = 7.3, 6.0 and 1.4 Hz, 1H), 7.44−7.49 (m, 2H), 7.51−7.59 (m, 3H), 7.70 (d, J = 8.2 Hz, 1H), 7.84−7.90 (m, 3H), 8.00 (d, J = 1.4 Hz, 1H), 9.05 (dd, J = 6.0 and 0.9 Hz, 1H). ^{13}C NMR (100 MHz, $CDCl_3$) δ 27.05, 28.30, 102.62, 119.35, 122.36, 122.57, 125.42, 128.11, 130.28, 132.18, 132.21, 137.42, 138.10, 138.46, 138.78, 147.76, 148.57, 167.19, 184.47, 186.00, 197.42. LDI-TOF MS: m/z $[M + H]^+$ calcd for $C_{23}H_{20}NO_3Pt$: 553; found: 553. Anal. calcd for $C_{23}H_{19}NO_3Pt$: C, 50.00; H, 3.47; N, 2.54. Found: C, 49.97; H, 3.48; N, 2.38.

Pt-2c. 36% yield. ^{1}H NMR (400 MHz, $CDCl_3$) δ 2.03 (s, 3H), 2.04 (s, 3H), 2.59 (s, 3H), 5.50 (s, 1H), 7.19 (ddd, J = 7.3, 6.0 and 1.4 Hz, 1H), 7.72−7.79 (m, 3H), 7.86 (ddd, J = 7.3, 7.3 and 1.4 Hz, 1H), 8.07 (s, 1H), 9.03 (d, J = 6.0 Hz, 1H). ^{13}C NMR (100 MHz, $CDCl_3$) δ 26.56, 27.18, 28.27, 102.69, 118.94, 121.98, 122.31, 129.50, 130.56, 133.16, 138.59, 145.32, 147.45,

148.25, 167.30, 184.53, 186.19, 198.09. LDI-TOF MS: *m/z* $[M]^+$ calcd for $C_{18}H_{17}NO_3Pt$: 490; found: 490. Anal. calcd for $C_{18}H_{17}NO_3Pt$: C, 44.08; H, 3.49; N, 2.86. Found: C, 44.01; H, 3.72; N, 2.87.

Pt-2d. 6.5% yield. ^{1}H NMR (400 MHz, $CDCl_3$) δ 1.991 (s, 3H), 1.987 (s, 3H), 5.46 (s, 1H), 6.98 (ddd, J = 9.7, 8.2 and 2.7 Hz, 1H), 7.11−7.17 (m, 2H), 7.50−7.57 (m, 2H), 7.81 (ddd, J = 7.5, 7.5 and 1.4 Hz, 1H), 9.00 (ddd, J = 6.3, 6.3 and 0.9 Hz, 1H). ^{19}F NMR (470 MHz, $CDCl_3$) δ −121.55 (1F). LDI-TOF MS: *m/z* $[M]^+$ calcd for $C_{16}H_{14}FNO_2Pt$: 466; found: 466. Anal. calcd for $C_{16}H_{14}FNO_2Pt$: C, 41.21; H, 3.03; N, 3.00. Found: C, 40.83; H, 2.91; N, 2.94.

3.1.4.3. X-Ray Crystallography

The single crystals of **Pt-1a**, **Pt-1b**, and **Pt-1c** suitable for the X-ray crystallography were grown by slow diffusion of their dichloromethane solutions to hexane. Diffraction data were collected on a Rigaku AFC-7 Mercury CCD diffractometer, using graphite monochromated Mo-Kα radiation (λ = 0.71075 Å). The cell parameters were collected to maximum 2θ values of 61.2−61.5° at the temperature of 25 ± 1 °C for **Pt-1a** and 20 ± 1 °C for **Pt-1b** and **Pt-1c**. The structures were solved by direct methods using the SIR92 [60] program and expanded using Fourier techniques on the DIRDIF99 [61] program. All calculations were performed using the Crystal Structure 3.8 [62] software packages. The crystal data and refinement details of the crystal structure determination are given in Table 1.

3.1.4.4. UV-vis and PL Spectroscopic Measurements

UV-vis absorption and PL spectra were recorded on a Shimadzu UV-3600 and a Horiba Jobin Yvon Fluorolog-3 spectrophotometer, respectively. Φ_{PL}s were measured on a Hamamatsu Photonics C9920-12 absolute PL quantum yield measurement system. PL lifetimes (τ_{PL}) were obtained on a Horiba Jobin Yvon FluoroCube spectroanalyzer using a 390

nm nanosecond-order LED light source. The sample solutions for the PL measurement were bubbled with nitrogen gas (flow rate; 0.5 mL min^{-1}) to remove oxygen. The poly(methyl methacrylate) (PMMA) films (thickness; *ca*. 60 nm) were fabricated on quartz substrates by a spin-coating method at a rate of 1500 rpm (2 s) followed by 3000 rpm (60 s) using toluene solutions of PMMA (14 mg ml^{-1}) and platinum(II) complexes. The obtained films were annealed for 1 h at 120 °C. Their spectra were measured under a nitrogen atmosphere.

3.1.4.5. Fabrication and Characterization of OLEDs

Pre-coated indium tin oxide (ITO; thickness, 150 nm; sheet resistance, *ca*. 10 Ω/sq) substrate, 1,3-bis(carbazol-9-yl)benzene (mCP), lithium fluoride, and aluminium were purchased from Kintec Company, Tokyo Chemical Industry, Sigma-Aldrich, and Kurt J. Lesker Company, respectively. 2,3,5,6-Tetrafluoro-7,7,8,8-tetracyanoquinodimethane (F4TCNQ) and tris(8-hydroxyquinolinato)aluminium (Alq_3) were purchased from e-Ray Optoelectronics Technology. *N*,*N*'-di(1-naphthyl)-*N*,*N*'-diphenyl-(1,10-biphenyl)-4,4'-diamine (NPB), 4,4'-cyclohexylidenebis[*N*,*N*-bis(4-methylphenyl)benzenamine] (TAPC), 1,3,5-tris(1-phenyl-1*H*-benzimidazol-2-yl)benzene (TPBi) were purchased from Luminescence Technology.

Patterned ITO substrates were cleaned with acetone to remove any residual photoresists and brushed with a liquid detergent. After soaking in hot water, they were consecutively sonicated in 2-propanol and de-ionized water. Then the dried substrates were treated by UV-O_3. The cleaned substrates were loaded in a deposition chamber. Successive layers of F4TCNQ, NPB, TAPC, mCP:**Pt-1c**, TPBi, Alq_3, lithium fluoride and aluminium were sequentially deposited using thermal evaporator under a reduced pressure of 10^{-8} Torr. The fabricated devices were encapsulated using UV-curable epoxy resin in nitrogen environment. The OLED performance was studied at room temperature, using a Keithley 2400 sourcemeter

and spectrascan PR655 spectroradiometer.

3.1.5. Notes and References

[1] X. Yang, G. Zhou and W.-Y. Wong, *Chem. Soc. Rev*., 2015, **44**, 8484−8575.

[2] T. Fleetham and J. Li, *J. Photonics Energy*, 2014, **4**, 040991 (17 pages).

[3] G. M. Farinola and R. Ragni, *Chem. Soc. Rev*., 2011, **40**, 3467−3482.

[4] M. Aparna, K. Pankaj, M. N. Kamalasanan and C. Subhas, *Semicond. Sci. Technol.*, 2006, **21**, R35−R47.

[5] M. A. Baldo, D. F. O'Brien, Y. You, A. Shoustikov, S. Sibley, M. E. Thompson and S. R. Forrest, *Nature*, 1998, **395**, 151−154.

[6] C. Adachi, M. A. Baldo, M. E. Thompson and S. R. Forrest, *J. Appl. Phys*., 2001, **90**, 5048−5051.

[7] S. Huo, J. Carroll and D. A. K. Vezzu, *Asian J. Org. Chem*., 2015, **4**, 1210−1245.

[8] V. Adamovich, J. Brooks, A. Tamayo, A. M. Alexander, P. I. Djurovich, B. W. D'Andrade, C. Adachi, S. R. Forrest and M. E. Thompson, *New J. Chem*., 2002, **26**, 1171−1178.

[9] J. Brooks, Y. Babayan, S. Lamansky, P. I. Djurovich, I. Tsyba, R. Bau and M. E. Thompson, *Inorg. Chem*., 2002, **41**, 3055−3066.

[10] W.-Y. Wong, Z. He, S.-K. So, K.-L. Tong and Z. Lin, *Organometallics*, 2005, **24**, 4079−4082.

[11] Y. Wang, X. Deng, Y. Liu, M. Ni, M. Liu, H. Tan, X. Li, W. Zhu and Y. Cao, *Tetrahedron*, 2011, **67**, 2118−2124.

[12] A. F. Rausch, L. Murphy, J. A. G. Williams and H. Yersin, *Inorg. Chem*., 2012, **51**, 312−319.

[13] T. Sato, H. Awano, O. Haba, H. Katagiri, Y.-J. Pu, T. Takahashi and K. Yonetake, *Dalton*

Trans., 2012, **41**, 8379−8389.

[14] S. C. F. Kui, P. K. Chow, G. S. M. Tong, S.-L. Lai, G. Cheng, C.-C. Kwok, K.-H. Low, M. Y. Ko and C.-M. Che, *Chem. -Eur. J*., 2013, **19**, 69−73.

[15] D. Kourkoulos, C. Karakus, D. Hertel, R. Alle, S. Schmeding, J. Hummel, N. Risch, E. Holder and K. Meerholz, *Dalton Trans*., 2013, **42**, 13612−13621.

[16] J. Luo, Y. Liu, Q. Chen, D. Shi, Y. Huang, J. Yu, Y. Wang, Z. Zhang, G. Lei and W. Zhu, *Dalton Trans*., 2013, **42**, 1231−1237.

[17] T. Shigehiro, S. Yagi, T. Maeda, H. Nakazumi, H. Fujiwara and Y. Sakurai, *J. Phys. Chem. C*, 2013, **117**, 532−542.

[18] T. Fleetham, L. Huang and J. Li, *Adv. Funct. Mater.*, 2014, **24**, 6066−6073.

[19] G. Li, T. Fleetham and J. Li, *Adv. Mater*., 2014, **26**, 2931−2936.

[20] H. Li, J. Li, J. Ding, W. Yuan, Z. Zhang, L. Zou, X. Wang, H. Zhan, Z. Xie, Y. Cheng and L. Wang, *Inorg. Chem*., 2014, **53**, 810−821.

[21] A. Poloek, C.-W. Lin, C.-T. Chen and C.-T. Chen, *J. Mater. Chem. C*, 2014, **2**, 10343−10356.

[22] P. Pinter, H. Mangold, I. Stengel, I. Münster and T. Strassner, *Organometallics*, 2016, **35**, 673−680.

[23] M. Z. Shafikov, D. N. Kozhevnikov, M. Bodensteiner, F. Brandl and R. Czerwieniec, *Inorg. Chem*., 2016, **55**, 7457−7466.

[24] T. Shigehiro, Q. Chen, S. Yagi, T. Maeda, H. Nakazumi and Y. Sakurai, *Dyes Pigm*., 2016, **124**, 165−173.

[25] F. K.-W. Kong, M.-C. Tang, Y.-C. Wong, M. Ng, M.-Y. Chan and V. W.-W. Yam, *J. Am. Chem. Soc.*, 2017, **139**, 6351−6362.

[26] G.-Z. Lu, Y.-M. Jing, H.-B. Han, Y.-L. Fang and Y.-X. Zheng, *Organometallics*, 2017, **36**, 448−454.

[27] S. Lamansky, P. Djurovich, D. Murphy, F. Abdel-Razzaq, H.-E. Lee, C. Adachi, P. E. Burrows, S. R. Forrest and M. E. Thompson, *J. Am. Chem. Soc*., 2001, **123**, 4304−4312.

[28] A. B. Tamayo, B. D. Alleyne, P. I. Djurovich, S. Lamansky, I. Tsyba, N. N. Ho, R. Bau and M. E. Thompson, *J. Am. Chem. Soc*., 2003, **125**, 7377−7387.

[29] C.-H. Yang, S.-W. Li, Y. Chi, Y.-M. Cheng, Y.-S. Yeh, P.-T. Chou, G.-H. Lee, C.-H. Wang and C.-F. Shu, *Inorg. Chem*., 2005, **44**, 7770−7780.

[30] S. Ikawa, S. Yagi, T. Maeda, H. Nakazumi, H. Fujiwara and Y. Sakurai, *Dyes Pigm.*, 2012, **95**, 695−705.

[31] K. H. Lee, J. S. Hwang, D. H. Chae, S. J. Lee, Y. K. Kim and S. S. Yoon, *Mol. Cryst. Liq. Cryst*., 2012, **563**, 185−194.

[32] H. Xu, R. Chen, Q. Sun, W. Lai, Q. Su, W. Huang and X. Liu, *Chem. Soc. Rev*., 2014, **43**, 3259−3302.

[33] N. Okamura, T. Nakamura, S. Yagi, T. Maeda, H. Nakazumi, H. Fujiwara and S. Koseki, *RSC Adv*., 2016, **6**, 51435−51445.

[34] Q. Wang, I. W. H. Oswald, X. Yang, G. Zhou, H. Jia, Q. Qiao, Y. Chen, J. Hoshikawa-Halbert and B. E. Gnade, *Adv. Mater*., 2014, **26**, 8107−8113.

[35] K.-H. Kim, J.-L. Liao, S. W. Lee, B. Sim, C.-K. Moon, G.-H. Lee, H. J. Kim, Y. Chi and J.-J. Kim, *Adv. Mater*., 2016, **28**, 2526−2532.

[36] D. Kim and J.-L. Brédas, *J. Am. Chem. Soc*., 2009, **131**, 11371−11380.

[37] L. Murphy, P. Brulatti, V. Fattori, M. Cocchi and J. A. G. Williams, *Chem. Commun*., 2012, **48**, 5817−5819.

[38] J. Kalinowski, V. Fattori, M. Cocchi and J. A. G. Williams, *Coord. Chem. Rev*., 2011, **255**, 2401−2425.

[39] T. Kayano, S. Takayasu, K. Sato and K. Shinozaki, *Chem. -Eur. J*., 2014, **20**, 16583−16589.

[40] M. Ebina, A. Kobayashi, T. Ogawa, M. Yoshida and M. Kato, *Inorg. Chem*., 2015, **54**, 8878−8880.

[41] Y. Xing, C. Liu, X. Song and J. Li, *J. Mater. Chem. C*, 2015, **3**, 2166−2174.

[42] C.-H. Chen, F.-I. Wu, Y.-Y. Tsai and C.-H. Cheng, *Adv. Funct. Mater*., 2011, **21**, 3150−3158.

[43] C. Li, S. Wang, Y. Huang, B. Zheng, Z. Tian, Y. Wen and F. Li, *Dalton Trans*., 2013, **42**, 4059−4067.

[44] Measured in deaerated dichloromethane at rt.

[45] T. Förster, *Angew. Chem., Int. Ed*., 1969, **8**, 333−343.

[46] P. Brulatti, V. Fattori, S. Muzzioli, S. Stagni, P. P. Mazzeo, D. Braga, L. Maini, S. Milita and M. Cocchi, *J. Mater. Chem. C*, 2013, **1**, 1823−1831.

[47] B. Stevens and M. I. Ban, *Trans. Faraday Soc*., 1964, **60**, 1515−1523.

[48] D. Escudero and W. Thiel, *Inorg. Chem*., 2014, **53**, 11015−11019.

[49] Y. Xu, Y. Luo, M. Li, R. He and W. Shen, *J. Phys. Chem. A*, 2016, **120**, 6813−6821.

[50] E. Rossi, L. Murphy, P. L. Brothwood, A. Colombo, C. Dragonetti, D. Roberto, R. Ugo, M. Cocchi and J. A. G. Williams, *J. Mater. Chem*., 2011, **21**, 15501−15510.

[51] J. B. Birks, D. J. Dyson and I. H. Munro, *Proc. R. Soc. London, Ser. A*, 1963, **275**, 575−588.

[52] B. D'Andrade and S. R. Forrest, *Chem. Phys*., 2003, **286**, 321−335.

[53] J. Zhang and C. H. Wang, *J. Phys. Chem*., 1986, **90**, 2296−2297.

[54] According to eqn (12), $k_M + k_{DM}[M]$ should be smaller than k_D when ${\tau_{D1}}^{-1}$ and ${\tau_{D2}}^{-1}$ correspond to $k_M + k_{DM}[M]$ and k_D, respectively. We verified the large/small relationship between $k_M + k_{DM}[M]$ and k_D. When [M] is lower than 1.0 mM, the value of $k_M + k_{DM}[M]$ is actually smaller than 2.9×10^6 s^{-1}, which is smaller than the k_D (4.9×10^6 s^{-1}).

[55] Upon varying the doping level of **Pt-1c**, the device structure was somewhat modified as

follows; ITO (150 nm, anode)/m-MTDATA (60 nm)/F4TCNQ (3 nm)/NPB (50 nm)/TAPC (15 nm)/mCP:**Pt-1c** (30 nm)/TPBi (15 nm)/Alq_3 (20 nm)/LiF (1.5 nm)/Al (100 nm), where the m-MTDATA is 4,4',4''-tris[phenyl(*m*-tolyl)amino]triphenylamine.

[56] A. B. Pawar and S. Chang, *Org. Lett*., 2015, **17**, 660−663.

[57] Y. Xiong, J. Wu, S. Xiao, J. Xiao and Song Cao, *J. Org. Chem*., 2013, **78**, 4599−4603

[58] J.-Y. Cho, K. Y. Suponitsky, J. Li, T. V. Timofeeva, S. Barlow and S. R. Marder, *J. Organomet. Chem*., 2005, **690**, 4090−4093.

[59] H. Tsujimoto, S. Yagi, Y. Honda, H. Terao, T. Maeda, H. Nakazumi and Y. Sakurai, *J. Lumin*., 2010, **130**, 217−221.

[60] A. Altomare, G. Cascarano, C. Giacovazzo, A. Guagliardi, M. C. Burla, G. Polidori and M. Camalli, *J. Appl. Crystallogr.*, 1994, **27**, 435−436.

[61] P. T. Beurskens, G. Admiraal, G. Beuskens, W. P. Bosman, R. d. Gelder, R. Israel and J. M. M. Smits, *The DIRDIF-99 program system; technical report of crystallography laboratory*, University of Nijimegen, Nijimegen, The Netherlands, 1999.

[62] *Crystal structure 3.8*, Rigaku and Rigaku Americas, Woodlands, TX, USA, 2000.

Chapter 3

Section 3.2

Control of Excimer Phosphorescence by Steric Effects in Cyclometalated Platinum(II) Diketonate Complexes Bearing Oligocarbazole Moieties towards Application to Non-Doped White OLED

3.2.1. Introduction

Non-doped organic light-emitting diodes (OLED) have been enthusiastically developed to attain the facile and low-cost device fabrication, the emitting layer (EML) of which consists of only a charge carrier transporting emitter [1,2]. To fabricate efficient OLEDs, phosphorescent emitters are frequently used because the phosphorescent devices raise the internal quantum efficiency (η_{int}) up to 100% in theory from the view point of spin statics, although the maximum η_{int} of the fluorescent devices is 25% at most [3,4]. This superiority of phosphorescent materials in OLED has so far been encouraging researchers to develop various types of phosphorescent platinum(II) [5−7] and iridium(III) [8−11] complexes bearing charge carrier transporting moieties. As shown in Section 2.2, the author also recently reported sky-blue phosphorescent cyclometalated iridium(III) complexes bearing hole-transporting oligocarbazole moieties, and they were employed as a non-doped EML of the solution-processed OLED with a multilayer device structure; transparent anode/hole-injection layer (HIL)/hole-transporting layer (HTL)/EML/electron-transporting layer (ETL)/electron-injection layer (EIL)/metal cathode [10]. Therein, as the hole-transporting iridium(III) complexes showed high solubility in an apolar solvent such as cyclohexane and insolubility in lower alcohols due to their peripheral bulky lipophilic groups,

the non-doped multilayer device was successfully fabricated by successively spin-coating the EML and ETL with cyclohexane and 2-propanol as the ink solutions, respectively, onto the cyclohexane-insoluble HTL. So far, OLEDs bearing multi-stacked organic layers are generally fabricated by vacuum deposition methods [12]. However, using the orthogonal solvent system, solution-processed multilayer devices are available.

In this study, the author demonstrates fabrication of a non-doped white OLED using a charge carrier-transporting platinum(II) complex. White OLEDs are attracting considerable attention from the viewpoint of application to room lightings and display backlights. Poulsen and co-workers developed a copolymer consisting of iridim(III)-containing blue-green and orange-red phosphorescent comonomers and charge carrier transporting ones, where the molar ratio of the comonomers was tuned to obtain an optimized EL spectrum corresponding to white emission [13]. However, the single emitter system is more favorable for reproducibility of the color coordinate for white EL. In this context, cyclometalated platinum(II) complexes are good candidates to this end. They adopt square planar coordination geometry and often exhibit excimer emission in the longer wavelength region than the intrinsic monomer emission [14−17]. One can produce white EL by combination of the monomer and excimer emissions, the spectrum of which covers whole visible regions [14]. As shown in Section 3.1, the author also recently reported that the heteroleptic platinum(II) complex **Pt-1c** (Fig. 1), bearing a 2-(5-benzoyl-4,6-difluorophenyl)pyridinate ligand and an acetylacetonate ancillary ligand, shows remarkable excimer emission due to facilitation of the excimer formation process by introduction of the benzoyl group. This complex has a high photoluminescence (PL) quantum yield (Φ_{PL}) of *ca*. 0.6 in polymer films [17]. In addition, the OLED having a **Pt-1c**-doped EML showed pseudo-white electroluminescence (EL) due to combination of blue monomer emission at 465 nm and excimer emission at *ca*. 600 nm. In this case, the excimer-to-monomer emission ratio was carefully tuned by controlling the

doping level of **Pt-1c**.

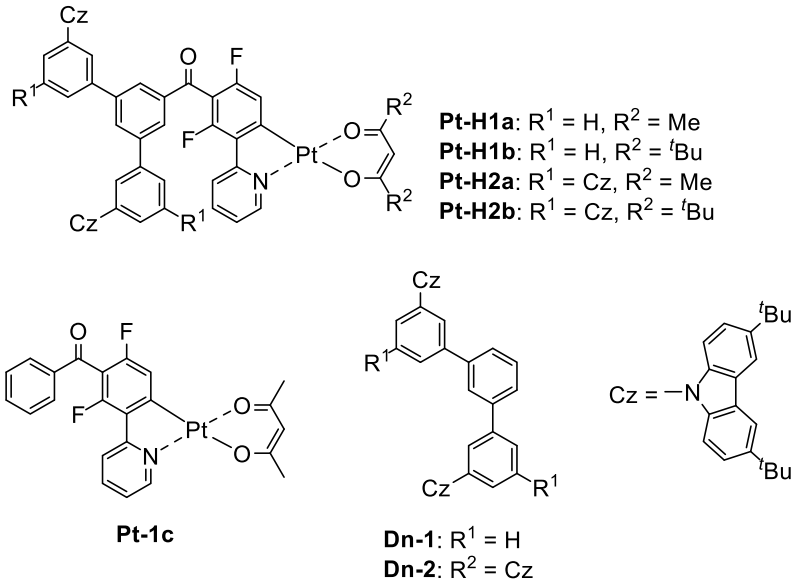

Fig. 1. Structures of cyclometalated platinum(II) complexes **Pt-H1** and **Pt-H2** and reference compounds **Pt-1c**, **Dn-1**, and **Dn-2**.

Aimed at fabrication of non-doped multilayer OLEDs showing excimer-based EL by solution processing, here we report the synthesis and luminescent (PL and EL) properties of novel heteroleptic cyclometalated platinum(II) complexes bearing *tert*-butylated oligocarbazole moieties on **Pt-1c**, namely, **Pt-H1** and **Pt-H2** (Fig. 1). The author introduced less bulky acetylacetonate (**Pt-H1a** and **Pt-H2a**) and bulky dipivaloylmethanate ligands (**Pt-H1b** and **Pt-H2b**) as the diketonate ancillary (*O^O*) ligands. Through the steric hindrance of cyclometalated and ancillary ligands, the excimer-to-monomer emission ratio in the film state is tuned to obtain white EL upon fabrication of a non-doped OLED.

3.2.2. Results and Discussion

3.2.2.1. Synthesis and Characterization

Scheme 1 shows the synthesis of **Pt-H1** and **Pt-H2**. The synthesis of **H*C*^*N*-H1** for the cyclometalated (*C*^*N*) ligand of **Pt-H1** was reported in Section 2.2. The 2-phenylpyridine derivative **H*C*^*N*-H2**, corresponding to the *C*^*N* ligand of **Pt-H2**, was newly synthesized through three steps from 1-bromo-3,5-difluorobenzene; sequential reactions of the nucleophilic aromatic substitution, the Miyaura-Ishiyama borylation, and the Suzuki-Miyaura coupling (93, 86, and 69% yield, respectively). The complexes **Pt-H1** and **Pt-H2** were synthesized by the reaction of potassium tetrachloridoplatinate(II) with **H*C*^*N*-H1** and **H*C*^*N*-H2**, respectively, followed by the reaction with the corresponding diketones in 21−30% yield. The prepared complexes were well characterized by ^{1}H and ^{19}F NMR, MALDI-TOF MS, and elemental analysis. Introduction of the *tert*-butylated oligocarbazole moieties affected the physical properties. That is, **Pt-H1** and **Pt-H2** are soluble in cyclohexane although **Pt-1c** is insoluble (solubility; < 0.01 mg ml^{-1}). In addition, these complexes showed excellent film forming properties, which are essential to prepare EMLs of non-doped OLEDs. The average roughness (R_a) of neat films of **Pt-H1** and **Pt-H2** (thickness; 80 nm) were 1.4−2.4 nm when they were prepared by spin-coating from the chloroform solutions (16 g ml^{-1}) at rates of 2000 rpm (10 s) and then 3000 rpm (20 s) followed by annealing for 30 min at 120 °C. On the other hand, **Pt-1c** provided a rough film surface with the R_a of 37 nm when the film was prepared in the same way.

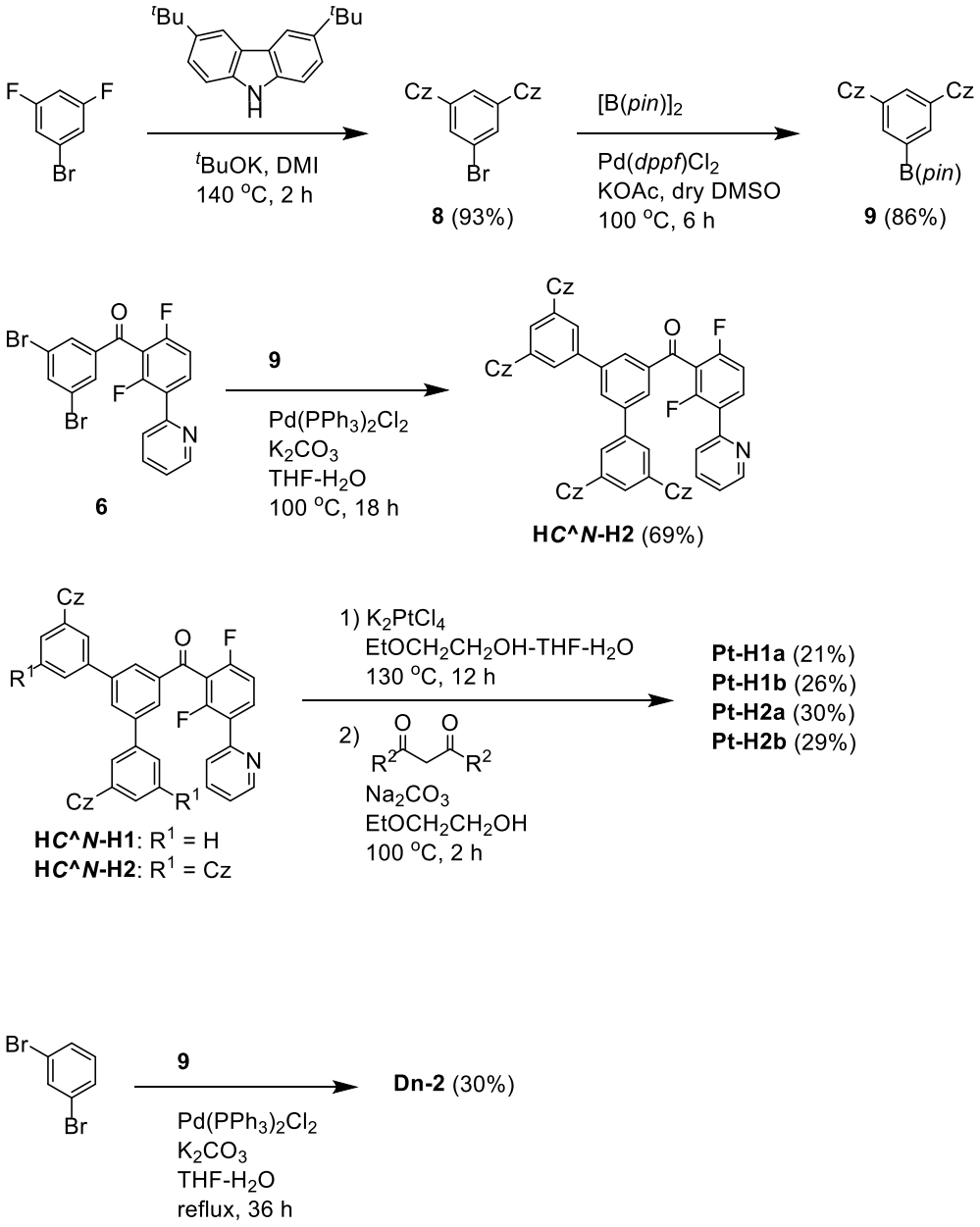

Scheme 1. Synthetic route of **Pt-H1**, **Pt-H2** and **Dn-2**. The ligands *pin* and *dppf* are pinacolate and 1,1'-bis(diphenylphosphino)ferrocene, respectively, and the solvents DMI, DMSO, and THF are 1,3-dimethyl-2-imidazolidinone, dimethylsulfoxide, and tetrahydrofuran, respectively. The structure of the functional group Cz is represented in Fig. 1.

3.2.2.2. Phostoluminescence Properties

The carbazole-appended complexes **Pt-H1** and **Pt-H2** exhibited greenish blue PL based on phosphorescence (PL lifetime (τ_{PL}); 0.16−0.21 μs, Table 1) at 463 nm in deaerated dichloromethane (10 μM) at rt, the spectra of which were almost identical to that of **Pt-1c** (Fig. 2a). As summarized in Table 1, the Φ_{PL}s of **Pt-H1** and **Pt-H2** are very low in solution (Φ_{PL}; 0.02−0.03), and thus the present complexes are comparably non-emissive to **Pt-1c** (Φ_{PL}; 0.06). On the other hand, a neat film of **Pt-H1a** exhibited orange PL at 618 nm with a broad spectrum (Fig. 2b), which is assignable to excimer emission from the platinum-based luminophores because the PL spectrum is almost identical to that of the excimer emission of **Pt-1c** doped into PMMA [17]. Interestingly, the Φ_{PL} was drastically improved to 0.43. The oligocarbazole moieties do not quench the emission from the platinum-based luminophore because the *m*-phenylene-type linkage keeps their triplet levels high to suppress the back energy transfer from the lumnophore to the oligocarbazole moieties [10,18]. The analogous complex **Pt-H1b**, bearing a dipivaloylmethanate ligand in place of the acetylacetonate ligand in **Pt-H1a**, exhibited both monomer and excimer emissions (λ_{PL}; 465 and 605 nm, respectively) to afford white PL. This should be because the bulky dipivaloylmethanate ligand moderately suppressed excimer formation through steric hindrance. In the case of **Pt-H2**, the acetylacetonate complex **Pt-H2a** also exhibited excimer-based orange PL similar to **Pt-H1a**, although the week monomer emission band was also observed at 465 nm. This indicates that the increase in the number of carbazole residue in the *C^N* ligand of **Pt-H2** also has an effect to suppress the excimer formation through steric hindrance. The bulkiest complex **Pt-H2b** exhibited bluish white PL, where the monomer emission mainly contributes to the spectrum rather than that of the excimer. Therefore, the ratio of monomer and excimer emissions is tunable by combination of the *C^N* and *O^O* ligands to obtain emission colors from orange to bluish white. The Φ_{PL}s of **Pt-H1b**, **Pt-H2a**, and **Pt-H2b** were 0.23, 0.41, and 0.18,

respectively. Thus, in the present system, the Φ_{PL} decreases with the decrease in the relative intensity of excimer emission, indicating that the excimer emission is more emissive in the film state.

Table 1. PL properties of **Pt-H1** and **Pt-H2**, where the excitation wavelength was 390 nm.

Compd	In dichloromethane (10 μM)			Neat film	
	λ_{PL} (nm)	Φ_{PL}	τ_{PL} (μs)[a]	λ_{PL} (nm)	Φ_{PL}
Pt-H1a	463, 496	0.03	0.21	618	0.43
Pt-H1b	463, 495	0.03	0.18	465, 498, 541, 605	0.23
Pt-H2a	463, 495	0.03	0.19	465, 499, 610	0.41
Pt-H2b	463, 495	0.02	0.16	465, 497, 529, 601	0.18
Pt-1c	465, 497[b]	0.06[b]	0.30[b]	---[c]	---[c]

[a]The χ^2 value was 1.0. [b]Reported values [17]. [c]No homogeneous films were obtained.

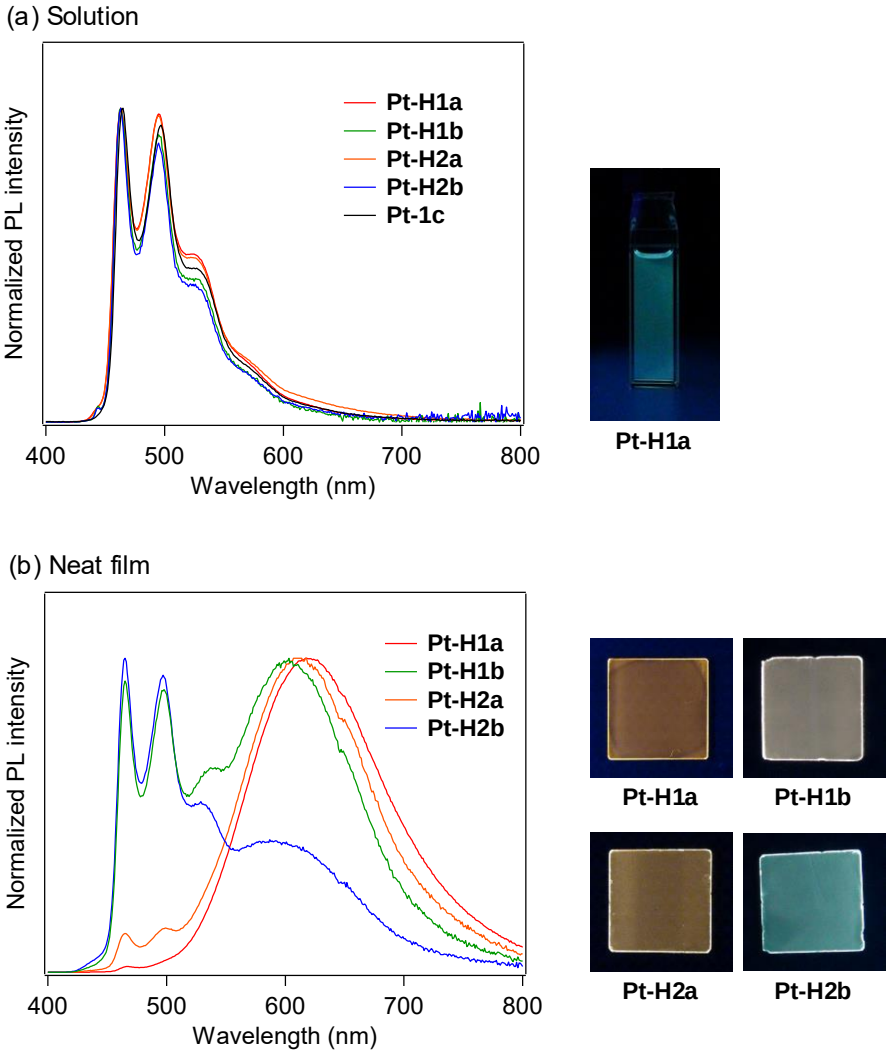

Fig. 2. PL spectra of (a) dichloromethane solutions (10 μM) and (b) neat films of **Pt-H1** and **Pt-H2** on quartz plates at rt under deaerated conditions, where the excitation wavelength was 390 nm. Photographs of the solution and films under UV irradiation are also shown.

3.2.2.3. Electrochemical Properties

The oxidation and reduction potentials of **Pt-H1** and **Pt-H2** were determined by cyclic voltammetry in dichloromethane and *N*,*N*-dimethylformamide (DMF), respectively, which are important upon fabrication of OLEDs. All the complexes exhibited pseudo-reversible oxidation and reduction cycles (Fig. 3). The redox potentials versus ferrocenium/ferrocene (Fc^+/Fc) redox couple ($E_{1/2,\,Ox}$ and $E_{1/2,\,Red}$) and the HOMO and LUMO energies (E_{HOMO} and E_{LUMO}) are summarized in Table 2. The E_{HOMO} and E_{LUMO} were calculated from the $E_{1/2,\,Ox}$ and $E_{1/2,\,Red}$ relative to the energy of the Fc^+/Fc redox couple (E_{HOMO}; −4.80 eV). The E_{HOMO} of the reference carbazole dimer **Dn-1** (−5.53 eV) corresponding to the hole-transporting moiety of **Pt-H1** has already been reported in Section 2.2. The E_{LUMO} of **Pt-1c** (−2.60 eV) and the E_{HOMO} of the reference carbazole tetramer **Dn-2** (−5.60 eV, Fig. 1, synthesized as shown in Scheme 1) corresponding to the hole-transporting moiety of **Pt-H2** were also determined in the same way. The E_{HOMO}s of **Pt-H1a**, **Pt-H1b**, **Pt-H2a**, and **Pt-H2b** are −5.37, −5.37, −5.48, and −5.47 eV, respectively, which are similar to that of the corresponding reference carbazole oligomer **Dn-1** or **Dn-2**. On the other hand, the E_{LUMO}s of **Pt-H1** and **Pt-H2**, ranging from −2.66 to −2.70 eV, are almost identical to that of **Pt-1c** (−2.60 eV). These results indicate that the HOMOs and LUMOs of **Pt-H1** and **Pt-H2** are localized on the oligocarbazole moieties and the platinum-based luminophore, respectively. This is supported by density functional theory calculation of **Pt-H1a** at the level of B3LYP/LANL2DZ (Pt) and 6-31G* (C, H, N, O and F), as shown in Fig. 4.

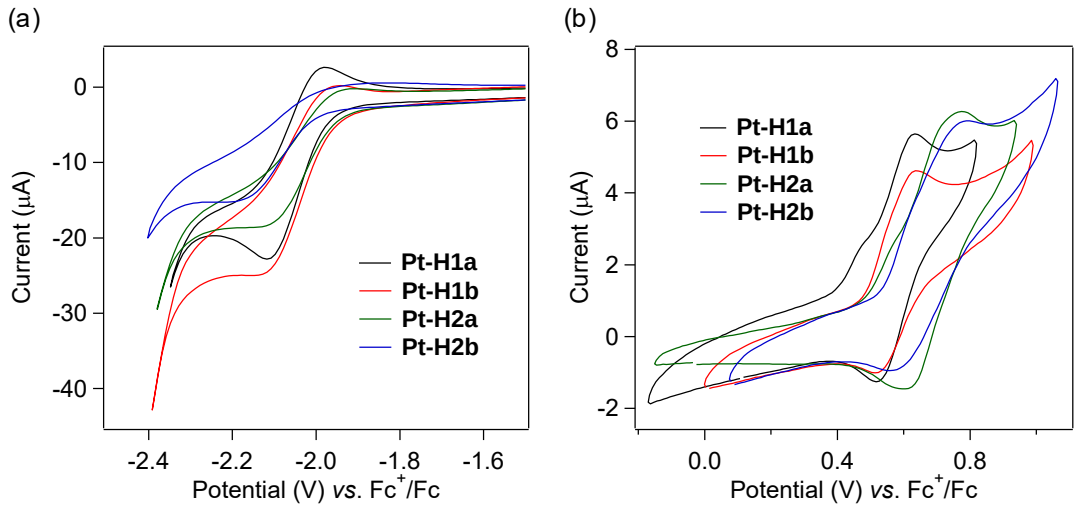

Fig. 3. Cyclic voltammograms of **Pt-H1** and **Pt-H2** (a) in deaerated dry DMF (3.1−4.9 mM) with 0.10 M tetrabutylammonium perchlorate (TBAP) and (b) in dry dichloromethane (0.50 mM) with 0.10 M TBAP. The scan rates were 500 mV s^{-1} and 100 mV s^{-1}, respectively.

Table 2. Electrochemical properties of **Pt-H1**, **Pt-H2**, **Pt-1c**, **Dn-1** and **Dn-2**.

Compd	$E_{1/2,\,Ox}$ (V) *vs*. Fc^+/Fc	$E_{1/2,\,Red}$ (V) *vs*. Fc^+/Fc	E_{HOMO}[a] (eV)	E_{LUMO}[b] (eV)
Pt-H1a	0.575	−2.13	−5.37	−2.67
Pt-H1b	0.575	−2.11	−5.37	−2.69
Pt-H2a	0.982	−2.10	−5.48	−2.70
Pt-H2b	0.669	−2.14	−5.47	−2.66
Pt-H1c	---[c]	−2.20	---[c]	−2.60
Dn-1	0.729[d]	−2.85[d]	−5.53[d]	−1.95[d]
Dn-2	0.800	---[c]	−5.60	---[c]

[a]E_{HOMO} [eV] = −($E_{1/2,\,Ox}$ [V] + 4.80). [b]E_{LUMO} [eV] = −($E_{1/2,\,Red}$ [V] + 4.80). [c]No reversible redox cycles were obtained. [d]Reported values [10].

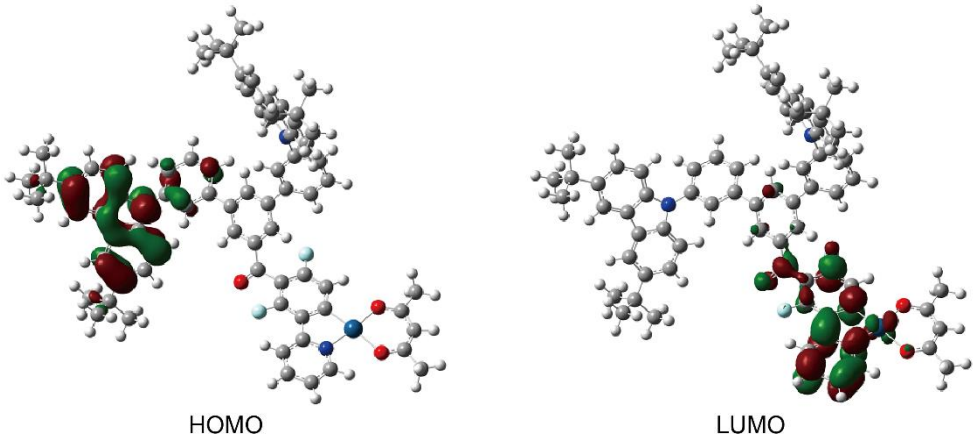

Fig. 4. The HOMO and LUMO of **Pt-H1a** optimized at the level of B3LYP/LANL2DZ (Pt) and 6-31G* (C, H, N, O and F) by Gaussian 09 [19].

3.2.2.4. Fabrication of OLEDs

Using the neat films of **Pt-H1** and **Pt-H2** as an emitting layer, the author fabricated two types of non-doped solution-processed OLEDs. The author first fabricated simple non-doped OLEDs S-1a, S-1b, S-2a, and S-2b, where **Pt-H1a**, **Pt-H1b**, **Pt-H2a**, and **Pt-H2b** were employed, respectively. The device structure was ITO (150 nm, anode)/PEDOT:PSS (40 nm)/**Pt-H1** or **Pt-H2** (80 nm)/CsF (1 nm)/Al (250 nm, cathode), as shown in Fig. 5a with the energy diagram, where the HIL material PEDOT:PSS is poly(ethylenedioxy-3,4-thiophene): poly(styrene sulfonate). The PEDOT:PSS, **Pt-H1** and **Pt-H2** layers were prepared by a spin-coating technique, and the cesium fluoride and aluminum layers were successively vacuum-deposited. The device performances of the fabricated devices are summarized in Table 3. In the case of S-1a, extremely remarkable excimer-based orange EL with the Commission Internationale de L'éclairage (CIE) chromaticity coordinate of (0.59, 0.40) (Fig. 5b) emerged at more than 7.5 V of applied voltage (Fig. 5c). The maximum luminance (L_{max}) and the maximum external quantum efficiency ($\eta_{ext,\,max}$) were 3700 cd m^{-2} at 19.5 V and 3.0% at 14.5 V, respectively. The L_{max}s of S-1b, S-2a, and S-2b were 760, 980, and 380 cd m^{-2},

respectively, and their $\eta_{ext,\ max}$ s were 1.0, 2.2, and 0.41%, respectively. The order of the device performances corresponds to the order of the Φ_{PL}s of **Pt-H1** and **Pt-H2** in the film state. The relative intensity of the excimer emission to the monomer one among these devices increases as observed in PL of the neat films of the employed complexes: the device S-1a employing less bulky **Pt-H1a** exclusively showed excimer-based EL, whereas relatively intense monomer-based EL was obtained for the device S-2b employing the bulkiest complex **Pt-H2b**. Obviously, for each complex, the excimer emission of EL was more remarkable than that of PL (Fig. 5b). It has been suggested that excimer emission is often facilitated in OLEDs due to direct formation of an excimer by the reaction of a monomer radical cation with a monomer radical anion [16,20]. According to this mechanism of excimer generation, the device S-1b showed orange-white EL with the CIE chromaticity coordinate of (0.47, 0.42), although the neat film **Pt-H1b** exhibited white PL. On the other hand, S-2b exhibited white PL with the CIE chromaticity coordinate of (0.38, 0.40) closest to the theoretical white of (0.33, 0.33) among these devices, although the monomer emission is more intense than the excimer emission in the film-state PL of **Pt-H2b**.

Table 3. Device performance of simple OLEDs S-1 and S-2, and multi-stacked OLEDs M-1 and M-2.

OLED	EML	L_{max} (cd m^{-2}) [@V]	$\eta_{ext,\ max}$ (%) [@V]	CIE (x, y)
S-1a	**Pt-H1a**	3700 [19.5]	3.0 [14.5]	(0.59, 0.40)[a]
S-1b	**Pt-H1b**	760 [14.0]	1.0 [9.5]	(0.47, 0.42)[a]
S-2a	**Pt-H2a**	980 [19.0]	2.2 [15.5]	(0.58, 0.41)[a]
S-2b	**Pt-H2b**	380 [14.0]	0.41 [11.0]	(0.38, 0.40)[a]
M-1a	**Pt-H1a**	12000 [15.5]	6.5 [9.5]	(0.58, 0.40)[b]
M-1b	**Pt-H1b**	2800 [10.5]	1.6 [7.0]	(0.37, 0.41)[b]
M-2a	**Pt-H2a**	6900 [15.5]	4.4 [10.0]	(0.56, 0.42)[b]
M-2b	**Pt-H2b**	2200 [12.0]	0.96 [10.0]	(0.35, 0.40)[b]

[a]At L_{max}. [b]At 1000 cd m^{-2}.

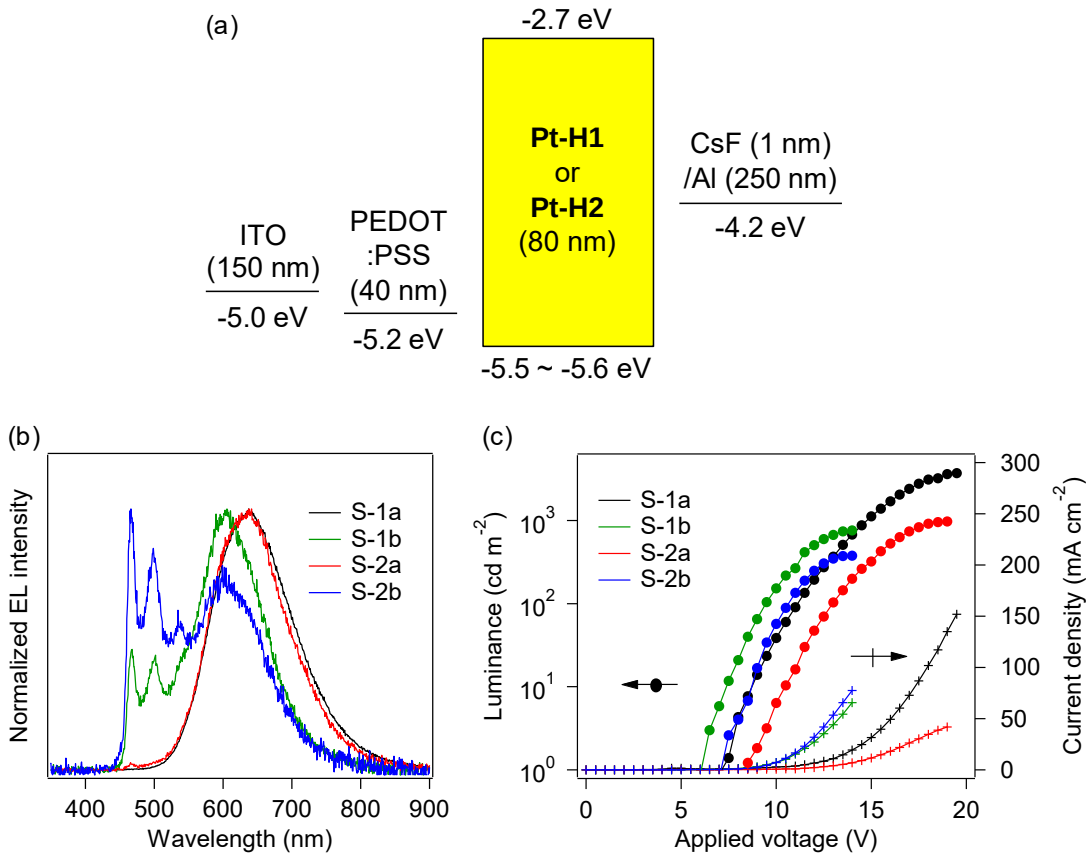

Fig. 5. (a) The device structure of S-1 and S-2. The highest energy levels of the valence bands of ITO, PEDOT:PSS and aluminium are reported values [21]. (b) EL spectra of S-1 and S-2 at L_{max}. (c) *J*-*V*-*L* curves of S-1 and S-2.

In order to improve the device efficiency, the author next fabricated multilayer OLEDs M-1a, M-1b, M-2a, and M-2b, employing **Pt-H1a**, **Pt-H1b**, **Pt-H2a**, and **Pt-H2b**, respectively. The device structure was ITO (150 nm, anode)/PEDOT:PSS (40 nm, HIL)/PVCz (20 nm, HTL)/**Pt-H1** or **Pt-H2** (30 nm, EML)/TPBi (40 nm, ETL)/CsF (1 nm)/Al (250 nm, cathode), where PVCz and TPBi are poly(9-vinylcarbazole) and 1,3,5-tris(1-phenyl-1*H*-benzo[*d*]imidazol-2-yl)benzene, respectively. As shown in Fig. 6a, this device structure is expected to give efficient charge recombination in the **Pt-H1** and **Pt-H2** layers because the PVCz and TPBi layers act as electron- and hole-blocking layers, respectively. All the organic layers were prepared by solution processing: a water/2-propanol (1:1, v/v) solution of

PEDOT:PSS, a toluene solution of PVCz, a cyclohexane solution of **Pt-H1** (or **Pt-H2**), and a methanol solution of TPBi were sequentially spin-coated on the pre-patterned ITO glass substrate. The device M-1a employing **Pt-H1a** exhibited excimer-based orange EL as observed in S-1a and afforded improved L_{max} and $\eta_{ext,\,max}$ of 12000 cd m^{-2} at 15.5 V and 6.5% at 9.5 V, respectively, in comparison with S-1a. The L_{max}s and $\eta_{ext,\,max}$ s of the devices M-1b, M-2a, and M-2b were also improved to 2200−6900 cd m^{-2} at 10.5−15.5 V and 0.96−1.6% at 7.0−10.0 V, respectively, as shown in Table 3. The devices M-1b and M-2b showed smaller excimer-to-monomer EL ratios than those of S-1b and S-2b (Fig. 6b). The possible reason is the narrow charge recombination zone of the present multilayer devices: the charge recombination should occur at the interface between EML and the hole- or electron-blocking layers, whereas it is possible in the whole region of EML in the case of the simple devices S-1 and S-2. When a lot of excited monomers were locally generated, the excimer formation reaction of an excited monomer with a ground state one should be suppressed due to lack of the ground-state monomers. As a result, the device M-1b employing **Pt-H1b** exhibited pseudo-white EL with the CIE chromaticity coordinate of (0.37, 0.41) at 1000 cd m^{-2}. In the case of M-2b, white EL with the CIE chromaticity coordinate of (0.35, 0.40) was obtained, accompanied with the excellent average color rendering index of 81. Interestingly, the conductivities of the multilayer devices were also improved in spite of the larger total thickness of their organic layers (130 nm) than those of S-1 and S-2 (120 nm): the current densities of M-1 and M-2 at 10.0 V were 7−21 times larger than those of S-1 and S-2, and the turn-on voltages (luminance; > 1 cd m^{-2}) of M-1 and M-2 were 4.5−5.5 V, smaller than those of S-1 and S-2 (6.0−8.5 V), as shown in Fig. 5c and 6c.

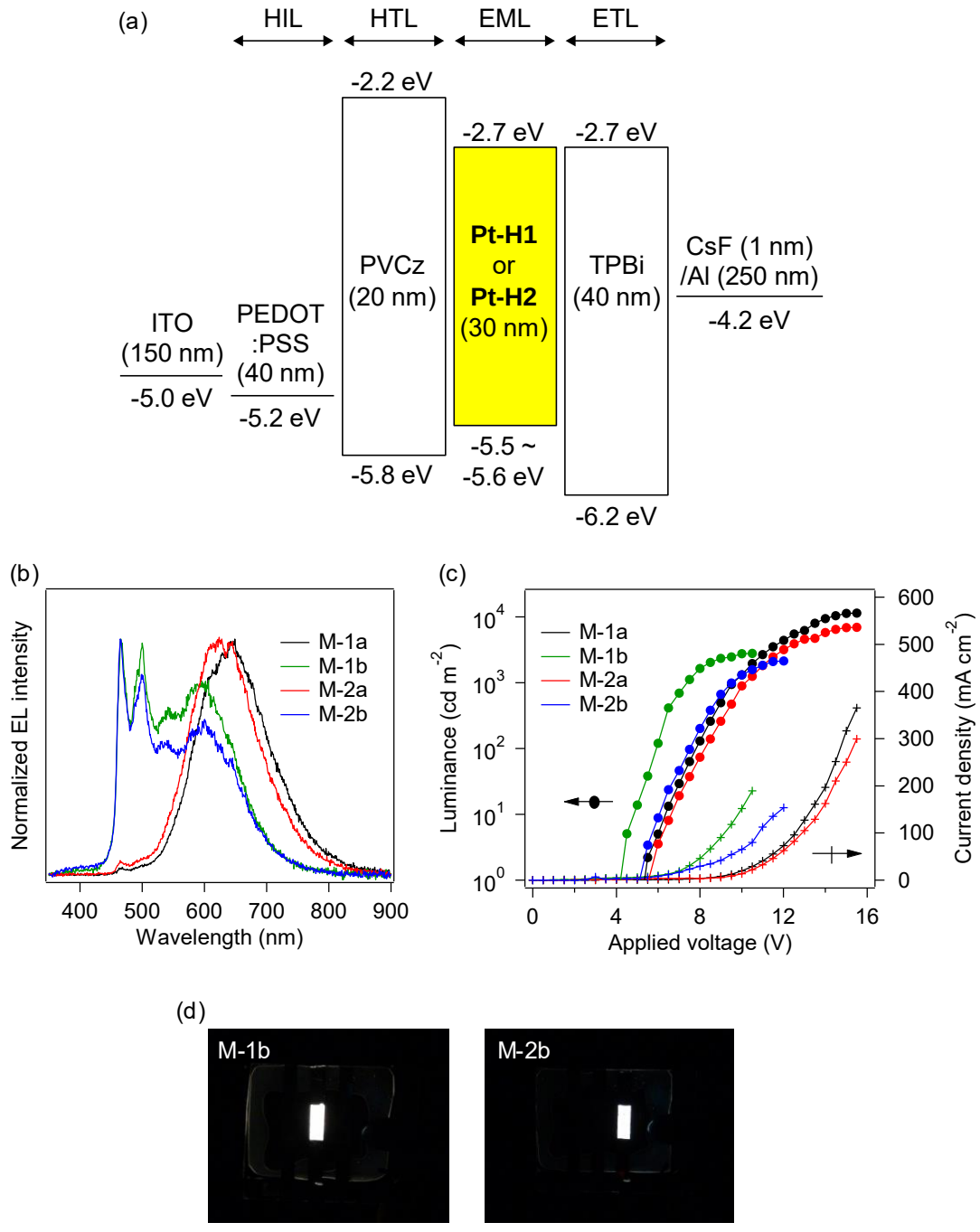

Fig. 6. (a) The device structure of M-1 and M-2. The E_{HOMO}s and E_{LUMO}s of PVCz [22] and TPBi [21] are reported values. (b) EL spectra of M-1 and M-2 at 1000 cd m^{-2}. (c) *J*-*V*-*L* curves of multilayer devices M-1 and M-2. (d) Photographs of emitting devices M-1b and M-2b.

3.2.3. Conclusions

In summary, organoplatinum(II) complexes bearing hole-transporting moieties were synthesized. Their excimer-to-monomer emission intensity ratio was tuned by the bulkiness of the cyclometalated and diketonate ligands, and thus the PL color in the film state was varied from orange to whitish blue *via* white. Their good film forming ability and solubility in the orthogonal solvents allowed us to fabricate non-doped multilayer OLEDs consisting of a stack of HIL/HTL/EML/ETL by solution processing. OLEDs employing the less bulky complexes **Pt-H1a** and **Pt-H2a** showed extremely remarkable excimer-based EL at around 610 nm. The bulkiest complex **Pt-H2b** allowed the author to obtain pseudo-white EL with the CIE chromaticity coordinate of (0.35, 0.40) and the excellent average color rendering index of 81. The author believes that the control of excimer emission of the charge carrier transporting phosphorescent emitter, as demonstrated here, will contribute to the development of low cost white OLED products.

3.2.4. Experimental Section

3.2.4.1. General Procedures

[2-(5-Benzoyl-4,6-difluorophenyl)pyridinato-*N*,$C^{2'}$]platinum(II) acetylacetonate (**Pt-1c**) was prepared as reported in Section 3.1. (3,5-Dibromophenyl)(2,6-difluoro-3-(pyridin-2-yl)-phenyl)methanone (**6**) and (3,3"-bis(3,6-di-*tert*-butyl-9*H*-carbazol-9-yl)-[1,1':3',1"-terphenyl]-5'-yl)(2,6-difluoro-3-(pyridin-2-yl)phenyl)methanone (**H*C*^*N*-H1**) were synthesized according to Section 2.2. 3,6-Di-*tert*-butyl-9*H*-carbazole was prepared as reported in the literature [23]. Poly(9-vinylcarbazole) (PVCz, M_w = 25,000−50,000) was purchased from Sigma-Aldrich Co. LLC., and it was purified by precipitation from a tetrahydrofuran solution (10.0 mg mL^{-1}, filtered through a 0.2 μm ADVANTEC® DISMIC filter) with methanol. The other starting materials and reagents were used as obtained from Wako Pure Chemical

Industries, Ltd., Tokyo Chemical Industry Co., Ltd., or Kanto Chemical Co., Inc. ^{1}H NMR (400 MHz), ^{13}C NMR (100 MHz), and ^{19}F NMR (376 MHz) spectra were obtained on a Jeol ECS-400 or a Jeol ECX-400 spectrometer, using TMS (0.00 ppm) as an internal standard for ^{1}H and ^{13}C NMR and $CFCl_3$ (0.00 ppm) as an external standard for ^{19}F NMR. Matrix-assisted laser desorption/ionization time-of-flight (MALDI-TOF) mass spectra were measured on a Shimadzu-Kratos AXIMA-CFR PLUS TOF mass spectrometer, using α-cyano-4-hydroxycinnamic acid as a matrix. Elemental analyses were carried out on a J-Science MICRO CORDER JM10 analyser.

Photoluminescence (PL) spectra were recorded on a Horiba Jobin Yvon Fluorolog-3 spectrophotometer. PL quantum yields were measured on a Hamamatsu Photonics C9920-12 absolute PL quantum yield measurement system. PL lifetimes were obtained on a Horiba Jobin Yvon FluoroCube spectroanalyzer using a 390 nm nanosecond-order LED light source. The solution samples for optical and photophysical measurements were deaerated by nitrogen bubbling followed by complete sealing, and the analyses were carried out just after sample preparation. For thin film samples, the spectroscopic measurements were carried out under nitrogen atmosphere.

Cyclic voltammogram was measured on a Hokuto Denko HZ-5000 potentiostat for dichloromethane and *N*,*N*-dimethylformamide (DMF) solutions containing tetrabutylammonium perchlorate (TBAP, 0.10 M) as a supporting electrolyte. Platinum wire was used as the working and counter electrodes, and silver wire in contact with $AgNO_3$ (0.1 M in acetonitrile) was used as the reference electrode. The potential value was recorded relative to the ferrocenium/ferrocene (Fc^{+}/Fc) redox couple, which was added to the electrolyte as an external standard.

Density functional theory (DFT) calculation was carried out using the Gaussian 09 program package [19]. The molecular geometry was optimized at the level of B3LYP/LANL2DZ (Ir)

and 6-31G* (C, H, N, O and F).

3.2.4.2. Syntheses and Characterizations

Synthesis of 9,9'-(5-bromo-1,3-phenylene)bis(3,6-di-*tert*-butyl-9*H*-carbazole) (8)

A mixture of 3,6-di-*tert*-butyl-9*H*-carbazole (35.4 g, 127 mmol) and potassium *tert*-butoxide (15.0 g, 134 mmol) in 1,3-dimethyl-2-imidazolidinone (DMI, 90 mL) was heated up to 120 °C. Then 3,5-difluorobromobenzene (12.1 g, 62.7 mmol) was added, and the mixture was stirred at 150 °C for 1 h under a nitrogen atmosphere. After cooling, the reaction mixture was poured into water (200 mL), and a precipitate was formed, which was collected by vacuum filtration. The collected precipitate was consecutively washed with ethanol (200 mL) and ethyl acetate (150 mL) to yield a white solid of **8** (58.5 mmol, 93%). ^{1}H NMR (400 MHz, $CDCl_3$) δ 1.46 (s, 36H), 7.44−7.52 (m, 8H), 7.76 (t, J = 1.8 Hz, 1H), 7.76 (d, J = 1.8 Hz, 2H), 8.13 (d, J = 0.9 Hz, 4H). ^{13}C NMR (100 MHz, $CDCl_3$) δ 32.1, 34.9, 109.2, 116.5, 123.0, 123.9, 123.9, 124.0, 127.7, 138.7, 140.9, 143.8. MALDI-TOF MS: m/z $[M + H]^+$ calcd for $C_{46}H_{52}BrN_2$: 711; found: 711. Anal. calcd for $C_{46}H_{51}BrN_2$: C, 77.62; H, 7.22; N, 3.94. Found: C, 77.28; H, 7.21; N 3.88.

Synthesis of 9,9'-(5-(4,4,5,5-tetramethyl-1,3,2-dioxaborolan-2-yl)-1,3-phenylene)-bis(3,6-di-*tert*-butyl-9*H*-carbazole) (9)

A mixture of compound **8** (5.00 g, 7.03 mmol), bis(pinacolato)diboron (3.91 g, 15.4 mmol), potassium acetate (2.01 g, 20.5 mmol), and [1,1'-bis(diphenylphosphino)ferrocene]-palladium(II) dichloride dichloromethane complex (0.306 g, 0.375 mmol) in dry dimethylsulfoxide (DMSO, 120 mL) was deaerated in vacuo and replaced by nitrogen three times. Then the solution was stirred at 100 °C for 6 h under a nitrogen atmosphere. After cooling, the reaction mixture was poured into water (200 mL), and the precipitate was

collected by vacuum filtration. The collected solid was dried and then purified by silica gel column chromatography using chloroform/hexane (1:1, v/v) as eluent to afford a crude solid of **9**. The solid was washed in refluxed ethanol, and vacuum filtration of the suspension gave a white solid of **9** (4.57 g, 6.02 mmol, 86%). ^{1}H NMR (400 MHz, $CDCl_3$) δ 1.35 (s, 12H), 1.46 (s, 36H), 7.43 (d, J = 8.7 Hz, 4H), 4.20 (dd, J = 8.7 and 1.8 Hz, 4H), 7.83 (t, J = 2.3 Hz, 1H), 8.05 (d, J = 2.3 Hz, 2H), 8.13 (d, J = 1.8 Hz, 4H). ^{13}C NMR (100 MHz, $CDCl_3$) δ 25.0, 32.2, 34.9, 84.4, 109.3, 116.4, 123.6, 123.8, 127.5, 131.4, 132.9, 139.2, 139.3, 143.1. MALDI-TOF MS: m/z $[M]^+$ calcd for $C_{52}H_{63}BN_2O_2$: 759; found: 759. Anal. calcd for $C_{52}H_{63}BN_2O_2$: C, 82.30; H, 8.37; N, 3.69. Found: C, 82.34; H, 8.55; N 3.56.

Synthesis of (2,6-difluoro-3-(pyridin-2-yl)phenyl)(3,3'',5,5''-tetrakis(3,6-di-*tert*-butyl-9*H*-carbazol-9-yl)-[1,1':3',1''-terphenyl]-5'-yl)methanone (H*C*^*N*-H2)

A mixture of the boronate ester **9** (1.84 g, 2.43 mmol), 2-phenylpyridine derivative **6** (0.500 g, 1.10 mmol), bis(triphenylphosphine)palladium(II) dichloride (0.0884 g, 0.126 mmol), and potassium carbonate (4.99 g, 36.1 mmol) in tetrahydrofuran (THF, 20 mL) and water (20 mL) was stirred at 100 °C for 24 h under a nitrogen atmosphere. After cooling, the organic layer was separated, and the aqueous layer was extracted with ethyl acetate (50 mL). The organic solutions were combined together and dried over anhydrous Na_2SO_4. Then the solvent was removed on a rotary evaporator, and the residue was purified by silica gel column chromatography using chloroform/hexane (2:1, v/v) as eluent. Further purification by addition of methanol to a chloroform solution gave a white solid of **H*C*^*N*-H2** (1.18 g, 0.758 mmol, 69%). ^{1}H NMR (400 MHz, $CDCl_3$) δ 1.43 (s, 72H), 7.13 (t, J = 8.2 Hz, 1H), 7.21 (ddd, J = 8.1, 4.9 and 1.2 Hz, 1H), 7.44 (dd, J = 8.7 and 1.8 Hz, 8H), 7.48 (d, J = 8.7 Hz, 8H), 7.58 (td, J = 7.8 and 1.8 Hz, 1H), 7.67 (d, J = 6.9 Hz, 1H), 7.82 (t, J = 1.8 Hz, 2H), 7.86−7.93 (m, 4H), 8.00−8.13 (m, 8H), 8.14−8.25 (m, 4H), 8.66 (d, J = 4.6 Hz, 1H). ^{19}F NMR (376 MHz, $CDCl_3$)

δ −114.9, −110.0. MALDI-TOF MS: *m*/*z* $[M]^+$ calcd for $C_{110}H_{111}F_2N_5O$: 1557; found: 1557. Anal. calcd for $C_{110}H_{111}F_2N_5O$: C, 84.85; H, 7.19; N, 4.50. Found: C, 84.94; H, 7.51; N 4.30.

Synthesis of platinum(II) complexes Pt-1 and Pt-2; the general procedure

A mixture of the 2-phenylpyridine derivative **HC^*N*-X** (**X** = **H1** or **H2**, 0.2 mmol) and potassium tetrachloridoplatinate(II) (0.2 mmol) in a water/THF/2-ethoxyethanol mixed solvent (1:5:10 for **X** = **H1**, 1:10:20 for **X** = **H2**, v/v/v, 16 mL) was stirred at 130 °C for 12 h under a nitrogen atmosphere. After cooling, the reaction mixture was concentrated to a minimum volume on a rotary evaporator, and methanol was added to obtain a white solid. A mixture of the obtained solid, sodium carbonate (2 mmol), and the 1,3-diketone derivative (acetylacetone (2 mmol) or dipivaloylmethane (1 mmol)) in 2-ethoxyethanol (20 mL) was stirred at 100 °C for 6 h under a nitrogen atmosphere. After cooling, the reaction mixture was evaporated to dryness. The residue was dissolved in dichloromethane (25 mL), and the solution was washed with water (25 mL) and sat. $NaCl_{aq}$ and then dried over anhydrous Na_2SO_4. The solvent was removed on a rotary evaporator, and the residue was purified by silica gel column chromatography using dichloromethane/hexane (1:1, v/v) as eluent. Further purification was carried out by recrystallization from dichloromethane-methanol to afford a yellow solid of **Pt-H1** or **Pt-H2**.

[2-(5-(3,3''-Bis(3,6-di-*tert*-butyl-9*H*-carbazol-9-yl)-[1,1':3',1''-terphenyl]-5'-carbonyl)-4,6-difluorophenyl)pyridinato-*N*,$C^{2'}$]platinum(II) acetylacetonate (Pt-H1a). 21% yield. ^{1}H NMR (400 MHz, $CDCl_3$) δ 1.43 (s, 36H), 2.01 (s, 3H), 2.03 (s, 3H), 5.50 (s, 1H), 7.13−7.19 (m, 1H), 7.27 (d, *J* = 9.1 Hz, 1H), 7.36 (d, *J* = 8.6 Hz, 4H), 7.43 (dd, *J* = 8.6 and 1.8 Hz, 4H), 7.56 (td, *J* = 7.3 and 1.8 Hz, 2H), 7.62−7.71 (m, 4H), 7.78−7.84 (m, 3H), 7.97 (d, *J* = 8.2 Hz, 1H), 8.06 (s, 1H), 8.11 (d, *J* = 1.4 Hz, 4H), 8.16 (s, 2H), 9.04 (dd, *J* = 5.9 and 0.9 Hz, 1H). ^{19}F NMR (376 MHz, $CDCl_3$) δ −114.8, −106.8. MALDI-TOF MS: *m*/*z* $[M]^+$ calcd for

$C_{75}H_{71}F_2N_3O_3Pt$: 1295; found: 1295. Anal. calcd for $C_{75}H_{71}F_2N_3O_3Pt$: C, 69.54; H, 5.52; N, 3.24. Found: C, 69.44; H, 5.56; N, 3.01.

[2-(5-(3,3''-Bis(3,6-di-*tert*-butyl-9*H*-carbazol-9-yl)-[1,1':3',1''-terphenyl]-5'-carbonyl)-4,6-difluorophenyl)pyridinato-*N*,$C^{2'}$]platinum(II) dipivaloylmethanate (Pt-H1b). 26% yield. ^{1}H NMR (400 MHz, $CDCl_3$) δ 1.26 (s, 9H), 1.28 (s, 9H), 1.44 (s, 36H), 5.86 (s, 1H), 7.16−7.21 (m, 1H), 7.30 (d, J = 9.2 Hz, 1H), 7.37 (d, J = 8.7 Hz, 4H), 7.44 (dd, J = 8.7 and 1.8 Hz, 4H), 7.57 (td, J = 7.8 and 1.4 Hz, 2H), 7.63−7.71 (m, 4H), 7.79−7.85 (m, 3 H), 7.98 (d, 1H), 8.08 (t, J = 1.8 Hz, 1H), 8.19 (s, 2H), 9.06 (dd, J = 5.5 and 0.9 Hz, 1H). ^{19}F NMR (376 MHz, $CDCl_3$) δ −114.7, −106.6. MALDI-TOF MS: *m*/*z* $[M]^+$ calcd for $C_{81}H_{83}F_2N_3O_3Pt$: 1379; found: 1379. Anal. calcd for $C_{81}H_{83}F_2N_3O_3Pt$: C, 70.52; H, 6.06; N, 3.05. Found: C, 70.78; H, 6.23; N 2.95.

[2-(4,6-Difluoro-5-(3,3'',5,5''-tetrakis(3,6-di-*tert*-butyl-9*H*-carbazol-9-yl)-[1,1':3',1''-terphenyl]-5'-carbonyl)phenyl)pyridinato-*N*,$C^{2'}$]platinum(II) acetylacetonate (Pt-H2a). 30% yield. ^{1}H NMR (400 MHz, $CDCl_3$) δ 1.42 (s, 72H), 1.98 (s, 3H), 2.01 (s, 3H), 5.47 (s, 1H), 7.10−7.15 (m, 1H), 7.25 (1H, masked by $CHCl_3$), 7.44 (dd, J = 8.7 and 1.8 Hz, 8H), 7.48 (d, J = 8.7 Hz, 8H), 7.73−7.79 (m, 1H), 7.81 (t, J = 1.8 Hz, 2H), 7.88 (d, J = 1.8 Hz, 4H), 7.95 (d, J = 8.6 Hz, 1H), 8.08−8.13 (m, 9H), 8.22 (s, 2H), 9.00 (dd, J = 5.9 and 0.9 Hz, 1H). ^{19}F NMR (376 MHz, $CDCl_3$) δ −114.7, −106.4. MALDI-TOF MS: *m*/*z* $[M+H]^+$ calcd for $C_{115}H_{118}F_2N_5O_3Pt$: 1851; found: 1851. Anal. calcd for $C_{115}H_{117}F_2N_5O_3Pt$: C, 74.65; H, 6.37; F, 2.05; N 3.79. Found: C, 74.71; H, 6.20; N 4.03.

[2-(4,6-Difluoro-5-(3,3'',5,5''-tetrakis(3,6-di-*tert*-butyl-9*H*-carbazol-9-yl)-[1,1':3',1''-terphenyl]-5'-carbonyl)phenyl)pyridinato-*N*,$C^{2'}$]platinum(II) dipivaloylmethanate (Pt-H2b). 29% yield. ^{1}H NMR (400 MHz, $CDCl_3$) δ 1.23 (s, 9H), 1.27 (s, 9H), 1.42 (s, 72H), 5.83 (s, 1H), 7.12−7.17 (m, 1H), 7.30 (d, J = 9.2 Hz, 1H), 7.43 (dd, J = 8.7 and 1.8 Hz, 8H), 7.49 (d, J = 8.7 Hz, 8H), 7.73−7.79 (m, 1H), 7.81 (t, J = 1.8 Hz, 2H), 7.89 (d, J = 1.8 Hz, 4H), 7.96 (d, J = 8.2 Hz, 1H), 8.10 (d, J = 1.4 Hz, 8H), 8.13 (t, J = 1.8 Hz, 1H), 8.26 (d, J = 0.9 Hz, 1H), 9.0 (dd, J = 5.7 and 0.9 Hz, 1H). ^{19}F NMR (376 MHz, $CDCl_3$) δ −114.5, −106.3. MALDI-TOF MS: m/z $[M]^+$ calcd for $C_{121}H_{129}F_2N_5O_3Pt$: 1934; found: 1934. Anal. calcd for $C_{121}H_{129}F_2N_5O_3Pt$: C, 75.13; H, 6.72; N, 3.62. Found: C, 74.84; H, 7.00; N 3.97.

Snythesis of 3,3'',5,5''-tetrakis(3,6-di-*tert*-butyl-9*H*-carbazol-9-yl)-1,1':3',1''-terphenyl (Dn-2)

A mixture of the boronate ester **9** (0.507 g, 0.669 mmol), 1,3-dibromobenzene (0.0717 g, 0.304 mmol), bis(triphenylphosphine)palladium(II) dichloride (0.0253 g, 0.0360 mmol) and potassium carbonate (1.38 g, 9.99 mmol) in nitrogen-bubbled THF (5.5 mL) and water (5.5 mL) was stirred at reflux for 36 h under nitrogen atmosphere. After cooling, the organic layer was separated and the aqueous layer was extracted with ethyl acetate (50 mL), and the solvent was removed on a rotary evaporator. The residue was dissolved to chloroform (50 mL) and the solution was washed with water (50 mL) and sat. brine (50 mL), and then dried over anhydrous $MgSO_4$. The solvent was removed on a rotary evaporator, and the residue was purified by silica gel column chromatography using chloroform/hexane (1:4) as eluent to afford a white solid of **Dn-2** (0.123 g, 0.0915 mmol, 30%). ^{1}H NMR (400 MHz, $CDCl_3$) δ 1.43 (s, 72H), 7.44 (dd, J = 8.7 and 1.8 Hz, 8H), 7.50 (d, J = 8.7 Hz, 8H), 7.61 (t, J = 7.7 Hz, 1H), 7.72 (dd, J = 7.7 and 1.8 Hz, 2H), 7.78 (t, J = 1.8 Hz, 2H), 7.88 (d, J = 2.3 Hz, 4H), 7.91 (s, 1H), 8.12 (d, J = 1.8 Hz, 8H). ^{13}C NMR (101 MHz, $CDCl_3$) δ 32.1, 34.8, 109.3, 116.5,

123.4, 123.7, 123.8, 123.9, 126.6, 127.2, 129.9, 139.0, 140.3, 140.8, 143.4, 144.3. MALDI-TOF MS: *m*/*z* $[M]^+$ calcd for $C_{98}H_{106}N_4$: 1340; found: 1340. Anal. calcd for $C_{98}H_{106}N_4$: C, 87.84; H, 7.97; N, 4.18. Found: C, 87.79; H, 8.01; N, 4.16.

3.2.4.3. Fabrication and Evaluation of OLEDs

Devices S-1 and S-2. A pre-patterned ITO glass substrate (thickness of ITO, 150 nm; sheet resistance, *ca*. 10 Ω/square) was cleaned by ultrasonication using a detergent and organic solvents (acetone, chloroform, hexane and 2-propanol), and then treated with UV-O_3. A solution of poly(ethylenedioxy-3,4-thiophene):poly(styrene sulfonate) (PEDOT:PSS, Heraeus Clevios P VP CH8000) in water/2-propanol (1:1, v/v) was filtered through a 0.2 μm ADVANTEC® DISMIC filter (Toyo Roshi Kaisha, Ltd.). The filtrate was spin-coated onto the ITO layer and then dried at 120 °C for 1 h. A solution of **Pt-H1** or **Pt-H2** in chloroform (*ca*. 16 mg mL^{-1}) was filtered through a 0.2 μm DISMIC filter and spin-coated onto the PEDOT:PSS layer, and the prepared stack of films was dried at 100 °C for 30 minutes. Next, cesium fluoride (purchased from Alfa Aesar) and aluminum (purchased from The Niraco Corporation) layers were successively embedded by vacuum deposition. Finally, the fabricated device was covered with a glass cap and encapsulated with a UV-curing epoxy resin to keep oxygen and moisture away. The area of the emitting part was adjusted to 10 mm^2 (2 mm × 5 mm). The device fabrication was carried out in a glove box filled with dry argon, except for the preparation of the PEDOT:PSS layer. The OLED performance was evaluated at room temperature, using a Hamamatsu Photonics C-9920-11 organic EL device evaluating system.

Devices M-1 and M-2. The PEDOT:PSS layer was prepared on the ITO glass substrate by the same procedure as the devices S-1 and S-2. A solution of purified PVCz in dry toluene (5.9 mg mL^{-1}) was filtered through a 0.2 μm ADVANTEC® DISMIC filter. The filtrate was

subjected to spin-coating onto the PEDOT:PSS layer under an argon atmosphere, and the prepared stack of films was dried at 120 °C for 1 h. Thereafter, a solution of **Pt-H1** or **Pt-H2** in cyclohexane (3 mg mL^{-1}) was filtered through a 0.2 μm ADVANTEC® DISMIC filter and spin-coated onto the PVCz layer under an argon atmosphere, and the prepared stack of films was dried at 100 °C for 30 minutes. Next, a solution of 1,3,5-tris(1-phenyl-1*H*-benzo[*d*]imidazol-2-yl)benzene (TPBi, purchased from Luminescence Technology Corp.) in methanol (6.0 mg mL^{-1}) was filtered through a 0.2 μm ADVANTEC® DISMIC filter and spin-coated onto the **Pt-H1** or **Pt-H2** layer under an argon atmosphere, and the prepared stack of films was dried at 80 °C for 10 minutes. Preparation of cesium fluoride and aluminum layers and encapsulation of the device with a glass cap were carried out in the same way as the devices S-1 and S-2, and finally the devices M-1 and M-2 were obtained. The OLED performance of M-1 and M-2 was evaluated under the same conditions as S-1 and S-2.

3.2.5. References

[1] A. Liang, L. Ying and F. Huang, *J. Inorg. Organomet. Polym. Mater.*, 2014, **24**, 905−926.

[2] X. Yang, G. Zhou and W.-Y. Wong, *Chem. Soc. Rev.*, 2015, **44**, 8484−8575.

[3] C. Adachi, M. A. Baldo, M. E. Thompson and S. R. Forrest, *J. Appl. Phys.*, 2001, **90**, 5048−5051.

[4] M. A. Baldo, D. F. O'Brien, Y. You, A. Shoustikov, S. Sibley, M. E. Thompson and S. R. Forrest, *Nature*, 1998, **395**, 151−154.

[5] H. Li, J. Li, J. Ding, W. Yuan, Z. Zhang, L. Zou, X. Wang, H. Zhan, Z. Xie, Y. Cheng and L. Wang, *Inorg. Chem.*, 2014, **53**, 810−821.

[6] F. K.-W. Kong, M.-C. Tang, Y.-C. Wong, M. Ng, M.-Y. Chan and V. W.-W. Yam, *J. Am. Chem. Soc.*, 2017, **139**, 6351−6362.

[7] W.-Y. Wong, Z. He, S.-K. So, K.-L. Tong and Z. Lin, *Organometallics*, 2005, **24**, 4079−4082.

[8] D. Xia, B. Wang, B. Chen, S. Wang, B. Zhang, J. Ding, L. Wang, X. Jing and F. Wang, *Angew. Chem. Int. Ed.*, 2014, **53**, 1048−1052.

[9] Y.-J. Pu, N. Iguchi, N. Aizawa, H. Sasabe, K.-i. Nakayama and J. Kido, *Org. Electron.*, 2011, **12**, 2103−2110.

[10] N. Okamura, T. Maeda and S. Yagi, *New J. Chem.*, 2017, **41**, 10357−10366.

[11] J. W. Levell, W.-Y. Lai, R. J. Borthwick, P. L. Burn, S.-C. Lo and I. D. W. Samuel, *New J. Chem.*, 2012, **36**, 407−413.

[12] L. Duan, L. Hou, T.-W. Lee, J. Qiao, D. Zhang, G. Dong, L. Wang and Y. Qiu, *J. Mater. Chem.*, 2010, **20**, 6392−6407.

[13] D. A. Poulsen, B. J. Kim, B. Ma, C. S. Zonte and J. M. J. Fréchet, *Adv. Mater.*, 2010, **22**, 77−82.

[14] V. Adamovich, J. Brooks, A. Tamayo, A. M. Alexander, P. I. Djurovich, B. W. D'Andrade, C. Adachi, S. R. Forrest and M. E. Thompson, *New J. Chem.*, 2002, **26**, 1171−1178.

[15] D. Kim and J.-L. Brédas, *J. Am. Chem. Soc.*, 2009, **131**, 11371−11380.

[16] T. Shigehiro, S. Yagi, T. Maeda, H. Nakazumi, H. Fujiwara and Y. Sakurai, *J. Phys. Chem. C*, 2013, **117**, 532−542.

[17] N. Okamura, T. Maeda, H. Fujiwara, A. Soman, K. N. N. Unni, A. Ajayaghosh and S. Yagi, *Phys. Chem. Chem. Phys.*, 2018, **20**, 542−552.

[18] N. Okamura, H. Funagoshi, S. Ikawa, S. Yagi, T. Maeda and H. Nakazumi, *Mol. Cryst. Liq. Cryst.*, 2015, **621**, 59−63.

[19] M. J. Frisch, G. W. Trucks, H. B. Schlegel, G. E. Scuseria, M. A. Robb, J. R. Cheeseman, G. Scalmani, V. Barone, B. Mennucci, G. A. Petersson, H. Nakatsuji, M. Caricato, X. Li, H. P. Hratchian, A. F. Izmaylov, J. Bloino, G. Zheng, J. L. Sonnenberg, M. Hada, M. Ehara, K. Toyota, R. Fukuda, J. Hasegawa, M. Ishida, T. Nakajima, Y. Honda, O. Kitao, H. Nakai, T. Vreven, J. A. Montgomery Jr., J. E. Peralta, F. Ogliaro, M. J. Bearpark, J. Heyd, E. N. Brothers, K. N. Kudin, V. N. Staroverov, R. Kobayashi, J. Normand, K. Raghavachari, A. P. Rendell, J. C. Burant, S. S. Iyengar, J. Tomasi, M. Cossi, N. Rega, N. J. Millam, M. Klene, J. E. Knox, J. B. Cross, V. Bakken, C. Adamo, J. Jaramillo, R. Gomperts, R. E. Stratmann, O. Yazyev, A. J. Austin, R. Cammi, C. Pomelli, J. W. Ochterski, R. L. Martin, K. Morokuma, V. G. Zakrzewski, G. A. Voth, P. Salvador, J. J. Dannenberg, S. Dapprich, A. D. Daniels, Ö. Farkas, J. B. Foresman, J. V. Ortiz, J. Cioslowski and D. J. Fox, *Gaussian 09*, Gaussian, Inc., Wallingford, CT, 2009.

[20] X. Hong, L. Yanfang, Z. Wenqing, X. Feng, L. Li, Y. Fangfang, W. Zixing and W. Bin, *J. Phys. D: Appl. Phys.*, 2011, **44**, 415102 (4 pages).

[21] N. Aizawa, Y.-J. Pu, M. Watanabe, T. Chiba, K. Ideta, N. Toyota, M. Igarashi, Y. Suzuri, H. Sasabe and J. Kido, *Nature Commun.*, 2014, **5**, 5756 (7 pages).

[22] M.-H. Kim, M. C. Suh, J. H. Kwon and B. D. Chin, *Thin Solid Films*, 2007, **515**, 4011−4015.

[23] J. Lv, Q. Liu, J. Tang, F. Perdih and K. Kranjc, *Tetrahedron Lett*., 2012, **53**, 5248−5252.

Chapter 4

Luminescent Properties of Novel Bis-cyclometalated Iridium(III) Complex Bearing a Phosphine Oxide-Appended Diketonate Ligand for Solution-Processed Multilayer OLEDs

4.1. Introduction

Organic light-emitting diodes (OLEDs) have been attracting much attention because of applicability to flat panel displays and lighting apparatuses [1,2]. In OLEDs, the excitons are divided into the singlet and triplet states in a 1:3 ratio according to the spin statistics; therefore, normal fluorescent OLEDs can achieve at most an internal quantum efficiency (η_{int}) of 25% for electroluminescence (EL). On the other hand, phosphorescent OLEDs can utilize both singlet and triplet excitons to achieve η_{int} as high as 100% [3], as seen in thermally activated fluorescence-based OLEDs utilizing upconversion of the triplet excitons to the singlets to achieve η_{int} up to 100% [4]. In this term, considerable numbers of phosphorescent OLEDs have so far been fabricated due to availability of highly phosphorescent organometallic complexes [5]. Especially, organoiridium(III) complexes are frequently used as phosphorescent emitters because the spin-orbit coupling caused by the iridium atom facilitates intersystem crossing from the singlet excited state to the triplet excited state to allow us to obtain efficient room-temperature phosphorescence [3]. The emitting layer of an OLED generally consists of charge carrier transporting material(s) doped with an emitter, and more efficient carrier injection into the luminescent center should be achieved when the charge carrier transporting functionality is appropriately appended to the emitter [6]. With this respect, bis- and tris-cyclometalated iridium(III) complexes bearing charge carrier transporting moieties on their cyclometalated ligands have so far been reported [1,6]. There

are, however, only a few reports of bis-cyclometalated iridium(III) complexes bearing an electron-transporting moiety on their diketonate ancillary ligands [7,8]. As demonstrated in a previous report by Leo and co-workers, OLEDs bearing double emitting layer structures (D-EML OLED) should achieve the high device efficiency as well as the long device lifetime. This type of device is, however, generally fabricated by vacuum deposition methods [9]. As reported in Section 2.1, the author demonstrated fabrication of D-EML OLEDs by solution processing, utilizing orthogonal solvents for preparation of the successively stacked emitting layers. Therein, alcohol-soluble organoiridium(III) complexes were essential to fabricate efficient D-EML OLEDs [10]. To the best of the author's knowledge, there are no reports of solution-processed D-EML OLEDs that employ electron-transporting organoiridium(III) complexes as emitting dopants although such emitting materials should give the chance to improve the device performances at convenience. In this study, the author demonstrate preparation of a novel bis(2-phenylpyridinato)iridium(III) complex bearing a phosphine oxide-appended diketonate ligand **Ir-E1** (Fig. 1) as a phosphorescent emitter for a solution-processed OLED. The author expected that the phosphine oxide moieties should add electron-transporting ability [1,2,11] as well as excellent solubility in alcohols [11]. The phosphine oxide-functionalized [1,1':3',1''-terphenyl]-5'-yl group should be distorted from the mean plane of pentan-2,4-dionate by steric hindrance [12], and the $^3\pi$-π^* excitation energy of the ancillary ligand should be kept high [13]. Thus the lowest triplet (T_1) state predominantly consists of triplet metal-to-ligand charge-transfer (^{3}MLCT) transitions, as is often seen in typical phosphorescent organoiridium(III) complexes [14].

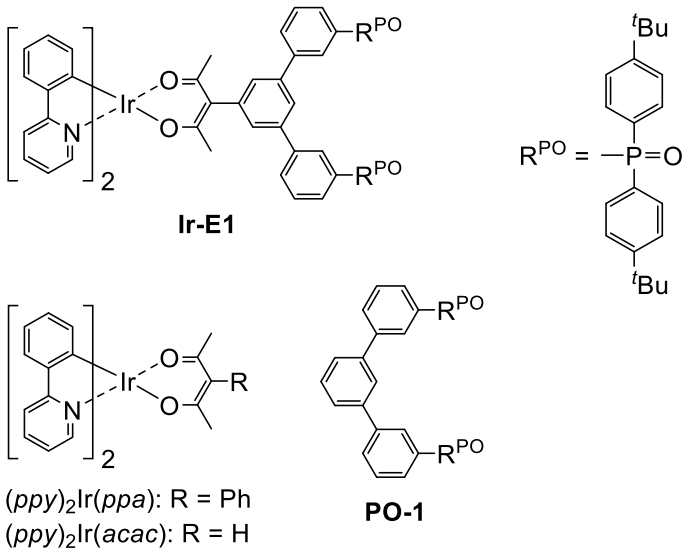

Fig. 1. Chemical structures of **Ir-E1**, $(ppy)_2$Ir(*ppa*), $(ppy)_2$Ir(*acac*) and **PO-1**.

4.2. Results and Discussion

4.2.1. Synthesis and Characterization

The synthesis of **Ir-E1** is shown in Scheme 1. The Pd-catalyzed *P*-arylation [15] of bis(4-*tert*-butylphenyl)phosphine oxide with *m*-diiodobenzene afforded iodo-functionalized triphenylphosphine oxide derivative **10**, which was subjected to the Suzuki coupling with 3,5-bis(4,4,5,5-tetramethyl-1,3,2-dioxaborolan-2-yl)benzaldehyde to give the phosphine oxide dimer **11**. Then the formyl group of **11** was converted to β-ketoenol by the reaction with 2,2,2-trimethoxy-4,5-dimethyl-1,3,2λ^5-dioxaphosphole [16] to obtain **HO^O-1**. Finally **HO^O-1** was reacted with the μ-chloro-bridged bis(2-phenylpyridinato)iridium(III) dimer to afford **Ir-E1**. This novel complex was characterized by ^{1}H NMR, ^{31}P NMR, MALDI-TOF mass spectra, and elemental analysis. An iridium(III) complex without the phosphine oxide moieties $(ppy)_2$Ir(*ppa*) (*ppy*, 2-phenylpyridinate; *ppa*, 3-phenylpentane-2,4-dionate; Fig. 1) and a phosphine oxide dimer **PO-1** (Fig. 1) are also prepared in this study as references. Bis(2-phenylpyridinato-*N*,$C^{2'}$)iridium(III) acetylacetonate $(ppy)_2$Ir(*acac*) (*acac*, acetylacetonate; Fig. 1) was prepared according to the literature [14].

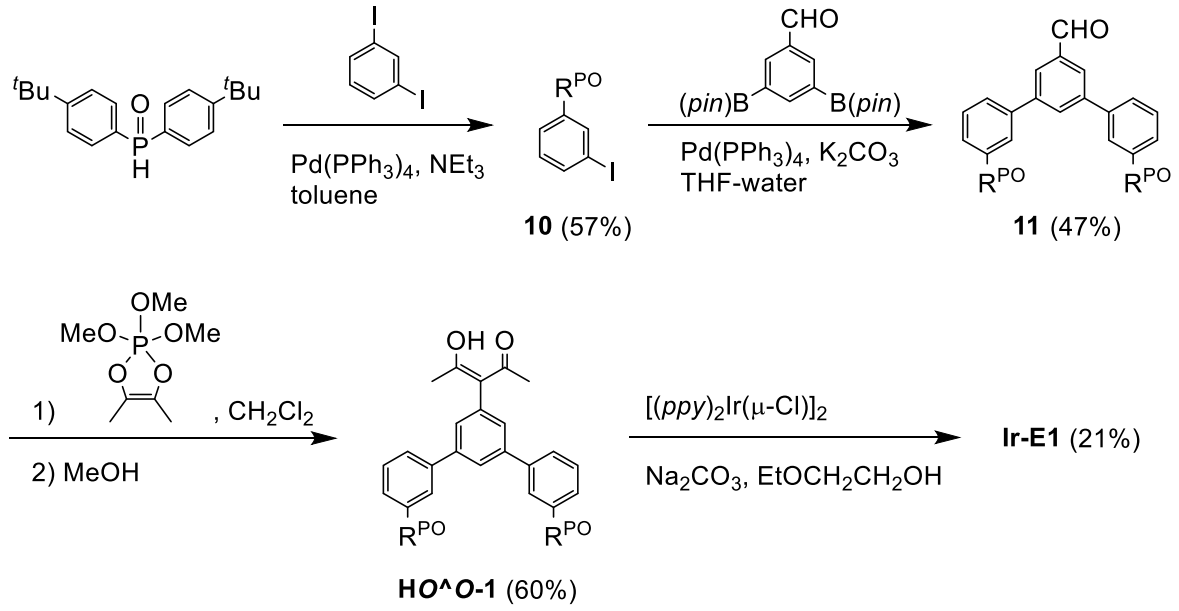

Scheme 1. Synthesis of **Ir-E1**. The ligands *pin* and *ppy* are pinacolate and 2-phenylpyridinate, respectively. The structure of R^{PO} is represented in Fig. 1.

4.2.2. Photoluminescence Properties

Photoluminescence (PL) properties of **Ir-E1**, (*ppy*)$_2$Ir(*ppa*) and (*ppy*)$_2$Ir(*acac*) were obtained in deaerated dichloromethane (concentration, 10 μM; excitation wavelength, 390 nm). PL spectra of **Ir-E1** and (*ppy*)$_2$Ir(*acac*) are shown in Fig. 2, and photophysical properties of all the complexes are listed in Table 1. In the case of **Ir-E1**, green emission was observed at 525 nm, red-shifted by 7 nm in comparison with (*ppy*)$_2$Ir(*acac*). As the PL spectrum of (*ppy*)$_2$Ir(*ppa*) was identical to **Ir-E1**, this red shift is caused by introduction of the 3-phenyl group to *acac*. The PL quantum yield (Φ_{PL}) of **Ir-E1** was determined as 0.33, lower than those of (*ppy*)$_2$Ir(*ppa*) (Φ_{PL}; 0.62) and (*ppy*)$_2$Ir(*acac*) (Φ_{PL}; 0.95). The radiative and nonradiative decay rate constants (k_r and k_{nr}, respectively) of these complexes were calculated from Φ_{PL}s and PL lifetimes (τ_{PL}s). Although the k_rs of these complexes are similar to one another

(0.55−0.59 μs^{-1}), the k_{nr}s are varied: 1.1, 0.36, and 0.030 μs^{-1} for **Ir-E1**, $(ppy)_2Ir(ppa)$ and $(ppy)_2Ir(acac)$, respectively. This clearly indicates that the modification of the diketonate ligand facilitates the nonradiative relaxation. To investigate this nonradiative decay process, density functional theory calculation was performed to optimize the structures of $(ppy)_2Ir(ppa)$ in the S_0 and the T_1 states at the level of UB3LYP/LanL2DZ (for Ir) and 6-31+G(d) (for C, H, N, and O) using the Gaussian 09 program package [17]. The mean plane of the 3-phenyl group in the ancillary ligand was almost orthogonal to the mean plane of the *acac* moiety in both the S_0 and T_1 states (88.8 and 89.8°, respectively), as expected (Fig. 3). This indicates that the nonradiative relaxation is not facilitated by a π-extension of the diketonate ligand to lower the $^3\pi$-π^* transition energy, but by vibrational motions at or around the phenyl group.

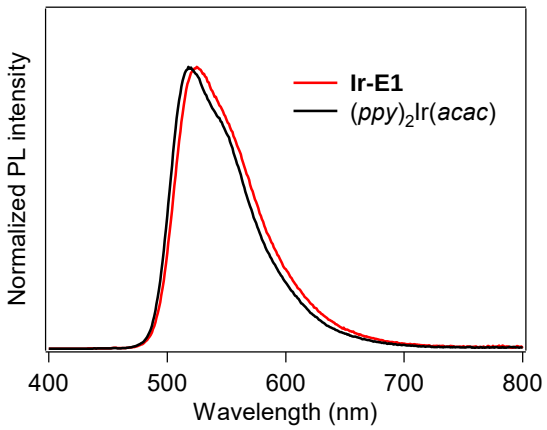

Fig. 2. PL spectra of **Ir-E1** and $(ppy)_2Ir(acac)$ in deaerated dichloromethane (10 μM).

Table 1. Photophysical properties of **Ir-E1**, $(ppy)_2Ir(ppa)$ and $(ppy)_2Ir(acac)$ in deaerated dichloromethane (concentration, 10 μM; excitation wavelength, 390 nm).

Compd	λ_{PL} (nm)	Φ_{PL}	τ_{PL} [a] (μs)	k_r [b] (μs^{-1})	k_{nr} [c] (μs^{-1})
Ir-E1	525	0.33	0.602	0.55	1.1
$(ppy)_2Ir(ppa)$	524	0.62	1.05	0.59	0.36
$(ppy)_2Ir(acac)$	518	0.95	1.65	0.58	0.030

[a]The value of χ^2 was 1.0−1.1. [b]$k_r = \Phi_{PL}/\tau_{PL}$. [c]$k_{nr} = (1 - \Phi_{PL})/\tau_{PL}$.

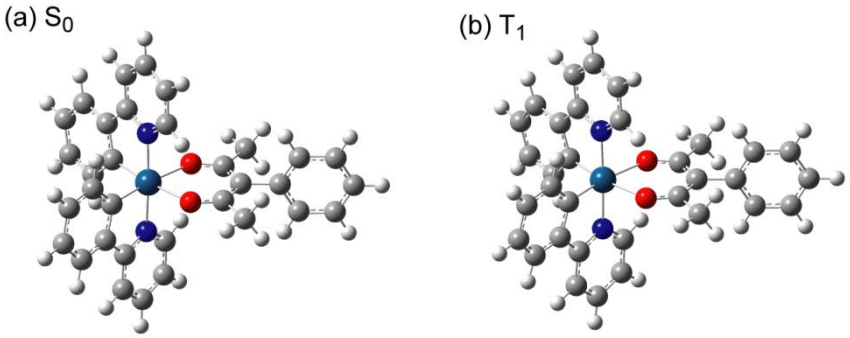

Fig. 3. Optimized structures of $(ppy)_2Ir(ppa)$ in (a) the S_0 and (b) the T_1 states.

4.2.3. Electrochemical Properties

The energy levels of HOMOs (E_{HOMO}) and LUMOs (E_{LUMO}) of **Ir-E1** and $(ppy)_2Ir(acac)$ were obtained by cyclic voltammetry (CV). The voltammograms are shown in Fig. 4 and the data are summarized in Table 2 together with the HOMO-LUMO energy gaps (E_g). The E_{LUMO} of the referential phosphine oxide dimer **PO-1** was also determined by CV. Since **PO-1** showed the irreversible oxidation potential, its E_{HOMO} was calculated using E_{LUMO} and E_g (E_g, estimated from the UV-vis absorption spectral onset of 310 nm). The E_{HOMO} and E_{LUMO} of **Ir-E1** are estimated as −5.10 and −2.17 eV, respectively, which are almost identical to those of $(ppy)_2Ir(acac)$ (E_{HOMO}, −5.12 eV; E_{LUMO}, −2.17 eV) and encapsulated by those of **PO-1** (E_{HOMO}, −6.00 eV; E_{LUMO}, −2.00 eV). This indicates that the HOMO and LUMO of **Ir-E1** are

localized on the $(ppy)_2Ir(acac)$-based luminescent center, and efficient electron injection from phosphine oxide moieties to the luminescent center is expected [2].

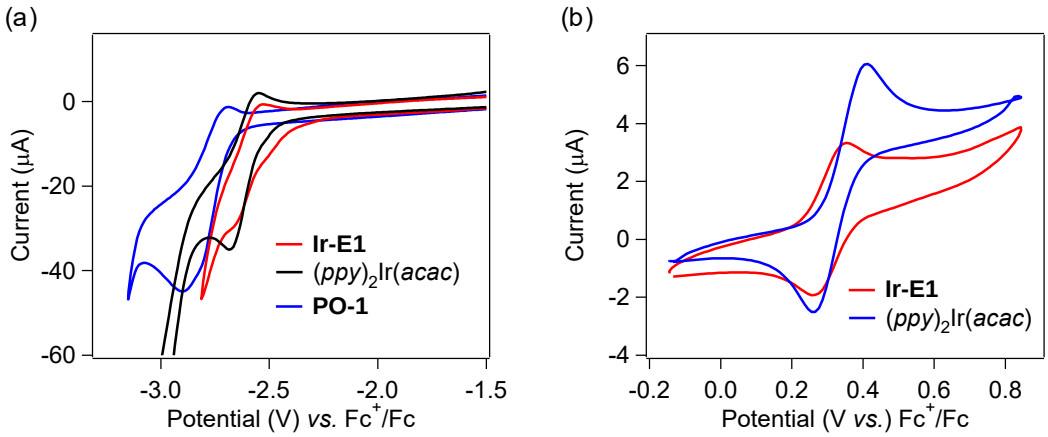

Fig. 4. Cyclic voltammogram of (a) **Ir-E1**, $(ppy)_2Ir(acac)$, and **PO-1** (3.0 mM in dry DMF) for reduction at the scan rate of 1000 mV s^{-1} and of (b) **Ir-E1** and $(ppy)_2Ir(acac)$ (1.0 mM in dry dichloromethane) for oxidation at the scan rate of 100 mV s^{-1}.

Table 2. E_{HOMO}, E_{LUMO}, and E_g of **Ir-E1**, $(ppy)_2Ir(acac)$, and **PO-1**.

Compd	E_{HOMO} (eV)	E_{LUMO}[c] (eV)	E_g (eV)
Ir-E1	−5.10[a]	−2.15	2.95[d]
$(ppy)_2Ir(acac)$	−5.12[a]	−2.17	2.95[d]
PO-1	−6.00[b]	−2.00	4.00[e]

[a] $E_{HOMO} = -((E_{1/2,\,Ox} - E_{1/2,\,Fc}) + 4.80)$, the values of $E_{1/2,\,Ox}$ and $E_{1/2,\,Fc}$ were obtained by CV. [b] $E_{HOMO} = E_{LUMO} - E_g$. [c] $E_{LUMO} = -((E_{1/2,\,red} - E_{1/2,\,Fc}) + 4.80)$, the value of $E_{1/2,\,red}$ was obtained by CV. [d] $E_g = E_{LUMO} - E_{HOMO}$. [e] Estimated from the spectral onset of the UV-vis absorption spectrum.

4.2.4. OLED Fabrication

The author fabricated a D-EML OLED using **Ir-E1** (Device-1), where poly(9-vinylcarbazole) (PVCz) [18], and [1,1':3',1''-terphenyl]-4,4''-diylbis(diphenyl-phosphine oxide) (BPOPB) [11] were used as p- and n-type host materials, respectively. The device structure of Device-1 is as follows; ITO (transparent anode, 150 nm)/PEDOT:PSS (40 nm)/L-1 (40 nm)/L-2 (40 nm)/CsF (1.0 nm)/Al (cathode, 250 nm), where L-1 is an **Ir-E1**-doped PVCz layer (PVCz:**Ir-E1** = 1.0:0.10, wt/wt) and L-2 is an **Ir-E1**-doped BPOPB layer (BPOPB:**Ir-E1** = 1.0:0.10, wt/wt). The energy diagram of Device-1 is also shown in Fig. 5. Good solubility of **Ir-E1** in an orthogonal solvent such as 2-propanol (IPA) enabled us to fabricate the PVCz-BPOPB-stacked D-EML structure by a spin-coating technique: L-2 was directly spin-coated onto IPA-insoluble L-1, using an IPA solution of a mixture of **Ir-E1** and BPOPB. Device-2−4, bearing different compositions of L-1 and/or L-2 were also fabricated as references. In comparison with Device-1, Device-2 has L-1 doped with $(ppy)_2$Ir(*acac*) instead of **Ir-E1**, and Device-3 lacks **Ir-E1** in L-2. In the case of Device-4, $(ppy)_2$Ir(*acac*) was doped into L-1 and no emitter was doped into L-2. The EL spectra and the current density-voltage-luminance (*J-V-L*) curves are shown in Figures 4a and 4b, respectively, and the device performances are summarized in Table 3. All the fabricated OLEDs exhibited green EL around 530 nm, showing almost the same spectral profiles. Device-1 exhibited the highest maximum luminance (L_{max}) of 11000 cd m^{-2} (@12.5 V) and the largest external quantum efficiency ($\eta_{ext,\,max}$) of 2.9% (@9.5 V) among the fabricated devices. In spite of the lower Φ_{PL} of **Ir-E1** than that of $(ppy)_2$Ir(*acac*), Device-1 showed higher performance than Device-2 (L_{max}; 7500 cd m^{-2}, $\eta_{ext,\,max}$; 2.7%). It is assumed at this point that this is due to improvement of the carrier balance in the p-type emitting layer L-1 of Device-1 with the help of the electron-transporting phosphine oxide moiety of **Ir-E1** [19]. Any improvement of OLED performance was not obtained for Device-3 (L_{max}; 5600 cd m^{-2}, $\eta_{ext,\,max}$; 1.6%) and Device-4

(L_{max}; 5200 cd m^{-2}, $\eta_{ext,\ max}$; 1.6%); thus, both doped p- and n-type EMLs are essential to obtain excellent device performance.

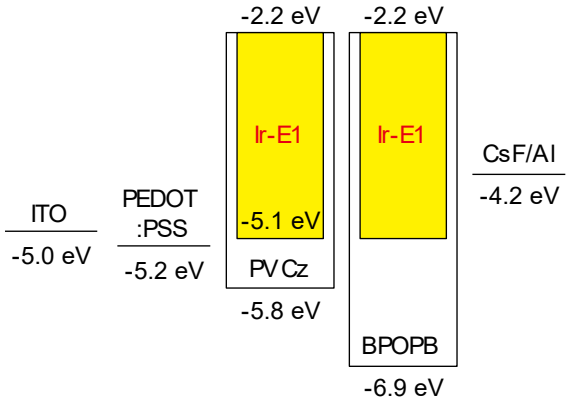

Fig. 5. Energy diagram of Device-1. The highest energy levels of the valence bands of ITO, PEDOT:PSS and Al are reported values [11]. E_{HOMO}s and E_{LUMO}s of PVCz [18], and E_{HOMO} of BPOPB [11] are reported values. E_{LUMO} of BPOPB was determined by CV.

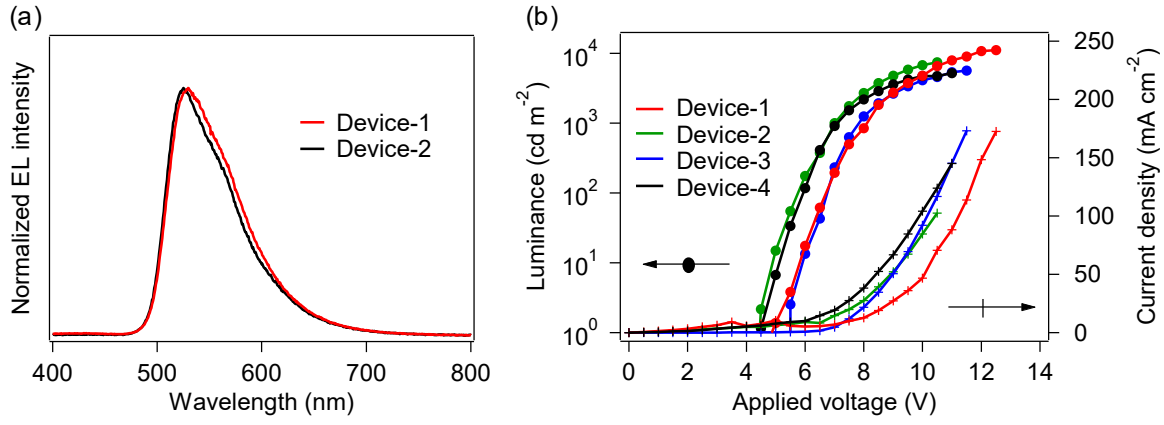

Fig. 6. (a) EL spectra of Device-1 and Device-2 at L_{max} and (b) *J*-*V*-*L* curves of Device-1−4.

Table 3. Device structures and performance of Device-1−4.

Device	L-1	L-2	$V_{\text{turn-on}}$[c] (V)	λ_{EL}[d] (nm)	L_{max} (cd m^{-2}) [@V]	$\eta_{\text{ext, max}}$ (%) [@V]
1	PVCz + **Ir-E1**[a]	BPOPB + **Ir-E1**[b]	5.0	530	11000 [12.5]	2.9 [9.5]
2	PVCz + $(ppy)_2$Ir(*acac*)[a]	BPOPB + **Ir-E1**[b]	4.5	525	7500 [10.5]	2.7 [8.0]
3	PVCz + **Ir-E1**[a]	BPOPB	6.5	531	5600 [11.5]	1.6 [8.0]
4	PVCz + $(ppy)_2$Ir(*acac*)[a]	BPOPB	4.5	528	5200 [11.0]	1.6 [8.0]

[a]PVCz:**Ir-E1** (or $(ppy)_2$Ir(*acac*)) = 10:1, wt/wt. [b]BPOPB:**Ir-E1** (or $(ppy)_2$Ir(*acac*)) = 10:1, wt/wt. [c]The voltage where the luminance more than 1 cd m^{-2} is observed. [d]Maximum EL wavelength at L_{max}.

To confirm the electron-transporting ability of **Ir-E1**, the author fabricated electron-only devices employing a poly(ethyleneimine) (PEI)-coated ITO as a cathode [20,21]. The device structure is as follows: ITO (cathode, 150 nm)/PEI (< 5 nm)/L-3 (70 nm)/CsF (1.0 nm)/Al (anode, 100 nm), where L-3 is a **Ir-E1**-doped (Device-E1) or $(ppy)_2$Ir(*acac*)-doped (Device-E2) PVCz layer (PVCz:**Ir-E1** or $(ppy)_2$Ir(*acac*) = 1.0:0.10, wt/wt) or a neat PVCz layer (Device-E3). The current density of Device-E1 was 1.9−3.1 and 1.9−8.0 times larger than those of Device-E2 and Device-E3, respectively, in a range of 5.0−15.0 V of applied voltage (Fig. 7), indicating that **Ir-E1** showed substantial electron-transporting ability, and thus improved the carrier balance in the p-type emitting layer of the OLEDs as above.

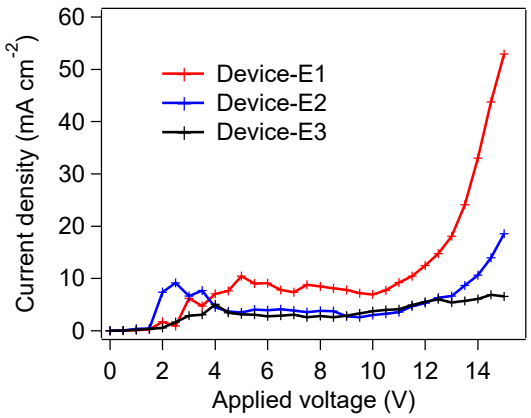

Fig. 7. *J-V* curves of electron-only devices Device-E1−E3.

4.3. Conclusions

In summary, a novel bis-cyclometalated iridium(III) complex bearing a phosphine-oxide-appended diketonate ligand was synthesized. It exhibited green phosphorescence corresponding to emission from an $(ppy)_2$Ir(*acac*)-based luminophore. The energy levels of the frontier orbitals promised efficient electron injection from the phosphine oxide moiety to the luminescent center because the LUMO of the complex is predominantly localized on the iridium core. The OLED bearing both p- and n-type layers doped with the

phosphine oxide-appended complex was fabricated by a spin-coating technique, and it exhibited higher device performance than the device employing the referential complex without any phosphine oxide moieties.

4.4. Experimental Section

4.4.1. General Procedures

Bis(4-(*tert*-butyl)phenyl)phosphine oxide [22], 3,5-bis(4,4,5,5-tetramethyl-1,3,2-dioxaborolan-2-yl)benzaldehyde [23], 2,2,2-trimethoxy-4,5-dimethyl-1,3,2λ^5-dioxaphosphole [24], $[Ir(ppy)_2(\mu\text{-}Cl)]_2$ [14], and [1,1':3',1''-terphenyl]-4,4''-diylbis(diphenyl- phosphine oxide) (BPOPB) [11] are prepared according to reported procedures. Other all starting materials, catalysts, and solvents were purchased from Wako Pure Chemical Industries Ltd. or Tokyo Chemical Industry Co., Ltd.. ^{1}H NMR (400 MHz), ^{13}C NMR (100 MHz), and ^{31}P NMR (162 MHz) spectra were obtained on a Jeol ECS-400 or a Jeol ECX-400 spectrometer, using TMS (0.00 ppm) as an internal standard for ^{1}H and ^{13}C NMR and H_3PO_4 (0.00 ppm) as an external standard for ^{31}P NMR, respectively. Matrix-assisted laser desorption/ionization time-of-flight (MALDI-TOF) mass spectra were measured on a Shimadzu-Kratos AXIMA-CFR PLUS TOF mass spectrometer, using α-cyano-4-hydroxycinnamic acid as a matrix. Elemental analyses were carried out on a J-Science MICRO CORDER JM10 analyzer. UV-vis absorption spectra were recorded on a Shimadzu UV-3600 spectrophotometer. Photoluminescence (PL) spectra were recorded on a Horiba Jobin Yvon Fluorolog-3 spectrophotometer. PL quantum yields were measured on a Hamamatsu Photonics C9920-12 absolute PL quantum yield measurement system. PL lifetimes were obtained on a Horiba Jobin Yvon FluoroCube spectroanalyzer using a 390 nm nanosecond-order LED light source. Cyclic voltammograms were recorded on a Hokuto Denko HZ-5000 electrochemical measurement system. The solution samples for optical and photophysical measurements were deaerated by nitrogen

bubbling followed by complete sealing, and the analyses were carried out just after sample preparation. The OLED performance was operated at room temperature, using a Hamamatsu Photonics C-9920-11 organic EL device evaluating system.

4.4.2. Syntheses and Characterizations

Bis(4-(*tert*-butyl)phenyl)(3-iodophenyl)phosphine oxide (10)

Bis(4-(*tert*-butyl)phenyl)phosphine oxide (2.32 g, 7.38 mmol), 1,3-diiodobenzene (4.87 g, 14.8 mmol), tetrakis(triphenylphosphine)palladium(0) (0.426 g, 0.369 mmol), and triethylamine (0.746 g, 7.38 mmol) in deaerated toluene (14.8 ml) were stirred at 130 °C for 45 min under nitrogen atmosphere. After cooling, the reaction mixture was filtered, and the filtrate was washed with water (50 mL × 2) and sat. brine (50 mL). Then the solvent was removed on a rotary evaporator, and the residue was purified by silica gel column chromatography using ethyl acetate/chloroform (1/6, v/v) as eluent to afford a pale yellow solid of **10** (2.18 g, 4.23 mmol, 57%). ^{1}H NMR (400 MHz, $CDCl_3$) δ 1.32 (s, 18H), 7.17 (dt, J = 7.8 and 2.8 Hz, 1H), 7.48 (dd, J = 8.7 and 2.8 Hz, 4H), 7.53−7.62 (m, 5H), 7.85 (dd, J = 8.2 and 1.4 Hz, 1H), 8.08 (ddd, J = 11.9, 1.4 and 1.4 Hz, 1H). ^{31}P NMR (162 MHz, $CDCl_3$) δ 27.83. MALDI-TOF MS: m/z $[M + H]^+$ calcd for $C_{26}H_{31}IOP$: 517; found: 517. Anal. calcd for $C_{26}H_{30}IOP$: C, 60.47; H, 5.86. Found: C, 60.30; H, 5.89; N, 0.00.

3,3''-Bis(bis(4-(*tert*-butyl)phenyl)phosphoryl)-[1,1':3',1''-terphenyl]-5'-carbaldehyde (11)

To a 4 M aqueous solution of potassium carbonate (4 mL) were added **10** (2.18 g, 4.22 mmol), bis(4,4,5,5-tetramethyl-1,3,2-dioxaborolan-2-yl)benzaldehyde (0.626 g, 1.75 mmol), tetrakis(triphenylphosphine)palladium(0) (0.103 g, 0.0892 mmol), and deaerated THF (20 mL). The obtained mixture was stirred at 80 °C for 12 h under nitrogen atmosphere. After cooling, the organic layer was separated and the aqueous layer was extracted with ethyl

acetate (50 mL × 2). Then the combined organic solution was dried over anhydrous $MgSO_4$. The solvent was removed on a rotary evaporator, and the residue was purified by silica gel column chromatography using ethyl acetate/chloroform (1/3, v/v) as eluent to afford a white solid of **11** (0.508 g, 0.984 mmol, 47%). ^{1}H NMR (400 MHz, $CDCl_3$) δ 1.31 (s, 36H), 7.45−7.65 (m, 20H), 7.77−7.83 (m, 2H), 8.00−8.05 (m, 3H), 8.13 (d, J = 12.2 Hz, 2H), 10.08 (s, 1H). ^{31}P NMR (162 MHz, $CDCl_3$) δ 29.38. MALDI-TOF MS: m/z $[M + Na]^+$ calcd for $C_{59}H_{64}O_3P_2Na$: 905; found: 905. Anal. calcd for $C_{59}H_{64}O_3P_2$: C, 80.24; H, 7.30. Found: C, 80.33; H, 7.33; N, 0.00.

(*Z*)-3-(3,3''-Bis(bis(4-(*tert*-butyl)phenyl)phosphoryl)-[1,1':3',1''-terphenyl]-5'-yl)-4-hydroxypent-3-en-2-one (H*O*^*O*-1)

The benzaldehyde derivative **11** (0.800 g, 0.906 mmol) in dry dichloromethane (6.4 mL) was stirred at rt under nitrogen atmosphere, and then 2,2,2-trimethoxy-4,5-dimethyl-1,3,2λ^5-dioxaphosphole (0.379 g, 1.80 mmol) was added dropwise. The mixture was heated at reflux for 12 h. After that, the volatiles were removed by distillation under reduced pressure, and dry methanol (6.4 mL) was added to the residue. The mixture was heated at reflux for 12 h. The solvent was removed on a rotary evaporator, and the residue was dissolved in chloroform (30 mL) and washed with water (30 mL × 2). The aqueous layer was extracted with chloroform (30 mL × 2), and the combined organic solution was dried over anhydrous $MgSO_4$. The solvent was removed on a rotary evaporator, and the residue was purified by silica gel column chromatography using ethyl acetate/chloroform (2/3, v/v) as eluent. The obtained solid was washed with refluxed hexane to afford a white solid of **H*O*^*O*-1** (0.520 g, 0.546 mmol, 60%). ^{1}H NMR (400 MHz, $CDCl_3$) δ 1.31 (s, 36H), 1.90 (s, 6H), 7.35 (d, J = 1.7 Hz, 2H), 7.45−7.56 (m, 12H), 7.58−7.65 (m, 8H), 7.74 (t, J = 1.7 Hz, 1H), 7.75−7.80 (m, 2H), 8.10 (d, J = 12.6 Hz, 2H), 16.70 (s, 1H). ^{31}P NMR (162 MHz,

$CDCl_3$) δ 29.52. MALDI-TOF MS: *m*/*z* $[M + Na]^+$ $C_{63}H_{70}O_4P_2Na$: 975; found: 975. Anal. calcd for $C_{63}H_{70}O_4P_2$: C, 79.38; H, 7.40. Found: C, 79.64; H, 7.64; N, 0.00.

Bis(2-phenylpyridinato-*N*,$C^{2'}$)iridium(III) 3-(3,3''-bis(bis(4-(*tert*-butyl)phenyl)phosphoryl)-[1,1':3',1''-terphenyl]-5'-yl)pentane-2,4-dionate-O^2,O^4 (Ir-E1)

A mixture of the β-keto-enol **H*O*^*O*-1** (0.0698 g, 0.0732 mmol), $[Ir(ppy)_2(\mu\text{-}Cl)]_2$ (0.0409 g, 0.0381 mmol), and sodium carbonate (0.0415 g, 0.392 mmol) in 2-ethoxyethanol (7.4 mL) were stirred at 80 °C for 1 h under nitrogen. After cooling, the solvent was removed on a rotary evaporator, and then the residue was dissolved in dichloromethane (30 mL) and washed with water (30 mL). The aqueous layer was extracted with dichloromethane (30 mL × 2), and the combined organic solution was dried over anhydrous Na_2SO_4. The solvent was removed on a rotary evaporator, and the residue was purified by alumina gel column chromatography using dichloromethane/ethyl acetate (10/1, v/v) as eluent. The obtained solid was dissolved again to a small amount of dichloromethane. To the solution, hexane was added to afford a yellow solid, which was collected by filtration to obtain **Ir-E1** (0.0219 g, 0.0151 mmol, 21%). ^{1}H NMR (400 MHz, CD_2Cl_2) δ 1.29 (s, 36H), 1.55 (s, 6H), 6.23 (d, *J* = 7.3 Hz, 2H), 6.67 (t, *J* = 7.3 Hz, 2H), 6.83 (t, *J* = 7.3 Hz, 2H), 7.25 (t, *J* = 7.3 Hz, 2H), 7.30 (s, 1H), 7.36 (d, *J* = 1.4 Hz, 2H), 7.44−7.66 (m, 22H), 7.75−7.81 (m, 4H), 7.89 (d, *J* = 8.2 Hz, 2H), 8.04 (d, *J* = 12.4 Hz, 2H), 8.64 (d, *J* = 5.0 Hz, 2H). ^{31}P NMR (162 MHz, CD_2Cl_2) δ 27.62. MALDI-TOF MS: *m*/*z* $[M + H]^+$ calcd for $C_{85}H_{86}IrN_2O_4P_2$: 1454 ;found: 1454. Anal. calcd for $C_{85}H_{85}IrN_2O_4P_2$: C, 70.27; H, 5.90; N, 1.93. Found: C, 70.48; H, 6.15; N, 1.96.

Bis(2-phenylpyridinato-*N*,$C^{2'}$)iridium(III) 3-phenylpentane-2,4-dionate-O^2,O^4 ((*ppy*)$_2$Ir(*ppa*))

A mixture of 3-phenylpentane-2,4-dione (0.062 g, 0.346 mmol), [Ir(*ppy*)$_2$(μ-Cl)]$_2$ (0.150 g, 0.141 mmol), and sodium carbonate (0.865 g, 8.16 mmol) in 2-ethoxyethanol (44 mL) were stirred at 100 °C for 2 h under nitrogen atmosphere. After cooling, the solvent was removed on a rotary evaporator, and then the residue was dissolved in dichloromethane (50 mL) and washed with water (50 mL) and sat. brine (50 mL). The organic solution was dried over anhydrous Na_2SO_4. The solvent was removed on a rotary evaporator, and the residue was purified by alumina gel column chromatography using dichloromethane/hexane (3/1, v/v) as eluent. The solvent was removed on a rotary evaporator, and the obtained solid was washed with hot hexane to afford a yellow solid of (*ppy*)$_2$Pt(*ppa*) (0.084 g, 0.124 mmol, 44%). ^{1}H NMR (400 MHz, $CDCl_3$) δ 1.50 (s, 6H), 6.28 (dd, J = 7.7 and 0.9 Hz, 2H), 6.68 (dt, J = 7.3 and 1.4 Hz, 2H), 6.80 (dt, J = 7.3 and 1.4 Hz, 2H), 7.10 (dd, J = 8.2 and 1.4 Hz, 2H), 7.18−7.23 (m, 3H), 7.29 (ddd, J = 7.3 and 1.4 Hz, 2H), 7.57 (dd, J = 7.7 and 0.91 Hz, 2H), 7.76 (dt, J = 7.7 and 1.6 Hz, 2H), 7.78 (d, J = 8.1 Hz, 2H), 8.66 (dd, J = 5.0 and 0.9 Hz, 2H). ^{13}C NMR (100 MHz, $CDCl_3$) δ 29.64, 115.67, 118.50, 120.62, 121.33, 123.93, 126.28, 128.56, 129.10, 132.36, 133.19, 136.93, 143.40, 144.78, 148.29, 148.46, 168.86, 183.75. MALDI-TOF MS: m/z $[M]^+$ calcd for $C_{33}H_{27}IrN_2O_2$: 676; found: 676. Anal. calcd for $C_{33}H_{27}IrN_2O_2$: C, 58.65; H, 4.03; N, 4.15. Found: C, 58.62; H, 4.15; N, 4.15.

[1,1':3',1''-Terphenyl]-3,3''-diylbis(bis(4-(*tert*-butyl)phenyl)phosphine oxide) (PO-1)

A mixture of **2** (0.508 g, 0.984 mmol), 1,3-benzenediboronic acid (0.0742 g, 0.448 mmol), tetrakis(triphenylphosphine)palladium(0) (0.0280 g, 0.0224 mmol), potassium carbonate (0.618 g, 4.47 mmol), deaerated toluene (4.5 mL), deaerated ethanol (4.5 mL), and deaerated water (2.2 mL) were refluxed for 24 h under nitrogen atmosphere. After cooling, the solvent

was removed on a rotary evaporator, and then the residue was dissolved in chloroform (30 mL) and washed with water (30 mL). The aqueous layer was extracted with chloroform (30 mL × 2), and the combined organic solution was washed with water (30 mL). The organic solution was dried over anhydrous $MgSO_4$. The solvent was removed on a rotary evaporator, and the residue was purified by silica gel column chromatography using ethyl acetate/chloroform (2/1, v/v) as eluent. The residue was washed with a boiled mixture of hexane (5 mL) and ethyl acetate (2 mL) to afford a white solid of **PO-1** (0.156 g, 0.182 mmol, 41%). ^{1}H NMR (400 MHz, $CDCl_3$) δ 1.31 (s, 36H), 7.43−7.59 (m, 15H), 7.59−7.66 (m, 8H), 7.73 (s, 1H), 7.76 (dd, J = 7.6 and 1.4 Hz, 2H), 8.02 (d, J = 12.4 Hz, 2H). ^{31}P NMR (162 MHz, $CDCl_3$) δ 29.41. MALDI-TOF MS: m/z $[M + H]^+$ calcd for $C_{58}H_{65}O_2P_2$: 855; found: 855. Anal. calcd for $C_{58}H_{64}O_2P_2$: C, 81.47; H, 7.54. Found: C, 81.34; H, 7.56; N, 0.00.

4.4.3. Electrochemical Properties

Oxidation and reduction potentials *vs*. the ferrocenium/ferrocene (Fc^+/Fc) redox couple (0.00 V) were determined by cyclic voltammetry (CV) in dry dichloromethane for oxidation and dry DMF (deaerated by nitrogen bubbling) for reduction, where 0.1 M tetrabutyl ammonium perchlorate was used as a supporting electrolyte. The redox potentials were recorded relative to an $Ag/AgNO_3$ (0.1 M in acetonitrile) reference electrode with a platinum wire used for both working and counter electrodes. The scanning rates were 100 mV s^{-1} for oxidation and 1000 mV s^{-1} for reduction.

4.4.4. Fabrication of OLEDs

A pre-patterned ITO (150 nm thickness with sheet resistance of *ca*. 10 Ω/square, Sanyo Vacuum Industries Co., Ltd) glass substrate was cleaned by an ultrasonic cleaner using a detergent and solvents, and then treated with UV-O_3.

Poly(ethylenedioxy-3,4-thiophene):poly(styrene sulfonate) (PEDOT:PSS, Heraeus Clevios P VP CH8000) was spin-coated onto the ITO layer and then dried at 120 °C for an hour. A solution of PVCz (Mw = 25,000−50,000, purchased from Aldrich) and **Ir-E1** (or $(ppy)_2Ir(acac)$) in dry toluene was filtered through a 0.2 μm Millex-FG filter (Millipore Co.). The obtained solution was subjected to spin-coating onto the PEDOT:PSS layer under argon atmosphere, and the prepared films were dried at 120 °C for an hour. Thereafter a solution of BPOPB or a solution of a mixture of BPOPB and **Ir-E1** in dry 2-propanol was filtered through a 0.2 μm Millex-FG filter and spin-coated onto the PVCz layer under argon atmosphere. The prepared films were dried at 80 °C for 10 minutes. Next, cesium fluoride (purchased from Aldrich) and aluminum (purchased from The Niraco Corporation) layers were successively embedded by vacuum deposition. Finally, the device was covered with a glass cap and encapsulated with a UV-curing epoxy resin under dry argon atmosphere to keep oxygen and moisture away. The area of the emitting part was adjusted to 10 mm^2 (2 mm × 5 mm). The device fabrication was carried out in a glove box filled with dry argon, except for the preparation of the PEDOT:PSS layer.

4.4.5. Fabrication of Electron-Only Devices

A pre-patterned ITO (150 nm thickness with sheet resistance of *ca*. 10 Ω/square, Sanyo Vacuum Industries Co., Ltd) glass substrate was cleaned by an ultrasonic cleaner using a detergent and solvents, and then treated with UV-O_3. The ITO glass substrate was immersed into an aqueous solution of poly(ethyleneimine) (PEI, 45 g L^{-1}) for 10 min at 30 °C [21]. After withdrawal, it was washed with water under sonication and then it was dried at 80 °C for an hour. A solution of PVCz or a solution of a mixture of PVCz and **Ir-E1** (or $(ppy)_2Ir(acac)$) was filtered through a 0.2 μm Millex-FG filter and spin-coated onto the PEI-coated ITO under argon atmosphere. The obtained film was dried at 120 °C for an hour.

Next, cesium fluoride and aluminum layers were successively embedded by vacuum deposition. Finally, the device was covered with a glass cap and encapsulated with a UV-curing epoxy resin under dry argon atmosphere to keep oxygen and moisture away. The area of the ITO/PEI/PVCz-based layer/CsF/Al stacked part was adjusted to 10 mm^2 (2 mm × 5 mm). The device fabrication was carried out in a glove box filled with dry argon, except for the PEI-coating of ITO glass substrate.

4.5. Notes and References

[1] X. Yang, G. Zhou, W.-Y. Wong, *Chem. Soc. Rev*., 2015, **44**, 8484−8575.

[2] Y. Tao, C. Yang, J. Qin, *Chem. Soc. Rev*., 2011, **40**, 2943−2970.

[3] C. Adachi, M. A. Baldo, M. E. Thompson, S. R. Forrest, *J. Appl. Phys*., 2001, **90**, 5048−5051.

[4] T. Nakagawa, S.-Y. Ku, K.-T. Wong, C. Adachi, *Chem. Commun*., 2012, **48**, 9580−9582.

[5] H. Xu, R. Chen, Q. Sun, W. Lai, Q. Su, W. Huang, X. Liu, *Chem. Soc. Rev*., 2014, **43**, 3259−3302.

[6] X. Zhang, Z. Chen, C. Yang, Z. Li, K. Zhang, H. Yao, J. Qin, J. Chen, Y. Cao, *Chem. Phys. Lett*., 2006, **422**, 386−390.

[7] L. Chen, J. Ding, Y. Cheng, Z. Xie, L. Wang, X. Jing, F. Wang, *Chem. -Asian J*., 2011, **6**, 1372−1380.

[8] T. Yu, Y. Shi, H. Chai, L. Niu, P. Liu, Y. Zhao, J. Kang, B. Gao, H. Zhang, *RSC Adv*., 2014, **4**, 11680−11688.

[9] X. Zhou, D. S. Qin, M. Pfeiffer, J. Blochwitz-Nimoth, A. Werner, J. Drechsel, B. Meannig, K. Leo, M. Bold, P. Erk, H. Hartmann, *Appl. Phys. Lett*., 2002, **81**, 4070−4072.

[10] N. Okamura, T. Nakamura, S. Yagi, T. Maeda, H. Nakazumi, H. Fujiwara, S. Koseki,

RSC Adv., 2016, **6**, 51435−51445.

[11] N. Aizawa, Y.-J. Pu, M. Watanabe, T. Chiba, K. Ideta, N. Toyota, M. Igarashi, Y. Suzuri, H. Sasabe, J. Kido, *Nat. Commun*., 2014, **5**, 5756 (7 pages).

[12] F. Spaenig, J.-H. Olivier, V. Prusakova, P. Retailleau, R. Ziessel, F. N. Castellano, *Inorg. Chem*., 2011, **50**, 10859−10871.

[13] Ir(*ppy*)$_2$(*dbm*) (*dbm*: dibenzoylmethanate) is almost nonemissive because the T_1 level is a *dbm*-centered excited state. See Ref. 14.

[14] S. Lamansky, P. Djurovich, D. Murphy, F. Abdel-Razzaq, H.-E. Lee, C. Adachi, P. E. Burrows, S. R. Forrest, M. E. Thompson, *J. Am. Chem. Soc*., 2001, **123**, 4304−4312.

[15] B. M. Trost, R. Radinov, *J. Am. Chem. Soc*., 1997, **119**, 5962−5963.

[16] J. B. Lambert, Z. Liu, *J. Chem. Crystallogr*., 2007, **37**, 629−639.

[17] M. J. Frisch, G. W. Trucks, H. B. Schlegel, G. E. Scuseria, M. A. Robb, J. R. Cheeseman, G. Scalmani, V. Barone, B. Mennucci, G. A. Petersson, H. Nakatsuji, M. Caricato, X. Li, H. P. Hratchian, A. F. Izmaylov, J. Bloino, G. Zheng, J. L. Sonnenberg, M. Hada, M. Ehara, K. Toyota, R. Fukuda, J. Hasegawa, M. Ishida, T. Nakajima, Y. Honda, O. Kitao, H. Nakai, T. Vreven, J. A. Montgomery, Jr., J. E. Peralta, F. Ogliaro, M. J. Bearpark, J. Heyd, E. N. Brothers, K. N. Kudin, V. N. Staroverov, R. Kobayashi, J. Normand, K. Raghavachari, A. P. Rendell, J. C. Burant, S. S. Iyengar, J. Tomasi, M. Cossi, N. Rega, N. J. Millam, M. Klene, J. E. Knox, J. B. Cross, V. Bakken, C. Adamo, J. Jaramillo, R. Gomperts, R. E. Stratmann, O. Yazyev, A. J. Austin, R. Cammi, C. Pomelli, J. W. Ochterski, R. L. Martin, K. Morokuma, V. G. Zakrzewski, G. A. Voth, P. Salvador, J. J. Dannenberg, S. Dapprich, A. D. Daniels, Ö. Farkas, J. B. Foresman, J. V. Ortiz, J. Cioslowski, D. J. Fox, *Gaussian 09*, Gaussian, Inc., Wallingford, CT, 2009.

[18] M.-H. Kim, M. C. Suh, J. H. Kwon, B. D. Chin, *Thin Solid Films*, 2007, **515**, 4011−4015.

[19] G. Zhou, Q. Wang, C.-L. Ho, W.-Y. Wong, D. Ma, L. Wang, Z. Lin, *Chem. -Asian J*., 2008, **3**, 1830−1841.

[20] L. Yao, T. Yu, L. Ba, H. Meng, X. Fang, Y. Wang, L. Li, X. Rong, S. Wang, X. Wang, G. Ran, X. Pi, G. Qin, *J. Mater. Chem. C*, 2016, **4**, 673−677.

[21] K. Matsuoka, H. Tahara, T. Akiyama, S. Yamada, *J. Photochem. Photobiol*. A, 2011, **221**, 239−243.

[22] D. Yu, L. Lu, Q. Shen, *Org. Lett*., 2013, **15**, 940−943.

[23] K. Ono, R. Aizawa, T. Yamano, S. Ito, N. Yasuda, K. Johmoto, H. Uekusac, N. Iwasawa, *Chem. Commun*., 2014, **50**, 13683−13686.

[24] R. Naef, A. Jaquier, A. Velluz, B. Maurer, *J. Agric. Food Chem*. 2006, **54**, 9201−9205.

Chapter 5

General Conclusions

In the present study, the author developed phosphorescent organometallic complexes aimed at fabrication of organic light-emitting diodes (OLED), particularly solution-processed multilayer devices. Three subjects were mainly focused on. The first one is establishment of the ligand design of organoiridium(III) complexes to achieve better blue electroluminescence (EL). The second one is evaluation and control of excimer emission from heteroleptic cyclometalated platinum(II) complexes aimed at fabrication of single-emitter white OLEDs. Through these two subjects, the author developed sky-blue phosphorescent bis- and tris-cyclometalated iridium(III) complexes with excellent Φ_{PL}s and highly excimer-emissive heteloleptic cycloemtalated platinum(II) complexes. The developed phosphorescent cores were functionalized with bulky oligocarbazole moieties to add suitable solubility in orthogonal solvents as well as hole-transporting ability, and successfully applied to fabricate non-doped OLEDs bearing double-heterojunction (DH) structures by solution processing. The last subject is functionalization of a green phosphorescent organoiridium(III) complex aimed at fabrication of double-emitting layer (D-EML) OLEDs. Therein, the author found that attachment of a triarylphosphine oxide-appended diketonate ancillary ligand to a bis-cyclometalated iridium(III) phosphorescent center is essential to obtain high solubility in alcohols and electron-transporting ability, and that doping the complex in both p- and n-type EMLs affords an efficient D-EML OLED. The results and findings of this thesis are summarized as follows.

In Chapter 2, the author demonstrated the ligand design for blue phosphorescent organoiridium(III) complexes and functionalization of them to fabricate non-doped multilayer

OLEDs by solution processing.

In Section 2.1, the author developed blue phosphorescent bis- and tris-cyclometalated iridium(III) complexes with excellent photoluminescence (PL) quantum yields (Φ_{PL}). It was found that fluorination of a 2-(5-benzoylphenyl)pyridinate ligand is effective to make their maximum PL wavelength (λ_{PL}) blue-shifted. Among a series of bis-cyclometalated complexes, a picolinate complex **Ir-3b** bearing two 2-(4,6-difluoro-5-benzoylphenyl)pyridinate cyclometalated (*C^N*) ligands exhibited the most blue-shifted λ_{PL} of 464 nm with an excellent Φ_{PL} of 0.82 in deaerated dichloromethane. Further ligand replacement with the identical *C^N* ligand afforded a facial isomer of a homoleptic tris-cyclometalated complex (**Ir-3c**), which exhibited λ_{PL} of 463 nm and Φ_{PL} of 0.90. From the results of electrochemical study and theoretical calculation, the author revealed that the blue-shifted emission is mainly brought about by stabilization of the highest occupied molecular orbital. Using **Ir-3b** and **Ir-3c** as emitting dopants, the author obtained sky-blue D-EML OLEDs with excellent device efficiency.

In Section 2.2, the author functionalized **Ir-3b** and **Ir-3c** with 3,6-di-*tert*-butylcarbazole-appended hole-transporting dendrons, aimed at fabrication of multilayer non-doped OLEDs by solution processing. These dendritic complexes exhibited sky-blue phosphorescence from their luminescent cores even in the neat film state due to suppression of aggregate formation by sterically hindered dendrons. In addition, the author found efficient energy transfer occurs from the dendrons to the luminescent core. The author successfully fabricated DH-type OLEDs employing the neat films of the dendritic complexes, where sucsessive spin-coating of the EML and the ETL by utilizing the solubility of the dendritic emitters in orthogonal solvents such as cyclohexane and 2-propanol allowed him to obtain the target devices. The devices showed an excellent electron-hole charge balance factor of *ca*. 0.9. Therefore, the author concluded that liposoluble and alcohol-insoluble

phosphorescent emitters have great potential for high performance non-doped OLEDs with multi-stacked structures.

In Chapter 3, the author photokinetically elucidated the excimer emission behavior of heteroleptic cyclometalated platinum(II) complexes and revealed that how the excimer emission is controlled by the *C^N* ligand modification. Also, using the highly excimer-emissive complex, he fabricated single-emitter-doped white OLEDs.

In Section 3.1, the author investigated PL properties of novel heteroleptic cyclometalated platinum(II) complexes consisting of 5'-benzoylated 2-phenylpyridinate *C^N* and acetylacetonate ancillary (*O^O*) ligands, focusing on their remarkable excimer emission at *ca*. 600 nm along with monomer emission at the blue−green region. From the kinetic analysis of the PL decay, the author found that introduction of a benzoyl group to the 5'-position of the 2-phenylpyridinate ligand facilitates the excimer emission formation process. The author also found that combination of fluoro group(s) with the 5'-benzoyl group affords further facilitation of the excimer emission, and thus the complex with 2-(5-benzoyl-4,6-difluorophenyl)pyridinate as the *C^N* ligand (**Pt-1c**) exhibited the most remarkable excimer emission and the most blue-shifted monomer emission among the discussed complexes. Using **Pt-1c** as a single emitting dopant, a pseudo-white OLED with the Commission Internationale de L'éclairage (CIE) chromaticity coordinate of (0.42, 0.42) was successfully fabricated when the doping level of **Pt-1c** in EML was optimized.

In Section 3.2, the author functionalized **Pt-1c** with hole-transporting oligocarbazole moieties to fabricate non-doped white OLEDs bearing a DH structure, using the technique developed in Section 2.2. As the author expected, the monomer-to-excimer emission ratio was controlled by bulkiness of the *C^N* and *O^O* ligands so that the PL color was varied from excimer-dominated orange to monomer-rich bluish white *via* white. The author fabricated non-doped DH-type OLEDs with the developed complexes, taking advantage of their

solubility in cyclohexane and insolubility in methanol. When the bulkiest complex was used as the EML, the device exhibited balanced monomer and excimer emissions whose spectra covered the whole visible region, and thus pseudo-white EL with the CIE chromaticity coordinate of (0.35, 0.40) was afforded, accompanied by the excellent average color rendering index of 81.

In Chapter 4, the author synthesized a novel bis-cyclometalated iridium(III) complex, **Ir-E1**, bearing a triarylphosphine oxide-appended diketonate ligand aimed at fabrication of D-EML OLEDs. The developed complex exhibited green phosphorescence based on the organoiridium(III) luminescent center. Because **Ir-E1** is soluble in lower alcohols due to its highly polar phosphine oxide moieties, the author successfully fabricated D-EML OLEDs by spin-coating a 2-propanol solution of a mixture of **Ir-E1** and an alcohol-soluble electron-transporting material on alcohol-insoluble p-type EML to prepare n-type EML. The D-EML devices showed improved external quantum efficiencies (η_{ext}) in comparison with single EML devices. In addition, the device doped with **Ir-E1** in both p- and n-type EMLs showed a higher η_{ext} than that with the reference complex bearing no triarylphosphine oxide moieties, in spite of the lower Φ_{PL} of **Ir-E1**. The author revealed that the relatively high device efficiency is due to electron-transporting ability of the triarylphosphine oxide-appended diketonate ligand to facilitate the charge recombination in the EMLs.

From the results described above, the author concludes that it is effective in fabrication of solution-processed multilayer OLEDs to functionalize phosphorescent organometallic complexes with charge carrier transporting moieties controlling the solubility in orthogonal solvents. The author has also demonstrated that ligand design to obtain electronic and steric effects is essential to tune the luminescent color: tuning of emission peak as well as suppression of aggregation was achieved for organoiridium(III) complexes, and facilitation of emissive excimer formation as well as control of the excimer-to-monomer emission ratio was

also achieved for organoplatinum(II) complexes. The author believes that the present study will not only make a great contribution to further development of organic optoelectronic devices with improved performances but also give valuable insights into photochemistry of organometallic complexes.

Acknowledgements

The author would like to express his sincere appreciation to his supervisor, Professor Shigeyuki Yagi, for his enthusiastic guidance and advice throughout this work. The author would also like to express his gratitude to Professor Akikazu Matsumoto and Professor Hiroshi Ikeda for their valuable comments and discussions.

The author also expresses his heartfelt thanks to Associate Professor Takeshi Maeda for his kind supports and meaningful discussions. The author appreciates Professor Hideki Fujiwara for his technical support in X-ray crystallographic analysis and Professor Shiro Koseki for his valuable suggestion about theoretical calculations. The author also appreciates Professor Ayyappanpillai Ajayaghosh for his valuable discussions about intermolecular interactions and Dr. K. N. Narayanan Unni for his technical support in fabrication of OLEDs.

The author really thanks to his co-workers, Dr. Shigeru Ikawa, Dr. Tatsuya Shigehiro, Messes. Hiroshi Funagoshi, Miho Miyazaki, Taiyo Nakamura, Kazuaki Egawa, Kazuya Ishiguro, Ayaka Ban, Yuichiro Hayashi, Hiroki Matsuura, Yuya Takahashi, Kohei Yamashita, Ryosuke Hiraoka, Ryota Kono, Yusuke Goto, Gyoshin Motiduki, Haruka Arizono, and Satoshi Ueda for their kind supports and valuable suggestions, and all the members of Professor Yagi's laboratory for their helpful comments and heartwarming encouragement.

Naoki Okamura

Department of Applied Chemistry

Graduate School of Engineering

Osaka Prefecture University

Osaka, Japan

February, 2018

List of Publications

Chapter 2, Section 2.1

Naoki Okamura, Taiyo Nakamura, Shigeyuki Yagi, Takeshi Maeda, Hiroyuki Nakazumi, Hideki Fujiwara and Shiro Koseki

"Novel Bis- and Tris-Cyclometalated Iridium(III) Complexes Bearing a Benzoyl Group on Each Fluorinated 2-Phenylpyridinate Ligand Aimed at Development of Blue Phosphorescent Materials for OLED"

RSC Adv., 2016, **6**, 51435−51445.

Chapter 2, Section 2.2

Naoki Okamura, Takeshi Maeda and Shigeyuki Yagi

"Sky-blue Phosphorescence from Bis- and Tris-Cyclometalated Iridium(III) Complexes Bearing Carbazole-based Dendrons: Fabrication of Non-Doped Multilayer Organic Light-Emitting Diodes by Solution Processing"

New J. Chem., 2017, **41**, 10357−10366.

Chapter 3, Section 3.1

Naoki Okamura, Takeshi Maeda, Hideki Fujiwara, Anjaly Soman, K. N. Narayanan Unni, Ayyappanpillai Ajayaghosh and Shigeyuki Yagi

"Photokinetic Study on Remarkable Excimer Phosphorescence from Heteroleptic Cyclometalated Platinum(II) Complexes Bearing a Benzoylated 2-Phenylpyridinate Ligand"

Phys. Chem. Chem. Phys., 2018, **20**, 542−552.

Chapter 3, Section 3.2

Naoki Okamura, Kazuaki Egawa, Takeshi Maeda and Shigeyuki Yagi

"Control of Excimer Phosphorescence by Steric Effects in Cyclometalated Platinum(II) Diketonate Complexes Bearing Oligocarbazole Moieties towards Application to Non-Doped White OLED"

ChemPhotoChem, submitted.

Chapter 4

Naoki Okamura, Kazuya Ishiguro, Takeshi Maeda and Shigeyuki Yagi

"Luminescent Properties of Novel Bis-Cyclometalated Iridium(III) Complex Bearing a Phosphine Oxide-Appended Diketonate Ligand for Solution-Processed Multilayer OLEDs"

Chem. Lett., 2017, **46**, 1086−1089.

Other related publications

Naoki Okamura, Hiroshi Funagoshi, Shigeru Ikawa, Shigeyuki Yagi, Takeshi Maeda and Hiroyuki Nakazumi

"Starburst-Type Carbazole Trimers as Host Materials for Solution-Processed Phosphorescent OLEDs"

Mol. Cryst. Liq. Cryst., 2015, **621**, 59−63.

Naoki Okamura, Miho Miyazaki, Shigeru Ikawa, Taiyo Maeda, Hiroyuki Nakazumi and Shigeyuki Yagi

"Luminescent Properties of Novel Bis-Cyclometalated Iridium(III) Complexes Bearing Methoxy-Substituted Dibenzoylmethanate Ligands"

Mol. Cryst. Liq. Cryst., 2017, **653**, 131−136.